

Multiphase Mass Transfer and Capillary Properties of Gas Diffusion  
Layers for Polymer Electrolyte Membrane Fuel Cells

by  
Jeff Gostick

A thesis  
presented to the University of Waterloo  
in fulfillment of the  
thesis requirement for the degree of  
Doctor of Philosophy  
in  
Chemical Engineering

Waterloo, Ontario, Canada, 2008

©Jeff Gostick 2008

## **Author's Declaration**

I hereby declare that I am the sole author of this thesis. This is a true copy of the thesis, including any required final revisions, as accepted by my examiners.

I understand that my thesis may be made electronically available to the public.

---

## Abstract

A detailed understanding of mass transport and water behavior in gas diffusion layers (GDLs) for polymer electrolyte membrane fuel cells (PEMFCs) is vital to improving performance. Liquid water fills the porous GDL and electrode components, hindering mass transfer, limiting attainable power and decreasing efficiency. The behavior of liquid water in GDLs is poorly understood, and the specific nature of mass transfer of multiphase flow in GDLs are not known. There is no clear direct correlation between easily measurable ex-situ GDL material properties and mass transfer characteristics. This thesis addresses this knowledge gap through a combination of test procedure development, experimentation and numerical pore scale modeling. Experimental techniques have been developed to measure permeability and capillary properties of water and air in the GDL matrix. Pore network modeling is used to estimate transport properties as a function of GDL water saturation since these are extremely difficult to determine experimentally.

A method and apparatus for measuring the relationship between air-water capillary pressure and water saturation in PEMFC gas diffusion layers is described. The developed procedure of Gas Controlled Porosimetry is more effective for understanding the behaviour of water in GDL material than traditional methods such as the method of standard porosimetry and mercury intrusion porosimetry. Capillary pressure data for water injection and withdrawal from typical GDL materials are obtained, which demonstrated permanent hysteresis between water intrusion and water withdrawal. Capillary pressure, defined as the difference between the water and gas pressures at equilibrium, is positive during water injection and negative during water withdrawal. The results contribute to the understanding of liquid water behavior in GDL materials which is necessary for the development of effective PEMFC water management strategies and the design of future GDL materials.

The absolute gas permeability of GDL materials was measured. Measurements were made in three perpendicular directions to investigate anisotropic properties of various materials. Most materials were found to be significantly anisotropic, with higher in-plane permeability than through-plane permeability. In-plane permeability was also measured as the GDL was

compressed to different thicknesses. Typically, compression of a sample to half its initial thickness resulted in a decrease in permeability by an order of magnitude. The relationship between measured permeability and compressed porosity was compared to various models available in the literature, one of which allows the estimation of anisotropic tortuosity. The results of this work will be useful for 3D modeling studies where knowledge of permeability and effective diffusivity tensors is required.

A pore network model of mass transport in GDL materials is developed and validated. The model idealizes the GDL as a regular cubic network of pore bodies and pore throats following respective size distributions of the pores. With the use of experimental data obtained the geometric parameters of the pore network model were calibrated with respect to porosimetry and gas permeability measurements for two common GDL materials. The model was subsequently used to compute the pore-scale distribution of water and gas under drainage conditions using an invasion percolation algorithm. From this information, transport properties of GDLs that are very difficult to measure were estimated, including the relative permeability of water and gas, and the effective gas diffusivity as functions of water saturation. Comparison of the model predictions with those obtained from constitutive relationships commonly used in current PEMFC models indicates that the latter may significantly overestimate the gas phase transport properties.

The pore network model was also used to calculate the limiting current in a PEMFC under operating conditions for which transport through the GDL dominates mass transfer resistance. The results suggest that a dry GDL does not limit the performance of a PEMFC, but water flooding becomes a significant source of concentration polarization as the GDL becomes increasingly saturated with water.

This work has significantly contributed to the understanding of mass transfer in gas diffusion layers in PEMFC through experimental investigation and pore scale modeling.

## Acknowledgements

I am very thankful to my advisors Michael Fowler and Mark Pritzker for all the time and support they have given me over the last 4 years. I consider myself very fortunate to have had such supportive and knowledgeable people whom I could approach without hesitation for help and advice. Their endless efforts securing funding for maintaining the lab, supplying equipment and paying me made this work possible.

I greatly appreciate the efforts of my committee members Dr. Richard Culham, Dr. Leonardo Simon, Dr. Marios Ioannidis and Dr. David Wilkinson, who contributed their valuable time to scrutinize me and my work and helped me produce the best possible results. I am especially grateful to Dr. Marios Ioannidis who has shown a keen personal interest in this project as well as my development. His input has been invaluable and his inexhaustible knowledge of porous media, infectious enthusiasm and exemplary academic standards elevated this project to new heights and inspired me to new heights as well.

My lab mates and fellow PhD students Sumit Kundu and Matt Stevens have been the best colleagues I could have hoped for and will be great friends for life. Sumit showed me the true meaning of dedication and hard work, always pretending to care about my research and taught me to lighten up. Matt is a whirlwind of activity, aspirations and ambitions and it has been a privilege to work with him.

I would also like to thank my parents who never once questioned the wisdom of spending 11 years in post secondary education and never hesitated to help in any and every way. The value of your support and of your belief in me is immeasurable.

Finally, I apologize to my fiancée Lisa Lachuta for neglecting her for the last 4 years and spending way too much time in the lab and the office. You always make me smile, no matter how badly things go. Let's get married.

# Table of Contents

List of Figures .....	x
List of Tables .....	xvii
Nomenclature .....	xviii
Abbreviations .....	xxii
1. Introduction and Background .....	1
1.1. Fuel Cell Background .....	2
1.1.1. Electrochemistry .....	2
1.1.2. Operation.....	4
1.1.3. Fuel Cell Internal Components and Transport Processes .....	7
1.1.4. Gas Diffusion Layer.....	8
1.1.5. The Microporous Layer .....	10
1.1.6. Limiting Current .....	11
1.1.7. Water Management .....	12
1.2. Outline of Thesis.....	13
2. Literature Review and Theory .....	15
2.1. Capillarity, Wettability and Contact Angle .....	18
2.2. Capillary Pressure Curves.....	25
2.3. Breakthrough Point and Percolation .....	36
2.4. Absolute Permeability.....	40
2.5. Relative Permeability .....	44
2.6. Effective Diffusivity .....	47
2.7. Relative Effective Diffusivity .....	49
3. Experimental .....	51
3.1. GDL Materials .....	51
3.2. Porosimetry .....	53
3.2.1. Mercury Intrusion Porosimetry.....	53
3.2.2. Method of Standard Porosimetry .....	54
3.2.3. Gas Controlled Porosimetry.....	57
3.2.3.1. Sample Holder .....	60

3.2.3.2.	Sample Mounting.....	62
3.2.3.3.	System Setup.....	63
3.2.3.4.	Procedure .....	63
3.2.3.5.	Data Analysis .....	65
3.3.	Water Breakthrough .....	68
3.4.	Single Point Injection.....	69
3.5.	Contact Angle.....	70
3.6.	Permeability .....	73
3.6.1.	Through-Plane Permeability .....	73
3.6.2.	In-Plane Permeability.....	74
3.6.3.	Data Analysis .....	76
3.6.4.	GDL Compression and Porosity Conversion.....	80
4.	Pore Network Modeling.....	82
4.1.	Cubic Lattice Pore Network Model .....	83
4.1.1.	Pore Network Construction.....	84
4.1.1.1.	Pore and Throat Size Distributions .....	84
4.1.1.2.	Spatial Correlation of Pores Sizes.....	87
4.1.2.	Capillary Pressure .....	89
4.1.3.	Late Pore Filling .....	89
4.1.4.	Drainage Simulation .....	90
4.1.5.	Transport Processes in the Network.....	91
4.1.5.1.	Convection .....	91
4.1.5.2.	Diffusion .....	92
4.1.5.3.	Multiphase Transport .....	93
4.1.6.	Model Calibration .....	95
4.1.6.1.	Pore and Throat Size Distribution.....	95
4.1.6.2.	Lattice Constant .....	98
4.1.6.3.	Absolute Permeability.....	100
4.1.7.	Model Validation.....	100
4.1.7.1.	Effective Diffusivity .....	100
4.1.7.2.	Liquid Water Injection .....	101

5.	Results and Discussion .....	102
5.1.	Porosimetry .....	102
5.1.1.	Mercury Intrusion Porosimetry.....	102
5.1.2.	Method of Standard Porosimetry .....	104
5.1.3.	Gas Controlled Porosimetry.....	109
5.1.3.1.	Comparison of GCP with Literature Data.....	111
5.1.3.2.	Comparison Between MIP, MSP and GCP .....	114
5.1.3.3.	Effect of PTFE on Air-Water Capillary Curves .....	116
5.1.3.4.	Effect of GDL Thickness .....	123
5.1.3.5.	Analysis of Capillary Pressure Hysteresis .....	128
5.1.3.6.	Wettability Index.....	134
5.1.3.7.	Water Breakthrough Point.....	138
5.2.	The Role of the Microporous Layer.....	141
5.2.1.	Percolation Concepts .....	142
5.2.2.	Experimental Evidence .....	144
5.3.	Absolute Permeability.....	147
5.3.1.	In-plane Permeability.....	147
5.3.2.	Through-Plane Permeability .....	151
5.3.3.	Inertial Coefficient .....	152
5.4.	Tortuosity .....	155
5.5.	Relative Permeability.....	156
5.6.	Relative Effective Diffusivity .....	161
5.7.	Limiting Current Calculations .....	163
6.	Conclusions.....	167
6.1.	Recommendations and Future Work.....	170
6.1.1.	Random pore network model.....	170
6.1.2.	Full fuel cell pore network modeling.....	170
6.1.3.	Heat transfer and condensation.....	171
6.1.4.	Repeatability of GCP method .....	171
6.1.5.	GDL hydrophobic coating .....	172
6.1.6.	GDL Degradation.....	172

6.1.7. Capillary properties of GDLs under compression .....	172
6.1.8. In-situ GDL testing .....	172
References.....	174
Appendices	
Appendix A. Related Publications.....	194
A.1. Refereed Journal Articles .....	194
A.2. Conference Presentations.....	194
Appendix B. SEM Images of GDLs.....	196

## List of Figures

Figure 1.1:	Galvanic cell representative of the PEM fuel cell.....	3
Figure 1.2:	Left: Typical polarization curves showing the additive contribution of each type of voltage losses. The limiting current is 1.25 A/cm <sup>2</sup> . Right: Power density curves showing the interplay between power generated and cell current. ....	6
Figure 1.3:	Schematic of fuel cell internal components. The section shown represents a single repeating unit that can be placed in series to form a high voltage stack. Typical dimensions are shown. ....	8
Figure 1.4:	SEM Images of Toray 090A GDL surface. Left: 100x magnification. Right: 1000x magnification.....	9
Figure 1.5:	SEM images of microporous layer. Left: Surface view. Right: Cross-section.....	11
Figure 2.1:	Capillary action between a solid tube and 2 fluids . Fluid 1 is wetting on Solid 1, but not Solid 2.....	18
Figure 2.2:	Definition of wetting and non-wetting phase based on solid-liquid contact angle .	20
Figure 2.3:	Practical limits of wetting and non-wetting phase based on solid-liquid contact angle .....	20
Figure 2.4:	Droplet on a rough surface. Left: Wenzel Effect. Right: Cassie-Baxter Effect. ...	22
Figure 2.5:	Contact angle hysteresis. The picture droplet is being moved to the left, creating an advancing and receding contact angle, $\theta_A$ and $\theta_R$ , respectively. ....	24
Figure 2.6:	The effect of solid structure on fluid configuration. ....	25
Figure 2.7:	Diagram of a typical capillary pressure curve.....	27
Figure 2.8:	Conceptual picture of non-wetting phase movement as pressure is increased from $P_1$ (left) to $P_2$ (center) and back to $P_1$ (right).....	27
Figure 2.9:	Schematic diagram of a sample holder using capillary barriers for water injection experiments .....	32
Figure 2.10:	Comparison of air-water capillary pressure curves available in the literature for Toray 090 or similar material. All curves are for GDLs with no PTFE except Roth <i>et al.</i> (7%).....	35
Figure 2.11:	Percolation on square lattices. (a) Normal percolation below the percolation threshold. (b) Normal percolation at the percolation threshold. A sample spanning	

cluster is formed by the addition of the dotted lines. (c) Invasion percolation below the percolation threshold. All grey sites and bonds are not invaded due to inaccessibility. (d) Invasion percolation at the percolation threshold. The same sample spanning cluster is recovered by the addition of the dotted lines. Some disconnected grey clusters remain. .... 38

Figure 2.12: Slices through simulated GDLs. (a) Edgewise view of the GDL (In-plane) (b) Face-on view of the GDL (Through-plane) ..... 42

Figure 3.1: Micrographs of assorted GDL materials. (a) SGL 10BA (b) Ballard P75 (c) SGL 24BA (d) SGL 34BA (e) Toray 090 (f) E-Tek Cloth ‘A’ ..... 52

Figure 3.2: Schematic of mercury porosimetry sample tube. The sample is inserted through the wide end and screw cap is used to seal to opening. .... 53

Figure 3.3: Configuration of sample and standards showing fluid movement occurring during method of standard porosimetry experiment..... 56

Figure 3.4: Schematic detailing data analysis used in the method of standard porosimetry. The open circles are points yet to be determined. .... 56

Figure 3.5: Gas controlled porosimetry setup..... 60

Figure 3.6: Schematic diagram of sample holder for GCP. (Left) Assembled view (right) Expanded view. .... 61

Figure 3.7: Sample of experimental data obtained from GCP. The region marked by the box in the top figure is shown in more detail in Figure 3.8. .... 64

Figure 3.8: Close up view of experimental data shown in Figure 3.7. .... 65

Figure 3.9: Sample of capillary pressure curves obtained by GCP test on Toray 090A. Top: Before evaporative correction. Bottom: After correction for evaporation. In this case the evaporation rate was 0.64  $\mu\text{g/s}$ . The triangle in the bottom figure is determined after the test by weighing the sample. .... 67

Figure 3.10: Pressure and saturation time traces for SGL10BA. The dotted line shows the expected saturation response and the point of divergence is circled as the breakthrough point. .... 69

Figure 3.11: Sample of sessile drop image. Water on SGL 10BA..... 71

Figure 3.12: Stacked screen model to determine fraction of solid and void under sessile drop on GDL surface ..... 73

Figure 3.13: Experimental apparatus for through-plane permeability measurement. (a) assembled view (b) exploded view (c) sectioned view to show internal components. ....	74
Figure 3.14: Experimental apparatus for in-plane permeability measurement. (a) assembled view (b) exploded view (c) sectioned view to show internal components. ....	76
Figure 3.15: Sample of experimental data for through-plane pressure drop as a function of air mass flux for two samples. Lines through the data are regression lines that yield $K$ values according to Eq.(3.7).....	78
Figure 3.16: Sample of experimental data for in-plane pressure drop as a function of air mass flux for SGL 34BA.....	79
Figure 3.17: Permeability vs. thickness and compressed volume fraction of sample from the raw data shown in Figure 3.16. ....	79
Figure 3.18: (a) Permeability vs. sample compressed thickness and (b) permeability vs. sample porosity converted using Eq.(3.10) for SGL 34BA GDL sample. The black line represents the Carman-Kozeny model. ....	81
Figure 4.1: The analogy between actual pore structure and an equivalent cubic lattice representation. Left: In-plane view of a GDL. Middle: Conceptual sectioning of pore space into pore bodies (red) and throats (blue). Right: Cubic lattice of equivalent properties. ....	83
Figure 4.2: Schematic of 2 neighboring pore bodies and connecting throat. Throat size ( $b_t$ ) is proportional to the size of the smaller of the two connecting pores ( $b_t = \alpha b_p$ ). Throat length ( $L_t$ ) is equal to the difference between the pore body sizes ( $b_p$ ) and the center-to-center distance between pores ( $L_c$ ). ....	85
Figure 4.3: 2D Schematic of pore network construction. (a) Relationship between pores, throats and solid. (b) Structure in terms of void and solid spaces.....	86
Figure 4.4: Examples of spatially correlated random fields. (a) Uncorrelated field. (b) Correlated field used to model Toray 090 with correlation distances [1, 1, 0] in the $x$ , $y$ and $z$ directions ( $z$ -direction not shown). (c) Correlated field used to model SGL 10BA with correlation distances [2, 1, 0] in the $x$ , $y$ and $z$ directions. ( $z$ -direction not shown).....	88
Figure 4.5: Conceptual schematic of late pore filling.....	90

Figure 4.6:	Comparison of computed capillary pressure curves with experimental porosimetry data. Top: Toray 090, Bottom: SGL 10BA. Left: MSP with Octane, Right: MIP.	96
Figure 4.7:	Pore size, throat size and throat length histograms. (left) Toray 090 and (right) SGL10BA.....	97
Figure 5.1:	MIP intrusion curves for SGL 10 series GDLs. 10AA = 0% PTFE, 10BA = 5% PTFE and 10DA = 20% PTFE. ....	103
Figure 5.2:	MIP intrusion curves for Toray 090 series GDLs .....	104
Figure 5.3:	MSP - Water and MSP – Octane for Toray 090A.....	106
Figure 5.4:	MSP – Water and MSP – Octane for SGL 10BA.....	106
Figure 5.5:	Typical capillary pressure curve obtained using the GCP method. Toray 090A (no PTFE). Arrows indicate the direction of capillary pressure increments. ....	111
Figure 5.6:	Comparison of various experimental air-water capillary pressure curves on Toray 90 or similar GDL with no PTFE except for the data of Roth <i>et al.</i> who used a GDL with 7% PTFE.....	112
Figure 5.7:	Comparison between MSP, MIP and GCP for Toray 090A .....	115
Figure 5.8:	Comparison between MSP, MIP and GCP capillary pressure curves for SGL 10BA .....	115
Figure 5.9:	Air-water capillary pressure curve for Toray 090A (top) 090D (bottom) obtained by GCP.....	118
Figure 5.10:	Air-water capillary pressure curve for SGL 10AA (top) 10BA (bottom) obtained by GCP.....	119
Figure 5.11:	Expanded view of water injection curves (top) and withdrawal curves (bottom) for various Toray materials with different PTFE loadings and thickness. A = 0%, C = 10% and D = 20% PTFE. 060 = 210 $\mu\text{m}$ , 090 = 290 $\mu\text{m}$ and 120 = 390 $\mu\text{m}$ . ....	121
Figure 5.12:	Expanded view of injection (top) and withdrawal (bottom) curves for SGL 10 Series with different PTFE loadings. AA = 0%, BA = 5%, CA = 10%, DA = 20% and EA = 30% PTFE.....	122
Figure 5.13:	Effect of number of layers on water injection into Toray samples of various thicknesses. Top: Untreated. Bottom: Treated. (C = 10 %, D = 20% PTFE).....	125
Figure 5.14:	Water injection curves for untreated Toray materials. Single point injection is compared with full face injection into Toray materials with different thicknesses.	

.....	127
Figure 5.15: Water injection curves for treated Toray materials. Single point injection is compared with full face injection in materials with different thicknesses.....	127
Figure 5.16: Internal scanning loops for removal of water from partially saturated GDLs. Top: Toray 090A with no PTFE. Bottom: Toray 120C with 10wt% PTFE.....	129
Figure 5.17: Internal scanning loops for injection of water into partially saturated SGL 10BA130	
Figure 5.18: Movement of a meniscus between two cylindrical solids. The interface curvature changes as a function of position with a constant contact angle.....	132
Figure 5.19: Spherical and anticlastic interfaces. Left: Spherical interface with principle radii of curvature $R_1$ and $R_2$ . Right: Anticlastic interface with the same two radii of curvature but with opposite signs.....	133
Figure 5.20: Fluid configuration leading to an anticlastic interface during retraction of a non-wetting phase. The grey contour lines show the positively curved interface.....	133
Figure 5.21: Area definitions used in US Bureau of Mines wettability index .....	135
Figure 5.22: Wettability of SGL 10 series GDLs as determined by the US Bureau of Mines index .....	137
Figure 5.23: Wettability of Toray GDLs of various thicknesses as determined by the US Bureau of Mines index.....	137
Figure 5.24: Breakthrough point and capillary pressure curve prior to breakthrough for SGL 10BA . The full capillary pressure curve obtained on a separate sample of SGL 10BA is also shown.....	138
Figure 5.25: Breakthrough points for SGL 10BA .....	139
Figure 5.26: Breakthrough points for Toray 090A .....	140
Figure 5.27: Breakthrough points for Toray 090D .....	140
Figure 5.28: The prevailing conceptual picture of the function of the MPL. (Top) Without MPL, liquid water flows through the cathode GDL to the cathode flow channels. (Bottom) With MPL liquid water is forced to flow through the membrane to the anode side. .....	142
Figure 5.29: Conceptual picture of water flow through GDL with full face injection and point source injection. Left: GDL with full face exposed to water. Middle: GDL with single point water injection. Right: GDL with MPL percolating through the MPL.	

Black is solid, grey represents liquid water and dotted lines show the location of the dead-end water clusters that are no longer filled. ....	144
Figure 5.30: Experimental results obtained using the GCP experiment modified to detect breakthrough. Breakthrough points are marked by solid circles.....	145
Figure 5.31: Standard gas diffusion layer (left) vs. gas diffusion layer with microporous layer added (right), showing the loss of GDL substrate pore volume due to MPL penetration.....	146
Figure 5.32: SEM images of MPL from top. (Left) The MPL consists of very small pores, although its porosity is fairly high ( $\approx 70\%$ ) [123]. (Right) Large cracks exist over the surface. Further images of the MPL are available in Appendix B. ....	147
Figure 5.33: In-plane permeability vs. porosity results for several samples. ....	149
Figure 5.34: Comparison of experimental results to the predictions of the TS model, Eq.(5.7). The solid lines were calculated using parameters for 2D parallel flow. The dashed line was calculated using parameters for 2D normal flow. ....	151
Figure 5.35: Inertial coefficient vs. permeability for all materials tested. Solid line represents the correlation of Liu et al. [218]. ....	153
Figure 5.36: Relative permeability predictions of the pore network modeling for SGL10BA .	158
Figure 5.37: Relative permeability predictions of the pore network model for Toray 090A ....	158
Figure 5.38: Through-plane relative gas permeability data collected from literature sources ..	160
Figure 5.39: Through-plane relative liquid permeability data collected from literature sources .....	160
Figure 5.40: Relative effective diffusivity results predicted by the pore network model for SGL10BA.....	162
Figure 5.41: Relative effective diffusivity results predicted by the pore network model for Toray 090A .....	162
Figure 5.42: Modeled domain for limiting current calculations.....	164
Figure 5.43: Limiting current predicted by pore network modeling as a function of GDL saturation.....	165
Figure B.1: SEM images of 10BA at increasing magnification.....	196
Figure B.2: SEM images of 10AA at increasing magnification.....	197
Figure B.3: SEM images of 10BB Microporous layer at increasing magnification .....	198

Figure B.4: SEM images of 24BA at increasing magnification .....	199
Figure B.5: SEM images of 34BA at increasing magnification .....	200
Figure B.6: SEM images of Toray 090 at increasing magnification .....	201
Figure B.7: SEM images of Ballard P75 with no PTFE at increasing magnification .....	202
Figure B.8: SEM images of E-Tek Cloth 'A' at increasing magnification .....	203

## List of Tables

Table 1.1:	GDL properties and preferred values for fuel cell functions.....	10
Table 2.1:	Comparison of air-water capillary pressure measurement techniques.....	36
Table 3.1:	List of materials tested during this study and selected properties.....	51
Table 4.1:	Model parameters used for each material .....	98
Table 4.2:	Transport results for each modeled material .....	100
Table 5.1:	Constants used in the TS model .....	151
Table 5.2:	Through-plane permeability values.....	152

## Nomenclature

Symbol	Description	Units
$A_s$	Surface Area	$m^2$
$A$	Area of lattice normal to flow direction	$m^2$
$a$	Electron Transfer Coefficient	
$\alpha$	Throat constriction factor	
$b$	Ratio of geometric area to projected area	$m^2 \cdot m^{-2}$
$\beta$	Spatial correlation distance	
$\beta$	Inertial Coefficient	$m^{-1}$
$c$	Bulk Concentration	$mol \cdot m^{-3}$
$\chi$	Random number in Weibull distribution	
$D_{AB}$	Binary Diffusion Coefficient	$m^2 \cdot s^{-1}$
$D_{eff}$	Effective Diffusion Coefficient	$m^2 \cdot s^{-1}$
$D_{rP}$	Relative Effective Diffusion Coefficient of Phase P	---
$d$	Diameter	
$d_f$	Fiber diameter	m
$\delta$	Sample Thickness	m
$\varepsilon$	Porosity	-/-
$\varepsilon_p$	Percolation Porosity used in TS model	
$F$	Faraday's Constant	$C \cdot mol^{-1}$
$Fo$	Forchheimer Number	---
$g$	Gravitational Constant	$m \cdot s^{-2}$
$g_h$	Hydraulic conductivity	$m^3 \cdot Pa^{-1} \cdot s^{-1}$
$g_d$	Diffusive conductivity	$m^3 \cdot s^{-1}$
$H$	Mean Interfacial Curvature	$m^{-1}$
$h$	Static Height	m
$\eta$	Filling exponent	
$I$	Current	A
$c$	Current density	$A \cdot m^{-2}$

$i_o$	Exchange current density	$A \cdot m^{-2}$
$J$	Leverett J-Function	
$K$	Permeability	$m^2$
$K_{rP}$	Relative permeability of phase P	---
$k_{CK}$	Carman-Kozeny Constant	---
$\kappa$	Parameter in Weibull distribution	
$L$	Length of conduit	m
$L$	Length of sample	m
$Lc$	Lattice constant	m
$L_t$	Throat length	m
$l$	Length of pore network domain	m
$\lambda$	Parameter in Weibull distribution	
$MW$	Molecular Weight	$kg \cdot mol^{-1}$
$m'$	Mass Flux	$kg/m^2 \cdot s$
$\mu$	Viscosity	$Pa \cdot s$
$N$	Diffusion rate through network	$mol \cdot s^{-1}$
$n$	Diffusion rate	$mol \cdot s^{-1}$
$P$	Pressure	Pa
$P_C$	Capillary Pressure	Pa
$Q$	Flow rate through network	$m^3 \cdot s^{-1}$
$q$	Flow rate through a pore conduit	$m^3 \cdot s^{-1}$
$\theta$	Contact Angle	°
$R$	Universal Gas Constant	$J \cdot mol^{-1} \cdot K^{-1}$
$\rho$	Density	$kg \cdot m^{-3}$
$Re$	Reynolds Number	---
$r$	Pore radius	m
$s$	Saturation (Fraction of pore volume filled with fluid)	---
$\sigma$	Surface Tension	$N \cdot m^{-2}$
$T$	Temperature	K
$\tau$	Tortuosity	---

$u$	Superficial Velocity	$\text{m}\cdot\text{s}^{-1}$
$V$	Voltage	V
$V$	Volume	$\text{m}^3$
$X$	Lattice size in x-direction (in-plane)	No. of Pores
$x$	Mole Fraction	
$Y$	Lattice size in y-direction (in-plane)	No. of Pores
$Z$	Lattice size in z-direction (through-plane)	No. of Pores
$z$	Stoichiometric electron generation	

### Subscripts

$act$	Actual
$ATM$	Atmospheric
$C$	Compressed
$CH$	Gas channel
$CL$	Catalyst layer
$eff$	Effective
$G$	Gas
$in$	Inlet
$L$	Liquid
$NWP$	Non-Wetting Phase
$OCV$	Open circuit voltage
$out$	Outlet
$obs$	Observed
$P$	Phase (L for liquid, G for gas, etc)
$p$	Pore
$R$	Reactant
$WP$	Wetting Phase
$x$	In-plane flow direction, perpendicular to y
$y$	In-plane flow direction, perpendicular to x
$z$	Through-plane flow direction
$0$	Uncompressed

### Superscripts

V Vapor Pressure

## Abbreviations

CFD	Computational Fluid Dynamics
GCP	Gas-Pressure Controlled Porosimetry
GDL	Gas Diffusion Layer
LBM	Lattice Boltzmann Method
MIP	Mercury Intrusion Porosimetry
MPL	Microporous Layer
MSP	Method of Standard Porosimetry
OCV	Open Circuit Voltage
PEM	Polymer Electrolyte Membrane
PEMFC	Polymer Electrolyte Membrane Fuel Cell
PTFE	Polytetrafluoroethylene
TS	Tomadakis and Sotirichos
USBM	United States Bureau of Mines

# 1. Introduction and Background

Hydrogen figures largely in most visions of a sustainable energy future and the term “hydrogen economy” is virtually synonymous with green energy, renewable resources and sustainability [1-4]. The fuel cell is a key component of the hydrogen economy since it converts hydrogen fuel into useful power, with only water and heat as byproducts. The role of the fuel cell in a hydrogen-based economy is analogous to that of the internal combustion engine in today’s oil-based economy.

Recent advances in fuel cell technology have brought the hydrogen economy vision closer to reality. The development of very thin proton conducting membranes [5] has dramatically improved cell performance by reducing ohmic losses while development of low platinum loading electrodes has significantly reduced cost [6-9]. Nonetheless, further improvements are needed before fuel cells will be ready for broad commercialization. One of the main target areas for improvement is overall fuel cell performance since this provides several benefits simultaneously. Fuel cell performance can be measured in terms of power density ( $\text{W}\cdot\text{m}^{-2}$ ). An increase in power density reduces the amount of active area required for a given power output. Less active area entails less platinum catalyst and ionomeric membrane, which helps to reduce the cost. It also results in smaller fuel cell modules, which is beneficial for packaging in commercial applications such as automobiles. Performance improvements can also be measured in terms of reduced voltage loss due to irreversible electrode processes. This leads to higher fuel conversion efficiency, which is desirable for energy conservation, and it also leads to lower waste heat rejection, which is crucial from a practical standpoint, particularly for automotive applications.

One of the main obstacles to increasing fuel cell performance is the fact that fuel cells generate water as a by-product. Although this feature is considered a benefit from an environmental point of view, it causes many engineering difficulties. Since the rate of water production is proportional to the rate of current generation, more water is generated as the generated current and power are increased. Excessive amounts of water inside the

cell lead to condensation of liquid water in the porous electrodes and electrode backing layers where it dramatically hinders the transport of gaseous reactants. The mass transfer limitations imposed by liquid water blockages in the electrode have two major impacts. Firstly, since they are heterogeneous catalytic reactions, electrode reactions in a fuel cell are limited by the rate at which reactants can be supplied to the catalyst sites. The presence of liquid water dramatically reduces the maximum current density ( $\text{A}\cdot\text{m}^{-2}$ ) that can be achieved by reducing the maximum mass flux. Secondly, the generated electrode voltage decreases as the reactant concentration at the catalyst sites decreases. Thus, for a given current density, the presence of liquid water results in lower cell voltage and therefore lower power output. Alternatively, for a given power output, concentration induced voltage losses result in lower efficiency and increased waste heat generation.

To alleviate the limitations placed on cell performance by the presence of liquid water, it is necessary to understand the behavior and effects of liquid water inside the cell. Better knowledge of these phenomena will enable the electrode structure and materials to be further optimized to accommodate and manage water so that performance is not hindered. The objective of this thesis is to study the behaviour of liquid water in the porous components of the fuel cell electrode, specifically the gas diffusion layer, and the resultant impact on mass transfer.

## **1.1. Fuel Cell Background**

Before providing a description of the internal fuel cell processes, an overall view of fuel cell operation is given.

### **1.1.1. Electrochemistry**

The PEM fuel cell is a galvanic cell, similar to a simple battery, but the reactants in a fuel cell are fed continuously and the reaction occurs on a catalytic surface. Figure 1.1 shows a schematic diagram of the electrode arrangement.

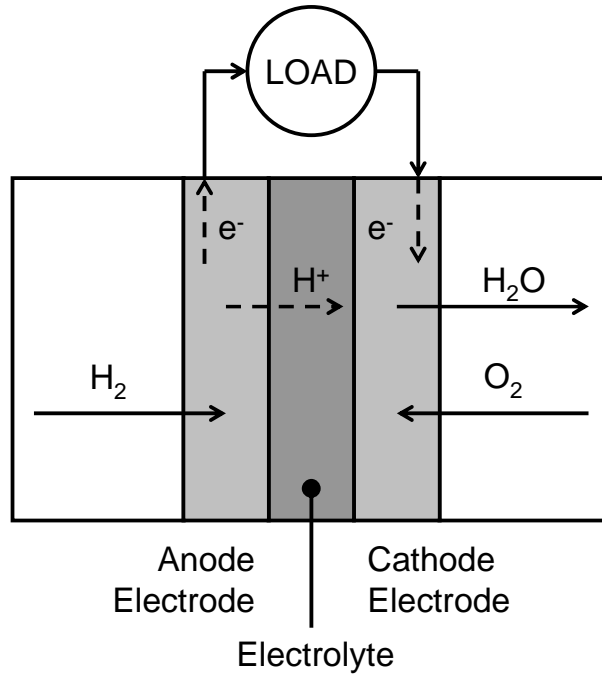


**Figure 1.1: Galvanic cell representative of the PEM fuel cell**

Hydrogen is fed continuously to the anode where it reacts over a platinum catalyst surface to form protons and electrons:



Electrons flow through the electrode to an external circuit to power a load. Protons travel through the electrolyte to the cathode where they combine with oxygen and electrons to form water:



The overall cell reaction is:



The Nernst potential for this reaction is 1.223 V and represents the theoretical maximum voltage that can be delivered by the fuel cell assuming that no losses in energy occur during operation.

### 1.1.2. Operation

The amount of power generated by a fuel cell is the product of the cell voltage,  $V$ , and the total current drawn,  $I$ . At open circuit, when no current is drawn, the cell theoretically provides a maximum voltage corresponding to the electrochemical potential of the two half-reactions, Eq.(1.1) and Eq.(1.2), which is about 1.223 V. At open circuit, the maximum voltage is available, but no power is generated since  $I = 0$ . For  $I > 0$ , several voltage losses are incurred due to the inefficiencies of various processes involved in current generation. This relationship is given by:

$$V_{CELL}(i) = V_{OCV} - V_{LOSS}(i) \quad (1.4)$$

where  $V_{CELL}(i)$  is the overall cell voltage,  $i$  is the current density ( $A/cm^2$ ),  $V_{OCV}$  is the cell voltage at  $i = 0$  and  $V_{LOSS}(i)$  is the cumulative voltage loss stemming from the generation of current. At sufficiently high current,  $V_{LOSS}(i)$  approaches  $V_{OCV}$  resulting in a cell that produces no power. For a fuel cell,  $V_{LOSS}(i)$  can be broken down into three components; activation polarization  $\eta_{act}$ , ohmic polarization  $\eta_{IR}$  and concentration polarization  $\eta_{conc}$ . It is convenient to express the cumulative effect of these three losses as [10,11]:

$$V_{LOSS} = \eta_{act} + \eta_{IR} + \eta_{conc} \quad (1.5)$$

Activation losses arise due to kinetic barriers occurring at the electrode catalyst, such as electron transfers, formation of intermediates, adsorption and desorption of species, etc. Activation losses are typically described by the Tafel equation:

$$\eta_{act} = \frac{RT}{naF} \ln \left[ \frac{i}{A_s i_o} \right] \quad (1.6)$$

where  $A_s$  is electrode catalyst surface area,  $F$  is the Faraday constant,  $R$  is the universal gas constant,  $T$  is the reaction temperature,  $a$  is the electron transfer coefficient,  $n$  is the number of electrons transferred by the reactions,  $i_o$  is the exchange current density which is related to the rate constant for the reaction. The exchange current density depends on the catalytic activity of the electrode catalyst material and on the concentration of the reactants at the surface of the electrode. Although activation losses occur at both electrodes, the kinetics of the oxygen electrode in fuel cells are significantly slower than that at the hydrogen electrode, even when highly active platinum catalyst electrodes are

used.

Ohmic losses are caused by the transport of protons through the electrolyte, electrons through the electrically conductive solids (electrodes and current collectors) and interfacial resistances. The development of thinner and more conductive membrane materials is aimed at reducing these ohmic losses. Each source of resistance in a cell has a cumulative effect on the total cell resistance:

$$\eta_{IR} = I \times (R_1 + R_2 + \dots) \quad (1.7)$$

where  $R_1, R_2, \dots$  are the various resistance in series that the charged particles must move through.

Losses due to concentration effects are incurred when insufficient reactants reach the electrode catalyst, thereby altering the concentration at the electrode, which has two repercussions. Firstly, a reduced reactant concentration at the electrode slightly reduces the open circuit potential of the reaction as described by the Nernst equation:

$$V'_{OCV} = V_{OCV} - \frac{RT}{nF} \ln \left( \frac{1}{x_{H_2} x_{O_2}^{0.5}} \right) \quad (1.8)$$

where  $x_i$  is the mole fraction of species  $i$  at the electrode. When the concentration of the reactants becomes very low, the second term on the right hand side of the equation above becomes large and causes  $V'_{OCV}$  to approach 0. Secondly, and more importantly, reduced concentration at the catalyst surface adversely affects the kinetics of the reaction by altering the exchange current density,  $i_o$ , in the Butler-Volmer equation, Eq.(1.6).

Concentration polarization effects are described by:

$$\eta_{conc} = \frac{RT}{naF} \ln \left( \frac{c_{R,ref}}{c_R} \right) \quad (1.9)$$

where  $c_R$  is the concentration at the catalyst surface and  $c_{R,ref}$  is the surface concentration at which  $i_o$  was determined.

Figure 1.2(left) shows the individual and combined effects of each of these contributions on the overall polarization curve. Activation losses are important in the low current

density region. The ohmic losses become increasingly important as current density is increased since it is proportional to current. Ohmic losses are largely dictated by the conductivity of the electrolyte membrane material, which is much lower than that of the solid electron conductors. The concentration polarization losses, or mass transfer induced losses, place an upper limit on the maximum current that can be generated in a cell. Concentration polarization also reduces the cell voltage for a given current density resulting in a lowered overall cell performance.

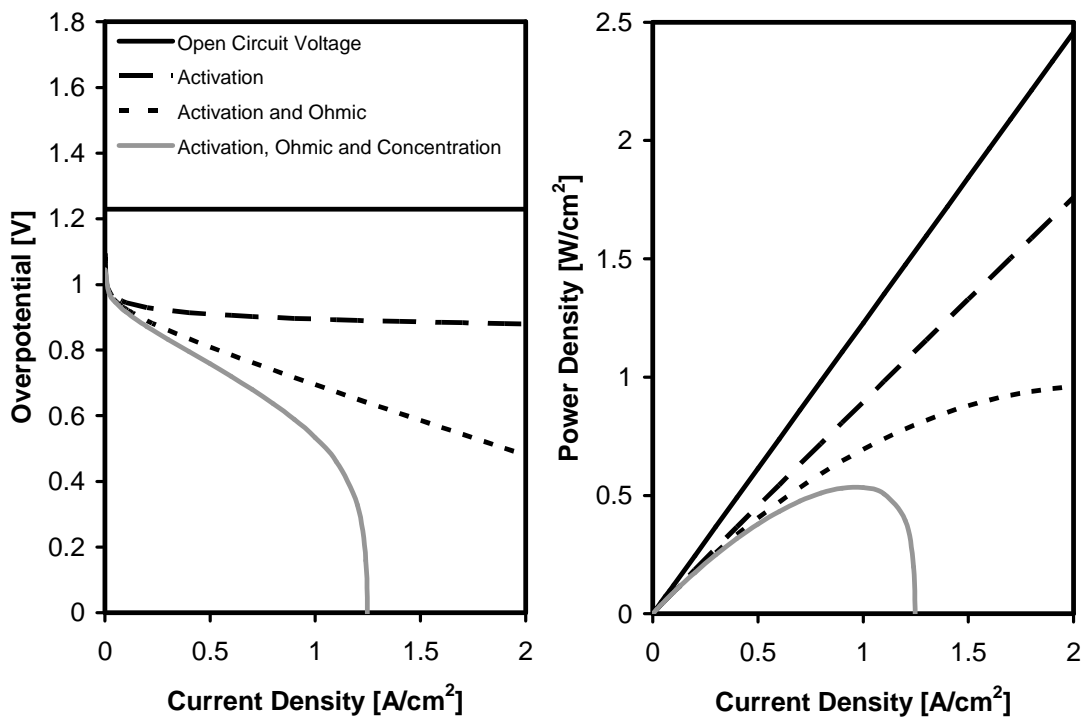


**Figure 1.2:** Left: Typical polarization curves showing the additive contribution of each type of voltage losses. The limiting current is 1.25 A/cm<sup>2</sup>. Right: Power density curves showing the interplay between power generated and cell current.

When the reaction rate or current is at its maximum no power is generated by the reaction since the corresponding cell voltage is zero. The interplay between the drawn current, voltage loss and power generation can be described in terms of power density vs. current as shown in Figure 1.2(right). The onset of severe mass transfer limitations around 1 A/cm<sup>2</sup> corresponds with the peak in power generation. It is clear that reducing mass

transfer resistances will shift the onset of mass transfer limited operation to higher currents and therefore increase the maximum power that can be achieved.

### **1.1.3. Fuel Cell Internal Components and Transport Processes**

A schematic diagram of a fuel cell cross-section is shown in Figure 1.3. The polymer electrolyte membrane acts as an ionic conductor and allows protons generated at the anode to be transported to the cathode. Also, since the membrane acts as a gas separator to prevent direct mixing of oxygen and hydrogen, it must be largely impermeable to gas. The catalyst layer is a porous reaction zone composed of a mixture of ionomer and carbon-supported platinum particles, which are adhered directly to surface of the membrane. The ionomer phase allows protons to reach the reactive sites, while the carbon particles provide pathways for electrons. Reactant gas enters into the catalyst layer through the pores, while product water, both vapor and liquid, leave through the same pores. The gas diffusion layer (GDL) is a carbon fiber paper that acts as both a spacer to allow gas access to areas of the catalyst layer located under the land and to allow electron access to areas located over the channel. The GDL is made of carbon to conduct electrons and is porous to allow transport of reactants and products. The bipolar plates are made from graphite or metal to be conductive, into which channels are stamped or machined. Gas flows through the channels parallel to the membrane surface and reactants diffuse from the channel to the catalyst layer through the GDL. Coolant channels are necessary to remove the heat generated by the reaction. Typical fuel cell operating temperatures are slightly below 100°C to prevent excessive evaporation of water and drying of the membrane.

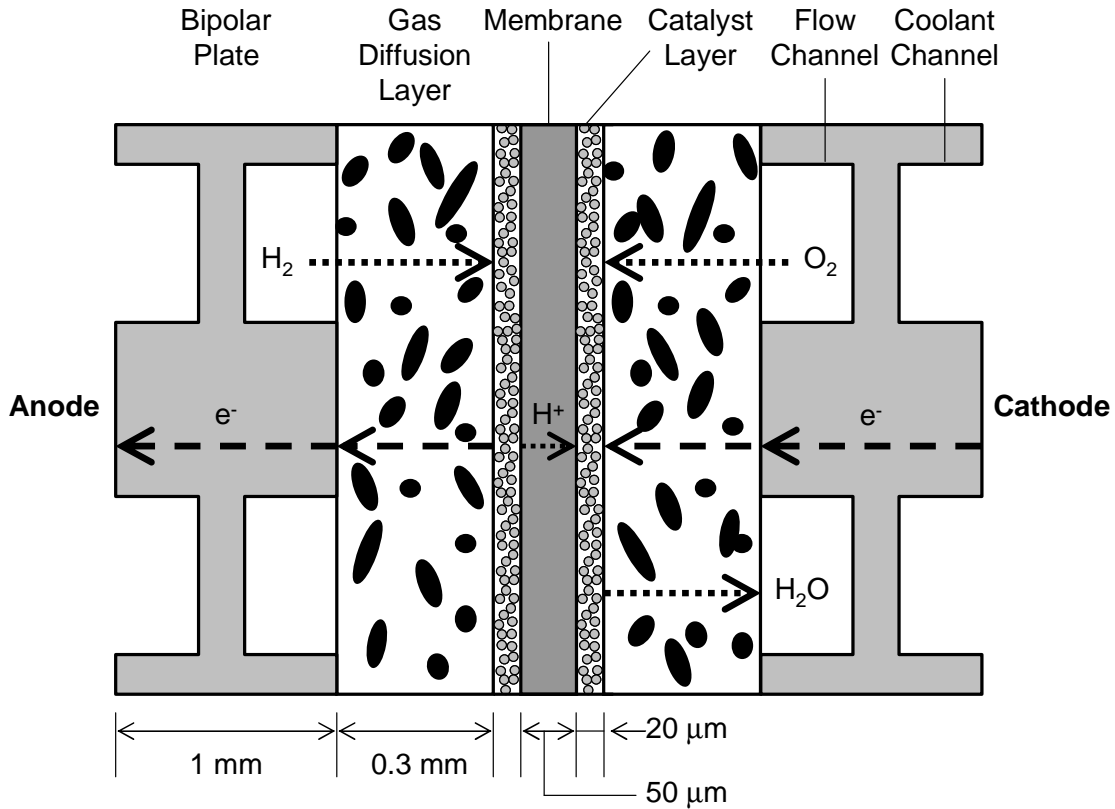


**Figure 1.3: Schematic of fuel cell internal components. The section shown represents a single repeating unit that can be placed in series to form a high voltage stack. Typical dimensions are shown.**

#### 1.1.4. Gas Diffusion Layer

The main purposes of the GDL are to act as a spacer to allow reactants to reach catalyst sites that lie under the rib and as a bridge to allow electron access to catalyst sites over the channel. GDLs are a porous material, usually a paper or woven cloth made from carbon graphite fiber. SEM images of a typical GDL are shown in Figure 1.4. A catalogue of SEM images of GDLs is given in Appendix B. Graphite is an ideal material since it is electronically conductive while also being chemically inert and stable inside the fuel cell. Gas transport occurs through the pore network while electron conduction occurs through the solid matrix. GDLs are typically between 150 and 400 μm thick with porosity between 70 and 90%. The properties of the GDL must be optimized for several competing requirements. Table 1.1 lists the main GDL properties along with the ideal value for each GDL function.

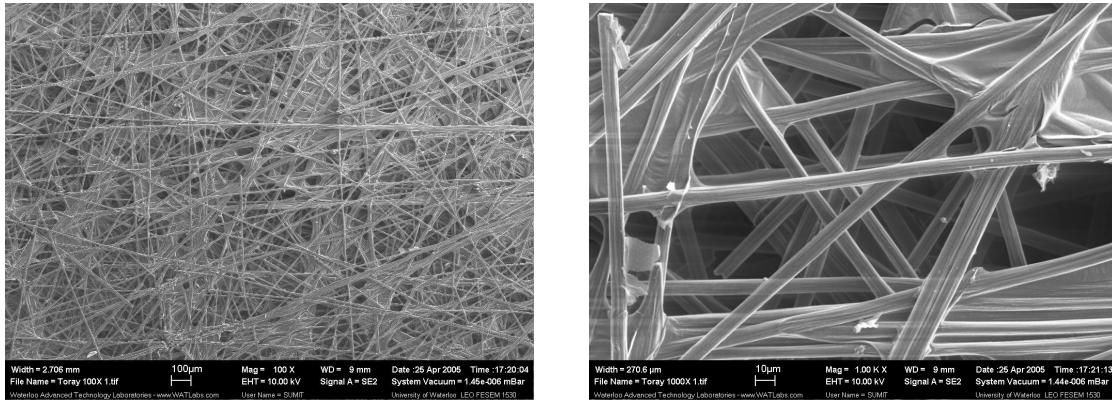


**Figure 1.4: SEM Images of Toray 090A GDL surface. Left: 100x magnification. Right: 1000x magnification.**

GDLs are usually treated with a coating of hydrophobic polymer, such as polytetrafluoroethylene (PTFE), to alter the behavior of liquid water inside the porous structure. This coating is applied by saturating the GDL with a PTFE emulsion and followed by drying to remove the liquid. The PTFE particles that remain are sintered at 650 K to ensure good adhesion to the carbon fibers and to promote spreading of the polymer coating. The particle concentration in the PTFE emulsion is adjusted to achieve the final loading. Details of coating procedures are considered to be intellectual property of the GDL manufacturers and distributors. It is reasonable to expect that different procedures will lead to different PTFE distributions, whether intentionally or not. Mathias *et al.* [12] demonstrated that a slow drying rate is critical to obtaining a uniform distribution throughout the sample and that PTFE migrates to the outer surfaces when dried quickly.

The GDL plays several important mechanical roles as well. It provides support to the thin ionomer membrane over the channel so pressure differentials across the membrane do not cause a rupture or intrusion into the channel. GDLs also act as a pad to protect the membrane from the channel ribs. Fuel cell stacks are compressed when assembled to ensure good electrical contact between all layers. Being the only compliant component in the cell, the GDL absorbs most of this strain. The effect of compression on the GDL is an important consideration since many of the GDL properties vary significantly with

compression.

**Table 1.1: GDL properties and preferred values for fuel cell functions**

	<b>Gas Diffusion</b>	<b>Electron Conductivity</b>	<b>Water Management</b>	<b>Mechanical Strength</b>
<b>Porosity</b>	High	Low	High	Low
Comments: A higher porosity is better for gas and liquid transport since more porous pathways exist, but a lower porosity is better for electrical conductivity since more conductive solid phase is present.				
<b>Thickness</b>	Medium	Medium	Medium	Thick
Comments: In theory, a thin GDL is better for gas and liquid transport as well as electron conduction since through-plane transport lengths are reduced. However, since a very thin GDL reduces gas access to areas under the land and electron access to areas over the channel, an optimum medium thickness exists.				
<b>Hydrophobicity</b>	Low	Low	High	High
Comments: Since liquid water is formed inside the cell, the GDL must be hydrophobic so water does not wick into its porous structure. A hydrophobic polymer coating is usually applied to promote hydrophobicity, but it must be applied as sparingly as possible since it is not electrically conductive.				

### 1.1.5. The Microporous Layer

The microporous layer (MPL) is a powdery mixture of carbon black and PTFE particles that is often applied to the side of the GDL facing the catalyst layer. This mixture is sprayed onto the GDL then sintered so the PTFE can bind the powder together. SEM images of the MPL are shown in Figure 1.5. The MPL treatment is known to be beneficial for fuel cell performance [13] but the actual function of this layer is still unclear. The MPL presumably creates better electrical and thermal contact between the catalyst layer and the GDL by providing a smoother, more continuous interface, but the benefits of the MPL are most noticeable at higher current conditions indicating that it somehow improves mass transfer. This is counter-intuitive since the MPL actually adds a diffusive resistance to mass transfer by increasing the diffusion length and adding a layer of lower porosity material through which gas must diffuse. Consequently, it is generally thought that the MPL somehow alters the liquid water distribution in the cell to a more favorable arrangement for gas phase transport. Although several theories on their function have been proposed, the question of how the MPL improves performance remains open.

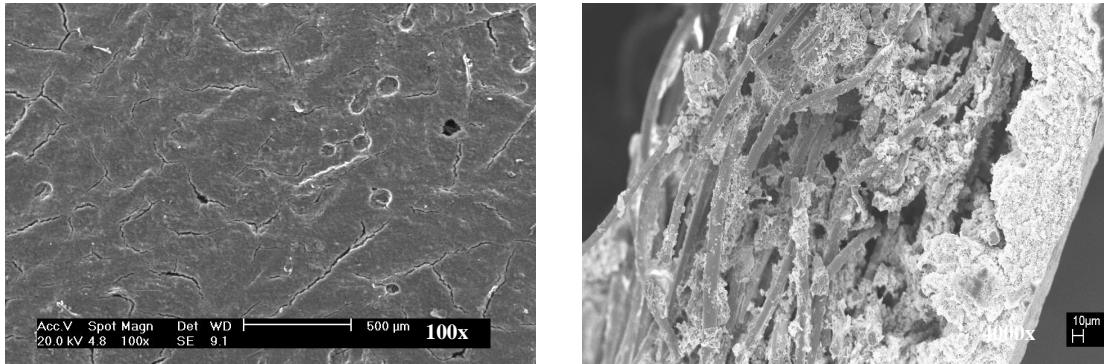


**Figure 1.5: SEM images of microporous layer. Left: Surface view. Right: Cross-section.**

### 1.1.6. Limiting Current

As with any catalytic reaction, the theoretical maximum current that can be attained in a fuel cell is limited by the rate at which reactants can be supplied to the catalyst sites. This rate corresponds to the limiting current. For the reaction to proceed, both hydrogen and oxygen must reach their respective catalyst layers; however, for several reasons the rate of oxygen transport is the rate limiting step under normal operation. Firstly, oxygen partial pressure is much lower than hydrogen since oxygen is obtained from air. This air is usually humidified prior to being introduced to the stack so that the oxygen partial pressure is further reduced. Secondly, the diffusion coefficient of oxygen is lower than that of hydrogen. Finally and most critically, the water generated by the electrochemical reaction forms on the cathode side. Not only does water vapor reduce the oxygen partial pressure even further, but it also tends to condense in the pores of the GDL and block gas phase mass transfer. The result of water-filled pores in the GDL is a reduced effective diffusion coefficient of oxygen. When enough pores become filled with water, there will no longer be a continuous pathway through the GDL. Such a situation is referred to as flooding. However, the detrimental effect of liquid water in the GDL to reduce the limiting current is observed even when partial flooding occurs. Controlling the formation and distribution of liquid water inside the cathode electrode is critical to achieving maximum performance. The next section discusses in more detail the various requirements and approaches used to manage water in fuel cells.

### 1.1.7. Water Management

One of the major appeals of hydrogen fuel cells is that their only byproduct is pure water. Ironically, the production of water is also one of the major engineering challenges since the water must be removed from the cell as it is generated. Accumulation of water inside the cell results in flooding of the internal porous electrode structures, specifically the GDL, and prevents gaseous reactants from reaching catalyst sites. Complete water removal from the cell is not an option since the currently used ionomeric membrane materials must be hydrated to function. In fact, their performance improves exponentially with relative humidity [14,15] as water partitions into the solid polymer phase and hydrates the sulfonic acid groups to impart ionic conductivity. Achieving a balance between water rejection from the cell to sustain high mass transfer rates and maintaining sufficient moisture inside the cell to ensure membrane hydration is a challenging task and is referred to as water management.

Unfortunately, the goal of maintaining the water content inside the cell at the optimum value is not practically achievable for several reasons. Since water is generated inside the cell, the relative humidity of the air stream increases as it passes through the cell, creating a distribution of humidity conditions throughout the cell. There are also temperature and current density variations across the active area creating altered humidity conditions from location to location. Another difficulty is the transient nature of the fuel cell operation under a duty cycle, which creates variable internal water contents at any given time. The end result is that ideal or optimum conditions can only be expected in limited locations and at certain operating conditions if at all. Since currently available membranes do not perform well when dry, it is necessary to supply highly humidified feed gases and design the cell to cope with liquid water.

Several design features are commonly employed to handle the liquid water that forms in the cell. The first and most commonly used method is to coat the GDL with a hydrophobic polymer, such as PTFE, to prevent liquid water from wicking throughout the GDL and completely blocking gas transport. A second technique is to apply a microporous layer (MPL), which is a highly hydrophobic layer of sintered carbon and

PTFE powder, to the side of the gas diffusion layer facing the catalyst layer. The actual function of the MPL is unclear, but it is known to significantly improve cell performance under humid conditions. Other adaptations to handle liquid water include application of PTFE coating on the gas channel walls to aid droplet removal by gas flow [16], porous bipolar plates that draw water into the coolant stream [17] and macro-holes through the GDL to act as water flow conduits [18,19].

The reality is that liquid water exists in the fuel cell. Although several techniques are employed to limit the detrimental effects on mass transfer, these are empirically developed. Little is known about how liquid water behaves in the materials or how different PTFE application techniques affect liquid water distribution. Almost nothing is known about the role of the MPL on water management. Improving the performance of PEM fuel cells by accommodating the presence of liquid water in the electrode requires a much deeper understanding of water behavior, mass transport properties and multiphase flow phenomena inside the GDL than currently exists.

## **1.2. Outline of Thesis**

This thesis addresses the issue of water flooding in the gas diffusion layer of the polymer electrolyte fuel cell. As part of this work, a number of experiments have been developed to characterize the transport properties of the GDL that relate to two-phase flow, such as capillary pressure and permeability tests. Pore network modeling has also been employed to simulate multiphase flow in GDLs and to predict transport properties that are difficult to determine experimentally, such as relative permeability and effective diffusivity through partially saturated media. The main theme of this work is the determination of multiphase transport properties of GDLs obtained through a combination of experiments and pore scale modeling. The larger picture of fuel cell performance is also addressed briefly.

One of the main contributions of this work is the development of the air-water capillary pressure measurement method. A solution to this problem was actively being sought by

numerous academic groups [20-22] and industrial interests including United Technologies Corporation [23] and General Motors [24]. The method developed in the present thesis is superior to all reported methods and has been used extensively throughout this work.

This thesis is organized into four main sections. The first section is a literature review of GDL transport properties, their role and use in fuel cell modeling, and a summary of in-situ and ex-situ experimental techniques and numerical predictions. The second section describes in detail the various experimental techniques that have been developed as part of this project. In the third section, the pore network model that has been developed to study multiphase flow and mass transfer in GDLs is presented. The final section combines the experimental and modeling results into a larger coherent discussion of transport phenomena in GDL and fuel cells.

## 2. Literature Review and Theory

Efforts to understand the effects of liquid water on fuel cell performance have been extensive. An astounding number of numerical models have been published [25-112] that attempt to incorporate equations for multiphase flow in porous media into multiphysics and computational fluid dynamics (CFD) packages in an effort to account for the effect of liquid water on PEM fuel cell performance. These models have evolved from one-dimensional, isothermal, steady-state models of only the GDL to highly elaborate three-dimensional, non-isothermal, dynamic full cell models, including flow channels, phase change, electron transport, anisotropy, cell compression and more. The limitation of this modeling approach is that physical and transport properties for each domain in the model must be known. As more coupled physical processes are included in the model for completeness, more physical properties are needed as input. Ironically, such efforts often only add more uncertainty since all the necessary physical parameters are not usually known.

One of the earliest attempts to model transport in the GDL as a multiphase-flow-through-porous-media problem can be attributed to Wang *et al.* [39,54]. Prior to this work, PEMFC models accounted for GDL water content by arbitrarily adjusting the GDL porosity to mimic reduced gas transport [113,114]. Due to the pioneering nature of their work, Wang *et al.* were forced to assume virtually all of the multiphase related transport properties of the GDL. Capillary pressure curves for unconsolidated sand packs were used, along with relative permeability relationships for oil reservoirs and tortuosity relationships for packed bed reactors. Many models have been published following the work Wang *et al.*, but the generation of modeling studies has dramatically outpaced the arrival of relevant experimental GDL transport data.

To illustrate the problem, a simple model coupling liquid flow through the GDL with oxygen diffusion to the catalyst layer is presented below. The typical formulation for liquid flow through a partially saturated porous media is unsaturated flow theory, also referred to as the modified Darcy's law or the Richards equation [115]:

$$\vec{v}_L = \frac{K \cdot K_{rL}(s)}{\mu_L} \frac{dP_C(s)}{ds} \nabla s \quad (2.1)$$

where  $v_L$  is the fluid velocity,  $s$  is the GDL water saturation, defined as the fraction of pore volume filled with water,  $\mu_L$  is the liquid viscosity,  $K$  is the absolute permeability,  $K_{rL}$  is the relative liquid permeability (i.e. the permeability of liquid in a partially liquid saturated porous medium) and  $P_C$  is the capillary pressure function of the porous medium. The use of Eq.(2.1) requires that the properties ( $K$ ,  $K_{rL}$  &  $P_C$ ) of the porous material being modeled (i.e. the GDL) are known. Coupled with Eq.(2.1) is the calculation of gas diffusivity through the partially saturated GDL to the catalyst layer. Full Stefan-Maxwell equations for multicomponent flow can be used, but for the simple case of unimolecular diffusion of species A (oxygen) through a stagnant film of B (water saturated nitrogen), Fick's law can be applied and is sufficient to illustrate the required transport properties [116]:

$$\vec{n}_A = cAD_{AB} \frac{\varepsilon}{\tau} D_{rG}(s) \nabla \ln(x_B) \quad (2.2)$$

where  $n_A$  is the molar flow of species A through an area A,  $D_{AB}$  is the binary diffusion,  $c$  is the bulk concentration,  $\varepsilon$  and  $\tau$  are the porosity and tortuosity of the dry GDL, respectively,  $x_B$  is the mole fraction of species B and  $D_{rG}$  is a function to account for the reduction in gas phase diffusivity by the presence of liquid water in the pores. As was the case with Eq.(2.1), this equation also requires numerous physical and transport properties of the porous material to be known; in this case  $\varepsilon$ ,  $\tau$  and  $D_{rG}$ .

If it is assumed that all of the water generated is in the liquid form, as would be the case when the air is fully humidified, then the following equation relates water production to current density,  $i$ :

$$\rho_L \vec{v}_L = \frac{i}{z_{H_2O} F} MW_{H_2O} \quad (2.3)$$

where  $\rho_L$  is the liquid density,  $F$  is Faraday's constant,  $MW$  is molecular weight and  $z$  is a stoichiometric constant relating the number of molecules produced per electron generated, which in the case of water is 2 (see Eq.(1.2)). Similarly, the oxygen flux is related to the current generation by:

$$-\bar{n}_{O_2} = \frac{i}{z_{O_2} F} \quad (2.4)$$

The value of  $z$  for oxygen is 4.

Equations (2.1) through (2.4) together form a very simple model of simultaneous gas and liquid transfer through the pores of the GDL. Other factors, such as electron and heat transfer through the solid matrix may also be important but the focus of this discussion (and thesis) is the mass transfer through the porous network. Solution of the above set of equations requires that six GDL properties must be known:  $K$ ,  $K_{rL}$ ,  $P_C$ ,  $\epsilon$ ,  $\tau$  and  $D_r$ . None of these are well known for GDLs and none are trivial to measure experimentally. Each property will be discussed in more detail in the sections that follow.

Testing of GDL transport properties is challenging because the dimensions and properties of the materials are incompatible with most established techniques used for studying other traditional porous media such as rock core samples and sand packs. For instance, relative permeability of a rock core sample is routinely obtained by measuring the electrical conductivity of a brine solution flowing through the sample [117], with the conductivity being proportional to the saturation. Because GDLs are themselves conductive, however, this technique cannot be applied. The conductive nature of the GDL also eliminates the use of NMR imaging to study water configuration, which is commonly employed for rock and sand packs [118]. Essentially, test methods for each transport property of interest must be developed and tailored specifically for GDLs. The other unique and challenging features of GDLs are their high porosity, fibrous structure, anisotropy, extreme thinness and chemical heterogeneity. Tests must be devised that can meet each of these challenges.

Recently, the need for systematic study of GDL transport properties has begun to be addressed. This chapter will attempt to collect and review the knowledge of GDL transport properties available in the literature. A full discussion of each GDL transport property will be given its own section; with each section describing the role of the property in PEMFC operation, a review of relevant literature, the state of knowledge or

understanding of that property and the techniques available for its measurement.

## 2.1. Capillarity, Wettability and Contact Angle

The wettability of a porous material, or more specifically the solid that comprises the porous material, has a major impact on capillary properties. Consider a tube of solid submerged into a pool of fluid, as shown in Figure 2.1. If Fluid 1 is wetting on Solid 1, it will rise (Figure 2.1 left). Conversely, if Solid 2 is not wet by Fluid 1, the surface will be depressed (Figure 2.1 right).

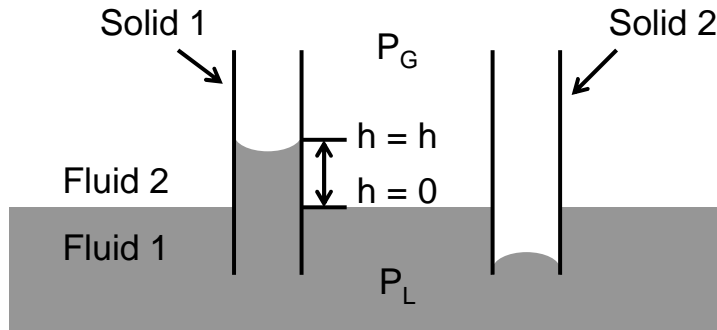


**Figure 2.1: Capillary action between a solid tube and 2 fluids . Fluid 1 is wetting on Solid 1, but not Solid 2**

The height of fluid rise (or depression) is a function of several variables, such as the surface tension and density of the fluids, the diameter of the tube and the wettability of the fluids on the solid. In the case where Fluid 1 is wetting and Fluid 2 is a gas with negligible density (i.e. water-air-glass), the height,  $h$ , of the fluid column corresponds to a static pressure that is equal to the capillary pressure of the system,  $P_C = \rho gh$ . The capillary pressure represents the difference in pressures across the Fluid 1 – Fluid 2 interface. At the free surface ( $h = 0$ ) there is no capillary effect and  $P_G = P_L(h=0)$ . At the surface inside the tube, however, the pressure in the liquid is equal to  $P_L = P_L(h=0) - \rho gh$ . Rearranging this equation leads to the general definition of capillary pressure:

$$P_C = P_{NWP} - P_{WP} \quad (2.5)$$

where  $P_{NWP}$  and  $P_{WP}$  are the pressures in each phase at the interface. On the left side of Figure 2.1, gas is the non-wetting phase (*NWP*) and liquid is the wetting phase (*WP*), and

on the right side liquid is the non-wetting phase and gas is the wetting phase.

Capillary pressure  $P_C$  is related to the curvature of the interface between the phases. The capillary pressure of an interface can be described by the Young-Laplace equation [117]:

$$P_C = 2\sigma H \quad (2.6)$$

where  $\sigma$  is the surface tension of the liquid-gas interface and  $H$  is the mean curvature of the interface defined as:

$$H = \frac{1}{2} \left( \frac{1}{r_1} + \frac{1}{r_2} \right) \quad (2.7)$$

where  $r_1$  and  $r_2$  are the principal radii of curvature measured in perpendicular directions.

For the simple case of a cylindrical tube shown in Figure 2.1 the curvature of the interface can be found from the radius of the tube and the contact angle formed where the interface meets the solid walls and Eq.(2.6) becomes:

$$P_C = -2\sigma \cos(\theta) \left( \frac{1}{r} \right) \quad (2.8)$$

where  $r$  is the radius of the tube and  $\theta$  is the contact angle, which is discussed below. For geometries more complex than cylindrical tubes, obtaining a solution to Eq.(2.6) is not trivial, if possible at all, thus Eq.(2.8) is typically used to convert between capillary pressure and pore size based on the assumption that pores are cylindrical tubes. Whether Eq.(2.8) is strictly valid or not, this inverse relationship between size and capillary pressure is generally true.

The wettability of a fluid on a solid can be determined by the contact angle formed between a droplet of fluid and a smooth surface of the solid in question, as shown in Figure 2.2. In general, a contact angle below  $90^\circ$  means the fluid is wetting and non-wetting if it is above  $90^\circ$ . In terms of the Young-Laplace equation (Eq.(2.8)) this definition leads to a change in the sign of the capillary pressure due the the change in the  $\cos(\theta)$  term at  $90^\circ$ .

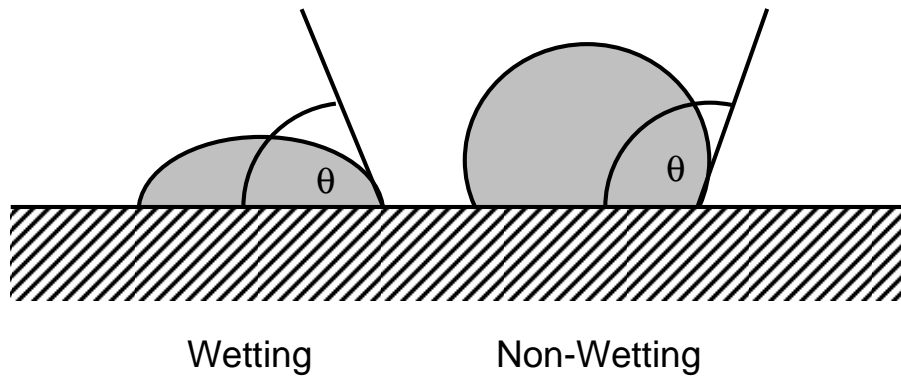


**Figure 2.2: Definition of wetting and non-wetting phase based on solid-liquid contact angle**

In practical terms, however, the appearance of true hydrophilic or hydrophobic behavior is not as clearly defined. A contact angle close to  $0^\circ$  indicates a highly wetting fluid, such as water on glass which has contact angle of  $0^\circ$  and spreads indefinitely instead of forming a droplet. Conversely, a large contact angle indicates a highly non-wetting fluid, such as mercury which has a contact angle of  $140^\circ$  on most solids and beads up. Contact angles near  $90^\circ$  ( $\pm 35^\circ$ ), however, are considered intermediate (Figure 2.3) and such fluids often exhibit mixed and complex wetting tendencies.

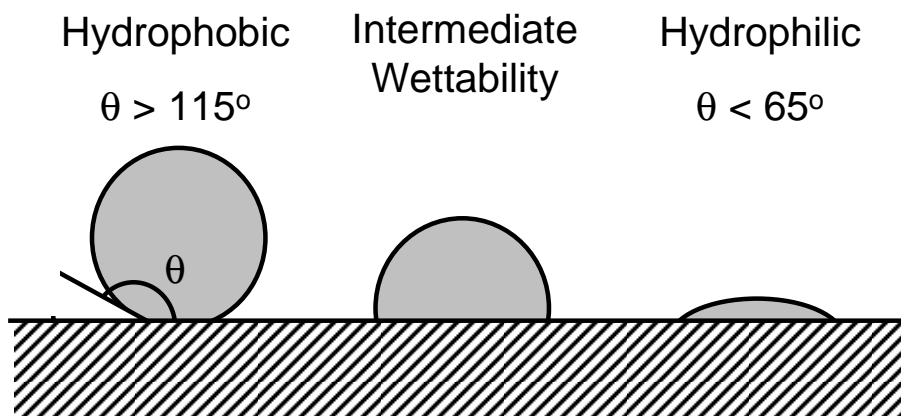


**Figure 2.3: Practical limits of wetting and non-wetting phase based on solid-liquid contact angle**

The wetting and non-wetting phase can be either fluid, depending on the chemical interactions of the fluids with the solid interface. Solids are often classified by their

wettability to various fluids. In oil recovery literature, for instance, an oil bearing sand is referred to as either oil-wet or water-wet. When water and air are the fluids, solid surfaces are termed hydrophilic if they are water-wet and hydrophobic if they are not.

Because the wettability of a porous material controls whether a phase will wick or imbibe into the porous structure, it is important to ensure that GDLs are not water-wet since imbibed water would spread and completely block gas transport. For this reason, a hydrophobic polymer treatment applied to GDLs is added to increase the water contact angle in the GDL in the hope of increasing GDL hydrophobicity. Although it is conceptually straightforward, there is confusion over the actual effect of hydrophobic polymer addition on GDL wettability. The fibers of the GDL are made of graphite, which is reported to have a water contact angle of  $86^\circ$  [119] and are therefore strictly hydrophilic, while the hydrophobic coating, usually PTFE, has a water contact angle of  $108^\circ$  [120,121]. Since both of these values are in the range of intermediate wettability (Figure 2.3), it is misleading to think of these surfaces as being solely hydrophilic or hydrophobic. The presence of these different materials is thought to give rise to a situation of mixed wettability. It is often assumed that GDLs are composed of a mixture of regions of singular wettability, leading to a conceptual picture of GDLs as having coexisting networks of hydrophilic and hydrophobic pores [30,122]. In such a picture, liquid water wicks into and flows through the hydrophilic pore network while gas transport occurs through the hydrophobic pores and the amount of PTFE added controls the relative amounts each network. Sinha and Wang [122] incorporated this concept into a pore network model of a GDL by randomly assigning either a hydrophobic or hydrophilic contact angle to each pore. Weber *et al.* [30] incorporated mixed wettability into a continuum model by assigning a fixed volume fraction of pores as hydrophilic. Some experimental support for this picture was provided in early work by Gostick *et al.* [123] who demonstrated that liquid suction (i.e. negative capillary pressure) was required to remove water from a GDL, indicating the existence of hydrophilic regions. Contradictory evidence exists, however, demonstrating that GDLs are hydrophobic. Benziger *et al.* [124] performed experiments to measure the breakthrough pressure of water and found that positive liquid pressure of at least several thousand Pa was required

to initiate water flow in all GDLs with or without PTFE. Clearly, GDL wettability and the behavior of liquid water is more complex than the simple picture described above.

There are several factors that influence wettability beyond the simple measure of static contact angle on a flat, smooth surface. In a classic paper, Wenzel [125] demonstrated that a rough surface yields a different contact angle than a smooth surface of the same material due to the increased contact between the solid and liquid for a given projected area created by the roughness. This is shown on the left of Figure 2.4 and is described by the Wenzel equation:

$$\cos(\theta_{obs}) = b \cos(\theta_{act}) \quad (2.9)$$

where  $\theta_{obs}$  is the observed macroscopic contact angle on the rough surface,  $\theta_{act}$  is the contact angle on smooth surface and  $b$  is the ratio of total area of the rough surface under the drop to the projected surface area if the drop were sitting on a flat surface. All contact angles are measured through the droplet so that roughness makes non-wetting fluids more non-wetting and wetting fluids more wetting.

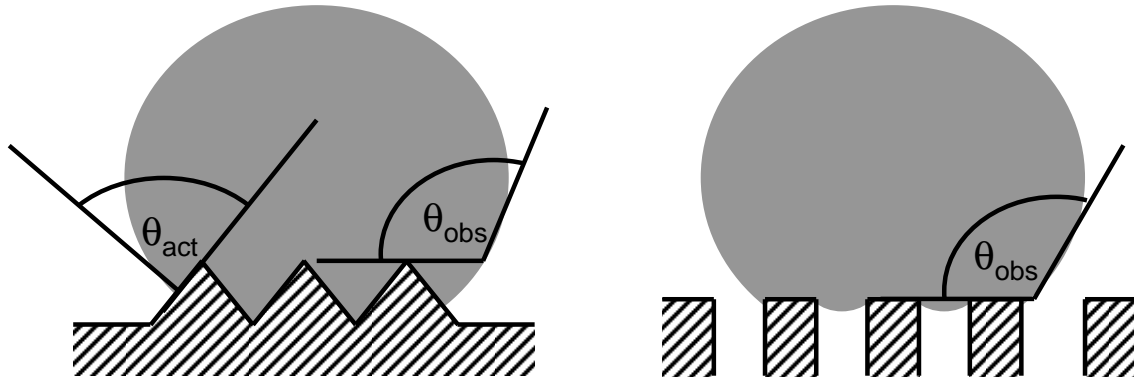


**Figure 2.4: Droplet on a rough surface. Left: Wenzel Effect. Right: Cassie-Baxter Effect.**

Also shown in Figure 2.4 is the Cassie-Baxter effect [126] which occurs on very rough or porous surfaces where the droplet is resting on both the solid portions of the surface and the void openings on the surface. The observed contact angle will be an area-weighted average of the contact angle on each surface:

$$\cos(\theta_{obs}) = f_1 \cos(\theta_1) - f_2 \cos(\theta_2) \quad (2.10)$$

where  $f_1$  is the fractional area of solid with a contact angle of  $\theta_1$ , and  $f_2$  is the fractional area of voids. The contact angle,  $\theta_2$ , of a liquid droplet on the air surface is  $180^\circ$ . The observed contact angle measured through a liquid droplet is always higher on a porous surface. Even for a liquid that is normally highly wetting on the solid and would be expected to spread over it, a droplet can still form if the surface is sufficiently porous; this is often referred to as the “lotus leaf effect” [127]. Since GDLs are porous and the individual fibers are rough, both the Wenzel effect and the Cassie-Baxter effect contribute to the appearance that GDLs are more hydrophobic than suggested by contact angle measurements alone. Lafuma and Quere [128] studied contact angles of water droplets on micropatterned hydrophobic surfaces and found contact angle increases of  $30^\circ$  for droplet in the Wenzel state (i.e. droplet filled the roughness) and  $50^\circ$  for droplets in the Cassie-Baxter state (i.e. air trapped in the roughness below the droplet). Gostick *et al.* [129] reported contact angles for water on GDL surfaces between  $130^\circ$  and  $150^\circ$ . They attempted to extract the actual contact angle from the observed value using a combined Wenzel and Cassie-Baxter equation:

$$\cos(\theta_{obs}) = bf_1 \cos(\theta_1) - f_2 \quad (2.11)$$

where  $b$  was included to account for the roughness caused by the round fibers as suggested by Adamson [119]. Using this approach, actual contact angles close to  $100^\circ$  were estimated for several GDLs, which is in line with known values for graphite and PTFE.

Although the Wenzel and Cassie-Baxter effects explain why GDLs behave hydrophobically and resist water penetration despite being only mildly hydrophobic or even mildly hydrophilic, the strong hydrophilic behavior observed by Gostick *et al.* [123] during water withdrawal requires explanation. There are several other mechanisms that further affect wettability. Contact angle hysteresis is a widely observed phenomenon where the contact angles differ between advancing and receding contact lines, with the advancing contact angle being larger than the receding one as shown in Figure 2.5. Zisman [130] gives a thorough account of numerous contact angle hysteresis mechanisms and cites roughness on the solid surface, which inhibits both the advancement and retraction of contact lines, as the main source. Contact angle hysteresis is usually not

observed on molecularly smooth surfaces [130]. Lafuma and Quere [128] studied contact angle hysteresis on their micropatterned surfaces and found that droplets in the Wenzel state exhibited a contact angle of  $\theta_A = 140^\circ$  during advancement and  $\theta_R = 40^\circ$  during retraction. Such a massive swing in contact angle effectively changed water from a highly non-wetting to a highly wetting phase. In the experiments of Gostick *et al.* [123] that showed hydrophilic behavior in GDLs, the water was most certainly in the Wenzel state, so that a large contact angle hysteresis likely existed.

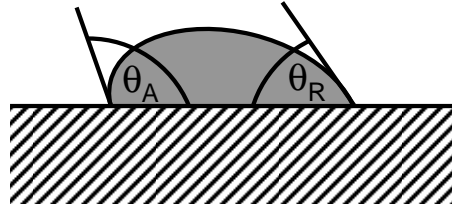


**Figure 2.5: Contact angle hysteresis.** The picture droplet is being moved to the left, creating an advancing and receding contact angle,  $\theta_A$  and  $\theta_R$ , respectively.

Yet another consideration is the effect that solid structure has on fluid interfacial shape. Consider the case shown in Figure 2.6 where liquid is injected into a converging or diverging pore throat. The contact angle is measured relative to the tangent where the liquid meets the solid. Even if the liquid is technically non-wetting on the solid,  $\theta_A > 90^\circ$ , the interface curvature can assume a negative value (Figure 2.6 left) or a positive value (Figure 2.6 right) depending on the angle of the solid wall. Such reversals in interfacial curvature would be most prevalent for systems with intermediate contact angles near  $90^\circ$ . This can be seen in Eq.(2.12) where the sum of the contact angle and the pore divergence angle dictates the sign of the cosine term, and therefore the direction of the interface curvature [131].

$$P_C = -\frac{2\sigma}{r}(\cos(\theta + \phi)) \quad (2.12)$$

where  $\theta$  is the fluid contact angle and  $\phi$  the angle of the pore wall relative to the normal of the interface. Reversal in interface curvature by this effect can change which fluid behaves as the wetting phase, and as a result, retraction of a non-wetting phase may require negative capillary pressures as observed by Gostick *et al.* [123].

Overall, the wettability of GDLs is a complex subject. Observed wettability behavior is the result of chemical heterogeneity (graphite and PTFE), roughness, porosity, configurational effects and history dependence. GDL are not highly hydrophilic, even without the addition of PTFE, since water does not wick into the pore structure. At the same time, they are not highly hydrophobic either, since air does not spontaneously displace water from a GDL once it is filled with water.

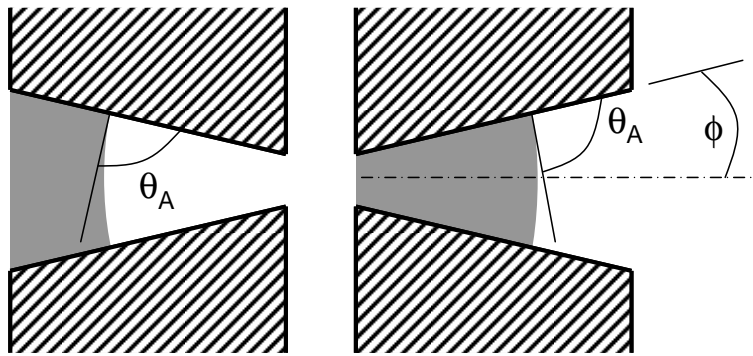


**Figure 2.6: The effect of solid structure on fluid configuration.**

## 2.2. Capillary Pressure Curves

Capillary pressure curves provide perhaps the most important information that can be obtained about a porous material. A great deal of information is contained in these curves, including pore size distribution, porosity, breakthrough pressure, phase trapping and fluid-solid wettability. Capillary pressure curves for GDLs are particularly interesting since the hydrophobic polymer coating is specifically intended to alter the capillary properties, without significantly changing the structural properties.

A porous medium consists of a network of many connected pores, each with a different size. Consequently a porous material will present a range of capillary pressures, where the pressure of each pore is described by a function similar to the form given in Eq. (2.8). The displacement of a wetting phase from a porous media occurs gradually as the pressure of the non-wetting phase is increased and individual pores are drained. A

capillary pressure curve is obtained by scanning through a range of pressures and monitoring the cumulative volume of non-wetting phase that is injected at each pressure. A simplified capillary pressure curve is shown in Figure 2.7. As the non-wetting phase pressure is increased from zero to positive values, invasion initially proceeds into the largest most easily penetrated pores according to Eq.(2.8). Further increases in pressure result in smaller pores being penetrated until all the pore volume in the sample is filled. The capillary pressure curve provides direct information about how much pore volume is accessible at any given pressure.

When pressure is relieved in a similar incremental fashion the non-wetting phase begins to withdraw from the sample and an extrusion curve is obtained. A hysteresis is observed in the withdrawal of the non-wetting phase, which for several reasons always occurs at lower capillary pressures than was required to inject it. The most basic reason is that injection is controlled by penetration of constrictions (throats) while withdrawal is controlled by bulges (bodies), as shown in Figure 2.8. A pressure of  $P_1$  is insufficient to penetrate the inlet throat. When the pressure is increased to  $P_2$  the inlet throat and pore body are filled simultaneously. When the pressure is returned to  $P_1$  the fluid retracts to a position that is consistent with the pressure  $P_1$ , but this corresponds to a size larger than the inlet throat since the inlet throat was impenetrable at  $P_1$ . In this scenario it is clear that more non-wetting phase exists in the sample than was attained during injection at the same pressure.

Contact angle hysteresis also contributes to the difference between the intrusion and extrusion curves as discussed in the previous section. Another feature shown in Figure 2.7 is the residual non-wetting phase saturation. This is caused by pockets of non-wetting phase becoming detached from the withdrawing fluid and becoming completely immobile.

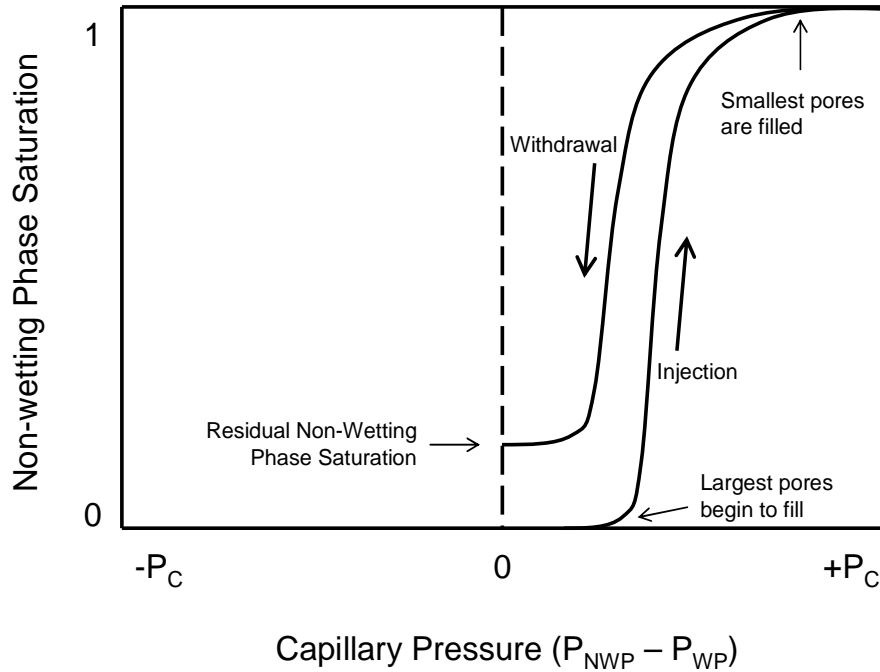


Figure 2.7: Diagram of a typical capillary pressure curve.

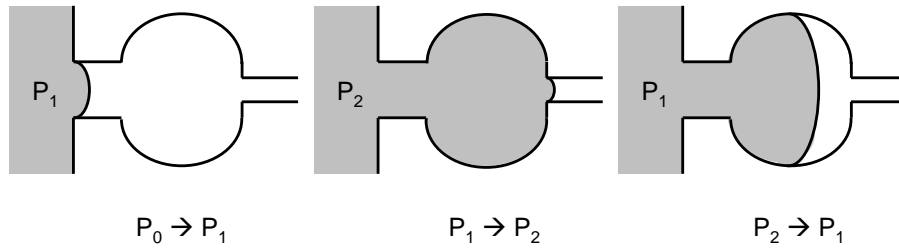


Figure 2.8: Conceptual picture of non-wetting phase movement as pressure is increased from  $P_1$  (left) to  $P_2$  (center) and back to  $P_1$  (right).

From the point of view of GDL transport modeling, the capillary pressure curve relates the applied fluid pressure to the resulting saturation of the porous material. Since the estimation of the GDL saturation is the main objective of two-phase-flow based PEMFCs models, an accurate knowledge of the capillary pressure behavior would seem essential. Yet, capillary pressure is perhaps the least known of GDL properties. In place of relevant capillary pressure curves, a very common practice is the use of the so-called  $J$ -function:

$$J(s) = a_0 s + a_1 s^2 + a_2 s^3 \quad (2.13)$$

where  $J(s)$  is a dimensionless capillary pressure,  $s$  is the water saturation and  $a_1$ ,  $a_2$  and  $a_3$  are empirical coefficients. The popular use of Eq.(2.13) to represent capillary pressure

curves for GDLs can be traced back to Wang *et al.* [39,54] who assumed values of most GDL properties for their early model since very little experimental information was available at that time. Wang *et al.* [54] chose a polynomial given by Udell [132], which was obtained by fitting Eq.(2.13) to the classic data of Leverett [131]. The appeal of these data (aside from the convenience of its polynomial form for numerical implementation) is that Leverett [131] had demonstrated that capillary pressure curves from several different sand pack samples could be collapsed into a single curve when normalized according to:

$$P_c(s) = \sigma \cos(\theta) \left( \frac{\varepsilon}{K} \right)^{0.5} J(s) \quad (2.14)$$

where  $\sigma$  is the surface tension of the fluid system,  $\theta$  is the contact angle,  $\varepsilon$  is the porosity and  $K$  is the permeability of the porous medium. Although it is true that Leverett [131] demonstrated some universality among capillary pressure curves of related materials, it is not true that the normalized data of Leverett (and fitting of that data by Udell) can be used to represent GDLs, which bare no structural resemblance to sand packs.

Furthermore, Eq.(2.13) is not a good representation of a capillary pressure curve function; it shows no breakthrough point since it passes through the origin, it tends to yield curves that are much too steep and it is abruptly terminated at  $s = 1$ . Ironically, a close analysis of Udell's polynomial reveals that it is not even a good fit to Leverett's results beyond the range that Udell originally intended for his own purposes (heat pipe modeling); nonetheless this polynomial has been used in over 50 publications [25,26,28,29,32,33,37-39,41-43,45,46,48-50,52-54,56-59,62,63,65,66,69-72,74,75,77-79,83,85,88,90-92,94,96,101,102,104-108,110,111]. The reliance on this equation has become so customary that some of the more recent works do not even provide a citation for its original use.

Only a small number of authors have acknowledged the inappropriateness of Eq.(2.13) for GDL modeling and attempted to find alternatives. Nguyen and co-workers proposed an equation that was obtained by comparing the results of their numerical fuel cell model to experimental fuel cell polarization data and using the parameters of the capillary pressure functions as a fitting parameter [27,35]. Others have simply treated the  $dP_c/ds$

term as a constant for lack of better information [31,34,44,87,89]. Gurau *et al.* [99] used a Brooks-Corey expression and explicitly stated that the parameters and exponents used were assumed values. Since the original paper of Wang *et al.* a vast number of similar models have been published that use the same inappropriate or other faulty capillary pressure data. Only now, almost 10 years later, are significant attempts being made to determine actual air-water capillary properties of GDLs.

The most widely accepted method for measuring capillary pressure curves is mercury intrusion porosimetry (MIP), which is a well established technique and has seen wide spread use by fuel cell researchers [64,133-138]. Although mercury intrusion porosimetry is a well established technique for measuring capillary curves of many porous materials, this method is not useful for GDLs for several reasons. Firstly, since mercury is highly non-wetting to both the graphite substrate and the PTFE coating in GDLs, it is insensitive to changes in the chemical heterogeneity of the solid surfaces, which is precisely what is of most interest. Secondly, conversion of mercury intrusion pressure data to an equivalent air-water pressure requires knowledge of the contact angles of mercury and water on GDL surfaces. Even if a single contact angle can be determined for mercury in the GDL, which is not straightforward [123], the water contact angle will vary for the graphite and PTFE surfaces, making this conversion impossible without additional knowledge of the PTFE distribution. Furthermore, this conversion requires the use of the Young-Laplace equation based on a bundle-of-tubes model (Eq.(2.8)), which is not necessarily valid for highly porous and fibrous GDLs. Clearly there is a need for direct measurement of the air-water capillary properties of GDLs. Despite the drawbacks of this approach Acosta *et al.* [64] attempted to obtain air-water capillary pressure curves from MIP data.

The problem of indeterminate contact angles and mixed fluid wettability in capillary pressure curves can be avoided by measuring capillary pressure curves directly with water as the working fluid. Several techniques are available for this measurement, but none of them have achieved widespread acceptability. Capillary flow porometry (CFP) [139,140] is based on forcing water to flow through the GDL. By comparing pressures

required for single phase flow of the wetting phase (i.e. air) and for two-phase flow (i.e. water displacing air) it is possible to obtain a pressure vs. flow rate distribution. If the porous media is assumed to be a bundle of tubes, then such data can be converted to a capillary pressure curve. This method has a number of drawbacks. The most serious problem arises due to the existence of a pressure gradient in the flowing phase across the sample which leads to varying applied capillary pressures applied at different locations. Mathias *et al.* [12] have performed a slight variation of this experiment that uses air as the non-wetting fluid to displace a strongly wetting organic fluid from GDLs. Although this is conceptually equivalent to MIP measurements, substantially different results were obtained by the two methods. Furthermore, this experiment is limited to scanning only in the direction of increasing water saturation and for  $P_C > 0$  and so provides only partial curves.

The method of standard porosimetry (MSP) [141-143] is another approach that can be used to obtain air-water capillary pressure curves. In this test, a GDL is initially saturated with water and placed in capillary contact with a saturated porous “standard” which has a known capillary pressure curve. While in contact, the standard and the sample are in capillary equilibrium, the known capillary pressure in the standard is the same as that in the sample. The capillary pressure is varied by allowing the standard and sample to dry slowly while in contact, thereby varying their capillary pressure together. By weighing the sample and standard periodically their saturations can be found. From this, the capillary pressure of the standard, and therefore also of the sample, can be obtained from the known capillary pressure curve of the standard. This method is limited to scanning only in the direction of decreasing water saturation and only for  $P_C < 0$ . The application of this method to GDLs was initially investigated by Gostick *et al.* [123]. More recently Mench and co-workers have used this technique to study a wide variety of GDLs with varying hydrophobic polymer contents [144], under different compressions [145] and at a range of temperatures [146]. They have further attempted to synthesize a single relationship that can describe the capillary properties of any GDL, with any combination of the above parameters (temperature, compression, hydrophobic polymer loading) [147], to generate a correlation that can be substituted directly for Eq.(2.13).

Gallagher *et al.* [23] have recently reported a method that is somewhat similar to MSP. The GDL is initially saturated with water and is placed on a porous plate that is also water saturated. Instead of changing the GDL saturation by drying, as in MSP, they control the capillary pressure directly by applying suction to the porous plate. Capillary equilibrium is established between the GDL and the plate as water flows from the GDL and to the plate and *vice versa*. The GDL saturation is determined by weighing after equilibration at each applied pressure. Since pressure is controlled directly it is possible with this method to scan along both increasing and decreasing water saturation paths, although this method is limited to  $P_C < 0$ .

Roth *et al.* [24] have developed a technique that involves submerging a sample in water and weighing the water uptake. Since water does not spontaneously imbibe into a GDL, even when submerged, they forced water into the sample in discrete amounts by first reducing the gas pressure inside the sample to a value of  $P_G < P_{ATM}$ , then submerging the sample under water and returning the gas pressure above the water to  $P_{ATM}$ . This has the effect of forcing water into the sample at a pressure of  $P_C = P_{ATM} - P_G$ . A capillary pressure curve can be obtained by repeated measurements at successively lower gas pressures. This method only scans in the direction of increasing water saturation and only for  $P_C > 0$ .

A more straightforward approach for measuring capillary pressure is adapting the MIP concept to use water as the injecting fluid. Using water introduces several difficulties that are not encountered when using mercury owing to the non-negligible vapor pressure of water. In MIP it is possible to evacuate the sample before mercury is injected since mercury has negligible vapor pressure so it does not cavitate or evaporate. This allows the sample to be contained in a sealed, dead-ended chamber since no air must be displaced by the invading mercury, vastly simplifying sample mounting. When water is the working fluid, allowances must be made for its volatility and the sample cannot be evacuated. This requires designing a sample holder that allows air to escape as water invades, but water must not be allowed to leave the sample. An example of a sample

holder for this approach is shown in Figure 2.9. In this arrangement, a porous hydrophobic membrane is used as a capillary barrier to prevent injected water from leaving the top of the sample. Also, a porous hydrophilic membrane is employed on the bottom side to prevent air from leaving the sample during water drainage.

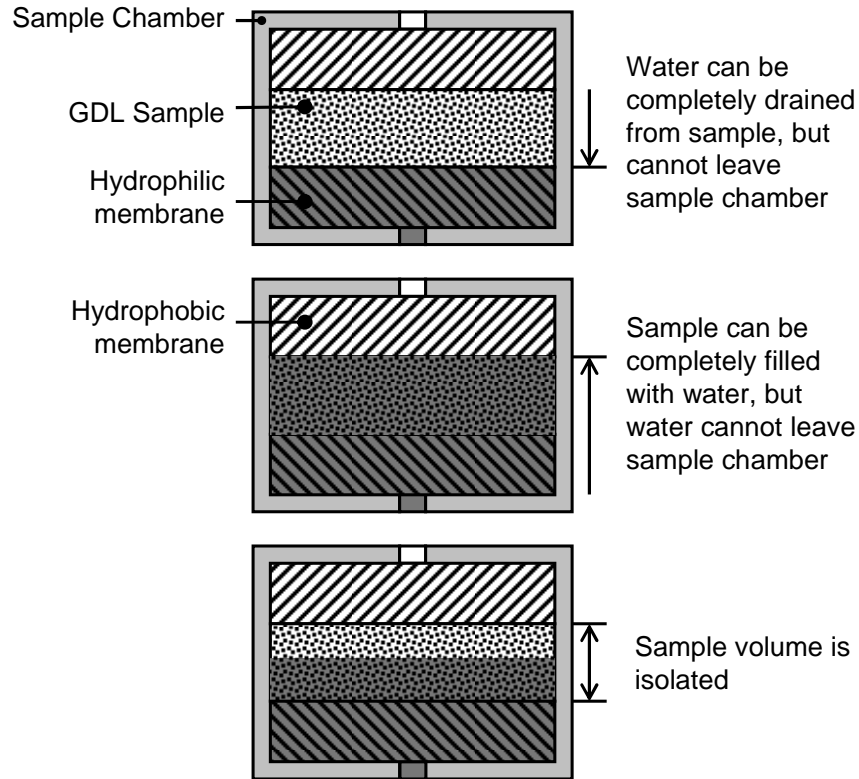


**Figure 2.9: Schematic diagram of a sample holder using capillary barriers for water injection experiments**

Several variations of this method have been recently employed. Fairweather *et al.* [20] used a syringe pump to inject discrete volumes of liquid into a sample and measured the resulting liquid pressure. The intention of using discrete volume injections was to allow time for capillary equilibrium before advancing to the next data point. Their technique allows scans along both increasing and decreasing water saturation paths and over a wide range of capillary pressures,  $P_{C,MIN} < 0 < P_{C,MAX}$ . Their results revealed for the first time a hysteresis effect, with water injection occurring at  $P_C > 0$ , as observed by Benziger *et al.* [124] and water withdrawal occurring at  $P_C < 0$ , as observed by Gostick *et al.* with MSP [123]. Despite the insights gained by this technique, it is not entirely satisfactory since

the controlled variable is the injected volume. When adding volume in fixed amounts it is possible that the pore space made accessible  $V_a$  at any given pressure  $P_i$  may not be completely filled by the volume  $V_i$  of fluid injected, (i.e.  $V_i < V_a(P_i)$ ). A capillary pressure curve is generally expected to represent the amount of pore volume accessible at a given pressure, making the results of this experiment difficult to interpret. Toledo *et al.* [148] were able to extract a great deal of useful information from volume-controlled injection experiments, but only with the aid of a well calibrated dynamic pore network model.

Sole [22] reports a method similar to that of Fairweather *et al.* [20]. This is also a volume-controlled method, but the water is injected into the GDL specimen at a constant rate while the pressure response is monitored with time. The GDL saturation at any point can be found from the injection rate and the elapsed time. A wide range of capillary pressure  $P_{C,MIN} < 0 < P_{C,MAX}$  can be scanned with this method but Sole [22] did not employ a hydrophilic membrane below the sample and so limited scans to the direction of increasing water saturation only. The difficulty with constant rate injection is that capillary equilibrium is never truly established in the sample since the fluid interfaces are continually altered by the additional fluid. Even if pseudo-equilibrium conditions are maintained, this approach still has the same drawback as that of Fairweather *et al.* [20] (i.e. volume-controlled capillary pressure experiments are not easily interpreted).

Another version proposed by Van Nguyen *et al.* [21] controls liquid pressure instead of liquid volume. Capillary pressure is controlled by adjusting the hydrostatic pressure between the sample and a horizontal graduated tube. As the static pressure is altered, the liquid saturation in the GDL can be monitored by tracking the movement of a meniscus in the graduated tube of known diameter. This work uses a hydrophobic capillary barrier but no hydrophilic membrane. Although they did not use a hydrophilic barrier, Van Nguyen *et al.* [21] managed to perform water withdrawal by carefully reducing the liquid pressure and ensuring gas breakthrough did not occur. The capillary loops obtained did not show any hysteresis, which is surprising and does not agree with the results of Fairweather *et al.* [20]. Van Nguyen and co-workers have recently attempted to

incorporate the data obtained from their curves into continuum models [86,100].

As an alternative to the various experimental approaches, Becker *et al.* [149] have attempted to determine capillary pressure curves computationally. They used morphological image opening on 3D images of GDLs obtained from x-ray tomography. This technique has the advantage of generating 3D images of partially saturated GDLs which can be further used in transport calculations as described in the following sections. The problem with this approach is that the contact angle is unavoidably assumed to be zero, since this is the contact angle formed when a spherical structuring element meets a solid wall. This approach has also been used by Schulz *et al.* [150] on artificially generated GDL images.

Figure 2.10 presents the air-water capillary curves obtained using each of the above methods. The results vary widely despite the fact that they were obtained for similar materials. The J-function typically used in fuel cell CFD models is shown to lie in the midst of all other obtained data, although it is far too steep. The computed curve of Becker *et al.* [149] shows water penetration at much higher pressures than observed experimentally, which can be attributed to the fact that the water contact angle was assumed to be  $180^\circ$ .

Overall, the methods for measuring air-water capillary pressure curves reported in the literature are flawed or limited. Table 2.1 summarizes each method discussed above with respect to its capillary pressure range and scan direction. An ideal method is one that can scan the entire range of capillary pressures in both directions (i.e. from  $-P_C \rightarrow +P_C$  as well as  $+P_C \rightarrow -P_C$ ). Also included in the table is the variable which is controlled by each method, which ideally should be pressure due to the difficulties associated with interpreting volume-controlled experiments. As can be seen from Table 2.1, each of the previously reported methods presented above falls short in at least one category. Also shown in the last line of Table 2.1 is a method that was developed as part of the present thesis and is one of the main contributions of the present work. This is described in detail in the experimental section (Section 3.2.3). This method meets all the requirements of

the ideal capillary pressure measure technique and it is highly accurate and fully automated. Results obtained from this method are presented and discussed at length in Chapter 5.

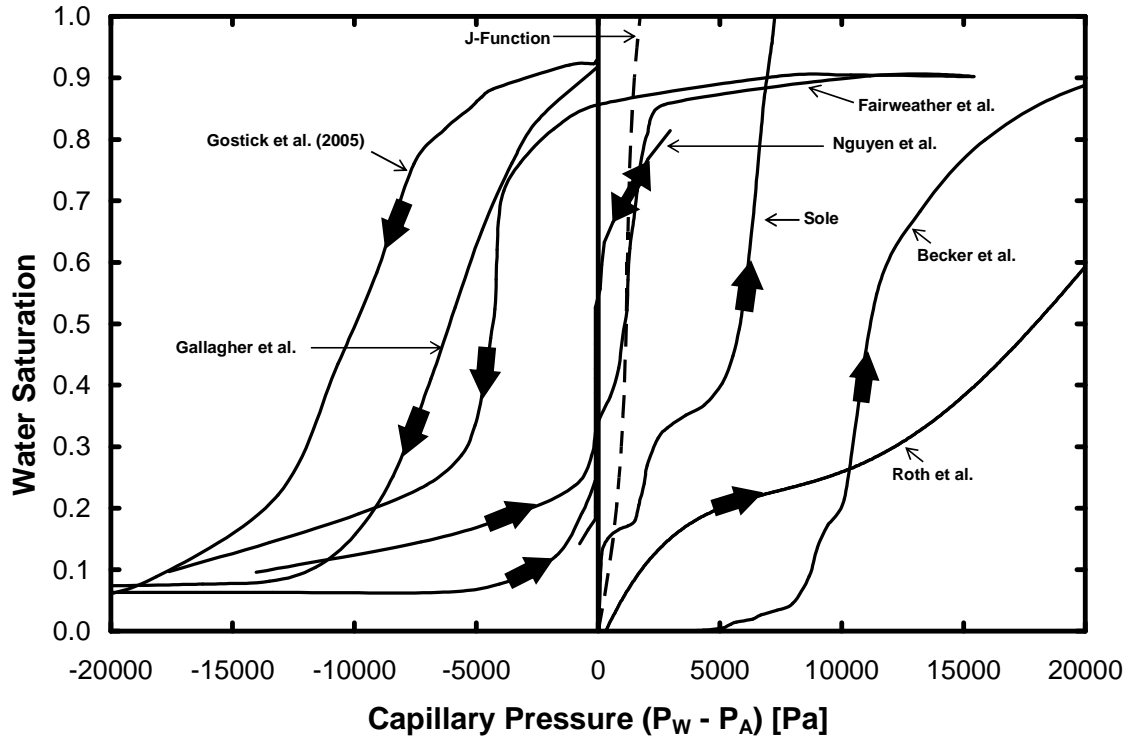


Figure 2.10: Comparison of air-water capillary pressure curves available in the literature for Toray 090 or similar material. All curves are for GDLs with no PTFE except Roth *et al.* (7%).

**Table 2.1: Comparison of air-water capillary pressure measurement techniques**

Method	$-P_c \rightarrow 0$	$0 \rightarrow -P_c$	$0 \rightarrow +P_c$	$+P_c \rightarrow 0$	$f(P_c)$
Mathius [12] (2001)		✓			✓
Gostick [123] (2005)		✓			
Fairweather [20] (2007)	✓	✓	✓	✓	
Roth [24] (2008)			✓		✓
Sole [22] (2008)	✓		✓		
Gallagher [23] (2008)	✓	✓			✓
Nguyen [21] (2008)			✓	✓	✓
Present Study [151] (2008)	✓	✓	✓	✓	✓

### 2.3. Breakthrough Point and Percolation

The breakthrough point of a porous material occurs when the first drop of an injected non-wetting phase emerges at the outlet face. In order to achieve breakthrough, a sufficiently high pressure must be applied to the non-wetting fluid so that it can invade enough pores to open a pathway through the sample. This threshold pressure or breakthrough pressure is an important property of fluid flow since it represents the minimum pressure that must be applied to initiate flow. In addition to pressure, the breakthrough point is also characterized by a breakthrough saturation, which indicates the volume fraction of pores that must be invaded to form a pathway that spans the sample. The breakthrough pressure and saturation of the GDL are highly relevant to fuel cell operation since liquid flow must be initiated for liquid to leave the cell and gas transport must occur through the unfilled pores. For gas mass transfer purposes it is important that this saturation be as low as possible, so it is desirable to have a GDL with a low breakthrough saturation.

The capillary behavior of a fluid in a porous medium is well described by percolation theory [3,148]. Percolation theory applies to networks of sites connected by bonds and a porous media can be viewed as a network of pores (sites) connected by throats (bonds).

One of the principal objectives of percolation theory is to determine the probability of a continuous path existing across the network as the number of connections between sites is increased. On an infinite cubic lattice, the probability of such a sample spanning cluster existing approaches 1 as the number fraction of connections between sites approaches 0.2488 [152,153]. This is called the percolation threshold. In pure percolation the connections are added at random locations in the network. In the porous medium analogy, connections are added at any throat that can be penetrated at a given pressure and the pressure is increased to create more connections. The percolation threshold then yields not only the fraction of filled pores, but also the pressure required to achieve percolation. Figure 2.11(a) shows a square lattice with connections drawn at random and the formation of connected clusters can be seen, although a sample spanning cluster does not exist. Figure 2.11(b) shows that by adding the dotted lines a sample spanning cluster is created.

The analogy between percolation theory described above and fluid invasion into a porous medium is not exact however, since fluid entering into a medium can only penetrate throats that are accessible from the injection face. A modified version of percolation theory, called invasion percolation [154,155], is used to simulate the invasion of fluid into a medium. In this case, a connection is made between two pores if the connecting throat can be penetrated at the applied pressure *and* the throat is connected to an invading cluster. Throats far away from the injection face that are penetrable but not connected to the invading fluid cluster are therefore not filled. This difference is illustrated in Figure 2.11(c), where the grey sites and bonds are not filled since they are not connected. Figure 2.11(d) shows the invasion percolation formation at the percolation threshold which occurs when the dotted bonds are connected. The percolating cluster is identical for both types of percolation if the lattice is infinite.

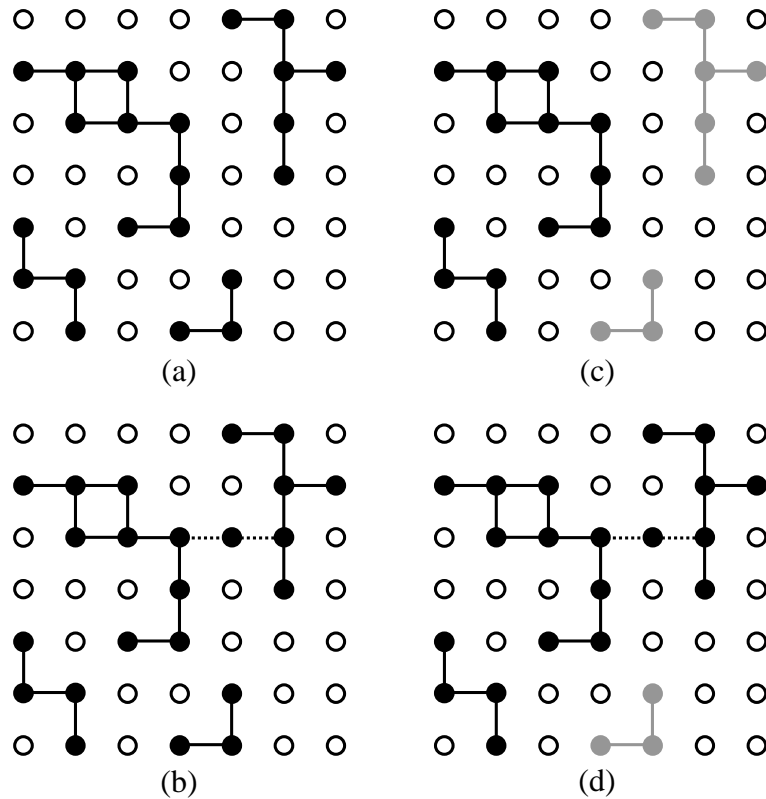


**Figure 2.11: Percolation on square lattices. (a) Normal percolation below the percolation threshold. (b) Normal percolation at the percolation threshold. A sample spanning cluster is formed by the addition of the dotted lines. (c) Invasion percolation below the percolation threshold. All grey sites and bonds are not invaded due to inaccessibility. (d) Invasion percolation at the percolation threshold. The same sample spanning cluster is recovered by the addition of the dotted lines. Some disconnected grey clusters remain.**

Most percolation properties are derived from infinite size lattices. Infinite lattices are applicable to reservoir scale media and are well approximated by rock core samples. The GDL, however, is very far from an infinite system. Mean pore sizes for GDLs have been reported between 20 and 50  $\mu\text{m}$  [149,150,156], while typical GDL thickness range from 200 to 500  $\mu\text{m}$ , meaning that GDLs are typically just 10-15 pores thick. Compared with percolation properties for infinite lattices, the percolation properties of GDLs present many unexpected results. For instance, one of the main artifacts due to finite sample size are surface effects that arise when a significant amount of pore volume is accessible from the surface of the sample well before breakthrough. On infinite or large lattices this volume is negligible. On GDLs however, this volume can represent half of the total pore volume or more. Surface effects in GDLs are not artifacts, but actual properties of

interest. Another feature of the extreme finite size effects in the GDL is that water breakthrough can occur without true percolation occurring. In other words, the pore volume that is accessible from the surface may form a sample spanning cluster. These finite size effects are so important to GDL percolation behavior that in Chapter 5 this effect is used explain the role of MPL in fuel cell performance improvement.

Experimental study of GDL breakthrough properties has been rather limited. Benziger *et al.* [124] measured breakthrough pressures for several GDLs by affixing them to the end of a pipe and increasing the water head above the sample incrementally until breakthrough occurred. They obtained values ranging from 4000 Pa to 7500 Pa for GDLs with 0% to 60wt% PTFE. This simple method was not able to measure the saturation at breakthrough, however. They attempted to calculate the saturation by applying the bundle-of-tubes model and found that a single tube (the diameter of which was determined from the Young-Laplace equation using Eq.(2.8)) was sufficient to carry the observed flow rate given the applied pressure gradient. This leads to an extremely low saturation estimate that is not realistic since it fails to consider GDLs as a connected network where water follows many dead-end paths. In fact, considering the finite size scale effects present in GDLs, such dead-end path may account for a substantial amount of pore volume. Various other similar reports of breakthrough pressure are scattered throughout the literature, but these are usually part of a larger study and do not give detailed results or procedures [157,158]. Nguyen *et al.* [21] reported the breakthrough pressure and saturation using their capillary pressure method by performing tests without a hydrophobic capillary barrier above the sample and observing the point at which water droplets emerged. They observed breakthrough occurring during a plateau in saturation, which is contrary to percolation concepts.

In this thesis, capillary pressure and saturation at breakthrough are measured for the first time. The capillary pressure measurement device developed during the course of this work is adapted to detect the breakthrough of water. Using this adapted method, a number of illuminating experiments are performed on GDLs with and without microporous layers.

## 2.4. Absolute Permeability

Permeability is a material-specific property that is a measure of the resistance to flow through that material. Permeability is generally a function of porosity and some characteristic particle length. The Carman-Kozeny equation is widely used for correlating permeability to the structure and properties of a porous material [117]:

$$K = \frac{d_c^2 \varepsilon^3}{16k_{CK}(1-\varepsilon)^2} \quad (2.15)$$

where  $K$  is the permeability,  $\varepsilon$  is the porosity,  $d_c$  is a characteristic length and  $k_{CK}$  is a constant specific to a given material that is determined experimentally. As can be seen from Eq.(2.15), permeability increases with porosity and characteristic length, which is usually an average particle diameter or fiber diameter in the case fibrous GDLs. Higher porosity offers more numerous and less obstructed pathways for flow. For a given porosity, a larger particle size leads to larger pores which offer less viscous resistance to flowing fluids.

For sufficiently low fluid velocities, single-phase flow through a porous medium is described by Darcy's Law [117]:

$$-\nabla P = \frac{\mu}{K} \bar{v} \quad (2.16)$$

where  $K$  is the absolute permeability of the porous material,  $\mu$  is the viscosity of the flowing fluid,  $\bar{v}$  is the superficial velocity of the fluid and  $P$  is the pressure in the medium. In the creeping flow regime, viscous interactions between the fluid and the porous solid are the dominant source of pressure loss. At higher velocities, an additional inertial pressure loss due to inertial effects is incurred by the acceleration and deceleration of the fluid as it flows along curved streamlines through the tortuous paths of the porous medium. This phenomenon, termed the Forchheimer effect, manifests itself as a non-linearity in the dependency of the flowrate on the pressure drop. Incorporation of this effect into Darcy's law results in the Forchheimer equation [117]:

$$-\nabla P = \frac{\mu}{K} \bar{v} + \beta \rho |\bar{v}| \bar{v} \quad (2.17)$$

where  $\rho$  is the fluid density and  $\beta$  is the inertial coefficient. The inertial coefficient is also

referred to as the Forchheimer coefficient or the non-Darcy coefficient.

Since Eq.(2.16) and Eq.(2.17) apply for single-phase flow, the  $K$  value is referred to as the absolute permeability coefficient since the flowing phase has access to the entire pore network. The topics of relative permeability and the effect of multiple phases flowing in the same domain are discussed in the next section. For isotropic media,  $K$  is a scalar quantity; however, for anisotropic media  $K$  depends on the direction of fluid flow and must be represented by a tensor:

$$\overline{\overline{K}} = \begin{bmatrix} K_x & 0 & 0 \\ 0 & K_y & 0 \\ 0 & 0 & K_z \end{bmatrix} \quad (2.18)$$

where the subscripts  $x$ ,  $y$  and  $z$  represent the direction of flow. Throughout this thesis  $x$  and  $y$  refer to in-plane directions and  $z$  is through-plane.

The alignment of fibers in the plane of GDLs imparts a significant amount of anisotropy. Figure 2.12 shows two slices through a simulated GDL to depict differences between the fiber structures facing the flow. In general, the permeability in the in-plane direction is higher since the fluid tends to hit most fibers obliquely, while through-plane flow is largely perpendicular to the axis of the fibers, creating more drag. This anisotropy is characteristic of fiber mats as discussed by Jackson and James [159] who reviewed numerous theoretical and semi-empirical permeability models for flow through fibrous media. Tomadakis and Robertson [160] have numerically simulated flow through solid models of fibrous materials similar to GDLs and noted similar anisotropy ratios. A further source of anisotropy occurs when fibers are not only aligned in-plane, but also oriented in the same direction in-plane, creating a cross-flow and a co-flow direction. This type of orientation may occur when during manufacturing when fibers become oriented in the ‘machine direction’ as is observed in some GDL materials [161].

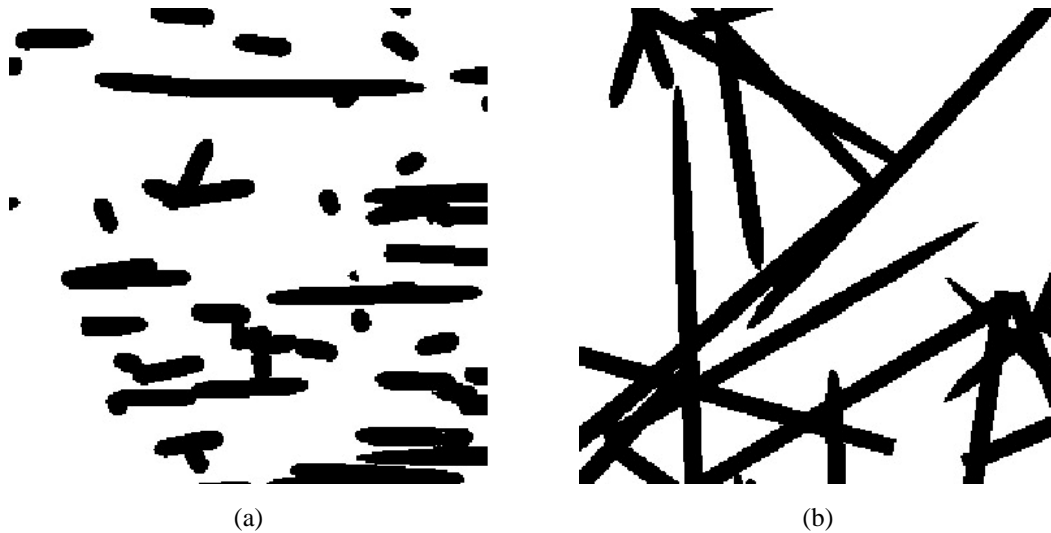


**Figure 2.12: Slices through simulated GDLs. (a) Edgewise view of the GDL (In-plane) (b) Face-on view of the GDL (Through-plane)**

The fuel cell components are compressed during operation to improve electrical conductivity between layers and ensure gas seals. This also has a significant influence on GDL permeability. Although compression of GDLs does not alter the amount of solid volume, it reduces the pore volume and porosity. According to Eq.(2.15), reduced porosity also lowers the permeability. The importance of GDL compression during cell assembly has been studied by numerous workers [134,162-168]. In general it has been found that fuel cell performance increases with slight compression due to improved electrical contact, but drops if the compression become too high which is attributed to loss of GDL permeability.

Although diffusion of oxygen from the flow channels to the catalyst layer is the main transport mechanism controlling cell performance, GDL permeability influences several aspects of PEMFC performance. Over-land convection of gas from one channel to a neighboring channel has recently been the subject of intense interest. Experiments have suggested that improved cell performance can result from the over-land flow of gases since it promotes convective flow of reactants to the catalyst layer [169]. Numerical studies of the fluid mechanics in flow field channels have verified this behavior [170-175]. The effective permeability of liquid water, which is discussed in more detail in Section 2.5, is proportional to the absolute permeability. Since the permeability is also

highly correlated with pore size, the capillary behavior and spatial distribution of liquid water is influenced by directional anisotropy in the permeability tensor [129]. Thus water will tend to spread laterally in a GDL in the direction of higher permeability. Obviously, a thorough understanding of GDL permeability is required.

Early attempts to measure permeability appeared as scattered experiments conducted within larger studies on PEMFC performance. Williams *et al.* [133] and Ihonen *et al.* [134] measured the through-plane permeability of several materials. However, all the materials tested in these studies were coated with a microporous layer. This confounding factor makes it impossible to determine the transport properties of the GDL substrate material alone. Through-plane permeability was also measured by Prasanna *et al.* [176] for two types of materials with varying PTFE content and no MPL. Mathias *et al.* [12] measured through-plane permeability of a single sample with no MPL, but reported the result only as an approximate range of values. Ihonen *et al.* [134] measured in-plane permeability for some materials as a function of compression. They found that the permeability decreased as the compression force applied to the GDL was increased. Dohle *et al.* [177] measured the in-plane permeability of a single type of GDL, but with different MPL properties. They reported the permeability as a function of GDL thickness instead of compression. Again, because of the presence of the MPL, neither of these studies revealed the intrinsic transport properties of the GDL. Mathias *et al.* [12] also measured in-plane permeability for a single sample, but again reported their results only as an approximate range.

Recently, more complete and systematic studies of GDL permeability have appeared. Feser *et al.* [178] and Nitta *et al.* [165] studied the in-plane permeability of materials without MPLs as a function of compressed thickness. Both utilized a radial test fixture which does not allow for determination of in-plane anisotropy that may exist due to preferred fiber orientation. More importantly, neither study investigated the through-plane permeability, which would show significant anisotropy relative to the in-plane direction. Therefore, no information about the permeability tensor was obtained. Gurau *et al.* [179] and Chang *et al.* [168] measured both through-plane and in-plane

permeability as a function of compression for samples without MPL. Both used a radial setup for the in-plane tests and therefore did not observe in-plane anisotropy due to fiber orientation.

Permeability tests that address the shortcomings of the above methods have been developed as part of the present thesis project and are presented in Section 3.6. In-plane permeability of a number of diverse GDL materials has been measured as a function of compressed thickness using a linear test fixture so that the effects of fiber orientation could be observed. Also, the through-plane permeability is measured to determine the complete permeability tensor.

## 2.5. Relative Permeability

In the presence of two or more phases, the permeability of each phase  $P$  is reduced since the number of available pathways is reduced by the presence of the other phase(s). This effect is expressed in terms of relative permeability  $K_{r,P}$  defined as the ratio of the effective phase permeability  $K_{eff,P}(s_P)$  in the presence of another phase to the absolute permeability, or single phase, permeability  $K$ , i.e.,

$$K_{eff,P}(s_P) = K \cdot K_{r,P}(s_P) \quad (2.19)$$

where  $s_P$  is the volume fraction of phase  $P$  in the network.  $K_{r,P}$  depends on the magnitude of saturation and varies between 0 and 1. In the GDL modeling literature, relative permeability is typically represented by a function of the form:

$$K_{r,P} = s_P^a \quad (2.20)$$

where the exponent  $a$  is a constant, usually taken as 3 in the fuel cell CFD modeling literature. The applicability of such a functional relationship must be immediately questioned since it indicates that phase  $P$  will have a non-zero permeability at all saturation levels. This is not true since a minimum saturation must be reached before phase  $P$  forms continuous pathways through the media, known as the percolation threshold. The same problem was noted concerning the functional relationship for  $J(s)$  given in Eq.(2.13) which also passes through the origin. This can be remedied by defining effective saturation  $S_{EFF}$  as:

$$S_{EFF} = \frac{S_{MIN} - S}{1 - S_{MIN}} \quad (2.21)$$

where  $S_{MIN}$  is the minimum saturation required to achieve fluid continuity through the medium. Unfortunately, this approach requires knowing  $S_{MIN}$  which is not generally known for GDLs.

Experimental measurement of the relative permeability relationships in GDLs is very difficult. Conceptually, the experiment simply involves flowing gas or water through a sample that is partially saturated with water and measuring the pressure drop. The main problem is determining the sample saturation or maintaining it during the experiment. A commonly used method used on rock cores is to flood the sample with ionically conductive brine. Measuring the resistance across the sample gives a signal proportional to the brine saturation. Since GDLs themselves are conductive, however, this method is not applicable. Alternative methods for tracking water saturation are available, but they involve complex experimental equipment. For instance Owejan *et al.* [180] have utilized neutron imaging to measure water density in the GDL of a running fuel cell with an interdigitated flow field. A complex analysis of the hydrodynamic conditions in the cell allowed them to extract an estimate of relative gas permeability values. Also using neutron imaging, Nguyen *et al.* [181] reported a more straightforward measurement of relative gas permeability where a wet GDL is mounted in a sample holder and gas is passed through it while the saturation is determined from the neutron images. This work was reported in a conference proceeding but has not yet reappeared as a full study. Koido *et al.* [95] and Sole [22] employ a simple method, based on the Penn State method [117], where water and gas flow through the sample simultaneously. Once the pressure drop is stable, the sample is removed and weighed to determine its saturation. This method requires that the capillary end effects are negligible, which is not possible for a 300  $\mu\text{m}$  thick sample. Although efforts were made to use stacks of several samples to increase the thickness, the issue of end effects is a complex one [117].

Experimental studies are only beginning to tackle the measurement of relative permeability. In the interim, several relative permeability predictions have been made by

pore scale modeling approaches. These include pore network modeling and microstructural simulations. Each of these techniques has merits and limitations. The microstructural approach, which is the most direct technique, involves performing fluid dynamic computations on a 3D image of the GDL microstructure. The Lattice-Boltzmann method (LBM) is typically used for these calculations since it is computationally less intensive than solving the full Navier-Stokes equations on a similar size domain. Relative phase permeability can be calculated by placing a certain amount of water in the microstructure and then simulating the flow of one phase as though the other phase is part of the solid. The difficulty with this approach is the placement of liquid water within the microstructure in a physically realistic manner. The use of morphological image opening using a spherical structuring element has been applied to GDLs by Schulz *et al.* [150] and Becker *et al.* [149], but this implicitly assumes that wetting phase (air in a GDL) has a contact angle of  $0^\circ$ . Nonetheless, Becker *et al.* [149] have predicted gas and liquid relative permeability functions for GDLs with water placed by this method. Other methods of water placement such as simulated annealing [182] are not able to generate invasion percolation configurations. Koido *et al.* [95] and Niu *et al.* [183] used the lattice-Boltzmann method to simulate the injection of liquid water by assigning a contact angle for the liquid-solid interface. This approach requires highly involved numerical treatment and is computationally expensive.

A more abstract, but still highly effective, alternative is pore network modeling, which involves modeling the porous medium as an interconnected 3D network of tubes. The size distribution of the tubes is chosen such that capillary pressure curves and flow through the network match the real medium. Relative gas and liquid permeability can be calculated by partially filling the network with water according to invasion percolation rules and then calculating the permeability of each phase. This technique is obviously a simplification of the real media, but it can reproduce the relevant phenomena with minimal computational complexity. Pore network modeling has been used by Gostick *et al.* [129] and is described in more detail in Chapter 4.

## 2.6. Effective Diffusivity

Effective diffusivity refers to the diffusion coefficient of species A diffusing through species B in a porous medium, in contrast to the diffusion coefficient in open space. Since the presence of the solid matrix lowers the overall diffusivity, the effective diffusion coefficient decreases as some function of porosity. For diffusion through a bundle of straight tubes, the diffusion coefficient decreases in proportion to the decrease in open area. For a real porous medium, however, the open conduits are not straight tubes, but contain longer tortuous paths with curves, constrictions and dead-ends. The combined effect of reduced transport area and increased transport length through a porous medium can be accounted for by:

$$D_{eff} = D_{AB} \frac{\varepsilon}{\tau} \quad (2.22)$$

where  $D_{eff}$  is the effective diffusion coefficient through the medium,  $\varepsilon$  is the porosity and  $\tau$  is the tortuosity. Although  $\varepsilon$  is usually known or can be measured without difficulty,  $\tau$  is not as easily obtained. Tortuosity is generally a function of porosity and a number of relationships have been proposed [184]. In general, as porosity decreases the tortuosity of the paths through the material increases. The Bruggeman correlation is commonly used in fuel cell literature to describe GDL tortuosity:

$$\tau = \varepsilon^{-0.5} \quad (2.23)$$

Tortuosity is also subject to any material anisotropy meaning that its value is direction dependent. Since porosity is a global measure it contains no information about anisotropy. Thus, Eq.(2.23) is insufficient for GDLs which are significantly anisotropic. A more detailed analysis specifically for fibrous media has been offered by Tomadakis and co-workers [185-189]. Using random walk simulations through generated fibrous microstructures, they arrived at the following relationship:

$$\tau = \left( \frac{1 - \varepsilon_p}{\varepsilon - \varepsilon_p} \right)^\alpha \quad (2.24)$$

where  $\alpha$  and  $\varepsilon_p$  are fitting parameters that depend on the arrangement of fibers (i.e. random 1D, 2D or 3D alignments) and on the direction of flow through the structure.

Like the permeability (Eq.(2.18)),  $\tau$  must be represented by a tensor in anisotropic media.

Experimental estimates of tortuosity through GDLs require measurement of the effective diffusivity and solving (2.22) for  $\tau$ . The through-plane diffusivity is the most relevant value since this is the direction of reactant transport in a fuel cell. Measuring the through-plane diffusivity is challenging, however, since GDLs are so thin that establishment of a partial pressure gradient while maintaining a zero total pressure differential across the sample is nearly impossible. For instance, by controlling partial pressures of flowing gases, Ye and Wang [190] measured highly erratic effective diffusivities which deviated from the theoretical value given by Eq.(2.23) by more than an order of magnitude. In contrast, Baker *et al.* [191] presented a simple method with a water reservoir on one side of the GDL and desiccant on the other side to generate a gradient in water vapor partial pressure. They used humidity sensors to determine and track the established vapor gradient and weighed the desiccant after the test to determine the water flux. They found tortuosity values close to 2, where Eq.(2.23) predicted 1.19. Kramer *et al.* [192] have developed an excellent, though elaborate, method to measure the through-plane and in-plane tortuosity of GDLs under compression. They completely filled the GDL with a conductive brine solution and measured its conductivity of the brine solution, which is related to the diffusivity through the analogy between Fick's law and Ohm's Law [116]. They managed to de-convolute the conductivity of the GDL solid and the brine by using AC impedance spectroscopy which can resolve different transport mechanisms by their respective time constants. The measured through-plane tortuosity agreed very closely with that of Baker *et al.* [191]. In-plane tortuosity was about half that of the through-plane value which is in accord with anisotropy ratios observed in permeability measurement of fibrous materials. Both Baker *et al.* [191] and Kramer *et al.* [192] found tortuosity values significantly higher than those predicted by Eq.(2.24).

Several computational estimates of effective diffusivity or tortuosity have also been made. Inoue *et al.* [193] used LBM to calculate through-plane diffusivity of artificially generated fiber structures. They found near perfect agreement with the model of Tomadakis [185-189] as the porosity of their structure was changed. This agreement is

not surprising since the results of Tomadakis and co-workers were also obtained in artificially generated structures. In contrast, Becker *et al.* [149] performed similar calculations on a GDL structure that was obtained from x-ray tomography. They found much higher tortuosity values that were closer to the experimentally determined results of Kramer *et al.* [192] and Baker *et al.* [191]. The persistent differences between values obtained from real materials (either experimentally or computationally) and values for artificial materials suggests that some important aspect of real materials is not represented by the artificially generated structures. This is most likely related to the overlap and intersection of fibers that is difficult to avoid in generated media. The real materials are also sintered which leaves a small web feature at each fiber-fiber contact point visible in Figure 1.4(right).

## 2.7. Relative Effective Diffusivity

Relative effective diffusivity is analogous to relative permeability. The presence of multiple phases in a porous medium limits the diffusivity through each phase. Eq.(2.25) is analogous to Eq.(2.19) for relative permeability:

$$D_{eff,P} = D_{eff} D_{r,P}(s_P) = D_{AB} \frac{\mathcal{E}}{\tau} D_{r,P}(s_P) \quad (2.25)$$

where  $D_{eff,P}$  is the effective diffusivity through phase  $P$  and  $D_{r,P}$  is a function that varies with the saturation of  $P$  between 0 and 1. As with the relative permeability function,  $D_{r,P}$  is often expressed as a simple relationship of the form:

$$D_{r,P}(s_P) = s_P^a \quad (2.26)$$

where the exponent  $a$  is a constant. Like the relative permeability  $K_{rP}$  function this form doesn't account for minimum saturation required for phase continuity. Nam and Kaviany [32] suggest a value of 2 for  $a$  based on an overly simple network model. Since their model did not use an explicit pore size distribution and capillary pressure curves were not simulated, the spatial structure used was not verifiable. Furthermore, water was placed randomly in the lattice with no consideration of the physics of immiscible displacement or capillary principles. Nonetheless, Eq.(2.26) with  $a = 2$  has been used in many published fuel cell CFD simulation studies. An alternative value of  $a = 1.5$  is often used

based on the assumption that tortuosity scales with saturation in the same way that tortuosity scales with porosity [26,29]. Combination of the Bruggeman correlation (Eq.(2.23)) with Eq.(2.22) shows that effective diffusivity is proportional to  $\epsilon^{1.5}$  and according to this reasoning is also proportional so  $s^{1.5}$ . This assumption is unjustified since liquid in a GDL does not reduce porosity uniformly, but instead fills pore volume according to capillary behavior (i.e. large pores are filled first).

Measurement of relative effective diffusivity is plagued by the same problems as that of relative permeability, namely saturation tracking, but is also more difficult for the same reasons that effective diffusivity (Section 2.6) is difficult to measure. As a result, no experimental values have been reported. Currently the only means of studying this highly inaccessible parameter is through modeling. Becker *et al.* [149] have calculated a number of transport parameters, including relative effective diffusivity, through a microstructural representation of a GDL obtained from x-ray tomography. Although the microstructure is accurate, the placement of water into the microstructure is not straightforward. Becker *et al.* [149] used morphological image opening to determine water configuration and placement, which unreasonably assumes a perfectly wetting gas phase. This assumption means that gas phase continuity is maintained for all capillary pressure ( $P_C < \infty$ ), leading to overestimates of gas phase effective diffusivity and transport coefficients in general (i.e. gas permeability). Pore network modeling is used to address the problem in the present thesis.

### 3. Experimental

In this chapter the experimental techniques developed are described in detail. Some results are shown for descriptive purposes, but full discussion and presentation of the results is given in Chapter 5.

#### 3.1. GDL Materials

A wide variety of GDL materials are examined in this study in order to investigate the effects of varying thickness, fiber arrangement and PTFE content. Additionally, samples with microporous layers have been tested. A list of all samples tested and relevant properties is given in Table 3.1.

**Table 3.1: List of materials tested during this study and selected properties**

<b>Brand</b>	<b>Material</b>	<b>Thickness [<math>\mu\text{m}</math>]</b>	<b>Porosity</b>	<b>PTFE Loading [wt %]</b>
SGL	10AA	380	90	0
	10BA	380	88	5
	10CA	390	87	10
	10DA	400	86	20
	10EA	400	85	30
	10BB	420	84	5
	24BA	265	80	5
	34BA	190	80	5
Toray	060A	210	78	0
	060D	210	75	20
	090A	300	78	0
	090D	300	74	20
	120A	400	78	0
	120C	400	73	10
Ballard	P75	240	75	0
E-Tek	Cloth 'A'	400	75	0

A selection of SEM images of various materials is given in Figure 3.1. Appendix B contains a more extensive library of SEM images at different magnifications.

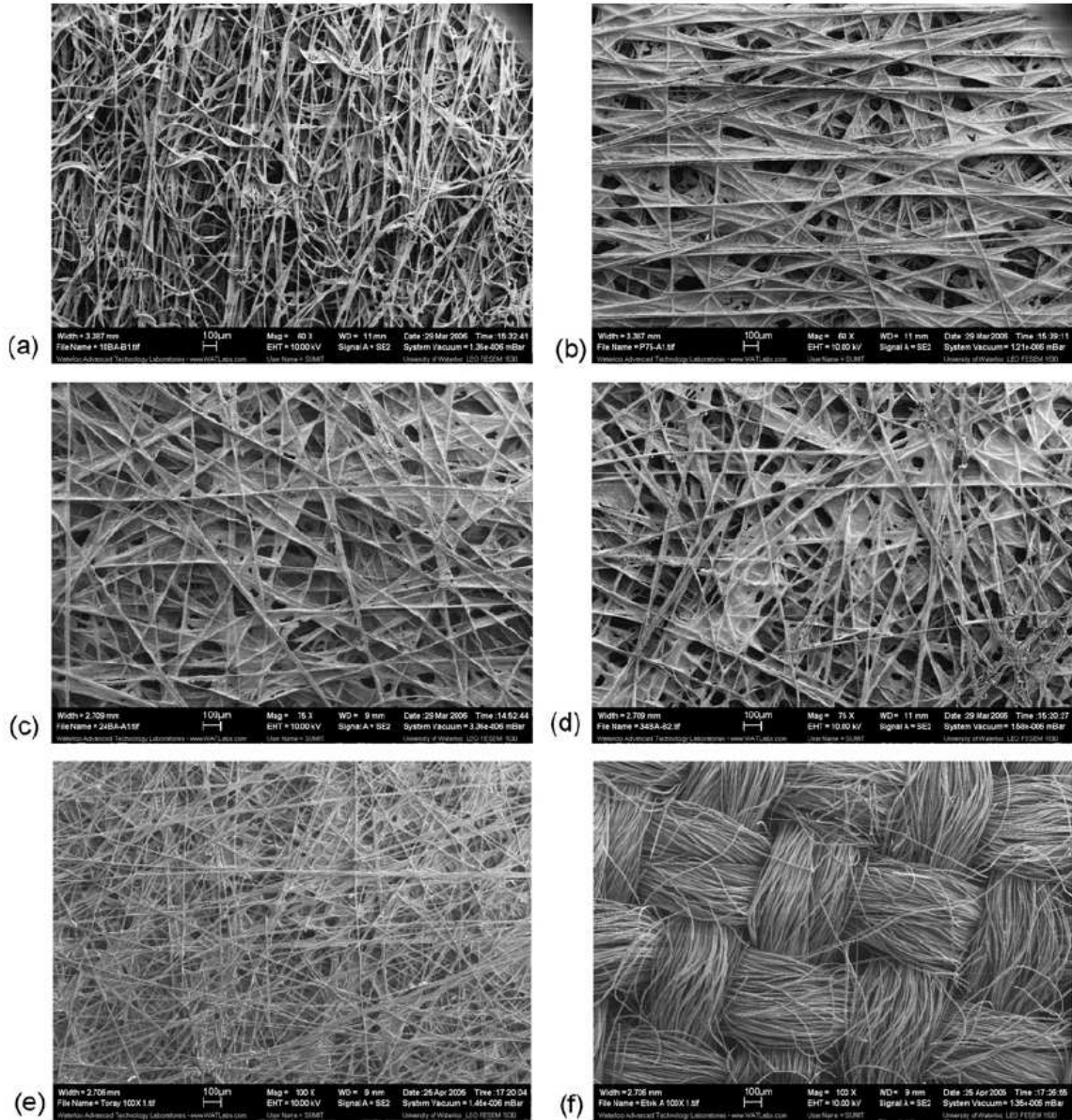
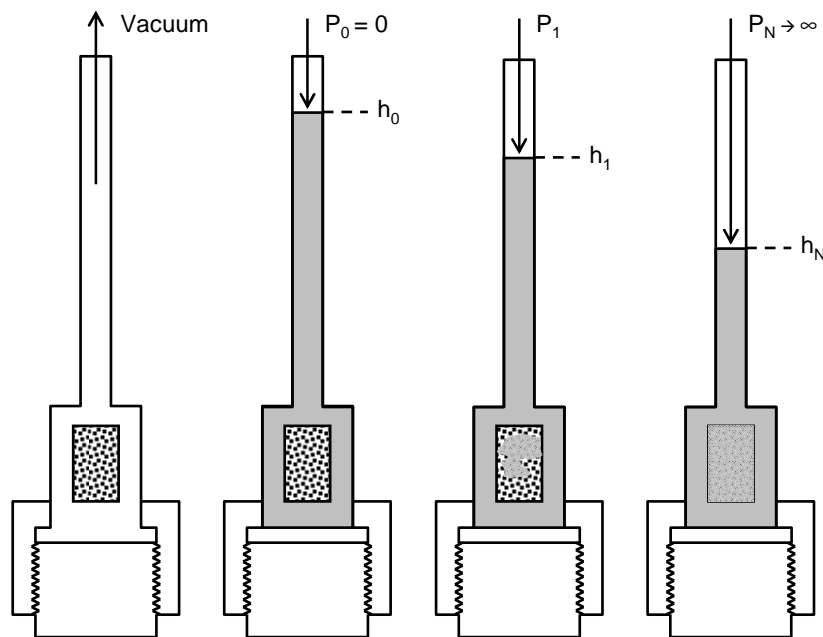


Figure 3.1: Micrographs of assorted GDL materials. (a) SGL 10BA (b) Ballard P75 (c) SGL 24BA (d) SGL 34BA (e) Toray 090 (f) E-Tek Cloth 'A'.

## 3.2. Porosimetry

### 3.2.1. Mercury Intrusion Porosimetry

Mercury intrusion porosimetry (MIP) is an established and widely used technique. The principles behind all mercury porosimeters are essentially the same. The porous sample is placed in a special glass sample tube, as shown in Figure 3.2. Air is evacuated from the sample tube and sample.



**Figure 3.2:** Schematic of mercury porosimetry sample tube. The sample is inserted through the wide end and screw cap is used to seal to opening.

Mercury is introduced into the sample tube without applying any pressure, so that it surrounds the sample but no pore volume is penetrated by mercury. The initial volume of mercury in the tube corresponding to  $h_0$  is noted. Next, pressure  $P_1$  is applied which forces a small amount of mercury into the largest and most easily penetrated pores of the sample. The volume penetrated at  $P_1$  corresponds to  $h_0 - h_1$ . Increasing the pressure incrementally forces mercury into smaller and smaller pores until the entire pore volume of the sample is filled, corresponding to  $h_0 - h_N$ . Plotting the pressure at each step with

the volume injected yields a capillary pressure curve.

One of the main advantages of mercury is its low volatility, which enables the sample to be completely evacuated so that air need not be displaced as mercury is injected. This vastly simplifies the sample mounting requirements. Since mercury also has a very high surface tension ( $\sigma = 0.460 \text{ N}\cdot\text{m}^{-2}$ ), the pressure range over which penetration occurs is much wider than for other fluids. For instance, the range of mercury penetration is almost 10 times larger than for water ( $\sigma = 0.072 \text{ N}\cdot\text{m}^{-2}$ ). This increased range of injection pressure gives MIP very high pressure resolution. Another feature of mercury is that it is highly non-wetting to almost every surface. This is an advantage when pore size information is sought since it eliminates effects caused by chemical heterogeneity of the internal surfaces. This can be also be a disadvantage, however, when true capillary pressure curves are desired. In the case of gas diffusion layers for fuel cells, the effects of hydrophobic polymer coatings on the capillary properties are of interest. MIP cannot differentiate between carbon/graphite and hydrophobic polymer surfaces since mercury is highly non-wetting to both materials. The only effect that MIP would detect is structural changes to the porous material due to addition of the additional polymer material, such as a reduced porosity and filling or blocking of some pores.

Mercury porosimeters are available commercially from several companies and are highly automated and well refined devices. In this work a Quantachrome Poremaster was used for MIP testing. Triply distilled ACS grade mercury (99.99% purity) was used to obtain the pore size distribution of the samples. Each sample was cut into small 20 mm by 5mm rectangular tabs to fit into the penetrometer cell. Tests with single samples as well as stacks of many tabs were performed.

### **3.2.2. Method of Standard Porosimetry**

When chemical heterogeneity is an important part of the capillary pressure behavior of a material, it becomes necessary to measure the capillary pressure curve with the fluids of interest – water and air in the case of gas diffusion layers. One method for measuring

capillary pressure curves with arbitrary fluids is known as the method of standard porosimetry (MSP). This method uses the principle of capillary equilibrium, where two partially saturated porous materials in contact will possess the same capillary pressure. The method requires the existence of a standard, which is a porous disk with a known capillary pressure curve. This disk is designed to be completely wetting to most fluids, such as water and organics. Complete wettability means that the fluid solid contact angle is known to be exactly  $0^\circ$ , which is required for data conversion. The samples are prepared by evacuating the standard and the sample to be tested, then flooding them with the wetting fluid (i.e. octane). This ensures no air is trapped in the materials when liquid enters. The samples are then stacked so they are in capillary contact and exposed to air. The wetting fluid will slowly evaporate from both the sample and the standard, resulting in a changed saturation. Figure 3.3 shows the arrangement of standards and samples during the evaporation stage. The generation of a capillary pressure curve from this process is shown in Figure 3.4. Periodically, the sample and standards are separated and weighed to determine their individual saturations (Step 1). Since the standards have a known capillary pressure curve, their capillary pressure can be found from knowledge of their saturation (Step 2). Since the sample and standards are assumed to be in capillary equilibrium, this value also corresponds to the capillary pressure of the sample being tested, so the sample saturation can be related to the standards capillary pressure (Step 3). The test is complete once the wetting fluid is fully evaporated from the sample.

Since the evaporation of a wetting fluid is conceptually equivalent to invasion of the sample with air, this test corresponds to the invasion of a non-wetting phase into a material filled with wetting phase which is analogous to MIP. In fact, the use of a highly wetting fluid such as octane provides the same information as MIP since octane wets all surfaces indiscriminately, just as mercury is non-wetting to all surfaces. Unlike MIP, however, MSP experiments can be performed with water as the working fluid. The procedure is identical to that described above, but the sample is initially saturated with water. The MSP method using both octane and water was attempted on several GDLs. The octane data are in good agreement with MIP data, as they should be, given that the techniques are essentially equivalent. MSP was also used on the same samples with

water as the wetting fluid to measure the so called hydrophilic pore network. The MSP technique is of limited use. Firstly, when using water as the wetting fluid the results are questionable since the assumption that water will spontaneously eject from hydrophobic pores is unjustified. Secondly, this method only scans along a path of increasing air saturation, and only for  $P_C > 0$ .

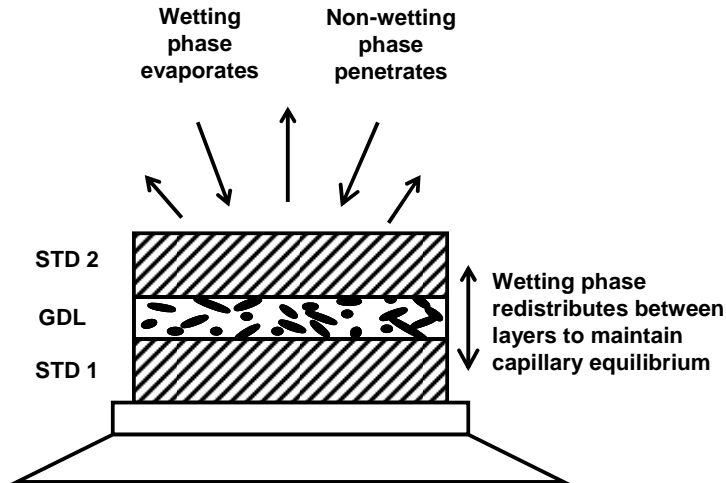


Figure 3.3: Configuration of sample and standards showing fluid movement occurring during method of standard porosimetry experiment.

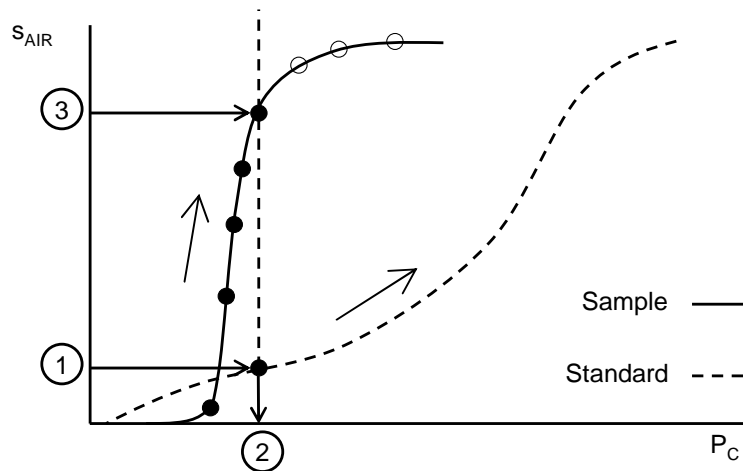


Figure 3.4: Schematic detailing data analysis used in the method of standard porosimetry. The open circles are points yet to be determined.

The MSP tests were run on a Porotech Automated Standard Porosimeter, which is a unique apparatus for the automated execution of the MSP procedure. Each GDL sample

tested was a 20 mm diameter circular section cut from the supplied material. The standards fitted onto the top and bottom of each sample were fabricated porous disks of proprietary composition, perfectly wettable by both octane and water. The working fluids used were ACS grade octane (99.99%) and deionized water (>18.0 MΩ).

### 3.2.3. Gas Controlled Porosimetry

Because of the practical limitations of the MSP technique and the lack of an acceptable air-water capillary pressure method in the literature, an alternative method was developed specifically with the aim of measuring air-water capillary pressure curves for thin materials, such as the GDL. As will be described below this method controlled the capillary pressure by adjusting the pressure of the gas phase, and so it will be referred to as Gas Controlled Porosimetry (GCP). It should be noted that the term ‘porosimetry’ is somewhat imprecise since the data obtained by GCP reflect wettability effects as well as pore size effect. The overarching objective was to develop a method that addressed all of the shortcomings and deficiencies of other reported methods. Specifically, a method with the following characteristics was sought:

1. **Scan the full spectrum of capillary pressures ( $P_{C,MIN} < 0 < P_{C,MAX}$ ):** Many of the methods described in Chapter 2 only scan on one side of the capillary pressure spectrum (i.e. either  $P_C > 0$  or  $P_C < 0$ ). Since phenomena of interest occur at both positive and negative capillary pressure, the ideal method must be able to seamlessly scan across the entire range.
2. **Scan in both directions ( $P_{C,1} \rightarrow P_{C,2}$ ,  $P_{C,2} \rightarrow P_{C,1}$ ):** Capillary pressure curves demonstrate significant hysteresis with dramatic differences in pressure required for water injection and water withdrawal. Simple injection or withdrawal of water does not reveal the full capillary pressure behavior. The ideal method must be capable of following both increasing and decreasing saturation paths.
3. **Change scanning direction at will ( $P_{C,2} \rightarrow P_{C,3} \rightarrow P_{C,1} \rightarrow \dots$ ):** Full control over the direction of pressure scanning allows the study of internal scanning loops, which are loops that begin at some intermediate saturation (e.g.  $s_w(P_{C,2}) = 0.3 \rightarrow$

- $s_w(P_{C,3}) = 0.5 \rightarrow s_w(P_{C,1}) = 0.2$ ). Such tests provide information about the injection or withdrawal of water from partially saturated samples.
4. **Begin testing at an arbitrary capillary pressure:** Since GDLs may display hydrophilic tendencies (i.e. imbibition of water at  $P_{C,i} < 0$ ), it is desirable to begin testing at  $P_C < P_{C,i}$  to test the GDL beginning with a fully dry state. Design of a sample holder or procedure that can maintain the sample at  $P_C < P_{C,i}$  prior to beginning the test is needed.
  5. **Control pressure, not saturation:** It is imperative that pressure is the controlled parameter in a capillary pressure experiment. Capillary pressure curves are expected to describe the amount of pore volume accessible at a given pressure. When liquid is injected in discrete volume increments, there is no reason to expect that all accessible pore volume is filled by the arbitrary amount of fluid added to the system. The ideal method must be pressure-controlled to avoid ambiguities in interpretation.
  6. **High saturation resolution and accuracy:** This is an important consideration when studying GDLs, which are very thin and therefore possess very small sample volumes. Instead of testing samples with very large areas or stacks of samples to increase pore volume, it is preferred that the method accommodate this characteristic of GDLs. It is also preferable that saturation is not determined by directly weighing the GDL which is prone to errors caused by droplets and general handling of the sample.

One of the major contributions of this thesis is the development of the GCP test method that meets all of the above requirements. In addition to the above requirements, this method also offers a number of additional features. Firstly, it is fully automated and computer controlled. Once the sample is mounted and connected to the system, the computer controls all aspects of the test including the determination of capillary equilibrium, thereby eliminating subjectivity and errors in not waiting long enough for equilibrium to be reached. Furthermore, sample preparation and mounting are very straightforward and require no artistry or skill. Capillary pressure control is very stable and can typically be achieved to within 50 Pa of the set point. This stability leads to

excellent capillary pressure resolution. Since a typical pressure range for GDL tests spans from -25,000 Pa to 25,000 Pa, measurement of data points at an interval of 500 Pa leads to a resolution of  $1\% \pm 0.1\%$  FS. The total pressure range of the system is much wider than that typically used for GDL tests. In theory, the range of capillary pressures is limited by the vapor pressure of water on one end ( $P_{C,MAX} = P_{ATM} - (P^V)_W \approx 95,000$  Pa @ 293 K) and the ability to pressurize gas on the other end ( $P_{C,MIN} \approx -\infty$ ), although this is limited by practical considerations.

The system consists of an analytical balance (Denver P-314), syringe pump (Harvard Pump 11 Plus), absolute pressure gauge (Omega PX303-030A5V) and a specially designed sample holder. The overall system setup is shown in Figure 3.5 and the details are discussed in the sections that follow. The sample is positioned in the sample holder so that water has access to its bottom face while gas escapes through the top. The syringe pump is used to control the gas pressure, by advancing and retracting the syringe to expand and compress the gas in the sample. The analytical balance is used to track the GDL saturation by monitoring the mass of water in the reservoir. The reservoir was very wide to ensure negligible movement of the free surface during the test to ensure the liquid pressure was constant. Use of an analytical balance provides excellent water saturation resolution. For a typical single layer piece of GDL, maximum saturation is about 100 mg of water. Thus a balance that has a resolution of 100  $\mu$ g, gives a resolution of 0.1% FS. The analytical balance also can measure masses over an extremely wide range so it is equally effective when thicker or multilayer samples with much more pore volume are tested. Part of the success of this method lies in the fact that the capillary pressure control is decoupled from the saturation measurement. Since the sample holder is also an integral part of this method, its design was carefully refined to achieve the final version as described in the next section.

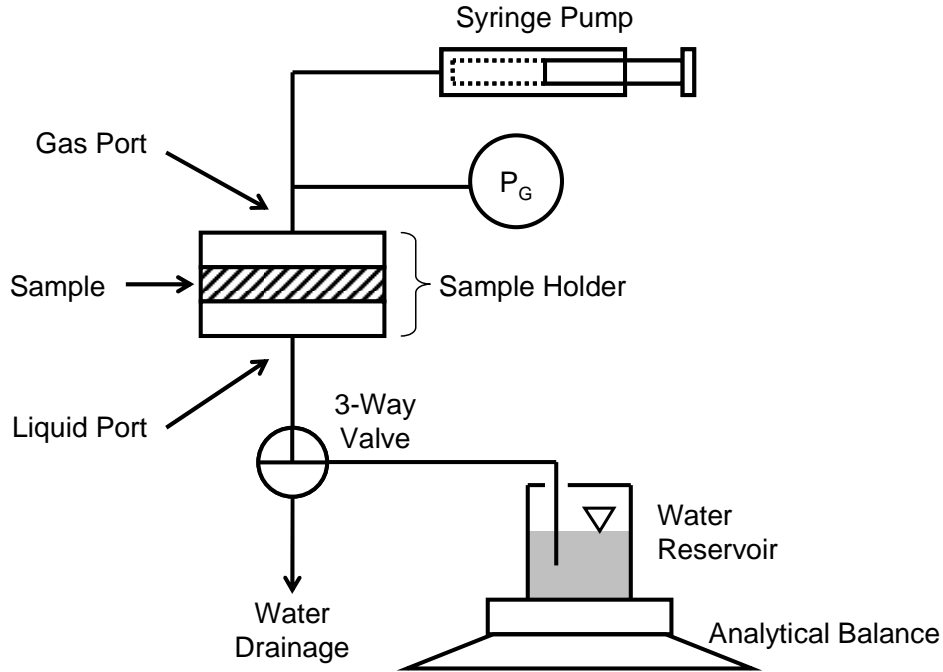
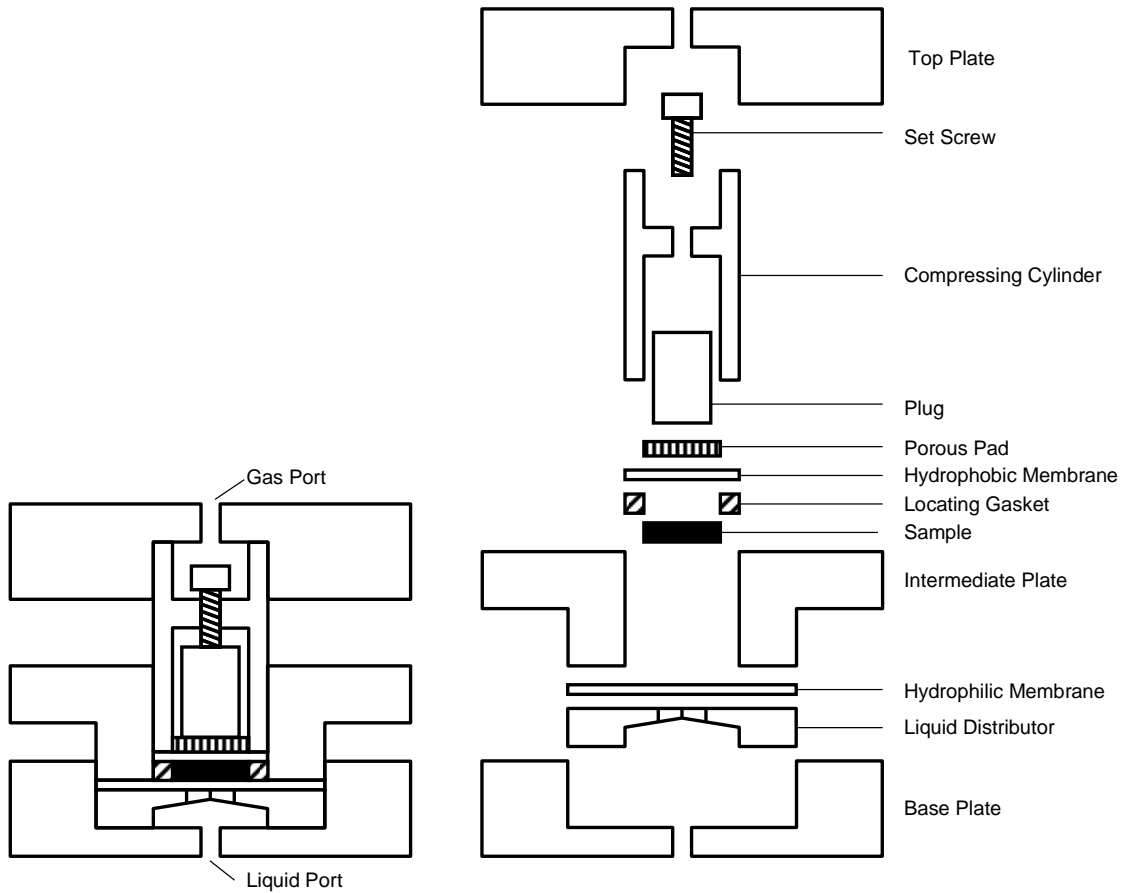


Figure 3.5: Gas controlled porosimetry setup.

### 3.2.3.1. Sample Holder

The sample holder shown in Figure 3.6 was designed and custom built. The holder features a porous hydrophobic membrane (Sartorius, 0.45  $\mu\text{m}$  #11806-25) above the sample and a porous hydrophilic membrane (Millipore, 0.22  $\mu\text{m}$  #GVWP04700) below the sample to act as capillary barriers. The porous hydrophobic membrane above the sample allows air to escape as water enters the GDL but prevents water from leaving the system after breakthrough of the sample. Large positive capillary pressures can thus be applied (limited only by the onset of cavitation in the liquid water since positive capillary pressures are affected by gas vacuum). The porous hydrophilic membrane below the sample serves the same function at highly negative capillary pressures by allowing water, but not air, to exit. The bubble point of the hydrophilic membrane is 300 kPa, which places a practical limit on the minimum capillary pressure although this limit is not approached during the present tests.



**Figure 3.6: Schematic diagram of sample holder for GCP. (Left) Assembled view (right) Expanded view.**

One of the main features of this setup is that the sample can be maintained at  $P_C \ll 0$  Pa during assembly which enables the measurement of capillary curves beginning with the GDL in a fully dry state. This is achieved by the piecewise assembly of the fixture, as shown in Figure 3.6 and described in the next section. The GDL in a fully dry initial state serves as a reference for tracking the sample saturation. The holder is designed to hold circular samples  $\frac{3}{4}$ " or 0.019 m diameter. A large range of sample thickness can be accommodated. The holder was designed to hold GDLs from 200 – 500  $\mu\text{m}$ , but samples up to 1 cm can be measured by simply adjusting the thickness of the locating gasket accordingly.

### 3.2.3.2. Sample Mounting

The first step in the assembly is to prime the piping and cavity in the base plate with de-ionized and de-gassed liquid water. Degassed water is critical since the formation of air bubbles in the liquid piping displaces water and interferes with the liquid saturation measurement. Once the cavity and piping are fully primed the liquid distributor is positioned. The liquid distributor contains of 20 holes of 800  $\mu\text{m}$  diameter. Small holes were used to prevent the hydrophilic membrane from sagging at very negative capillary pressure since this would also interfere with the saturation measurement. The hydrophilic membrane is laid on top of the liquid distributor. Prior to placement, the hydrophilic membrane is pre-saturated by evacuating it and submerging it under water. This is necessary to ensure no air is trapped in the membrane, which interfered with the measurement at highly positive capillary pressures. Next, the intermediate plate is bolted to the base plate to hold the hydrophilic membrane tightly in place. At this point,  $-10,000$  Pa of suction is applied to system through a hose connected to the liquid port. This suction drains free water from the sample cavity and creates a  $-10,000$  Pa capillary pressure at the surface of the hydrophilic membrane. This is a key feature since it ensures that a dry sample can be placed onto the hydrophilic membrane without imbibing water and ensuring the sample is initially dry. The amount of suction applied to the liquid port can be increased to any value (less than the vapor pressure of water), but  $-10,000$  Pa is sufficient for GDLs since they do not exhibit strong water wicking tendencies. The dry GDL sample is then loaded along with the locating gasket, which has an inside diameter equal to the sample diameter to prevent any gaps. The thickness of the locating gasket must be matched to the thickness of the sample to prevent inadvertent compression in the following steps. Next, the hydrophobic membrane, porous pad, plug, compressing cylinder and set screw are inserted. The plug prevents bulging of the hydrophobic membrane at high capillary pressures, which would create extra water volume in the system. The porous pad allows improved gas access to the area under the plug. The set screw holds the plug in place with only slight pressure to prevent GDL compression. It is also possible to use the set screw to apply firm pressure to the plug to study capillary pressure curves of GDLs while under compression. The extent or amount of compression cannot be controlled with this setup as is, but it can be estimated after the experiment

since the reduction in pore volume can be found from the data. Finally, the top plate is bolted to the intermediate plate to apply a downward force on the compression cylinder and seal the assembly. The assembly is made from stainless steel and all tubing from clear polycarbonate so that the presence of air bubbles can be detected.

### **3.2.3.3. System Setup**

The setup of the system is shown in Figure 3.5. After the sample holder is assembled, the syringe pump is connected to the gas port and gas pressure of 10,000 Pa is applied. This pressure combined with the liquid suction already existing at the liquid port from the sample mounting step, temporarily creates a capillary pressure of  $-20,000$  Pa in the hydrophilic membrane, which is still well below its bubble point ( $\sim 300$  kPa). After the gas pressure is established, the liquid suction is relieved and the sample chamber is connected to the water reservoir on the balance by turning the 3-way valve. Since the water reservoir is at approximately the same level as the sample, no liquid suction exists when the reservoir is connected. Thus the positive gas pressure must first be applied to ensure that the net capillary pressure never rises above  $-10,000$  Pa. This assembly and setup ensures that the GDL never contacts water with a capillary pressure greater than  $-10,000$  Pa. It was confirmed that the samples do not take up any water during assembly by performing the above assembly and setup steps several times followed by immediate disassembly and weighing of the samples.

### **3.2.3.4. Procedure**

Following system setup, the gas pressure in the sample is  $P_G \approx 10000$  Pa and liquid suction is 0 and so  $P_L = 0$ . Thus, the initial capillary pressure is  $P_C = P_L - P_G \approx -10000$  Pa. The syringe pump is used to expand and compress the gas above the sample, thereby effecting changes in capillary pressure. It must be stressed that the liquid pressure does not change during the experiment. The test proceeds by adjusting the syringe pump to decrease gas pressure and thereby increase capillary pressure. After each change in gas volume and therefore capillary pressure, the mass of liquid on the balance is monitored

for change. The slope of the plot of water mass versus time is calculated using a moving window of the most recent 180 seconds. If the slope is below a threshold value, the system is deemed stable. Otherwise, the system holds at a constant capillary pressure until the water mass reading on the balance is stable. The transient response of the water uptake to changes in capillary pressure is shown in Figure 3.7. A closer look at the data shows that the water uptake is indeed stable before each subsequent change in gas pressure (Figure 3.8). Constant capillary pressure conditions are maintained by utilizing the syringe pump in a feedback control loop, generally allowing the pressure to be controlled to within 50 Pa of the set point. The set points are specified by creating a data file list of capillary pressures at which readings are desired. The system scans through the data file line by line, ensuring stable water uptake readings are obtained at each capillary pressure point before advancing. In this way, full control of the pressure scan profiles can be specified. For regions of interest, readings were obtained every 750 Pa, while they were spaced 5000 Pa apart for less important regions such as plateaus. The syringe pump and balance are controlled through an RS-232 interface. The entire system was controlled from a computer program created in LabView.

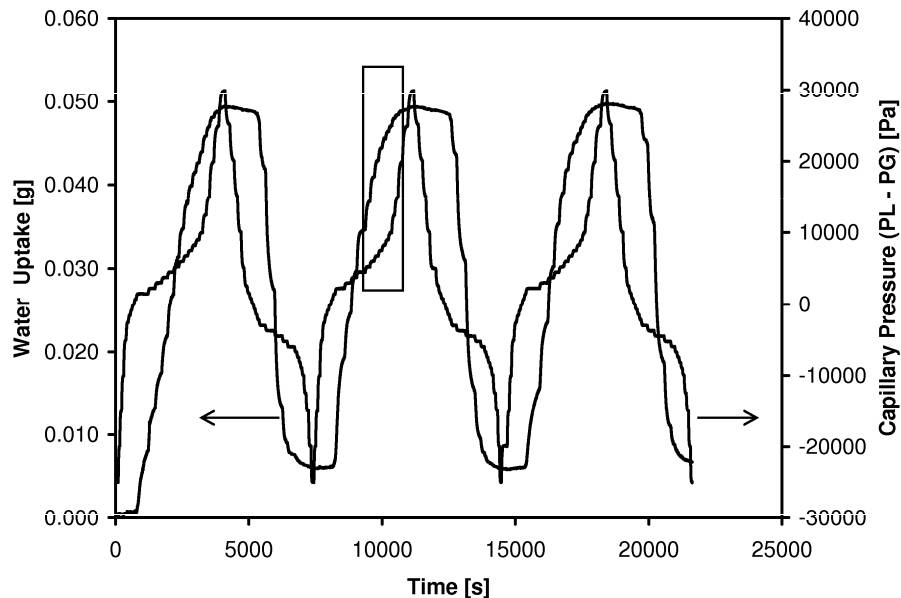


**Figure 3.7:** Sample of experimental data obtained from GCP. The region marked by the box in the top figure is shown in more detail in Figure 3.8.

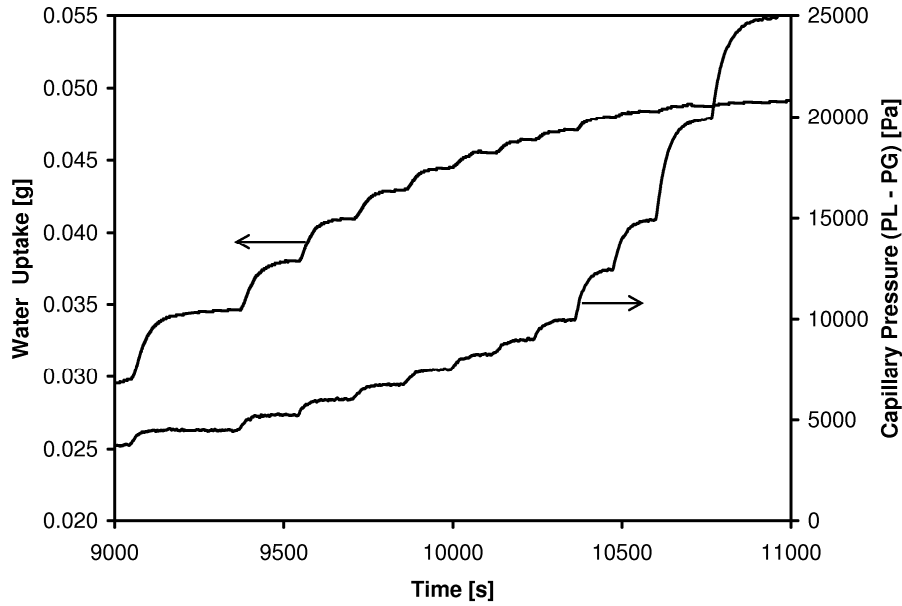


Figure 3.8: Close up view of experimental data shown in Figure 3.7.

### 3.2.3.5. Data Analysis

Capillary pressure is controlled by adjusting the gas pressure above the sample and determined as follows. The distance  $h$  between the liquid reservoir level and the sample surface is set to approximately 0 cm. Also, the barometric pressure ( $P_{ATM}$ ) acts on the surface of the liquid reservoir, but not on the liquid in the sample since the gas chamber is sealed. The capillary pressure is therefore given as follows:

$$P_C = P_L - P_G = \rho gh + P_{ATM} - P_G \quad (3.1)$$

A main advantage of controlling capillary pressure via gas pressure control is that the liquid pressure does not have to be monitored. This is helpful since most liquid pressure sensors exhibit some membrane displacement that could be incorrectly construed as sample pore volume. A constant liquid pressure also alleviates potential problems with gas dissolution and bubble formation, which interfere with liquid volume measurement.

Since the sample is initially dry, the water uptake into the sample is simply equal to the water loss from the reservoir. The water saturation is computed as:

$$S_w = \frac{V_w}{V_p} = \frac{m_w \cdot \rho^{-1}}{\frac{\pi}{4} d^2 \delta \cdot \varepsilon} \quad (3.2)$$

where  $V_w$  is the volume of water in the sample,  $V_p$  is the GDL pore volume,  $m_w$  is the mass of water in the sample,  $\rho$  is the density of water,  $d$  is the sample diameter,  $\delta$  is the sample thickness and  $\varepsilon$  is the sample porosity.

Evaporative loss of water from the system during the course of a run (*ca.* 5 hr) is minimized by covering the top of the beaker on the balance and maintaining the gas inside the syringe fully humidified. Nevertheless, a small correction to  $m_w$  is still required. Several measurements of the evaporation rate for the system with no sample show it to be in the range of  $0.8 \mu\text{g/s} \pm 0.2 \mu\text{g/s}$ . The value depends on the temperature and relative humidity of the room and varies from day to day. Instead of attempting to measure the precise evaporation rate for each run, the evaporation rate is found by a fitting procedure as follows. The top graph in Figure 3.9 shows three loops of a capillary pressure curve without correction for evaporative loss. The repeated offset of each arm with the previous loop occurs due to evaporation. The fact that saturation values greater than 1.0 were obtained from the second and third loop indicates that these offsets do not arise due to some phenomena inside the sample. An evaporation rate is found that forces these arms to coincide, as shown in the bottom graph of Figure 3.9. The evaporation rate found in this way is always equal to or less than the values measured with no sample ( $\sim 1 \mu\text{g/s}$ ). Furthermore, the plateau values at both very high and very low capillary pressure is always found to coincide, regardless of the number of loops or the test duration.

In order to ensure that the evaporation correction procedure was effectively accounting for water loss from the system, the GDL saturation was determined after the run by simply weighing the sample. The sample was extracted from the holder while the capillary pressure was at  $P_C = -10,000 \text{ Pa}$  in the same manner used for sample mounting. The saturation determined in this way is shown on Figure 3.9(bottom) as a triangle and near perfect agreement with the evaporation corrected value is obtained.

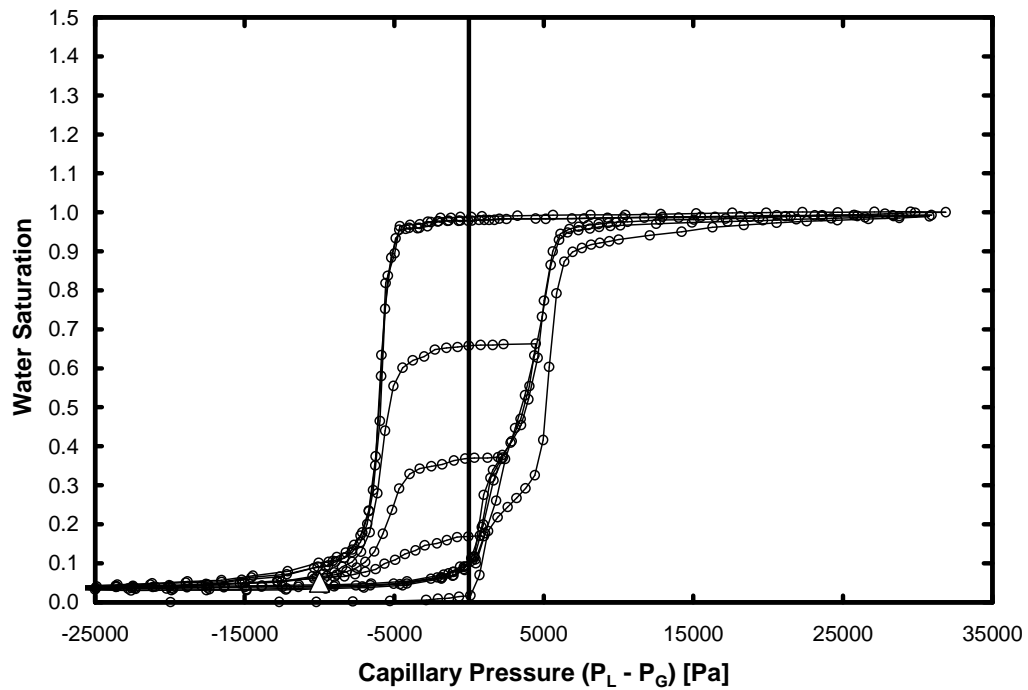
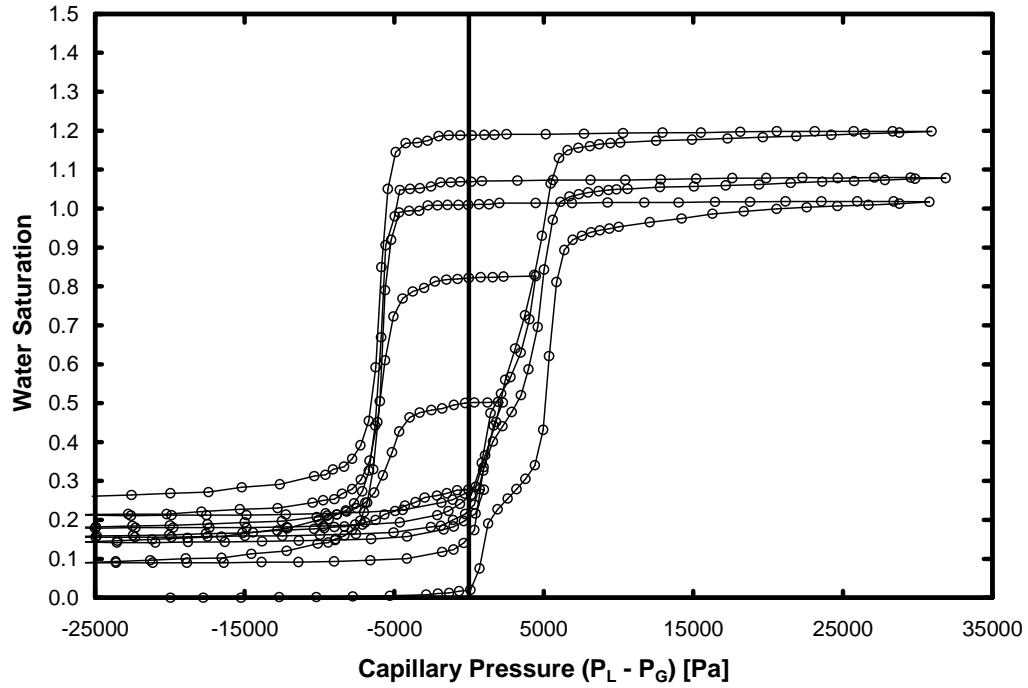


Figure 3.9: Sample of capillary pressure curves obtained by GCP test on Toray 090A. Top: Before evaporative correction. Bottom: After correction for evaporation. In this case the evaporation rate was  $0.64 \mu\text{g/s}$ . The triangle in the bottom figure is determined after the test by weighing the sample.

### 3.3. Water Breakthrough

A property of particular interest in GDLs is the liquid pressure and water saturation when the first liquid droplet emerges from the outlet face of the GDL. This represents the minimum saturation required to establish continuous liquid pathways through the GDL.

The simultaneous measurement of pressure and saturation at breakthrough is accomplished using a modified version of the GCP technique described above. The only necessary modification is determination of the point on the capillary pressure curve where breakthrough occurred. This can be achieved by inserting a small, circular piece (1 cm diameter) of *dry* hydrophilic membrane above the GDL sample, but below the hydrophobic capillary barrier (see Figure 3.6). The test proceeds as normal and each variation in capillary pressure leads to a change in saturation up to the point of water breakthrough. The breakthrough point is easy to determine since the saturation changes drastically and rapidly due to wicking of water into the dry hydrophilic membrane located above the sample. Figure 3.10 shows the transient mass response obtained from this test. The point of water breakthrough is clearly visible as a sudden and unexpected change in GDL water uptake, and the saturation and capillary pressure just before breakthrough can be easily determined. Upon water contact with the hydrophilic membrane the test is terminated.

To independently verify the breakthrough pressures measured using the modified capillary pressure device, a second test is performed similar to that presented by Benziger *et al.* [124]. A 1” diameter piece of sample is affixed to the end of a pipe and water-head above the sample is increased in 5 cm increments and held for approximately 10 minutes at each point until breakthrough is observed. Although this simple test does not provide saturation at breakthrough it provides the breakthrough pressure. The results obtained from this test confirm that the modified capillary pressure device detects the correct breakthrough point. This confirms that water leakage around the sample does not occur when using the modified GCP method.

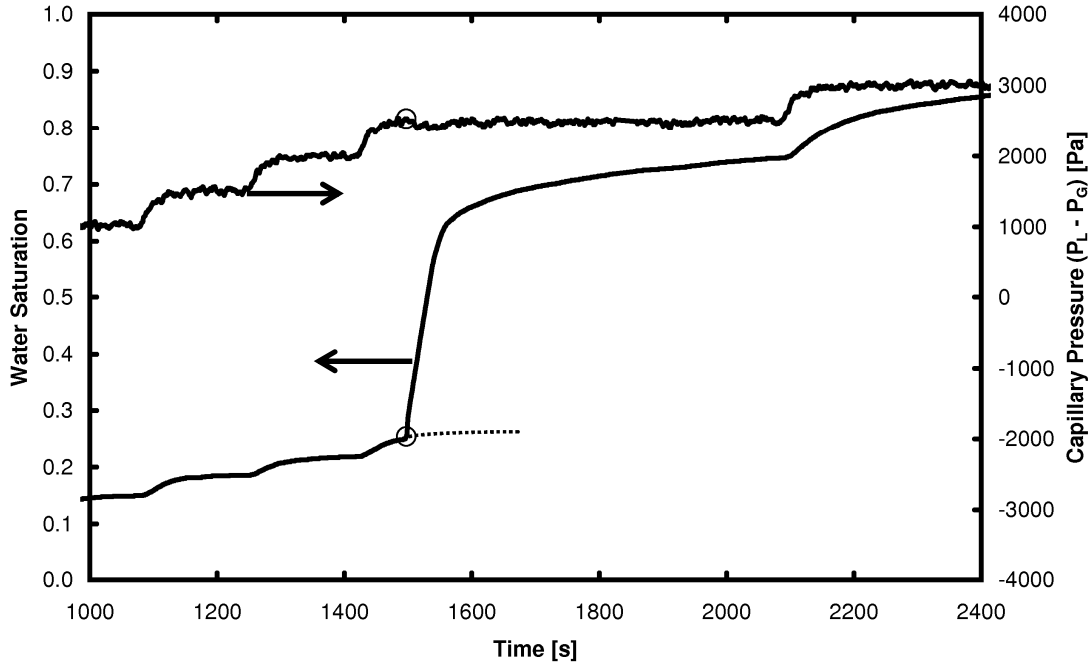


**Figure 3.10: Pressure and saturation time traces for SGL10BA. The dotted line shows the expected saturation response and the point of divergence is circled as the breakthrough point.**

### 3.4. Single Point Injection

Another variation of the GCP experiment is devised to test the finite size scale effects of GDLs. Finite size scale effects refer to the deviations from expected percolation theory behavior in small samples. Injection of liquid into the GDL from a single point removes surface effects from the capillary pressure curve and enables the study of the bulk GDL properties in isolation. This objective was achieved by simply placing a disk of solid PTFE sheet with a small hole below the sample, but above the hydrophilic membrane. The PTFE sheet has a thickness of  $< 50 \mu\text{m}$  and the hole is approximately  $500\mu\text{m}$  in diameter. The breakthrough pressure of this hole can be reliably estimated from the Young-Laplace equation to be below 100 Pa, which is well below the entry pressure of the GDL so that the capillary properties of the hole are not significant. The volume of the hole is also insignificant compared to the pore volume of the GDL. Only water injection could be tested with this arrangement since the water in the sample becomes disconnected from hydrophilic membrane at  $P_C < 0$  due to snap-off in the hole.

### 3.5. Contact Angle

Determining GDL wettability to water is very important, yet a reliable quantitative measurement has remained elusive. Contact angle measurements are useful for measuring the wettability of a fluid on a solid, but this approach can only be used on flat, smooth surface of the solid in question. For oil reservoirs it is possible to obtain a single crystal of the reservoir material for the measurement that is representative of the internal pore surfaces in the real media [194]. GDLs are made of round fibers so obtaining a flat smooth sample on which to take the measurement is not possible. The contact angle on graphite material similar to the fibers has been reported as  $86^\circ$  [119], but the water contact angle on carbon surfaces is known to be highly variable [195]. Moreover, GDL are impregnated with a PTFE coating, so the internal surfaces of a GDL pore are a mixture of two types of surfaces of unknown proportions. Lacking a solid, flat surface that is representative of the internal GDL pores, the only alternative is the measure the contact angle of water on the surface of the GDL. Attempts to use contact angle as a qualitative indicator of GDL wettability and the effect of PTFE [12,196,197] have had some limited success. For the present work, however, it is necessary to obtain an actual numerical value for the water contact angle inside a GDL pore since this is required for pore scale physics and displacement calculations in the pore network model described in Chapter 4. To this end, an estimate can be made by measuring the contact angle of a water droplet on the GDL surface and using the Cassie-Baxter equation to correct for the porosity of the surface and the Wenzel equation to compensate for the effects of roughness, which at the scale of the large drop corresponds to the roughness of the GDL surface due to fiber ridges and not the microscopic roughness of the fibers themselves. The effective contact angle obtained by this means represents the combined effect of graphite and PTFE on the droplet.

The contact angle of water on the surface of each GDL was measured by the sessile drop technique. A video contact angle system (AST Products 2500XE) was used to capture a photo of the droplet and image analysis software included with the video system was used to extract the contact angle from the photo. A sample image with the analysis lines is shown in Figure 3.11. The observed contact angles were corrected for the effects of

surface roughness and porosity using the Cassie-Baxter equation for porous surfaces [126] modified for surface roughness [119]:

$$\cos \theta_{obs} = b f_1 \cos \theta_{Eff} - f_2 \quad (3.3)$$

where  $\theta_{obs}$  is the measured contact angle,  $b$  is the ratio of actual area of contact between the drop and the solid portion of the surface to the projected area ( $b = \pi/2$  for cylinders) and  $f_1$  and  $f_2$  are the fractions of the GDL surface occupied by fiber and void, respectively. The value of  $\theta_{Eff}$  thus obtained is a rough estimate of the contact angle of the water inside the pores of the material.

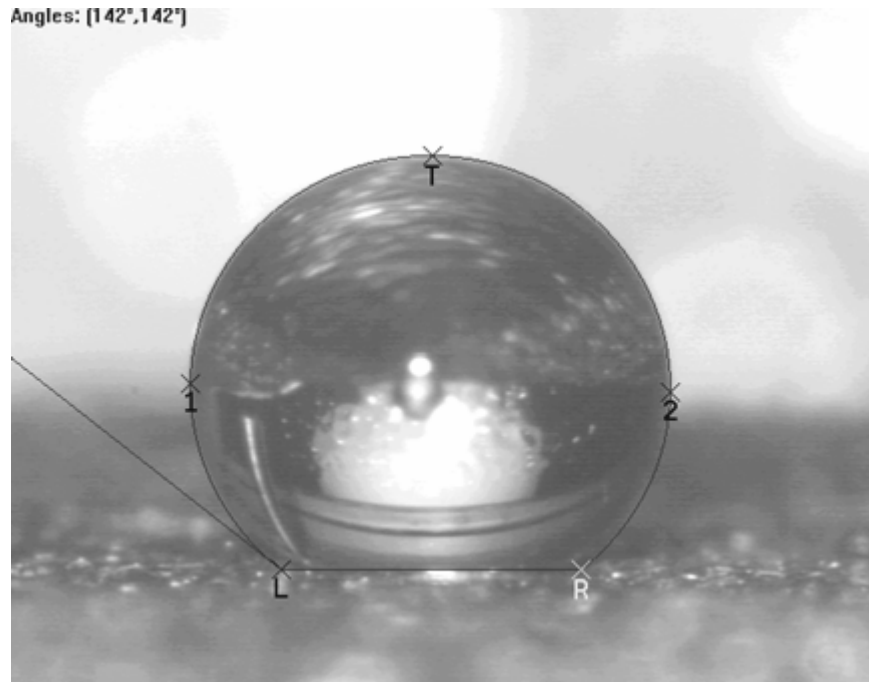


**Figure 3.11: Sample of sessile drop image. Water on SGL 10BA.**

To estimate the values of  $f_1$  and  $f_2$  the GDL it is not enough to simply use the porosity for the fraction of solid and void (i.e.  $f_1 = 1 - \varepsilon$  and  $f_2 = \varepsilon$ ). Because of the alignment of fibers in the plane a droplet sitting in the GDL surface will be in contact with much more fiber than a drop sitting on the edge of the GDL. To account for this additional area, a simple geometric model of the GDL was developed by assuming that the fibers in the GDL can be represented by a stack of interwoven screens (Figure 3.12). Spacing  $S$  between each parallel fiber is equal in both directions and this is also the spacing between the layers.

For simplicity the fibers of diameter  $d_f$  are allowed to intersect. The unit cell in this model has dimensions of  $S + d_f$  in all three directions, giving a volume of  $(S + d_f)^3$ . To calculate porosity, the fiber volume is subtracted from the volume of the unit cell and the following relationship is obtained:

$$\begin{aligned} \varepsilon &= \frac{V_{Unit\ Cell} - 2V_{Fiber} + V_{Intersection}}{V_{Unit\ Cell}} & (3.4) \\ &= \frac{(S + d_f)^3 - 2 \cdot \frac{\pi}{4} d_f^2 (S + d_f) + \frac{2}{3} d_f^3}{(S + d_f)^3} = \\ &= \frac{\left(\frac{S}{d_f}\right)^3 + 3\left(\frac{S}{d_f}\right)^2 + 3\left(\frac{S}{d_f}\right) + 1 - \frac{\pi}{2}\left(\frac{S}{d_f}\right) - \frac{\pi}{2} + \frac{2}{3}}{\left(\frac{S}{d_f}\right)^3 + 3\left(\frac{S}{d_f}\right)^2 + 3\left(\frac{S}{d_f}\right) + 1} \end{aligned}$$

Eq.(3.4) may be solved for  $S/d_f$  given  $\varepsilon$ , thus enabling the calculation of the fractions  $f_1$  and  $f_2$  from the following expressions:

$$f_1 = \frac{d_f}{S + d_f} = \frac{1}{\frac{S}{d_f} + 1} \quad (3.5)$$

and:

$$f_2 = \frac{S}{S + d_f} = \frac{\frac{S}{d_f}}{\frac{S}{d_f} + 1} \quad (3.6)$$

Using this approach, contact angles between  $102^\circ$  for untreated Toray 090A and  $109^\circ$  for SGL10BA were typically obtained for the air-water fluid system. These values are in the expected range for graphite ( $86^\circ$ ) and PTFE ( $108^\circ$ ) materials, so the correction of Eq.(3.3) seems to provide a reasonable approximation.

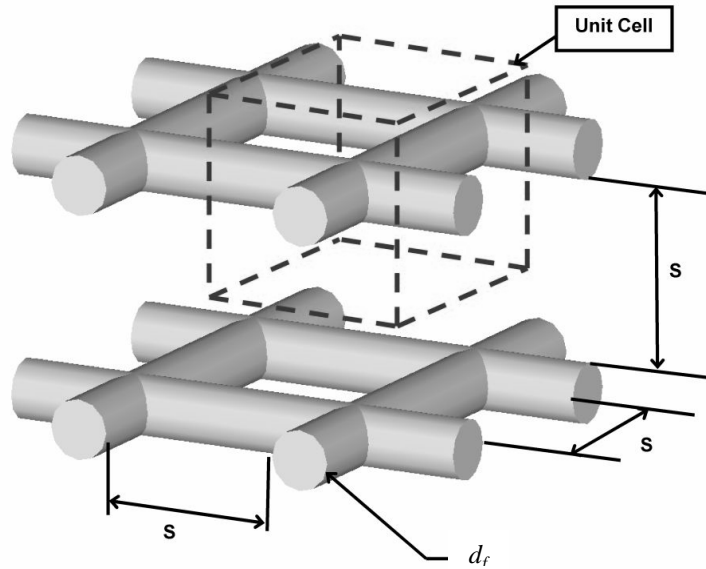
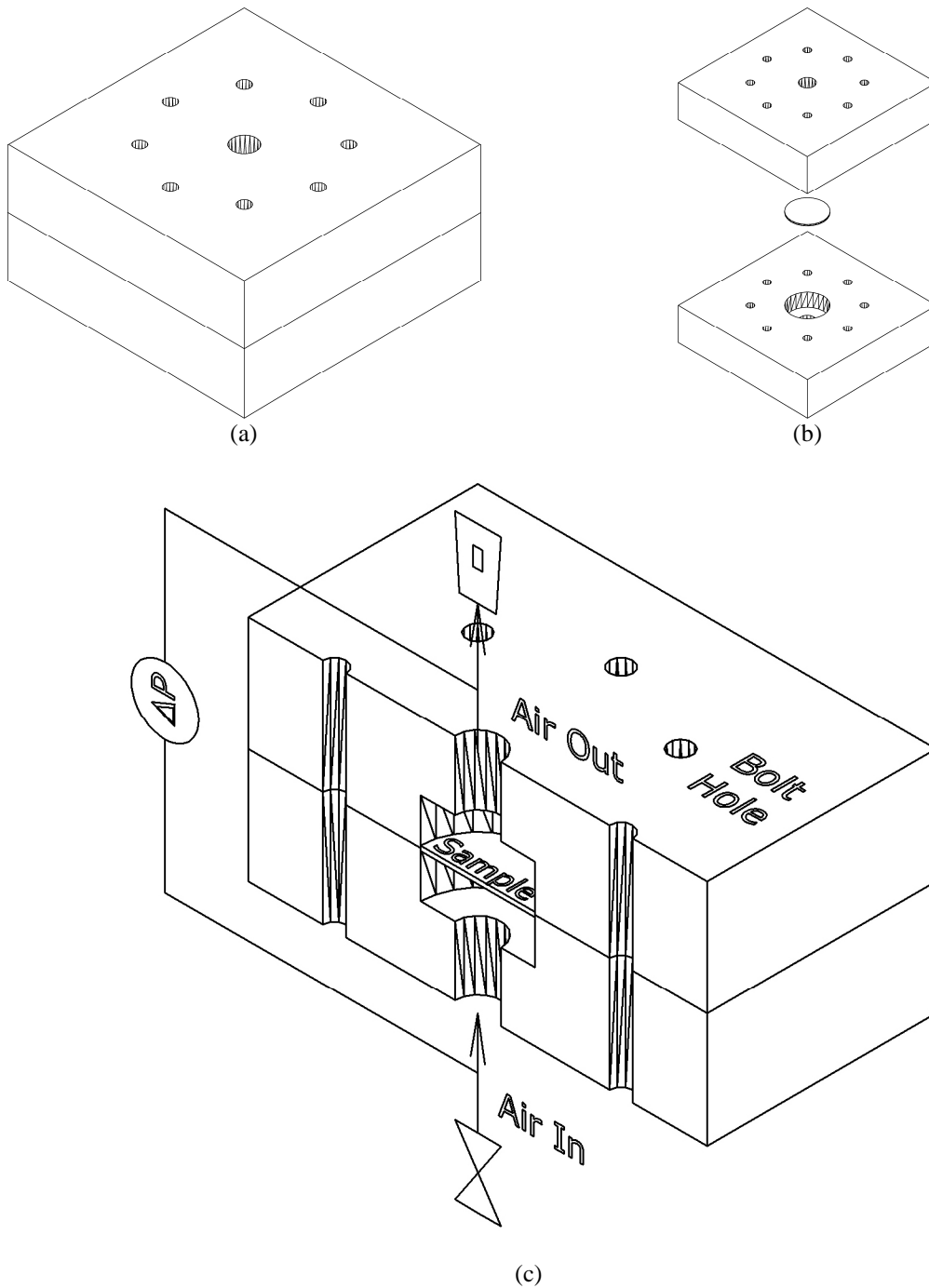


Figure 3.12: Stacked screen model to determine fraction of solid and void under sessile drop on GDL surface

## 3.6. Permeability

### 3.6.1. Through-Plane Permeability

Through-plane permeability is measured using the set-up shown in Figure 3.13. In this arrangement, gas is fed through the sample at a fixed flow rate and the resultant pressure drop is measured. The sample is circular with a diameter of 25.4 mm. The GDL is secured between the two plates and a gas-tight seal is easily obtained given the low gas pressures used during the experiment ( $<15$  Pa). The differential pressure sensor (Omega PX653, accuracy  $\pm 0.1\%$  FS) spans a range of -0.05 to 0.05 inches of water column ( $\sim 15$  Pa to 15 Pa). The flow rate is measured at the outlet using a digital flow meter (Omega FVL-1604-A,  $\pm 0.5\%$  FS). The pressure drop is obtained for at least 10 flow rates for each sample. The local barometric pressure is also recorded.



**Figure 3.13: Experimental apparatus for through-plane permeability measurement. (a) assembled view (b) exploded view (c) sectioned view to show internal components.**

### 3.6.2. In-Plane Permeability

The in-plane gas permeability is measured as a function of GDL thickness to simulate conditions in an assembled cell, which is significantly compressed in order to promote

good electrical contact between layers and ensure a tight gas seal. The experimental apparatus for these measurements is shown in Figure 3.14. The sample size for this test is 63.2 mm wide by 20 mm long. The sample is compressed between two plates with the spacing controlled by placing feeler gauges of known thickness between them. Using a torque wrench, the plates are tightened by two bolts to a torque of about 20 N·m each. Tests were performed to confirm that the test cell was sufficiently rigid and that the results did not depend on the bolt torque (i.e. the test cell did not deform when tightened). A bolt torque of 20 N·m was found to be sufficient to compress all samples and so was maintained at this level throughout all experiments for consistency. It was also verified that the test cell presented negligible pressure drop in the absence of sample to ensure that all observed pressure loss could be attributed to the sample alone. The sides of the cell are sealed by clamping a face plate on each side. A rubber gasket between the face plates and the body of the cell provides the gas seal. Seals along the back edge of the header slots are created using silicone putty. This malleable material yields as the spacing between the plates is reduced and provides a reliable seal. The seal is tested before each run by closing the outlet and pressurizing the system to 400 kPa. The setup can hold pressure indefinitely after the air supply was stopped.

The flow rate is measured on the outlet side using a digital flow meter (Omega FVL-1604-A, +/-0.5% FS). A pressure gauge (Setra 209, +/-0.25% FS) monitors the inlet pressure and the outlet is taken as atmospheric pressure since the presence of the flow meter in the line presents a negligible pressure drop. Measurements for at least 10 flow rates are obtained at each GDL thickness. The local barometric pressure is recorded since absolute pressure is required in the data analysis.

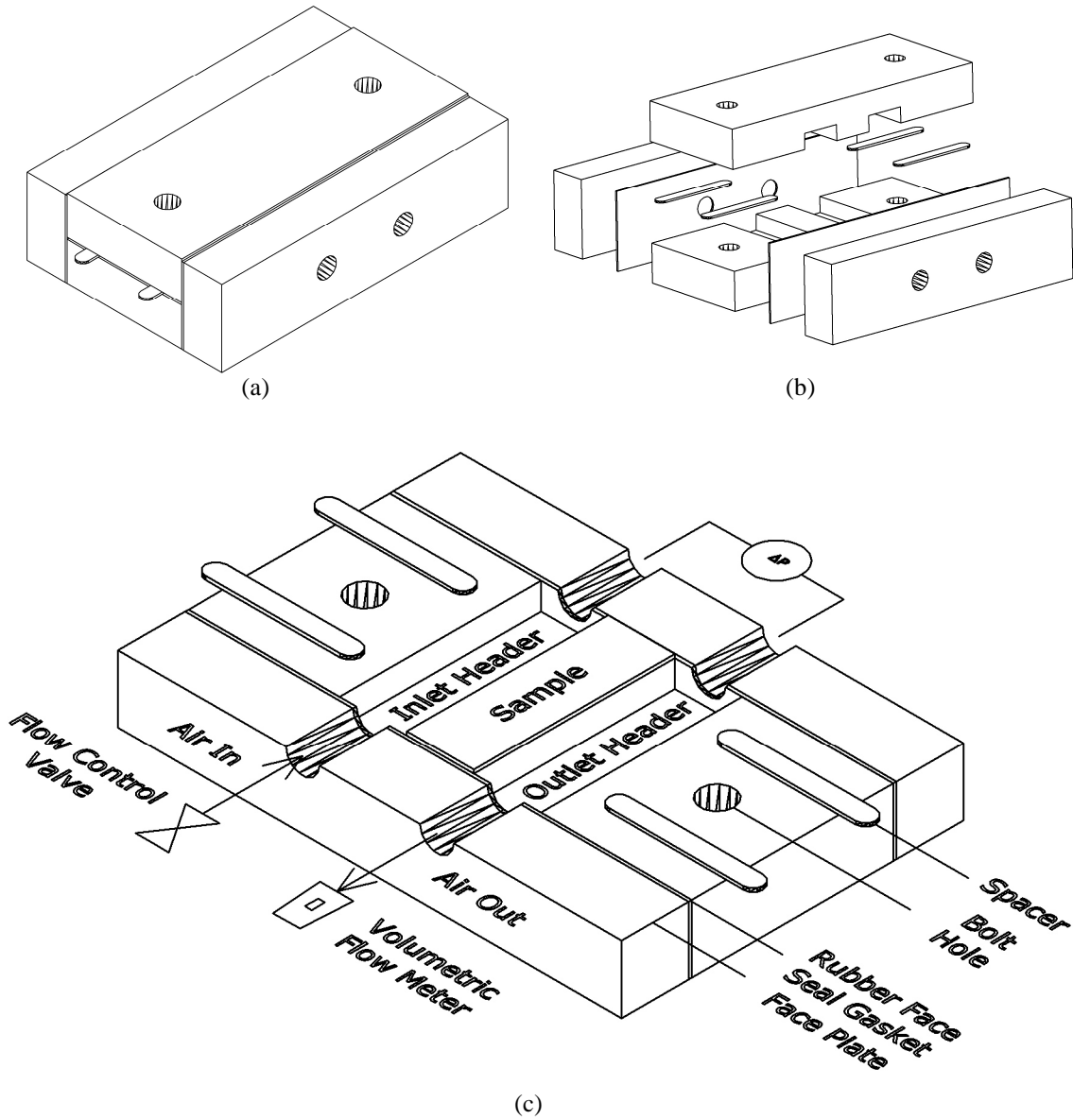


Figure 3.14: Experimental apparatus for in-plane permeability measurement. (a) assembled view (b) exploded view (c) sectioned view to show internal components.

### 3.6.3. Data Analysis

Consideration of Darcy's law for steady, one-dimensional flow of a compressible ideal gas in the absence of inertial effects results in the following equation [198]:

$$\frac{(P_{IN}^2 - P_{OUT}^2)}{2LRT / MW_{AIR}} = \frac{\mu}{K} (m') \quad (3.7)$$

where  $P_{IN}$  is the inlet pressure,  $P_{OUT}$  is the outlet pressure,  $L$  is the length of the sample,  $R$  is the universal gas constant,  $T$  is the temperature,  $MW_{AIR}$  is the molecular weight of air and  $m'$  is the mass flux through the sample. Eq.(3.7) is valid when the gas velocity is small and viscous drag is the dominant cause of pressure loss. At high velocity, inertial pressure losses become significant and Darcy's law must be modified to account for this effect. For a compressible fluid behaving as an ideal gas, solution of the modified Darcy's law, or Forchheimer equation, leads to [198]:

$$\frac{(P_{IN}^2 - P_{OUT}^2)}{2LRT / MW_{AIR}} = \frac{\mu}{K} (m') + \beta(m')^2 \quad (3.8)$$

At low velocities, the second term on the right hand side vanishes and Darcy's law is recovered. The permeability and inertial coefficient can be obtained by fitting Eq.(3.8) to experimental data and extracting the linear and quadratic coefficients, respectively. The viscosity of air was taken to be  $1.85 \times 10^{-5}$  Pa·s for all runs and assumed to be independent of gas pressure over the range of pressure used here [116].

Figure 3.15 shows a sample of experimental results from through-plane permeability tests. Data for two types of GDL are shown. In each case, the results include measurements from three samples of a large GDL sheet. Differences are observed in the measurements from the three sections of each sample, but they are minimal. The linearity of the data indicates that Darcy flow is occurring and inertial effects are not important. Permeability values are obtained by fitting Eq.(3.7) to the data using least squares regression and obtaining the coefficient value, from which  $K$  can be calculated.

The in-plane permeability measurements show a non-linearity due to the Forchheimer effect. Figure 3.16 shows typical data obtained from these experiments. The permeability can be determined for each sample compression by fitting Eq.(3.8) to the data, yielding the results shown in Figure 3.17. The coefficient of correlation ( $R^2$ ) is 0.99 or higher for all runs. As expected, the permeability decreases significantly as the GDL is compressed.

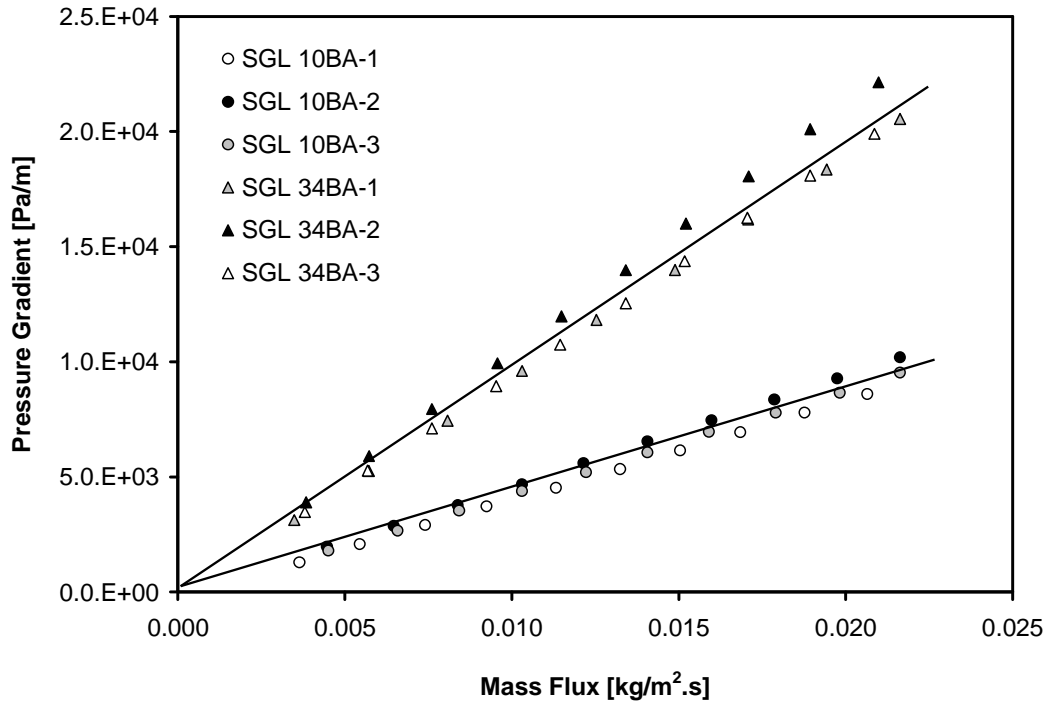


**Figure 3.15:** Sample of experimental data for through-plane pressure drop as a function of air mass flux for two samples. Lines through the data are regression lines that yield  $K$  values according to Eq.(3.7).

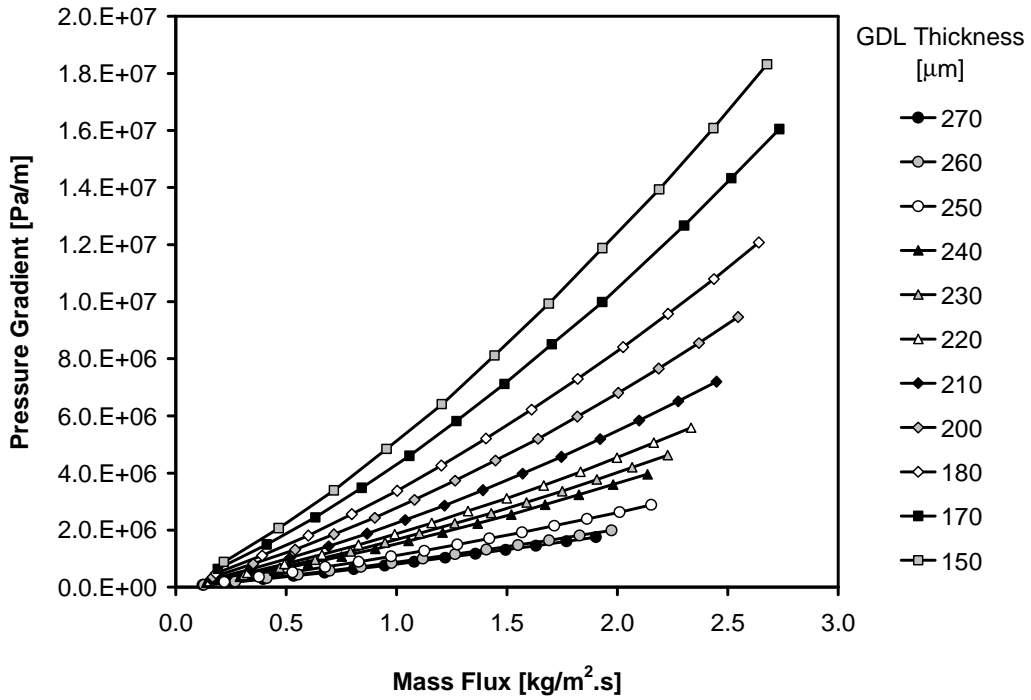


Figure 3.16: Sample of experimental data for in-plane pressure drop as a function of air mass flux for SGL 34BA.

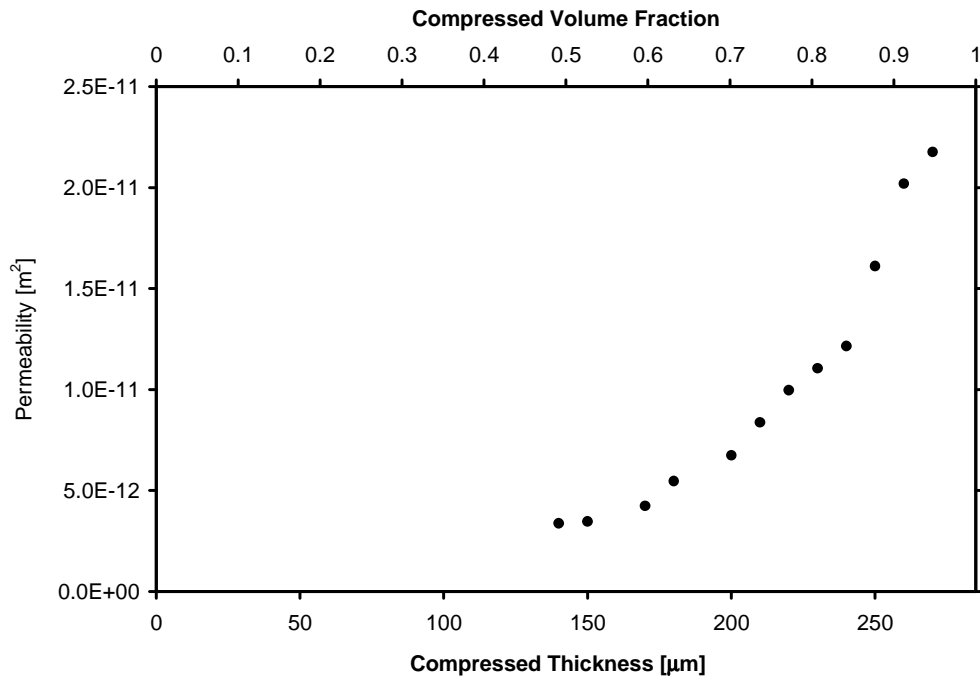


Figure 3.17: Permeability vs. thickness and compressed volume fraction of sample from the raw data shown in Figure 3.16.

### 3.6.4. GDL Compression and Porosity Conversion

During this work, the in-plane permeability is measured as a function of GDL compressed thickness to better understand compression effects during cell assembly. In order to compare experimental results with permeability models, it is necessary to convert the change in GDL thickness to a change in porosity. To this end, it is assumed that the fibers of the GDL are incompressible and all the reduction in bulk volume during compression arises from the reduction of pore volume. If it is additionally assumed that the sample deforms only in the direction of compression, then the porosity of the compressed sample may be determined from its compressed thickness as follows:

$$V_{p,C} = V_{b,C} - V_s = V_{b,C} - (1 - \varepsilon_o) V_{b,o} \quad (3.9)$$

where  $V_{p,C}$  is the pore volume of the compressed sample,  $V_{b,C}$  is the bulk volume of the compressed sample and  $V_s$  is the solids volume, which is assumed to remain constant as the sample is compressed.  $V_{b,o}$  and  $\varepsilon_o$  are the bulk volume and porosity of the uncompressed sample, respectively. Eq.(3.9) can be rearranged to give the porosity of the compressed sample as:

$$\varepsilon_c = \frac{V_{p,C}}{V_{b,C}} = 1 - \frac{(1 - \varepsilon_o)}{V_{b,C} / V_{b,o}} = 1 - \frac{\delta_o}{\delta_c} (1 - \varepsilon_o) \quad (3.10)$$

where  $\delta_o$  is the thickness of the uncompressed sample and  $\delta_c$  is the compressed thickness. The substitution of volume for thickness can be made since only the thickness of the samples changes during compression and their cross-sectional areas remain constant. Figure 3.18 shows the permeability results obtained from Figure 3.16 as a function of thickness (left) and as a function of porosity calculated by (3.10) (right).

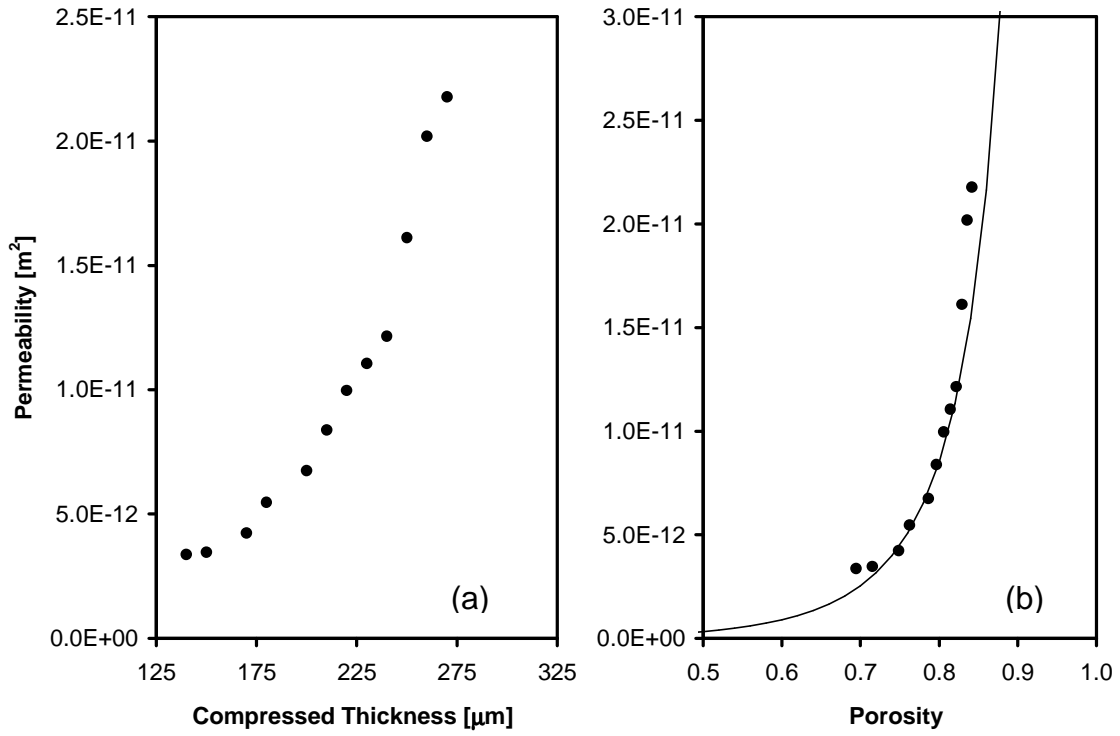


**Figure 3.18: (a) Permeability vs. sample compressed thickness and (b) permeability vs. sample porosity converted using Eq.(3.10) for SGL 34BA GDL sample. The black line represents the Carman-Kozeny model.**

## 4. Pore Network Modeling

Nearly 100 studies on the modeling of multiphase flow through porous GDL using CFD packages have been published. However, the lack of knowledge concerning the appropriate transport properties and constitutive relationships, particularly highly inaccessible properties such as relative permeability and relative effective diffusivity, has significantly limited the validity of modeling results obtained based on continuum geometry. The work of this thesis presented so far has focused on measuring various GDL transport properties. This chapter describes the modeling of transport through the GDL using an approach aimed at avoiding the problems faced by the popular continuum models, namely the lack of constitutive relationships.

Pore network modeling is an alternative approach to modeling multiphase transport processes in GDL materials. This approach has a long history in the study of porous media of geologic origin (soil and rock) [117,199-201]. The basis of this approach is a mapping of a complex pore space continuum onto a regular or irregular lattice of sites and bonds. To derive a geometrical model, it is assumed that the pore space can be conceptually partitioned into a collection of pore bodies connected by local constrictions termed pore throats, as illustrated in Figure 4.1. A slice through a fibrous GDL is shown in Figure 4.1(left) where the black regions correspond to solid fibers and white represents void space. Conceptually, this structure can be sectioned into pore bodies demarcated by the red lines in Figure 4.1(middle) so that each pore body is connected to its neighbors via throats, shown by the blue lines. A regular cubic pore network can be constructed as shown in Figure 4.1(right) with equivalent properties to the conceptual picture of the sectioned pore space. This equivalent model pore network is constructed by assigning pore and throat sizes to the lattice sites and bonds, respectively.

Simplifying assumptions regarding the shape of pores and throats are invariably made to facilitate the computation of capillary and transport characteristics of the pore network elements [202]. Pore network models are ideally suited for the simulation of low-capillary number (quasi-static) immiscible displacement using percolation concepts [117].

A main advantage of pore network models is that they account explicitly for pore-level physics and pore space geometry/topology. Prediction of various macroscopic transport and capillary properties of porous media is relatively straightforward if the geometric, topological and correlation properties of the porous microstructure are properly specified. The task of extracting this information is, however, non-trivial, typically requiring extensive characterization of 3D volume data [203].

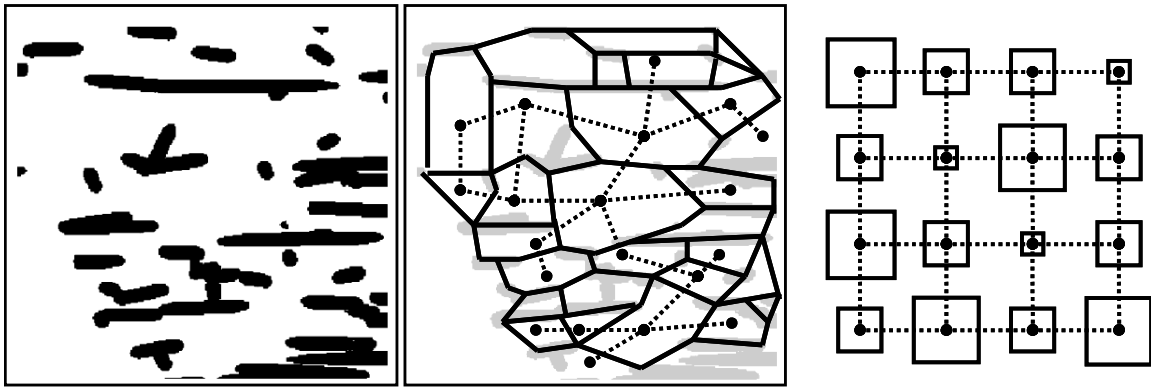


**Figure 4.1:** The analogy between actual pore structure and an equivalent cubic lattice representation. **Left:** In-plane view of a GDL. **Middle:** Conceptual sectioning of pore space into pore bodies (red) and throats (blue). **Right:** Cubic lattice of equivalent properties.

#### 4.1. Cubic Lattice Pore Network Model

The following sections describe the development of a regular cubic 3D pore network model to study multiphase transport in GDLs. The work carried out as part of this project [129] represents the first attempt to apply pore network modeling for the study of the gas diffusion layer of a PEMFC. Several other pore network models of GDLs have subsequently been published. Markicevic *et al.* [204] attempted to predict multiphase transport properties of a GDL using a 2D pore network model. Since multiphase transport is highly dependent on the pore network dimensionality [205], the results based on a 2D domain are of limited applicability. Sinha *et al.* [206] developed a 3D model but the size and structural aspects of their model were not calibrated to known GDL properties. Furthermore, they focused on water configurations at breakthrough and did not report multiphase transport results.

In the present model, extensive efforts are made to develop a quantitatively accurate model of the GDL that can be reliably used to make specific predictions about GDL transport. Numerous modifications are made to the traditional pore network modeling framework in order to account for the unique geometric aspects of fibrous GDLs. In the absence of 3D volume data for the GDL materials studied, the network parameters are obtained by calibration to experimental gas permeability and drainage capillary pressure data. The model is then used to simulate multiphase transport scenarios of interest to PEMFC operation, such as the diffusion of gas through a partially water-filled GDL and the convective flow of water under conditions of partial water saturation.

#### **4.1.1. Pore Network Construction**

One of the distinguishing features of GDLs is that they have very high porosity ranging from 0.75 to above 0.90, meaning that GDLs are predominantly void space. Moreover, there is little constriction between pores, creating a highly open structure. Figure 2.12 shows a cross-sectional slice obtained from a simple solid model of a GDL. With such a small solid phase fraction, it is difficult to define distinct pore bodies or to identify pore throats. This situation is quite different from that encountered in rocks and soils, for which pore bodies and pore throats can be intuitively delineated in images of the pore space.

##### **4.1.1.1. Pore and Throat Size Distributions**

The pore network model developed here for GDLs is based on the one described by Ioannidis and Chatzis [202] and Chang and Ioannidis [207]. The pores are modeled as nodes on a regular cubic 3D lattice interconnected through throats. The pores are idealized as cubic bodies and the throats are treated as ducts of square cross-section. This arrangement is shown in Figure 4.2 with the relevant dimensions labeled. The use of square pores is convenient in order to achieve sufficiently high porosities and to qualitatively describe the presence of corners and crevices in the pore space. The pore network is constructed by assigning pore body sizes from a truncated Weibull cumulative distribution:

$$r_{p,i} = \lambda [-\ln(1 - \chi \cdot \chi_{\max})]^{-1/\kappa} + r_{\min} \quad (4.1)$$

where  $r_{p,i}$  is the radius of the  $i^{\text{th}}$  pore,  $\chi$  is a random number between 0 and 1,  $\chi_{\max} (< 1)$  scales the random number and truncates the upper end of the distribution to prevent excessively large pores from being generated,  $r_{\min}$  is the minimum pore radius and  $\lambda$  and  $\kappa$  are adjustable parameters that control the location/spread and shape of the distribution. A Weibull distribution is used since it is highly flexible and contains only two adjustable parameters; features which are advantageous when pore size distribution is adjusted to calibrate the model as described in Section 4.1.6.

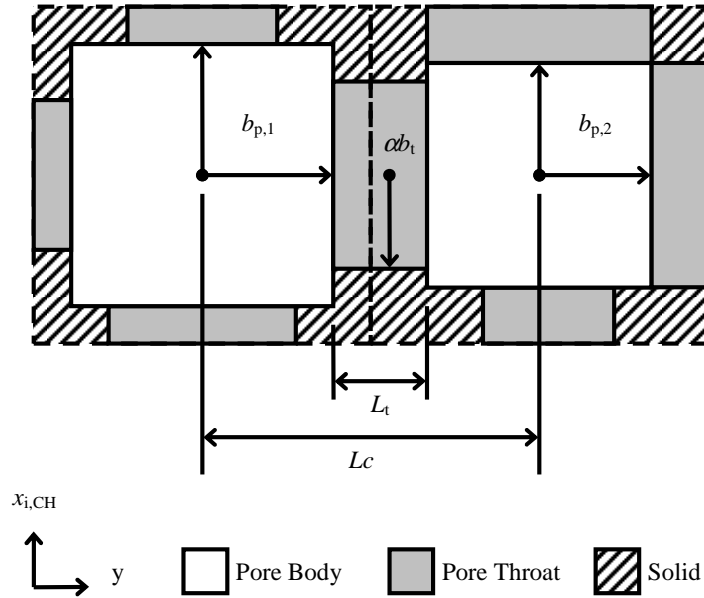


**Figure 4.2:** Schematic of 2 neighboring pore bodies and connecting throat. Throat size ( $b_t$ ) is proportional to the size of the smaller of the two connecting pores ( $b_t = \alpha b_p$ ). Throat length ( $L_t$ ) is equal to the difference between the pore body sizes ( $b_p$ ) and the center-to-center distance between pores ( $L_c$ ).

Once pore sizes are assigned, throat sizes are assigned by assuming that the size of each throat is equal to the size of the smallest of the two adjacent pores. This throat assignment scheme is chosen because it allows for minimum constriction between pore bodies, creating a highly open structure characteristic of GDLs. Figure 4.3a shows the construction of the lattice with pores and throats identified. Figure 4.3b shows only the

void and solid space of the same lattice. The open nature of the pore space obtained by this method of throat size assignment is apparent.

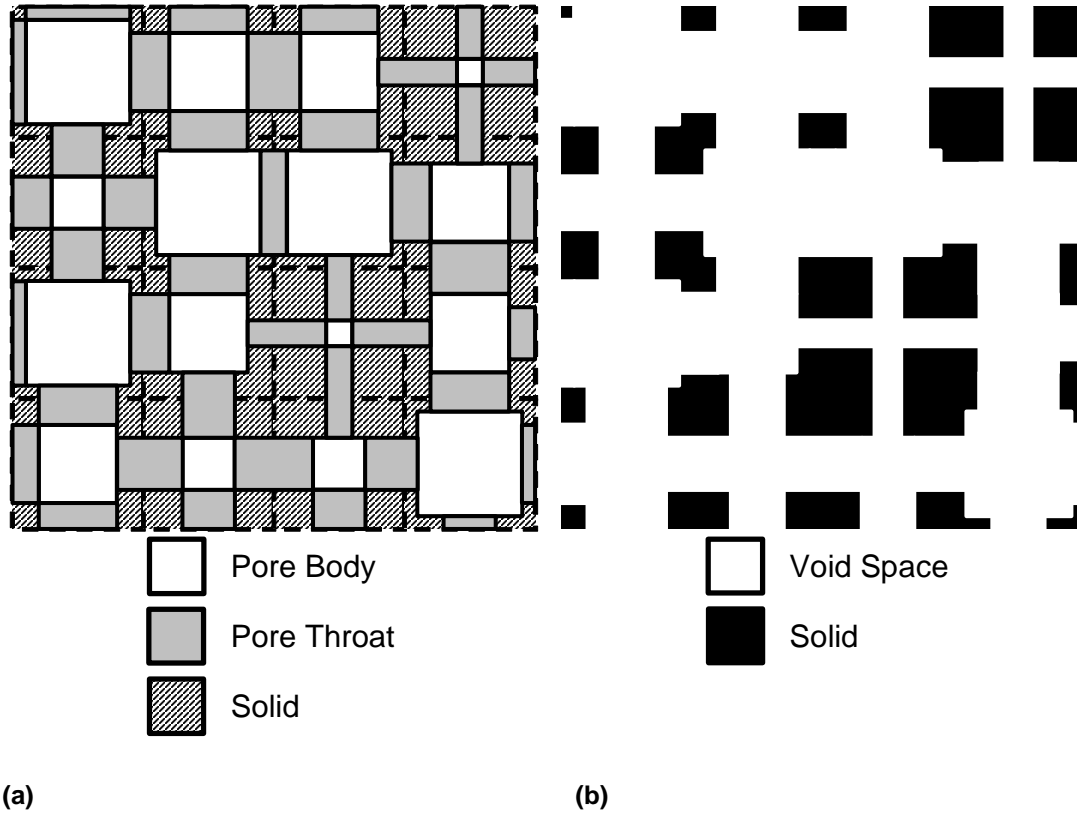


**Figure 4.3: 2D Schematic of pore network construction. (a) Relationship between pores, throats and solid. (b) Structure in terms of void and solid spaces.**

The length of each throat is calculated as the difference between the lattice constant  $L_c$  and the size of the two connecting pores. The lattice constant is the spacing between pore centers and is adjusted to match the porosity of the network model to the known porosity of the material. This is discussed further in Section 4.1.6.2. Consequences of this size assignment scheme are that throats and pores have similar size and their volume cannot be neglected in the calculation of the total lattice volume. In fact, a throat is actually an extension of the pore body to which it is attached and the lattice is basically an assembly of pores connected directly to pores.

It should be clear that the aforementioned description is by no means an attempt to reproduce the actual geometry of GDL pore space. Instead, the aim is to develop a pore network model sufficiently flexible to reproduce experimental measurements of capillary pressure and gas permeability (in-plane and through-plane). Clearly, a better way to construct the pore network would be to extract its geometric and topological properties from experimental 3D volume data of the GDL materials. Such data are neither readily available nor easily analyzed to extract geometric and topological parameters.

#### 4.1.1.2. Spatial Correlation of Pores Sizes

One of the key features included in the model is spatial correlation of pore sizes. A highly porous material such as a GDL contains regions of extended continuous void space with no solid to mark distinct boundaries between pore bodies. In terms of the pore network model, these regions are analogous to multiple neighboring pores of similar size. Imposing spatial correlation of pore sizes in the model results in pores of similar size being placed next to each other in the lattice. These pores are invaded by the non-wetting phase at similar capillary pressures and offer similar resistance to fluid flow, therefore acting as a single, large pore. The effect of introducing spatial correlation of pores into the model is to increase the permeability of the network by more than 20% and bring it into closer agreement with measured values. Experience has shown that without spatial correlation, it is very difficult to match both the experimental permeability and the capillary pressure curves since both depend on pore size distribution.

Spatial correlation also partially accounts for the observed directional anisotropy in the permeability tensor [161]. When pores are correlated in certain directions, the permeability along these directions is increased. It was found that correlation of pores in the direction of fiber alignment helps to create the observed anisotropy trends. For instance, since the fibers of Toray 090 are aligned in the  $x$ - $y$  plane, correlation of neighboring pores in this plane, but not in the through-plane ( $z$ -direction), produces the correct trend. This is summarized with the notation  $[\beta_x, \beta_y, \beta_z] = [1, 1, 0]$  where  $\beta$  is the

correlation distance. The fibers in SGL 10BA are also predominantly aligned in the  $x$ - $y$  plane, but are also directionally aligned in the  $x$ -direction. The use of correlation distances  $[\beta_x, \beta_y, \beta_z] = [2, 1, 0]$  partially reproduces the observed anisotropy. Figure 4.4a shows a structure obtained using a field of random, uncorrelated numbers, whereas Figure 4.4b and Figure 4.4c show the structures obtained when the correlations  $[1, 1, 0]$  and  $[2, 1, 0]$ , respectively, are imposed.

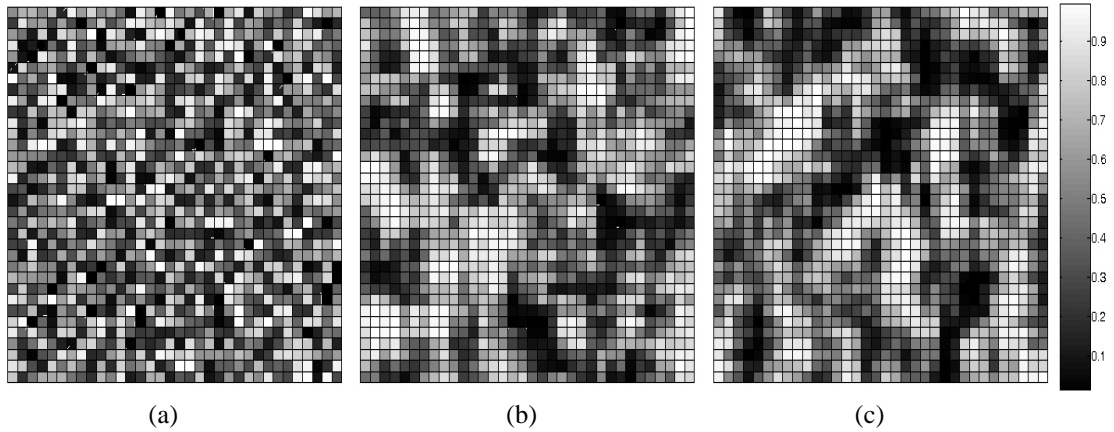


**Figure 4.4: Examples of spatially correlated random fields. (a) Uncorrelated field. (b) Correlated field used to model Toray 090 with correlation distances  $[1, 1, 0]$  in the  $x$ ,  $y$  and  $z$  directions ( $z$ -direction not shown). (c) Correlated field used to model SGL 10BA with correlation distances  $[2, 1, 0]$  in the  $x$ ,  $y$  and  $z$  directions. ( $z$ -direction not shown).**

Anisotropy can also be created in the model by constricting throat sizes along specific directions. In addition to the imposition of spatial correlation, a small amount of throat constriction is necessary to completely match the experimentally observed anisotropy in permeability. Throats are uniformly constricted according to the expression:

$$r_{t,ij} = \alpha r_{p,i} \quad (4.2)$$

where  $r_{t,ij}$  is the size of the throat connecting pores  $i$  and  $j$ ,  $r_{p,i}$  is the size of pore  $i$  with  $r_{p,i} < r_{p,j}$  and  $\alpha$  is the throat constriction factor. The throat constriction factor is direction dependent and described with the notation  $[\alpha_x, \alpha_y, \alpha_z]$ . In general, it is necessary to constrict throats slightly (5-10%) in the direction perpendicular to the axis of fiber alignment. For Toray 090, throats are constricted in the through-plane  $z$ -direction according to  $[\alpha_x, \alpha_y, \alpha_z] = [1, 1, 0.9]$ . In SGL 10BA, the fibers are aligned in the  $x$ - $y$  plane with some additional alignment in the  $x$ -direction. Accordingly, throat constriction

factors  $[\alpha_x, \alpha_y, \alpha_z] = [1, 0.95, 0.95]$  are used. Constriction of the throats in this way is consistent with the structure of GDLs since flow in the cross-fiber direction is more obstructed.

#### 4.1.2. Capillary Pressure

All pore throats and pore bodies in this model are assumed to be of square cross-section. The capillary pressure  $P_C$  required for a non-wetting fluid to penetrate a throat of square cross-section is estimated by the Young-Laplace equation:

$$P_C = -2\sigma \cos \theta \left( \frac{1}{r_t} \right) \quad (4.3)$$

where  $\sigma$  is the surface tension,  $\theta$  is the contact angle and  $r_t$  is the radius of the largest circle that can be inscribed in the square capillary.

#### 4.1.3. Late Pore Filling

In reality, pore geometry is more complex than any simple geometric shape, albeit angular, can describe. Unresolved length scales due to the presence of cracks, corners, crevices and interstitial regions at fiber-fiber contact points amount to pore space from which the wetting phase is displaced at capillary pressures higher than that corresponding to first entry of the non-wetting phase into any pore in the network. Figure 4.5(left) shows a conceptual picture of the non-wetting phase fluid (water) configuration in a pore at the entry pressure and Figure 4.5(right) shows the configuration as the non-wetting phase pressure increases. The corners of the pore gradually fill as the pressure is increased. To account for the gradual drainage of the wetting phase from such small scale features, the following expression is employed [207]:

$$s_{wp} = s_{wp}^* \left( \frac{P_C^*}{P_C} \right)^\eta, \quad P_C > P_C^* \quad (4.4)$$

where  $\eta$  is the filling exponent,  $s_{wp}$  is the wetting phase saturation of a given pore at capillary pressure  $P_C$  and  $s_{wp}^*$  is the wetting phase saturation of the same pore at the

capillary pressure  $P_c^*$  corresponding to first entry (breakthrough) of the non-wetting phase. The parameters  $\eta$  and  $s_{wp}^*$  are taken to be adjustable in this model. Late pore filling enables smaller scale features to affect the capillary pressure behavior of the network without explicitly including them as individual pores. This treatment is found to be necessary to correctly model the experimental capillary pressure curves.

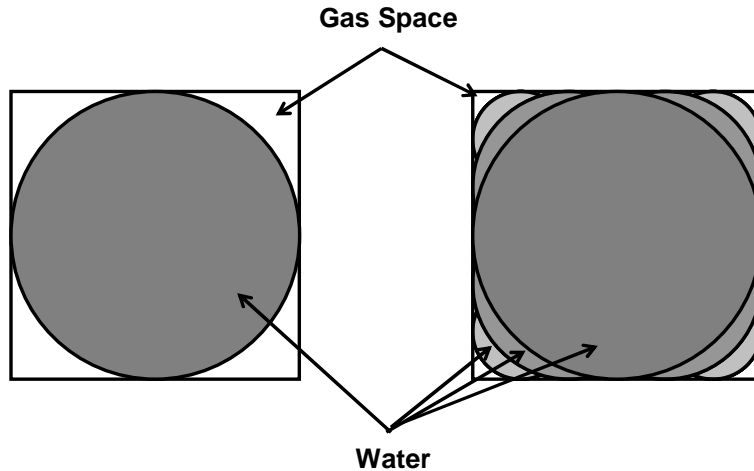


Figure 4.5: Conceptual schematic of late pore filling.

#### 4.1.4. Drainage Simulation

The process considered by the present model is the drainage of a wetting phase by slow (quasi-static) invasion of a non-wetting phase. In terms of fuel cell operation, this simulation corresponds to the flow of liquid water (the non-wetting phase) from the catalyst layer through the GDL to the flow channel via a path of the largest accessible pores. The algorithm for simulating drainage in the network is as follows. First, an initial low capillary pressure is selected. The network is then scanned and all pore throats that *can* be penetrated at the given capillary pressure are marked as ‘open’, along with the pore bodies to which they are connected. Next, all distinct clusters of contiguous open throats and pores are found and labeled. Finally, all clusters that are connected to the injection face are identified and are counted as penetrated by the invading fluid. All pores and throats not connected to the injection face are returned to a ‘closed’ state. In

this way, the invading front of the non-wetting phase only reaches pores that are both topologically accessible from the injection face (i.e. through other invaded pores) and penetrable at the given capillary pressure. The algorithm proceeds by increasing the capillary pressure in small increments and repeating the procedure until all pores and throats are open or filled with the invading fluid. The volume of non-wetting phase within pores invaded at each capillary pressure step is calculated and a capillary pressure curve is generated. In the present simulations, the injection of the non-wetting phase occurs always in the through-plane ( $z$ ) direction. In terms of a GDL, the injection face is on one side and the exit face is the other side. This corresponds to the situation where liquid water is generated at the catalyst layer and flow through the GDL to the flow channel.

#### 4.1.5. Transport Processes in the Network

##### 4.1.5.1. Convection

Determination of the flow rate and pressure drop across the pore network requires solution of the following mass conservation equation around each pore:

$$q_i = \sum_{j=1}^n g_{h,ij} (P_j - P_i) = 0 \quad (4.5)$$

where  $i$  denotes the current pore,  $j$  denotes the neighboring pore,  $n$  is the number of neighbors,  $q_i$  is the net flow through pore  $i$ ,  $g_{h,ij}$  is the hydraulic conductivity for flow between pore  $i$  and the neighboring pore  $j$ , while  $P_i$  and  $P_j$  are the pressures in each pore. The hydraulic conductivity  $g_h$  of the pores and throats depends on their size and length and is determined from the following expression for square ducts [208]:

$$g_h = \frac{2.28r^4}{2L\mu} \quad (4.6)$$

where  $2r$  is the size of the conduit opening,  $\mu$  is the fluid viscosity and  $L$  is the conduit length.  $L$  is equal to  $r$  for pore bodies and calculated for pore throats as discussed in Section 4.1.1. The total hydraulic conductivity for flow between two adjacent bodies is taken as the net conductivity for flow through half of body  $i$ , the connecting throat and half of body  $j$ . The hydraulic conductivity  $g_h$  for each section is calculated using Eq.(4.6)

and the net conductivity for the pore-throat-pore assembly, as shown in Figure 4.2, is found from linear resistor theory:

$$\frac{1}{g_{h,ij}} = \frac{1}{g_{h,bi}} + \frac{1}{g_{h,t}} + \frac{1}{g_{h,bj}} \quad (4.7)$$

Eq.(4.7) is written for each pore in the network to yield a system of linear equations that can be solved in conjunction with the prescribed boundary pressures on each side of the network to give the total flow  $Q$  across the network. Once  $Q$  is known, the permeability of the network can be found from Darcy's law:

$$Q = \frac{KA}{\mu l} (P_{in} - P_{out}) \quad (4.8)$$

where  $K$  is the absolute permeability,  $P_{in}$  and  $P_{out}$  are the inlet and outlet boundary pressures,  $A$  is the area of the pore network normal to the direction of flow calculated as  $X \cdot Y \cdot Lc^2$  and  $l$  is the length of the pore network in the direction of flow calculated as  $Z \cdot Lc$ .  $X$ ,  $Y$  and  $Z$  are the dimensions of the network expressed in terms of the number of pores and  $Lc$  is the lattice constant.

#### 4.1.5.2. Diffusion

The diffusivity of the network is found in the same manner as the fluid flow. Fick's law for diffusion of  $A$  through stagnant  $B$  is:

$$N_A = -\frac{cD_{AB}}{1-x_A} \frac{dx_A}{dl} = \frac{cD_{AB}}{x_B} \frac{dx_B}{dl} = cD_{AB} \frac{d \ln x_B}{dl} \quad (4.9)$$

where  $D_{AB}$  is the binary diffusion coefficient,  $c$  is the molar concentration,  $x_A$  is the mole fraction of species A,  $x_B$  is the mole fraction of species B ( $x_B = 1 - x_A$ ) and  $l$  is the length of the domain. Diffusion of  $A$  through stagnant  $B$  is applicable to fuel cell operation since air is fully humidified, meaning that water vapor does not diffuse and it can be treated as stagnant along with nitrogen. On the basis of Eq.(4.9), the species conservation equation at each network node is then written:

$$n_i = \sum_{j=1}^n g_{d,ij} (\ln x_{B,j} - \ln x_{B,i}) = 0 \quad (4.10)$$

where  $n_i$  is the mass transfer rate through pore  $i$ ,  $x_{B,j}$  is the concentration in the neighboring pore  $j$  and  $x_{B,i}$  is the concentration in pore  $i$ .  $g_d$  is analogous to the hydraulic conductivity and is calculated for a given conduit as:

$$g_d = \frac{cD_{AB}(2r)^2}{L} \quad (4.11)$$

where  $D_{AB}$  is the diffusion coefficient and  $2r$  is the width of the conduit. The conductivity for diffusion through each half-pore and throat is calculated using Eq.(4.11) and the net conductivity for the entire conduit is found from:

$$\frac{1}{g_{d,ij}} = \frac{1}{g_{d,bi}} + \frac{1}{g_{d,t}} + \frac{1}{g_{d,bj}} \quad (4.12)$$

Upon solution of the system of species conservation equations, the effective diffusivity of the network is found using Fick's law:

$$N_A \approx \frac{cD_{eff}A}{l} (\ln x_{B,in} - \ln x_{B,out}) \quad (4.13)$$

where  $D_{eff}$  is the effective diffusivity of the network.  $x_{B,in}$  and  $x_{B,out}$  are the inlet and outlet mole fractions of the stagnant species B.

#### 4.1.5.3. Multiphase Transport

In order to study conditions relevant to PEMFC operation, it is necessary to model the transport of gas and liquid as a function of water saturation in the GDL. This can be done by calculating the water and gas effective permeability and the gas diffusivity after the network has been partially invaded by the non-wetting phase (water) over a range of saturations. The general approach is to modify the conductivity of individual pores and throats as they become invaded by the non-wetting fluid and to recalculate the overall transport through the network. Since a certain amount of wetting phase is always present within pores and throats invaded by the non-wetting phase due to late pore filling effects (Section 4.1.3), careful attention must be paid to this modification, particularly in view of the fact that the precise geometry and connectivity of the remaining wetting phase are unknown. Two limiting cases are considered:

Case 1 – Once a pore is penetrated with the invading fluid (water), the residual wetting phase is no longer conductive. This case represents the most pessimistic scenario for gas transport since it leads to a highly obstructed and disconnected network with increasing invading fluid saturation.

Case 2 – The residual wetting phase within pores and throats invaded by the non-wetting phase maintains a connection with neighboring pores and offers limited conductivity to mass transfer through films and corners, which is modeled by assuming that the area for mass transport varies directly with the volume fraction of the conducting phase in a given pore. This case represents the most favorable scenario for gas transport since it neglects the tortuosity of the pore space containing the residual wetting phase.

In general, for both cases, the expressions for hydraulic and diffusive conductivity (Eq.(4.6) and Eq.(4.11)) become:

$$g_{h,i} = \frac{2.28r_i^4}{2L\mu} (s_p)^m \quad (4.14)$$

and:

$$g_{d,i} = \frac{cD(2r_i)^2}{L} (s_p)^n \quad (4.15)$$

where  $s_p$  is the volume fraction of conducting phase in pore  $i$ . The exponents  $m$  and  $n$  control the behavior of the pore saturation correction and depend on the conducting phase and case of interest. For Case 1,  $m = 2$  and  $n = 1$  for the non-wetting phase, while  $m$  and  $n$  are both equal to infinity for the wetting phase. The latter situation sets the conductivity to 0 for all pores that are invaded ( $s_{wp} < 1$ ) regardless of how much wetting phase remains in the corners. For Case 2,  $m = 2$  and  $n = 1$  for both phases. The values of  $m$  and  $n$  arise from the assumption that the area for transport is proportional to the saturation. Diffusive conductivity is directly proportional to area, therefore  $n = 1$ , while hydraulic conductivity is proportional to the square of the area thus  $m = 2$ .

## 4.1.6. Model Calibration

### 4.1.6.1. Pore and Throat Size Distribution

The first step in the calibration of a pore network model is to identify the pore size distribution that enables the model to match experimentally determined drainage capillary pressure data. The computed drainage capillary pressure curves for SGL 10BA and Toray 090 are compared to previously reported MIP data [123] for the displacement of air by mercury. Figure 4.6 shows a comparison of the experimental data and the model curves obtained, while

Figure 4.7 shows histograms of pore size and throat size distributions used to generate these curves.

The parameters for the Weibull distribution (Eq.(4.1)) obtained by fitting to experimentally observed pore structures are listed in Table 4.1. The mean number-averaged pore diameters for Toray 090 and SGL 10BA obtained from these fit distributions are 19  $\mu\text{m}$  and 33  $\mu\text{m}$ , respectively. These values agree well with the results of Tomadakis and Robertson [209], who calculated pore size distributions and mean pore sizes for solid models of various fiber arrangements and porosities. They also agree with similar data obtained recently by Schulz et al. [150] for simulated Toray 090 and SGL 10BA materials. On the other hand, both of the computed capillary pressure curves shown in Figure 4.6 rise more sharply than the experimental ones due to the use of a rather narrow pore size distribution, which is necessary to match the high porosity. This is discussed further in Section 4.1.6.2.

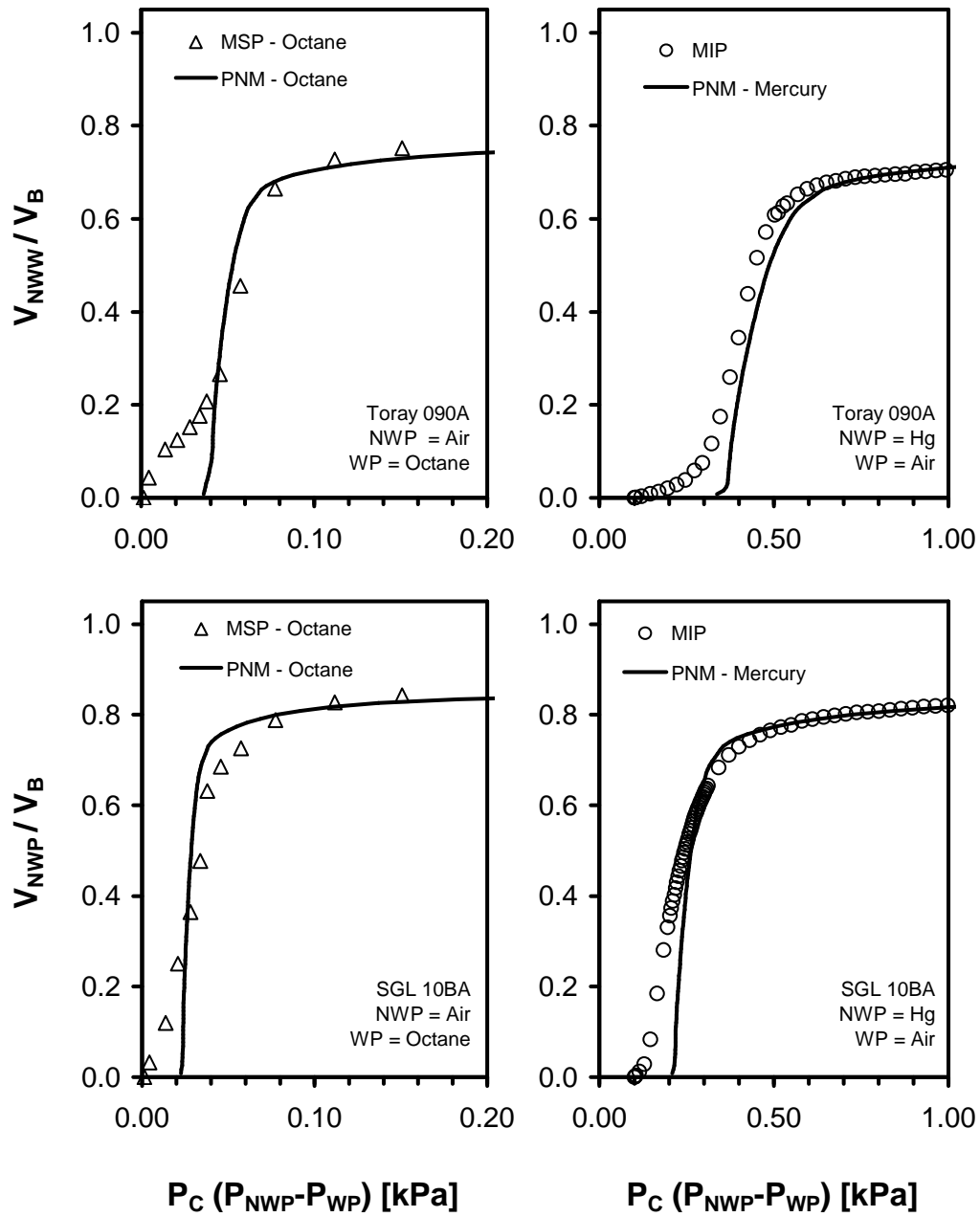
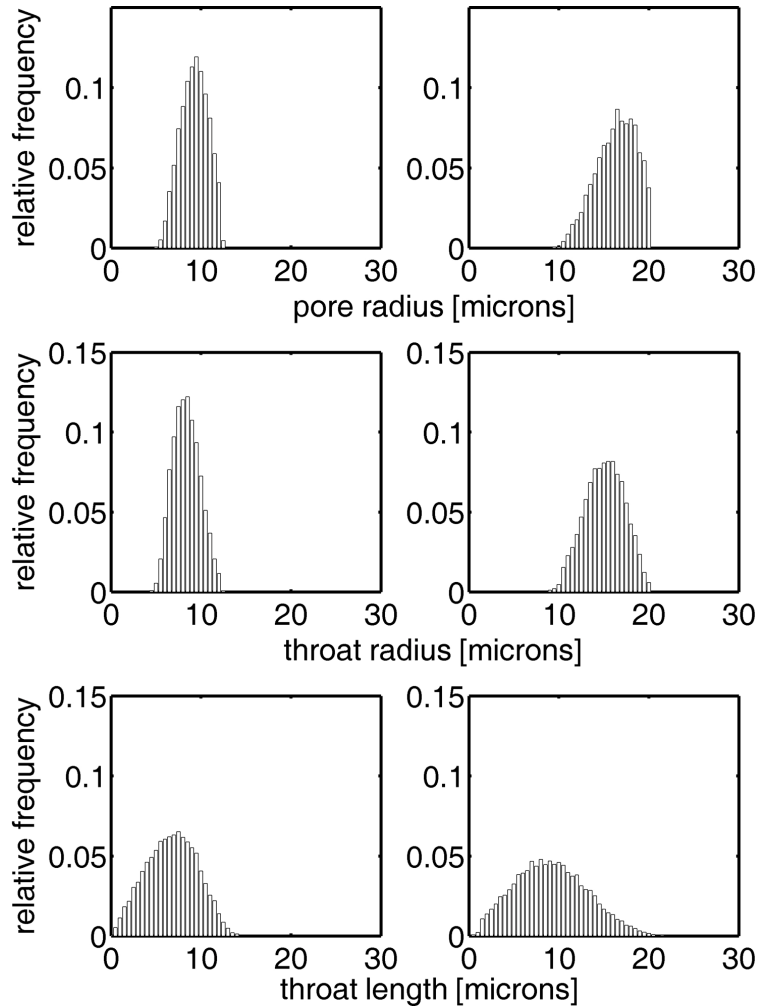


Figure 4.6: Comparison of computed capillary pressure curves with experimental porosimetry data. Top: Toray 090, Bottom: SGL 10BA. Left: MSP with Octane, Right: MIP.



**Figure 4.7: Pore size, throat size and throat length histograms. (left) Toray 090 and (right) SGL10BA.**

To further assess the validity of the capillary pressure curves generated by the model, simulations are also conducted with octane as the wetting fluid and air as the invading fluid. This corresponds to experiments performed using the method of standard porosimetry [123]. The advantage of considering this system is that octane is a highly wetting fluid and its contact angle can be confidently taken equal to  $0^\circ$ . It should be noted that the Weibull distribution parameters in Table 4.1 and obtained above by fitting the model to the MIP data have also been used for the octane-air system. The only parameters that differ are the surface tension and contact angle of octane. The good agreement between the simulated and experimental capillary pressure curves also shown in Figure 4.6 supports the validity of the pore and throat size distributions selected. It is

possible, however, that other pore and throat size distributions than those given in Table 4.1 could also lead to a match between the computed and measured capillary pressure curves. It is necessary to compare model predictions to other experimental results, such as absolute permeability and porosity, to improve confidence in the characterization of the two GDL materials in terms of the distributions given in Table 4.1.

**Table 4.1: Model parameters used for each material**

	Toray 090	SGL 10BA
Network Size Parameters		
$L_C$	25.2 $\mu\text{m}$	40.5 $\mu\text{m}$
Pore Size Distribution Parameters		
$\lambda$	5.25	9
$\kappa$	3	3.5
$r_{min}$	5 $\mu\text{m}$	9 $\mu\text{m}$
$\chi_{max}$	0.95	0.9
Late Pore Filling Parameters		
$s^*$	0.20	0.20
$\eta$	1.00	1.00
Throat Constriction Factors		
$[\alpha_x, \alpha_y, \alpha_z]$	[1, 1, 0.9]	[1, 0.95, 0.95]
Pore Correlation Distances		
$[\beta_x, \beta_y, \beta_z]$	[1, 1, 0]	[2, 1, 0]

#### 4.1.6.2. Lattice Constant

The lattice constant is the distance between pore centers in the cubic lattice. For a given set of pore sizes, adjustment of the lattice constant controls the porosity of the network. For instance, if the lattice constant is large, then the pores are separated by a significant distance, thereby increasing the solid fraction and reducing the porosity. In the present work, the lattice constant is determined in the following manner. First, a pore size distribution is selected. Then an initial guess is made for the lattice constant and corresponding throat volumes (i.e. lengths) determined. This also allows the porosity  $\mathcal{E}$  of the network for a fixed total void volume to be calculated from:

$$\mathcal{E} = \frac{V_{VOID}}{V_{BULK}} = \frac{V_p + V_t}{Lc^3 \cdot X \cdot Y \cdot Z} \quad (4.16)$$

where  $V_p$  is the total pore volume of the network,  $V_t$  is the total throat volume,  $X$ ,  $Y$  and  $Z$  are the dimensions of the network expressed in terms of the number of pores and  $Lc$  is the

lattice constant. The value of  $L_c$  is adjusted until the calculated porosity matches the experimental value for the material. Finally,  $L_c$  is verified to be larger than the largest pore in the network to ensure that no pores overlap. If this criterion is not met, then the pore size distribution is adjusted and the process repeated.

Avoiding pore overlap is necessary to avoid several inconsistencies in the network geometry such as pore volumes being counted twice, throat lengths being negative and the center-to-center distance between pores being larger than  $L_c$ . Also, if pores were allowed to overlap, it would be trivial to match porosity since any pore size distribution will suffice. Allowance for such flexibility in the pore size distribution will also enable a near-perfect matching of the capillary pressure curve since an arbitrarily broad distribution could be used. On the contrary, the requirement that no pores overlap tightly constrains the range of pore size distributions that can be used. For instance, if the pore size distribution is very wide, the network contains many small pores. Since the lattice constant is on the order of the largest pore, these small pores are surrounded by a substantial amount of solid, making it impossible to have a sufficiently high porosity. In the present work, it is necessary to use a pore size distribution that gives a slightly steeper capillary pressure curve than the experimental data in order to match the porosity. The ability to match the porosity, while still achieving a good agreement of the capillary pressure curves, is a strong indicator of the appropriateness of the pore size distributions for such high porosity materials.

The value of  $L_c$  obtained also indicates the appropriateness of the model geometry since  $L_c$  has units of length and represents the spacing between pore centers. The lattice constant for Toray 090 has a value of 25.2  $\mu\text{m}$  and indicates that 11 pores on average span the thickness of the material. SGL 10BA has a lattice constant of 40.5  $\mu\text{m}$  corresponding to 10 pores across its thickness. These values are consistent with information on their structures obtained from SEM images of GDL cross-sections [123].

### 4.1.6.3. Absolute Permeability

The final aspect of the model calibration is to compare the permeability of the network with measured values. This permits verification of pore information such as pore length and connectivity that is not reflected in the capillary pressure curve. It has been experimentally observed [161] that the in-plane permeability is higher than the through-plane permeability, a result that has been verified numerically [188] and analytically [159]. Spatial correlation of pore sizes is included in the network in combination with slight throat constrictions in order to reproduce the observed anisotropy in the model. Measurements of Toray 090 indicate that the in-plane permeability is about 1.5 – 2 times higher than that in the through-plane direction. Spatial correlation distances  $[\beta_x, \beta_y, \beta_z] = [1, 1, 0]$  and throat constriction factors  $[\alpha_x, \alpha_y, \alpha_z] = [1, 1, 0.9]$  have been used in order to fully match the permeability data. This procedure reproduces the anisotropy and gives good agreement between experimental data and model results, as can be seen in Table 4.2. The anisotropy of SGL 10BA is somewhat more complicated due to the alignment of fibers, which causes the permeability to differ from one in-plane direction to the other. To capture this, correlation distances  $[\beta_x, \beta_y, \beta_z] = [2, 1, 0]$  are used along with throat constriction factors  $[\alpha_x, \alpha_y, \alpha_z] = [1, 0.95, 0.95]$ .

**Table 4.2: Transport results for each modeled material**

Permeability ( $\times 10^{12} \text{ m}^2$ )	Toray 090		SGL 10BA	
	Experimental [161]	Model	Experimental [161]	Model
$K_x$	15	14	57	54
$K_y$	15	14	45	48
$K_z$	9.0	9.5	37	39
Effective Diffusivity	Numerical [188]	Model	Numerical [188]	Model
$D_{eff,x}$	0.67	0.54	0.78	0.64
$D_{eff,y}$	0.67	0.54	0.75	0.61
$D_{eff,z}$	0.62	0.46	0.75	0.58

### 4.1.7. Model Validation

#### 4.1.7.1. Effective Diffusivity

Determination of the effective diffusivity of the network provides a useful means of independently verifying the chosen network geometry. Although experimental data for

diffusion through GDLs are not yet available, limited numerical results have been presented by Tomadakis and Sotirichos [188] for fibrous materials with various arrangements of fiber alignment that correspond to GDL materials. The effective diffusivities predicted by the present model are compared with those of Tomadakis and Sotirichos [188] in Table 4.2. The model under-predicts the effective diffusivity estimates of Tomadakis and Sotirichos by about 20%, which is reasonable considering that no efforts were made to fit the model to their predictions.

#### **4.1.7.2. Liquid Water Injection**

Experiments have been performed by Benziger *et al.* [124] to measure the breakthrough pressure of liquid water in GDLs. In these experiments, the static pressure of a column of liquid water above a GDL is increased until liquid penetrates the sample. The pressure required for water breakthrough on various samples has been reported, including a sample of Toray 120 with no PTFE treatment. This material is thicker than the Toray 090 considered here, but otherwise similar in structure. An experimental value of 3300 Pa was found, which compares with a value of 2483 Pa predicted by the present model. These values are within 25% of each other, which is reasonable considering that the materials are not necessarily identical. The reasonable agreement between the model and data suggest that the contact angle used for water on Toray 090 is reasonably correct. Similar data are not available for SGL 10BA.

## 5. Results and Discussion

### 5.1. Porosimetry

In this section, capillary pressure curves obtained by mercury intrusion porosimetry (MIP), the method of standard porosimetry (MSP) and gas controlled porosimetry (GCP) are presented for various GDL materials. As discussed previously, MIP is insensitive to surface chemistry and so only provides structural information. The GCP method developed in the course of the present work uses water as the working fluid and so directly measures the air-water capillary pressure curves and the effect of hydrophobic polymer additions. As indicated earlier, the MSP technique is of limited use, particularly with the advent of the GCP technique, but some results are presented for comparison. Toray and SGL 10 materials are tested over a range of hydrophobic polymer loadings from 0% to 30%. Toray GDLs consist of straight rigid fibers, while SGL 10 series samples are made from curved intertwined fibers. The Toray materials are available in a range of thicknesses from 200  $\mu\text{m}$  to 400  $\mu\text{m}$ . Thus, testing of these materials permits the effects of GDL thickness, structure and surface treatment to be investigated. In addition to the parametric analysis of GDLs, experiments have been conducted on single layer samples as well as multi-layer stacks. This allows the investigation of surface effects on the capillary properties of the bulk materials, which are significant for thin GDLs. These tests will be supported by a variation of the GCP method to allow for single point injection. Finally, the GCP setup is adapted to measure breakthrough pressure and saturation at breakthrough. This is important information since it bears directly on actual fuel cell operation.

#### 5.1.1. Mercury Intrusion Porosimetry

Figure 5.1 and Figure 5.2 show MIP intrusion and extrusion curves for SGL 10 and Toray 090 GDLs, respectively. Each experiment has been extended until a capillary pressure of 350 kPa is reached, although only the portion up to the point where the saturation has leveled off is included in the plots for clarity. The curves in Figures 5.1 and 5.2 have been obtained on single GDL layers to reveal the surface effects. Figure 5.1 shows the

results for SGL 10 with 0%, 5% and 20% PTFE content and indicates little difference between these curves. A slight shift of the curves to higher capillary pressures as the PTFE loading increases could be attributed to a slight constriction of pores by the PTFE coating. The amount of actual pore constriction is not likely significant however, since the addition of 20% PTFE only reduces the porosity from 90% to 86% for the SGL materials shown in Figure 5.1. Apparently, the addition of a PTFE coating does not significantly alter the GDL physical structure.

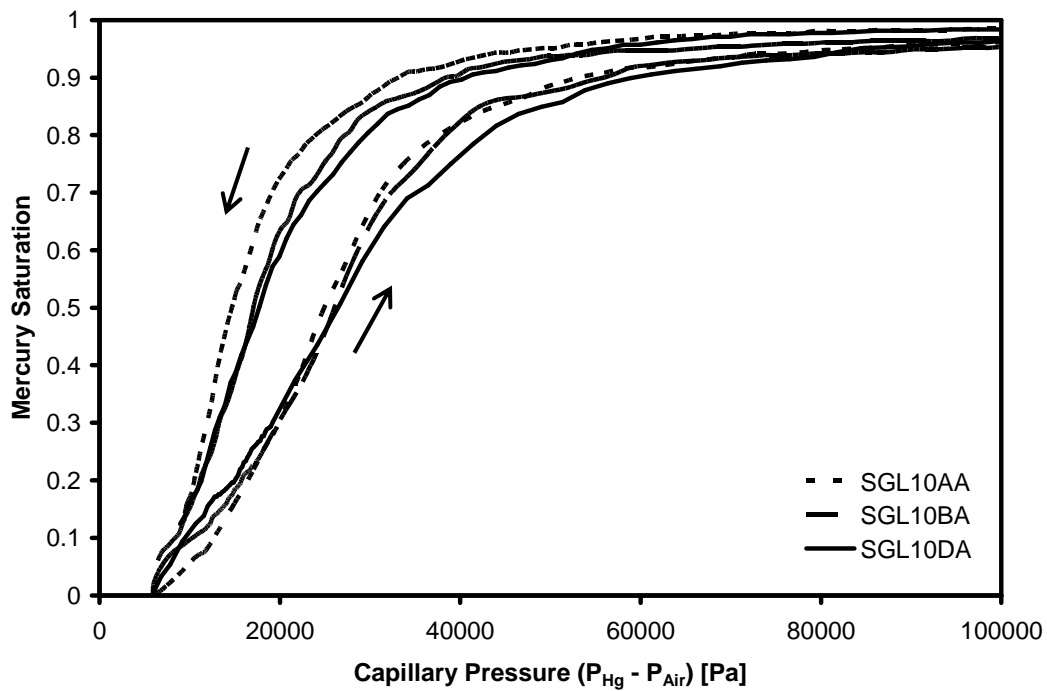


**Figure 5.1:** MIP intrusion curves for SGL 10 series GDLs. 10AA = 0% PTFE, 10BA = 5% PTFE and 10DA = 20% PTFE.

The MIP curves for Toray 090 with 0%, 10% and 20% PTFE content are shown in Figure 5.2. The intrusion curves are very similar for each PTFE content; moreover, the shift to higher capillary pressures does not follow the order of increasing PTFE content. As with the SGL 10 samples, the addition of PTFE appears to have no effect on the mercury intrusion curve. On the other hand, the extrusion curves show dramatic differences depending on PTFE content, particularly between those samples containing PTFE (090C and 090D) and the one without any PTFE (090A). Since the addition of the PTFE has

little effect on the structure of the GDL, as suggested by the similarity in the intrusion curves, the difference in the extrusion curves must be caused by an alternative effect. Although PTFE treatment does not alter the pore sizes of the GDLs significantly, PTFE does impart a certain amount of roughness to the solid surfaces. Furthermore, the SGL 10 samples also contain a significant amount of carbonaceous binder which adds some surface roughness. Thus, these GDL materials will have a certain degree of roughness even in the absence of PTFE. Although the difference is presumably due to roughness, it is unclear why this effect appears during the retraction step only. According to the Wenzel equation (Eq.(2.9)), surface roughness makes mercury more non-wetting and leads to a high retraction pressure, but this effect should also be observed during injection.

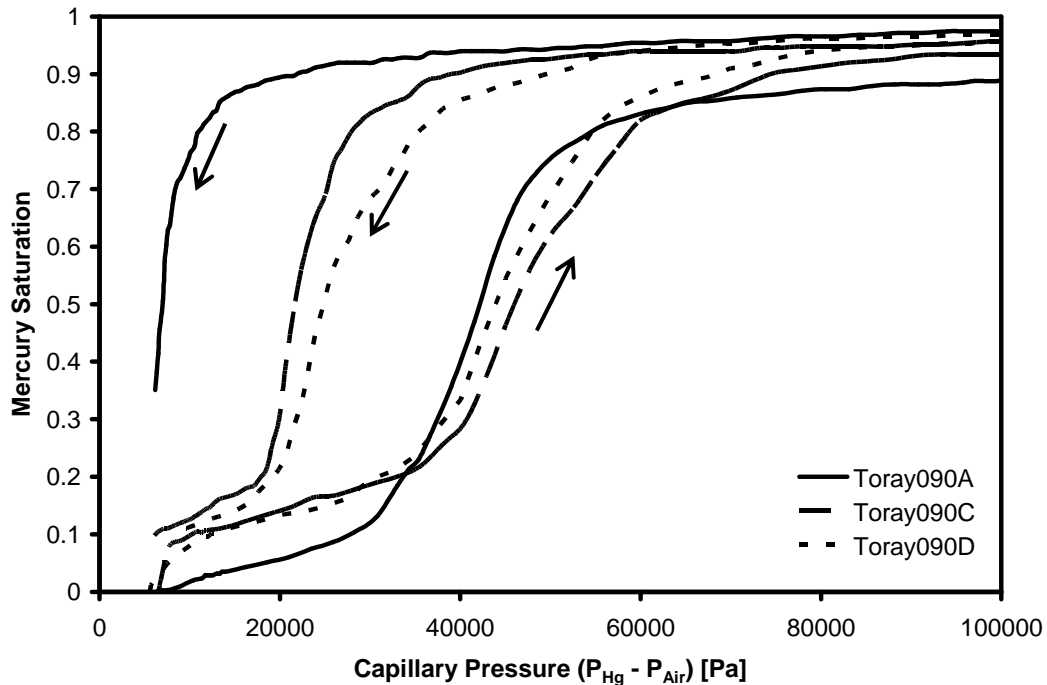


Figure 5.2: MIP intrusion curves for Toray 090 series GDLs

### 5.1.2. Method of Standard Porosimetry

MSP tests have been performed with both octane and water as the wetting fluids on Toray 090A and SGL 10BA to yield the capillary pressure curves shown in Figure 5.3 and Figure 5.4, respectively. In order to compare the MSP-octane and MSP-water curves, it

is necessary to plot the data with a common capillary pressure axis. In these figures, the octane-air capillary pressure data are converted to an equivalent water-air capillary pressure. Note that the capillary pressure is defined as the difference between the non-wetting phase and wetting phase pressures.

Conversion of capillary pressures from one set of fluids to another requires the assumption that the Young-Laplace equation is a valid expression for the dependence of the capillary pressure on pore size in the material. If so, the capillary pressure required for fluid 1 to displace fluid 2 from a pore of size  $r$  is:

$$P_{C,1-2} = \frac{-2\sigma_{1-2} \cos(\theta_{1-2})}{r} \quad (5.1)$$

where the subscript 1-2 refers to the properties pertaining to the displacement of fluid 2 by fluid 1. Similarly, the capillary pressure for fluid 3 to displace fluid 4 from the *same sized pore* is:

$$P_{C,3-4} = \frac{-2\sigma_{3-4} \cos(\theta_{3-4})}{r} \quad (5.2)$$

Eq.(5.1) and Eq.(5.2) can be solved for  $r$  and equated to yield the following formula for the relationship between the capillary pressures for the two sets of fluid pairs:

$$P_{C,3-4} = \frac{\sigma_{3-4} \cos(\theta_{3-4})}{\sigma_{1-2} \cos(\theta_{1-2})} P_{C,1-2} \quad (5.3)$$

Eq.(5.3) is used to convert the MSP-octane data to an equivalent water-air capillary pressure. This requires knowledge of the surface tensions of the water-air and octane-air interfaces as well as the corresponding contact angles. Since octane strongly wets the GDL, its contact angle can be confidently taken as  $0^\circ$ . The contact angle of water on GDLs is not well known, but estimates have been made in the present work using the sessile drop method and corrected for porosity and roughness effects, as described in Section 3.5.

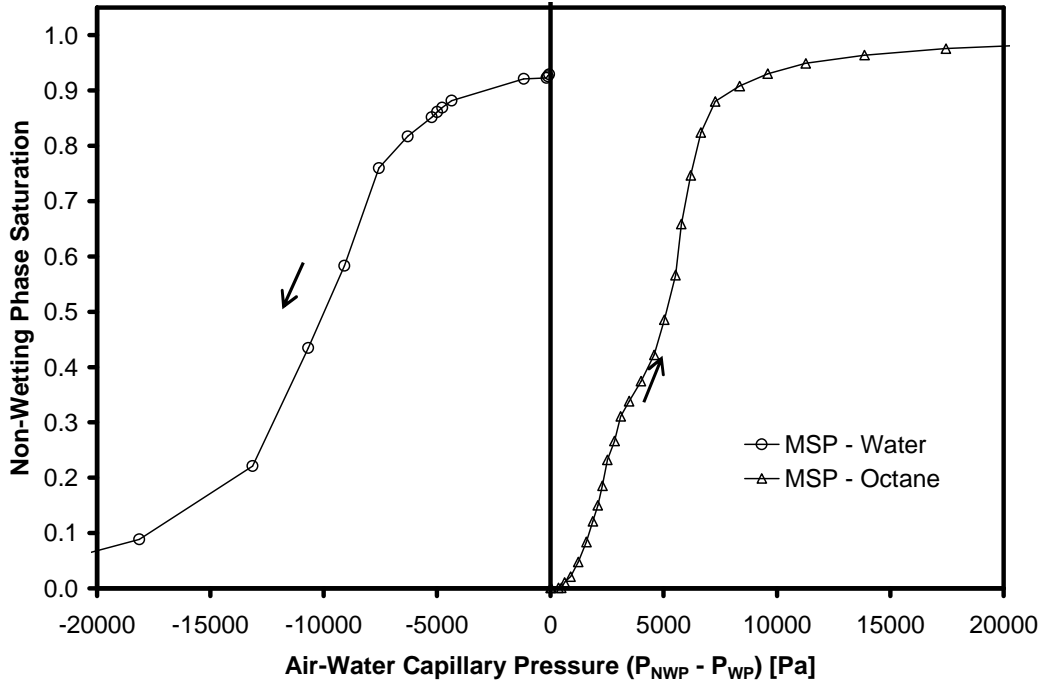


Figure 5.3: MSP - Water and MSP - Octane for Toray 090A.

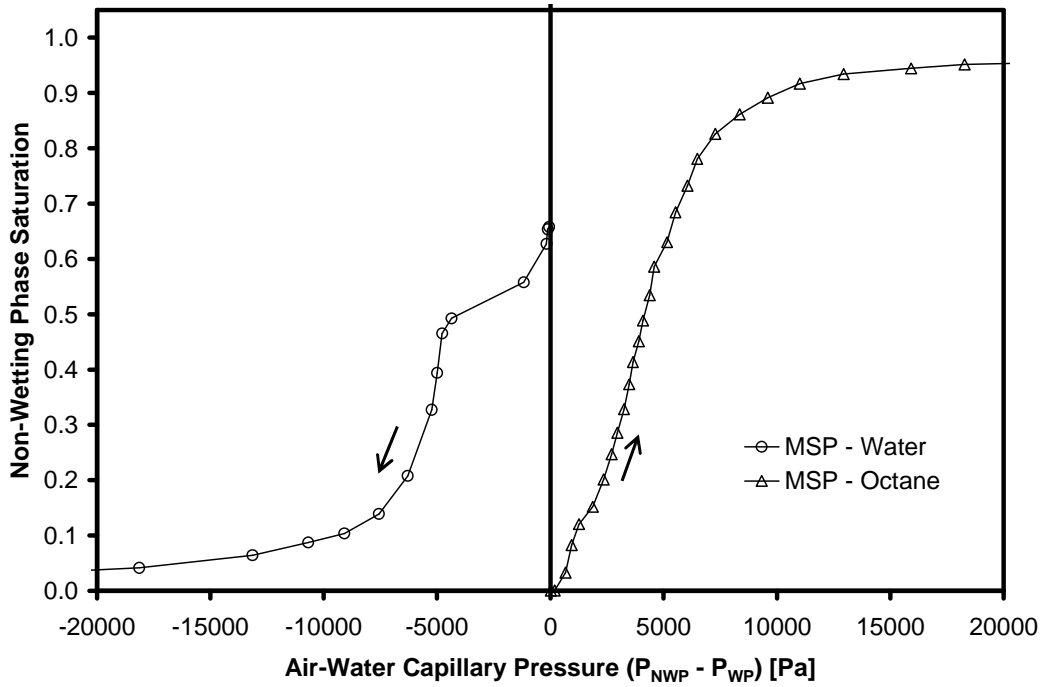


Figure 5.4: MSP - Water and MSP - Octane for SGL 10BA.

Interpretation of the MSP-octane data is straightforward since octane is a highly wetting fluid on all surfaces. The evaporation of octane and its replacement with air corresponds to the injection of a highly non-wetting phase (air) as capillary pressure is increased ( $P_C = P_{NWP} - P_W$ ). This corresponds directly to the intrusion curves obtained using MIP shown in Figure 5.1 and Figure 5.2 where non-wetting phase saturation increases with increasing capillary pressure.

The MSP-water data are also shown in Figure 5.3 and Figure 5.4. These curves are plotted with water as the non-wetting fluid. This has been done based on the findings of the GCP method discussed in the next section and also suggested by the results of Fairweather *et al.* [20]. Since water is a non-wetting phase, its injection into the GDL requires a positive capillary pressure. Upon withdrawal, however, negative capillary pressure is required to remove water. Since MSP experiments using water are analogous to the withdrawal of water from the GDL, the MSP-water data are plotted with water saturation decreasing in the negative capillary pressure direction. A plot of the data in this manner makes the MSP results directly comparable to the GCP results presented in the next section.

The results of the MSP-water experiments are difficult to interpret. The premise of the MSP-water technique is that in a sample with mixed wettability, water will spontaneously eject from the hydrophobic pores when the sample is exposed to atmospheric pressure after the initial flooding procedure. In such a case, the sample will contain some air-filled pores at the start of the test (i.e. at  $P_C = 0$ ) which corresponds to the hydrophobic pore volume of the sample. Furthermore, the resulting capillary pressure curve should reflect the drainage of water from the network of hydrophilic pores only. This technique would seem to be well suited for the gas diffusion layer, which possesses a fractional wettability due to the presence of graphite fibers and PTFE coating. There are two problems with this concept, however. The first is the premise that water will spontaneously eject from hydrophobic pores. With a contact angle of  $\theta_{W-AIR} = 110^\circ$  [119], PTFE is only slightly hydrophobic. Since it is known that a wetting fluid will not imbibe into a material if  $\theta_{WP} < 50^\circ$  [210], one would not expect air to imbibe into a mildly hydrophobic material such

as air on PTFE ( $\theta_{AIR-WATER-PTFE} = 70^\circ$ ). For this reason, the spontaneous ejection of water from, or the spontaneous imbibition of air into, PTFE pores in a GDL should not be expected. Nonetheless, the MSP-water results show this effect. The Toray 090A sample with no PTFE exhibits a small amount of air imbibition whereas the SGL 10BA sample with 5wt% PTFE displays significant air imbibition at  $P_C = 0$ . Although this agrees with the concept of hydrophobic pores, it is not consistent with other experimental evidence [20,151] or the extent of the hydrophobicity of the so-called hydrophobic pores. The second complication concerning the interpretation of the MSP-water data is that the concept of hydrophilic and hydrophobic pores is overly simplistic. PTFE is not neatly segregated to be present in some pores and totally absent in others. A more realistic picture is that most pores contain mostly carbon fiber walls with some patches of PTFE, which alters the capillary properties of a pore partially. The effect that the hydrophobicity distributed in this fashion might have on the MSP-water technique is not known, but it is at odds with the conceptual basis of the method.

Furthermore, the MSP-water data show that water removal requires significantly larger capillary pressures than octane removal even after the effect of surface tension differences is considered by conversion to a common air-water capillary pressure basis. This is not consistent with the knowledge that octane is clearly a much more wetting fluid with a far lower contact angle than air-water and so should require higher pressure to displace. This apparent anomalous behavior could be caused by the fact that evaporation of water is not necessarily equivalent to the drainage of water. During drying, any water that becomes disconnected from the other portions of the fluid is still able to leave the sample via the gas phase. Furthermore, drying a material with intermediate wettability is expected to lead to significant disconnection of the liquid phase volume [211]. In a highly wettable material, liquid films on the pore walls provide liquid conductivity throughout the media and allow clusters to exchange fluid and remain in capillary equilibrium. Such films do not exist in materials with intermediate wettability such as GDLs.

Overall, the MSP method is not satisfactory. The results provided by MSP-octane

experiments are reasonable but can be easily obtained using the more accepted and widespread MIP method. The data given by the MSP-water technique shows several anomalies that call into question the validity of the method, particularly for materials that are neither strongly wetted by water or air such as GDLs. The limitations of the MSP-water technique and the uncertainty of the results on GDLs has prompted the development of the gas controlled porosimetry (GCP) method to measure air-water capillary properties of GDLs directly.

### 5.1.3. Gas Controlled Porosimetry

The GCP method developed as the major part of this thesis project offers the ability to directly measure air-water capillary curves of GDLs and enables the observation of GDL wetting properties and the effect of hydrophobic treatments. This versatile method tests both water injection and withdrawal and can scan a wide spectrum of capillary pressures ( $P_{C,MIN} < 0 < P_{C,MAX}$ ). A typical capillary pressure curve obtained using GCP is shown in Figure 5.5 with important features labeled and described below.

The test begins at Point 1 with a completely dry GDL and the system held at a negative capillary pressure. This starting condition not only allows for the study of water injection into fully dry GDLs, but also enables accurate water saturation tracking since the initial condition of the GDL is well known. The ability to start with a completely dry sample is one of the unique features of this setup. From Point 1, the capillary pressure is increased stepwise but the saturation of the GDL remains at zero until Point 2 is reached where some water begins to penetrate into the dry GDL. The main leg of water injection occurs at positive capillary pressures (Point 3), indicating that GDLs are hydrophobic since water must be forced into the sample. At about 10000 Pa, the water saturation begins to level off to a plateau (Point 4), indicating that the pores of the GDL are mostly filled with water. After scanning the capillary pressure far enough along the plateau in water saturation to ensure full saturation is achieved, the direction of pressure scanning is reversed (Point 5). As capillary pressure is relieved towards zero, the water saturation remains completely stable. Not until a negative capillary pressure is applied does water

begin to retract from the sample (Point 6). Contrary to the injection leg of the test (Point 3), this behavior indicates that GDLs are hydrophilic since water must be forced from the sample. Water retraction begins to level off at about -10000 Pa (Point 7) and a non-zero water saturation remains in the sample even at very negative capillary pressures (Point 8). After reversing the pressure scanning direction once again to reinject water, a long plateau in saturation is observed. At about -2500 Pa, a noticeable amount of water is imbibed into the sample (Point 9). This imbibition is not observed during the initial water injection, suggesting that either the presence of residual water in the GDL aids the reintroduction of water or the contact with water has somehow altered the solid wettability [130]. The second water injection leg (Point 10) is also altered by the previous water injection since it does not coincide with the initial injection. The secondary water injection rises to a full saturation plateau much more sharply than observed during the initial injection (Point 11). This would be the case if small crevices and surface roughness features remain filled with water from the initial injection. Subsequent water withdrawal exactly follows the initial water withdrawal and all subsequent water injections correspond to the secondary injection. Fairweather *et al.*[20] also reported this highly repeatable behavior, although they were unable to obtain the initial water injection into a dry GDL with their method. Also shown in Figure 5.5 is an internal scanning loop marked by Point 12. This loop is started by reversing the direction of pressure change before the sample has reached full saturation. In this case, the sample reaches a saturation of about 65% when the scan direction is reversed. Finally, Point 13 marks a data point obtained by weighing the sample at the completion of the test. This demonstrates that the saturation is being accurately tracked during the course of the run.

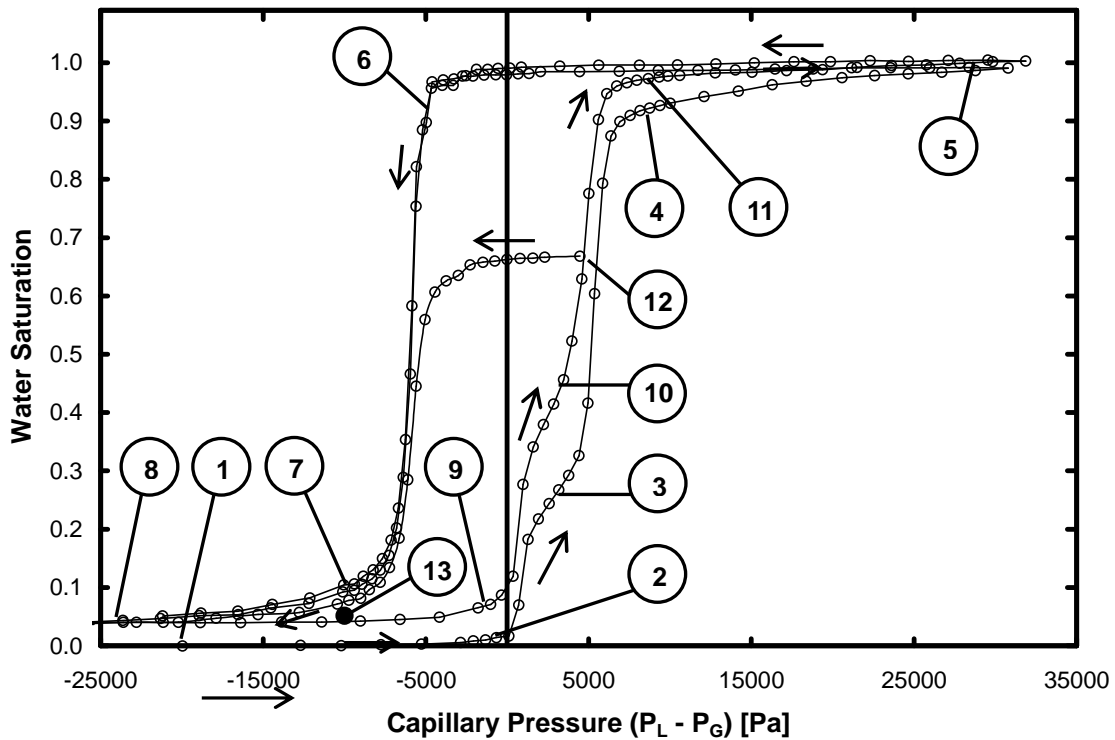


**Figure 5.5:** Typical capillary pressure curve obtained using the GCP method. Toray 090A (no PTFE). Arrows indicate the direction of capillary pressure increments.

### 5.1.3.1. Comparison of GCP with Literature Data

In Figure 5.6 the capillary pressure curve values obtained by the GCP method are compared with the results reported in the literature based on other methods. The data shown are all for Toray 090 with no hydrophobic polymer coating (same as shown in Figure 5.5). The wide scatter of the data is apparent.

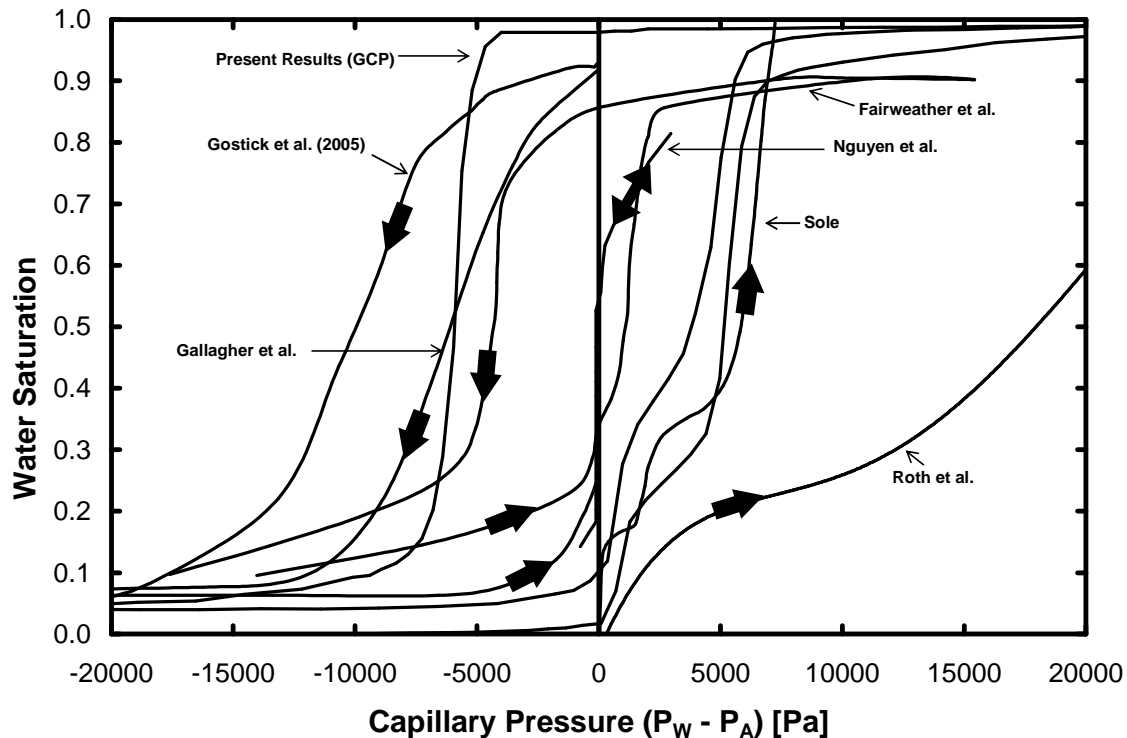


Figure 5.6: Comparison of various experimental air-water capillary pressure curves on Toray 90 or similar GDL with no PTFE except for the data of Roth *et al.* who used a GDL with 7% PTFE.

The injection curve of Sole [22] compares favorably to the initial injection curve obtained in the present study. The slightly higher injection pressures found by Sole [22] can be attributed to non-equilibrium effects caused by the continuous volume displacement method. The smaller shoulder in his low pressure data is likely an artifact caused by the method used to prime the system, which involves injecting water from below the sample until it touches the GDL, signaling the beginning of the curve. Determination of the precise moment of contact and ensuring the entire water surface contacts the GDL simultaneously are difficult to achieve, however. Furthermore, the curve reported by Sole does not display a saturation plateau at high pressure, which is clearly anomalous. More anomalous are the results of Nguyen *et al.* [21], visible near the  $P_C = 0$  region, which are in strong disagreement with all other reported data. In principle, their method is sound but the large saturation swings occurring over a narrow pressure range near  $P_C = 0$  are inexplicable and suggest problems with sample mounting and the existence of large gaps and spaces in the system. Gallagher *et al.* [23] investigated drainage of water from a wet

GDL and re-imbibition into a previously wet GDL. Their results are in qualitative agreement with those of the GCP method of the present study although some quantitative differences exist. They determined saturation by weighing the GDL to determine water uptake. It is difficult to ensure the GDL is free of extraneous water droplets without disturbing the water in the GDL. Roth *et al.* [24] avoided this problem by weighing the sample while under water and correcting for the various buoyancy forces. Nonetheless, the results of Roth *et al.* [24] show anomalously high water entry pressures. Their method does not allow for gas displacement as water invades, which means that gas becomes pressurized by the invading water, leading to lower than expected capillary pressures and shifting their data to higher pressures. Therefore they may have assigned the measured saturation values to erroneously high capillary pressures. The data of Gostick *et al.* [123] using the MSP method show water withdrawal occurring at much more negative capillary pressures than the other methods. The MSP technique begins with a fully saturated sample which is obtained by vacuum filling. This leads to a complete absence of air in the sample and virtually assures that water is in the Wenzel state, which is characterized by very high contact angle hysteresis. Fairweather *et al.* [20] report both water injection and withdrawal curves. Their injection curve corresponds to the secondary injection data from the GCP method. Qualitative agreement is seen with GCP, but both injection and withdrawal legs are closer to  $P_C = 0$  in the data of Fairweather *et al.* A close look at their data analysis reveals some errors that explain the observed discrepancies. Their raw data consist of pressure traces which rise during periods of water injection, then decay slightly when injection is paused. They wait for the pressure decay to stabilize before initiating the next water injection, citing this as capillary equilibrium. The problem with their analysis is that this pressure decay is caused by fluid redistribution within the pore space that becomes accessible at the peak pressure, yet they assign the volume to the plateau pressure. This mistaken assignment of pressure tends to shift both the water injection and withdrawal curves towards  $P_C = 0$ . Overall, the GCP method gives values that are well within the range obtained by the various other methods.

### 5.1.3.2. Comparison Between MIP, MSP and GCP

It is possible to compare the capillary pressure curves obtained by MIP, MSP and GCP directly. The intrusion of mercury in MIP, the evaporation of octane (i.e. the invasion of air) in MSP-octane and the injection of water in GCP should theoretically match since they all correspond to drainage of a wetting phase. The difficult part about comparing capillary data from different methods is converting the capillary pressure axis to that of a common fluid system. For the following comparisons, all data are converted to equivalent air-water capillary pressures. Obviously the MSP-water and GCP data require no conversion since they are measured in the air-water system. The conversion of the MSP-octane data is described in Section 5.1.2. The conversion of MIP data follows the same procedure. A sessile drop of mercury is placed on the GDL surface and the measured contact angle is corrected using the combined Wenzel-Cassie-Baxter equation to obtain an effective contact angle. The converted capillary pressure data for Toray 090A and SGL 10 BA are shown in Figure 5.7 and 5.8, respectively.

The agreement between the non-wetting phase injection experiments is very good. All curves coincide and show the same qualitative features. This is not unexpected for the Toray 090A data since only one material (graphite) is present. Since the SGL 10BA sample contains 5% PTFE loading, it is somewhat surprising that the GCP curves do not show some differences due to its mixed wettability to water but not octane or mercury. This suggests that the effect of PTFE addition is small. The water withdrawal curves do not show such agreement. The discrepancies between the MSP-water and GCP curves are large. However, since the MSP-water technique has some deficiencies, as discussed above, this is not unexpected. Qualitatively, the GCP results for water withdrawal are similar to the injection curves, which is to be expected since the material is the same.

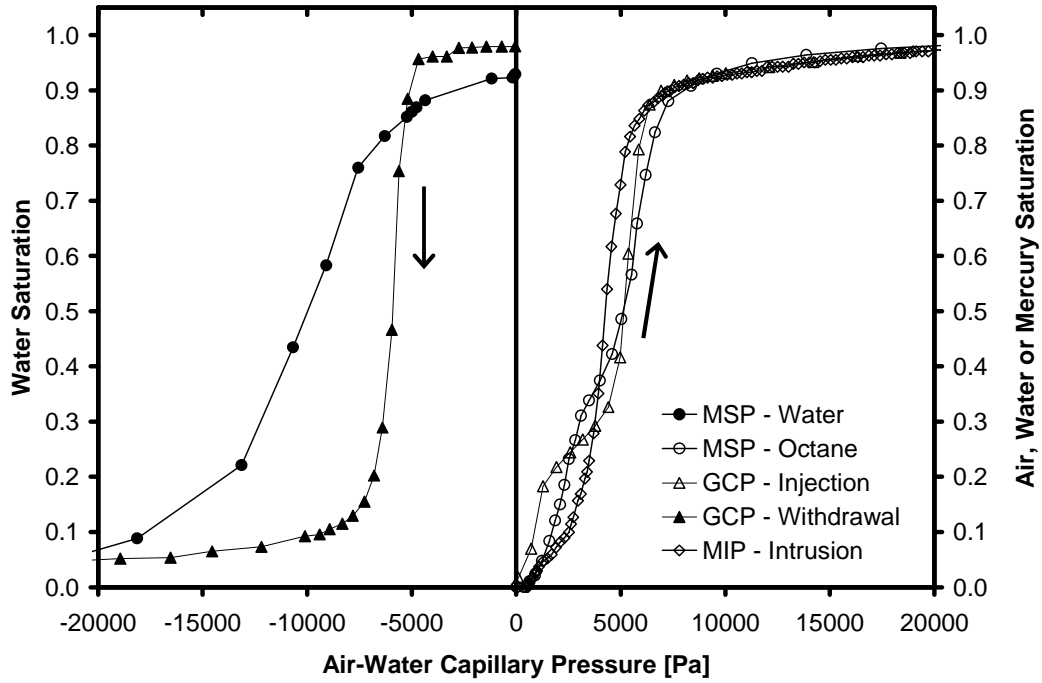


Figure 5.7: Comparison between MSP, MIP and GCP for Toray 090A

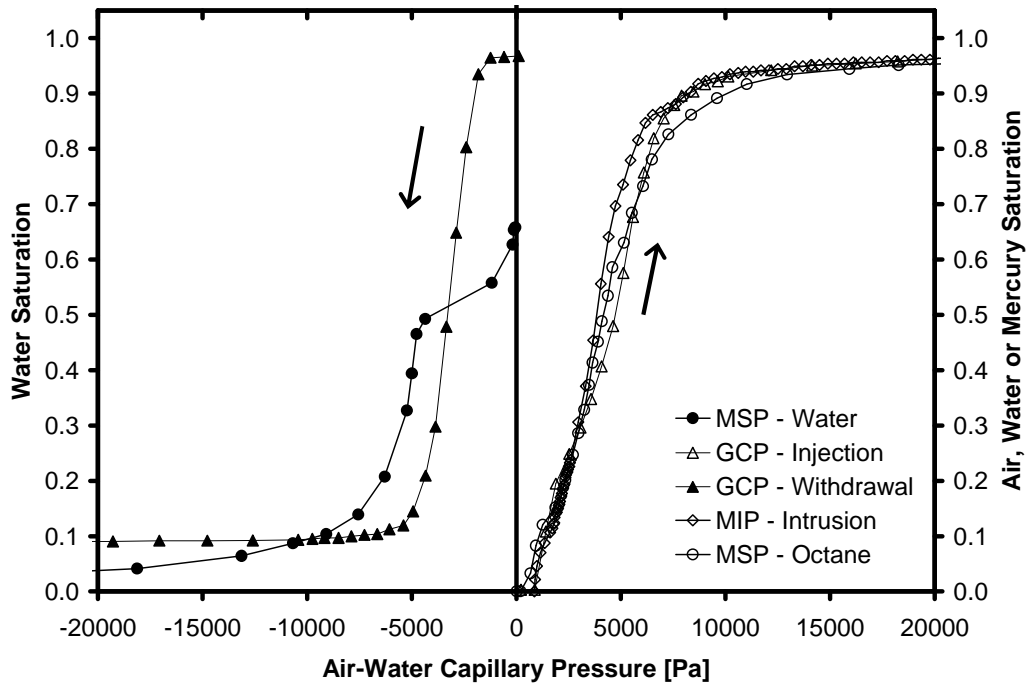


Figure 5.8: Comparison between MSP, MIP and GCP capillary pressure curves for SGL 10BA

The agreement between the GCP water injection data and the data from the well established MIP method serve to validate the newly developed GCP technique. Overall the GCP method provides very satisfactory results.

### 5.1.3.3. Effect of PTFE on Air-Water Capillary Curves

The GCP method has been developed to study the air-water capillary properties of gas diffusion layers. The primary aim of this tool is to measure the effect of hydrophobic polymer addition on the wettability and capillary properties of GDLs. To this end, a variety of different materials with a range of PTFE contents is tested. The PTFE coatings were applied by the manufacturer or distributor and tests were run on these samples in their as-received form. Specific details of each material are listed in Table 3.1.

Figure 5.9 shows GCP curves obtained on Toray 090 with no PTFE (top) and 20% PTFE (bottom). The curves for each sample are strikingly similar, which is surprising given that one samples has no PTFE coating (090A, top) while the other has a rather high loading of 20wt% (090D, bottom). The initial injection of water into the dry 090A sample requires positive capillary pressure despite the fact that the pure graphite substrate is supposedly hydrophilic. This highlights the importance of structural and physical effects on observed wettability as opposed to chemical heterogeneity. Water injection into both samples begins at the same capillary pressure ( $\approx 750$  Pa).

Once water injection begins, the saturation rises sharply to a small plateau before the main injection leg. This feature is due to surface effects caused by the finite size of the sample. The main leg of the water injection occurs at noticeably different capillary pressure for the two samples. For Toray 090A, the rise begins about  $P_C \approx 4000$  Pa, while for Toray 090D the rise is delayed until  $P_C \approx 6000$  Pa. This offset represents a 50% increase and can be attributed to the hydrophobic effects of the PTFE coating since the MIP data show very little structural difference between the materials. As capillary pressure is increased, the water saturations of both samples reach a plateau indicating that the pore volume is filled. Upon reduction of the capillary pressure, the water saturation

remains unchanged until a significantly negative capillary pressure is applied. Water retraction begins abruptly at  $P_C \approx -5000$  Pa for Toray 090A and  $P_C \approx -2000$  for Toray 090D. The presence of PTFE in the Toray 090D sample does not dramatically alter the wettability of the sample, but merely shifts the curve to more positive pressures.

Similar behavior is observed in the SGL 10 series of materials. Capillary pressure curves for SGL 10AA (0wt% PTFE) and SGL 10BA (5wt% PTFE) are shown in Figure 5.10. The SGL 10 series materials are structurally quite different than Toray 090. They are significantly more porous (90% vs. 78%), thicker (400  $\mu\text{m}$  vs. 300  $\mu\text{m}$ ) and have much larger pores (40  $\mu\text{m}$  vs. 20  $\mu\text{m}$ ). The effect of the large pore size can be immediately seen from the position of the main injection and withdrawal legs which both occur much closer to zero pressure for SGL 10 since large pores are more easily penetrated. Even the addition of PTFE to SGL 10BA does not increase the pressure of its injection leg above that of the untreated Toray 090A. The shoulder arising from surface effects is also smaller, which is expected since the SGL 10 materials are thicker and more porous, thus the volume accessible from the surface is a smaller proportion of the total amount. The effect of the PTFE coating in the SGL 10 materials is similar to that observed for Toray 090 materials. The addition of PTFE increases the main injection leg from  $P_C \approx 2000$  Pa for SGL 10AA to  $P_C \approx 4000$  Pa for SGL 10BA. Similarly, the addition of PTFE shifts the onset pressure for withdrawal from  $P_C \approx -2500$  Pa to  $P_C \approx -1800$  Pa.

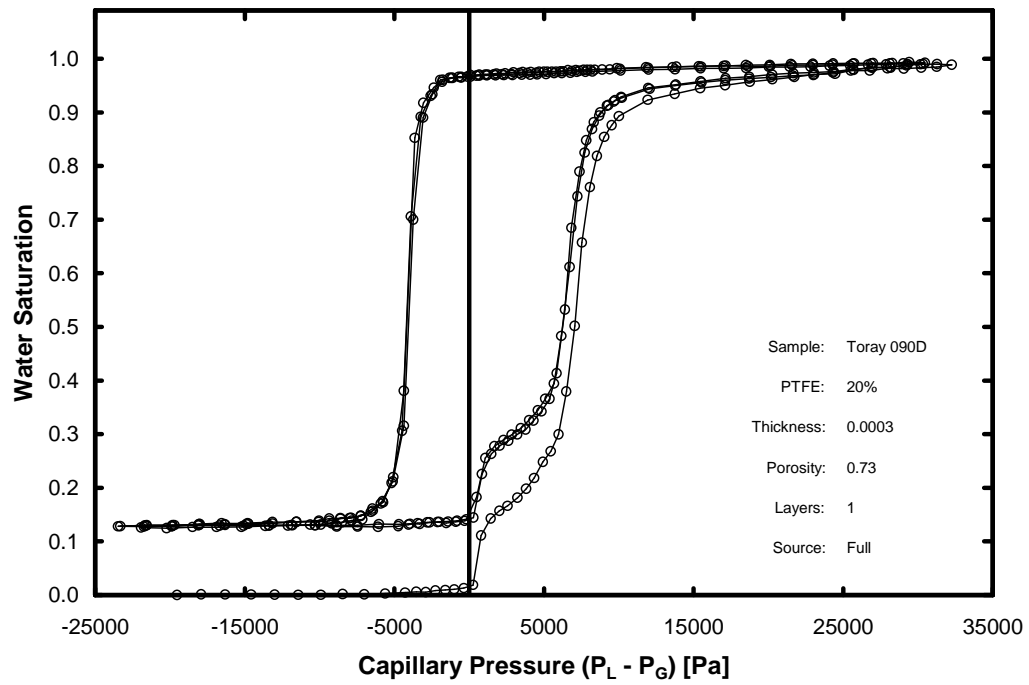
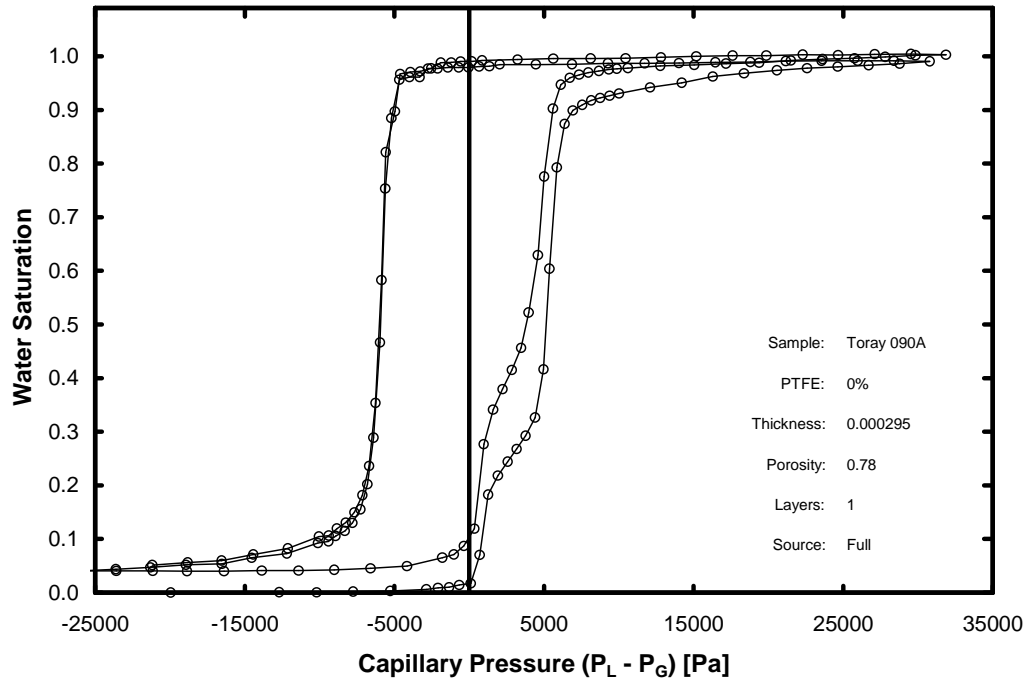


Figure 5.9: Air-water capillary pressure curve for Toray 090A (top) 090D (bottom) obtained by GCP

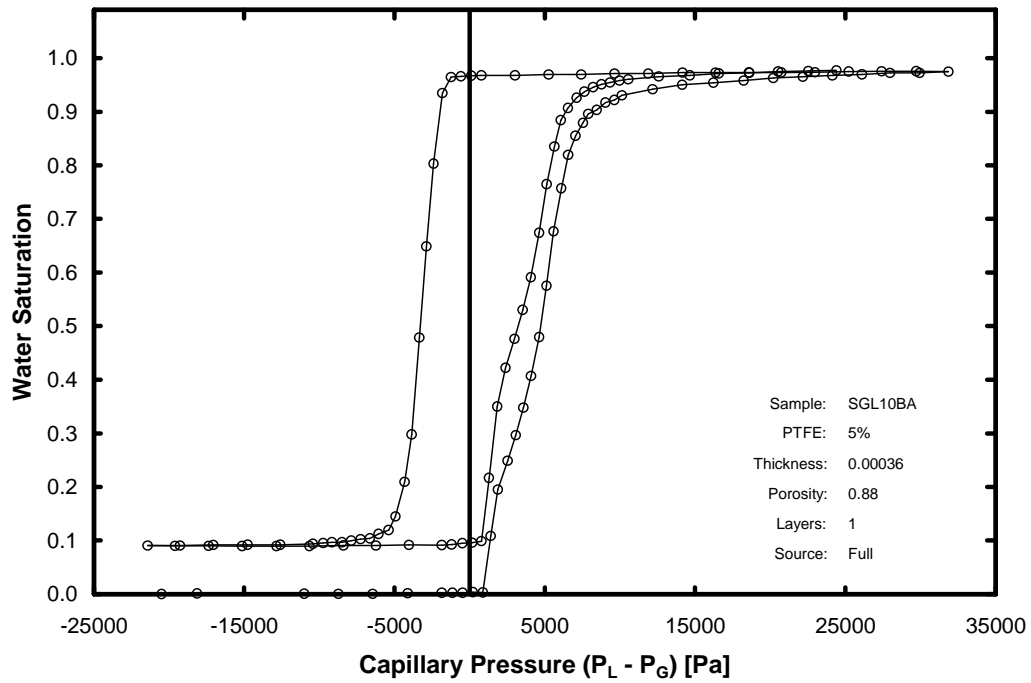
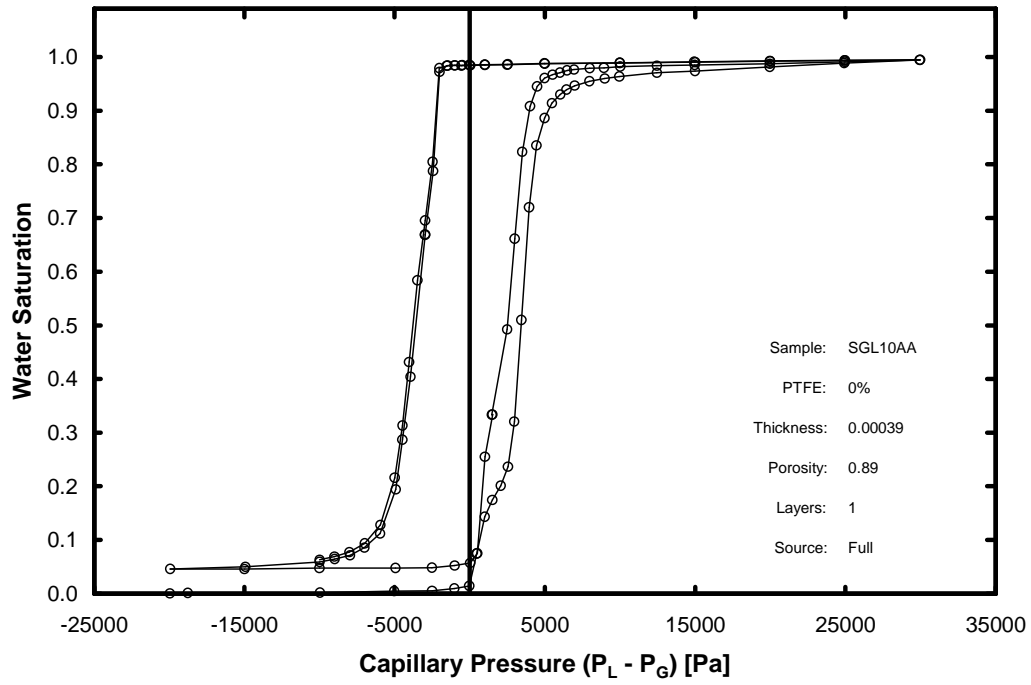


Figure 5.10: Air-water capillary pressure curve for SGL 10AA (top) 10BA (bottom) obtained by GCP

A closer examination of the effect of hydrophobic coating can be made by directly comparing water injection and withdrawal curves for several materials with different PTFE loading. Figure 5.11(top) shows the water injection curves for Toray with three different thicknesses (Toray 060 = 210  $\mu\text{m}$ , Toray 090 = 290  $\mu\text{m}$  and Toray 120 = 390 $\mu\text{m}$ ), with and without PTFE. The effect of thickness is apparent from the importance of surface effects on the shape of the curves which become less prevalent in the thicker materials. A more detailed analysis of surface effects and material thickness is provided in the next section. The effect of PTFE loading is also very apparent. Samples without PTFE converge into one set of lines and those with PTFE into another at much higher pressure. The water withdrawal curves display a similar behavior. It is interesting to note that one of the treated Toray samples (120C) contains only 10% PTFE loading, while the others (Toray 090D and 060D) contain 20%. Yet, the data obtained for the 120C material coincide closely with the curves of 060D and 090D. This would indicate that doubling the PTFE loading does not significantly increase the hydrophobicity, suggesting that the primary effect of the additional PTFE is to make them thicker rather than more hydrophobic as intended. The ability to directly observe the behavior of a hydrophobic coating in this detailed way has not been previously available. With this new tool, it should be possible to improve coating application techniques and procedures to optimize GDL wetting properties.

Figure 5.12 shows an expanded view of the water injection (top) and withdrawal (bottom) curves for SGL 10 samples with 0% (10AA), 5% (10BA) and 10% (10CA) PTFE. These curves do not show the effects of PTFE addition as consistently as the Toray materials in Figure 5.11. The injection curves of the treated samples do not overlap closely and the sample with the intermediate PTFE level (10BA) appears to be the most hydrophobic. The curves again do not coincide during withdrawal and the sample with the highest PTFE loading (10CA) appears to be the most hydrophobic.

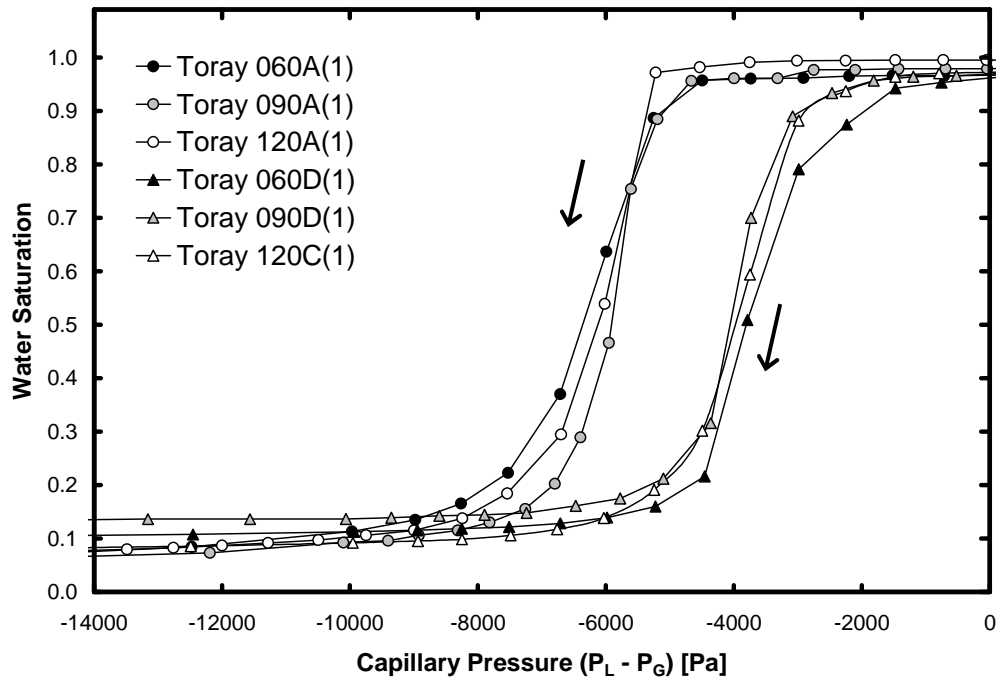
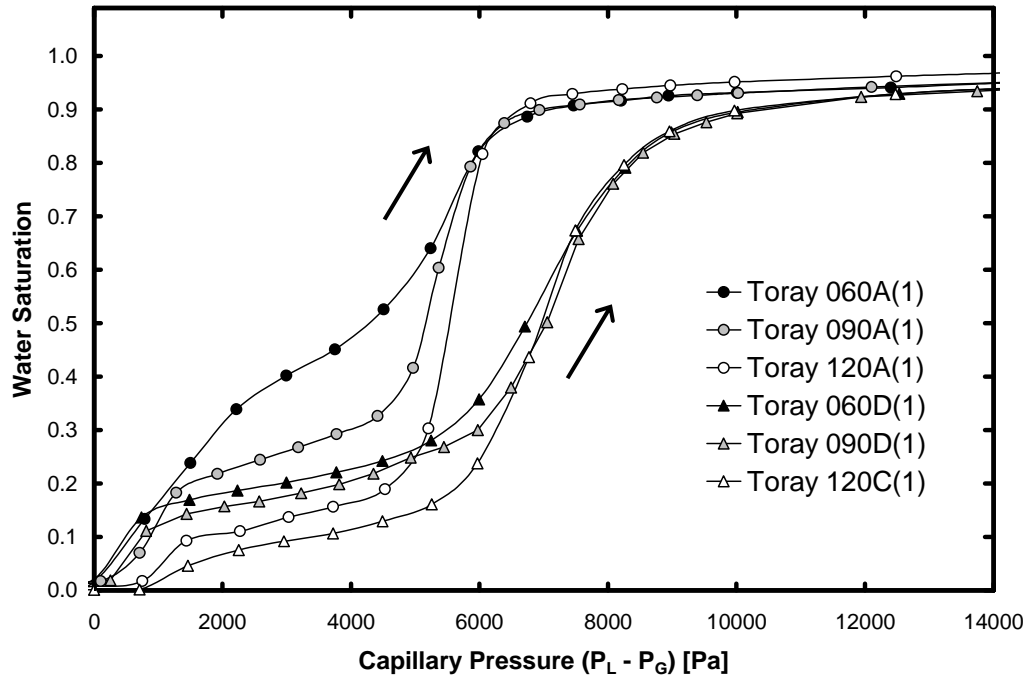


Figure 5.11: Expanded view of water injection curves (top) and withdrawal curves (bottom) for various Toray materials with different PTFE loadings and thickness. A = 0%, C = 10% and D = 20% PTFE. 060 = 210  $\mu\text{m}$ , 090 = 290  $\mu\text{m}$  and 120 = 390 $\mu\text{m}$ .

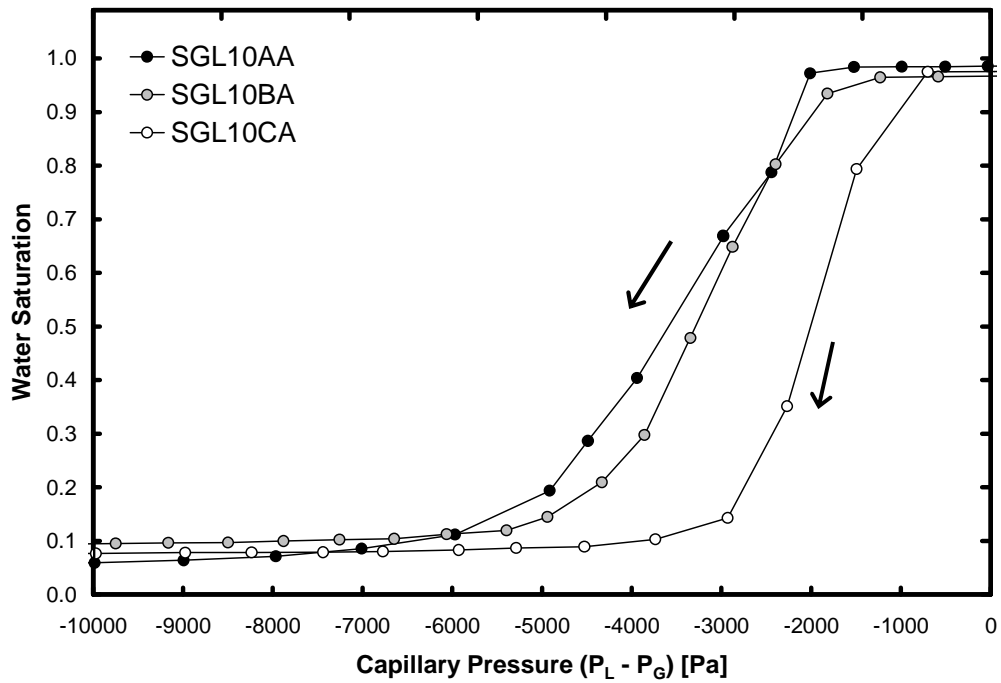
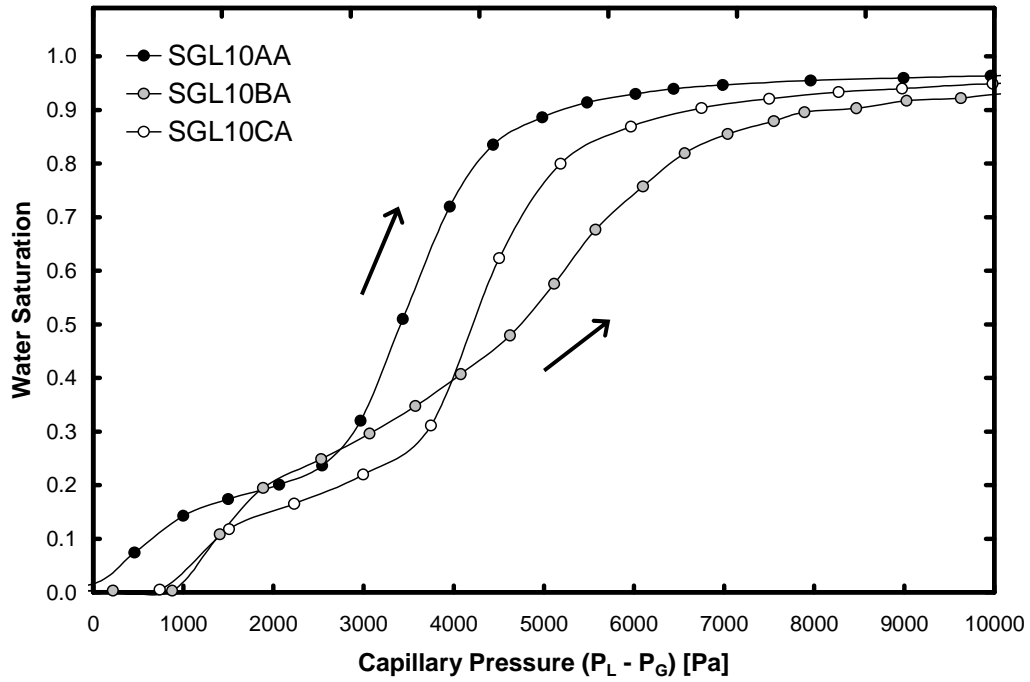


Figure 5.12: Expanded view of injection (top) and withdrawal (bottom) curves for SGL 10 Series with different PTFE loadings. AA = 0%, BA = 5%, CA = 10%, DA = 20% and EA = 30% PTFE.

Clearly, the 10BA and 10CA samples exhibit some differences that cannot be explained by the amount of PTFE alone. The inconsistent hydrophobic behavior of the SGL 10 samples may be due to non-uniform distribution of PTFE in the GDL. For instance, PTFE may be concentrated near the outer surfaces of the 10CA sample and cause it to fill quickly once the outer layers are penetrated. Alternatively, the PTFE in the 10BA sample may be concentrated in smaller pore spaces and cause the final stages of the injection process to fill pores more slowly. Unfortunately, the GCP does not yield any direct information about the spatial distribution of wettability and so explanations for the observed capillary behavior are only speculation without further information. A preferred approach would be to apply PTFE in such a way that known heterogeneous spatial distributions are deliberately obtained and then measuring the resulting capillary pressure curves to observe their effects.

If an explanation for differences in capillary pressure behavior were available, the benefits of directly observing the air-water capillary properties of GDLs would be tremendous. For instance, if fuel cell performance tests were to reveal that 10CA outperforms 10BA, then it could be concluded that whatever leads to the difference in their capillary pressure curves is beneficial and efforts could be made to exaggerate this effect during GDL manufacture and processing. At the very least, the tests on the SGL 10 samples reveal that GDLs can display varying hydrophobic behavior which can only be due to the PTFE application since the substrates are identical.

#### **5.1.3.4. Effect of GDL Thickness**

The effect of GDL thickness on the shape of the capillary pressure curves shown in Figure 5.11 is very pronounced. Because the percolation properties of GDLs are highly influenced by finite size effects, the effect of GDL thickness is explored further in this section. The design of the sample holder used in GCP is very flexible with regard to allowable sample thicknesses. Materials ranging from 50  $\mu\text{m}$  thin to 10 mm thick can be tested by simply matching the thickness of the sample locating gasket to the sample thickness. To study the effect of sample thickness and surface effects, tests have been

done on stacks of 3 samples, in addition to the single layer tests presented above. This triples the pore volume without changing the area of the injection face. A further set of tests are performed using single point injection, as described in Section 3.4. This eliminates all surface effects on samples regardless of thickness.

Figure 5.13(top) shows water injection curves for Toray materials of different thickness (i.e. 1 and 3 layers) with no hydrophobic treatment. The open symbols are data obtained from a single layer sample, whereas the dark symbols correspond to a stack of three GDLs. As previously noted, the shoulder induced by surface effects has a larger impact on the curves for thinner samples. Data from the three-layer stack closely coincide on the same line, which also correspond to that of the injection curve for a single layer of Toray 120A. The fact that a single layer of this material displays similar surface effects as a three layer stack indicates that a thickness of 400  $\mu\text{m}$  is large enough for its behavior to approach that of an infinite medium. Figure 5.13(bottom) shows the results of the same set of tests performed on samples with PTFE coating. Much less difference between the single layer and three layer tests is now observed. The small water injection that is observed into the single layer samples occurs between 0 and 750 Pa, which is more likely due to liquid water filling the large pores and macroscopic contours of the GDL surface than to water accessing the interior pores. The presence of PTFE seems to mitigate the surface effects. Perhaps PTFE reduces the number of locations through which water can enter the GDL. It is also possible that PTFE limits the ability of water to spread laterally inside the GDL so that each invading water cluster fills less pore space. The latter explanation also relates to the fact that GDLs are highly anisotropic, with twice the permeability in-plane than through-plane. Since permeability is controlled by pore size, it is likely that capillary flow also experiences anisotropy effects. The lateral, in-plane flow of water could then be expected to contribute significantly to the filling of the GDL. Preventing such spreading would result in reduced surface effects and cause a more gradual rise in the capillary pressure curve, as seen in Figure 5.13(bottom). There are a number of conceivable ways PTFE could hinder in-plane flow. For instance, it could occur if it were concentrated at fiber intersections, since water moving along fibers must encounter fiber intersections, while water moving across the fibers can avoid them.

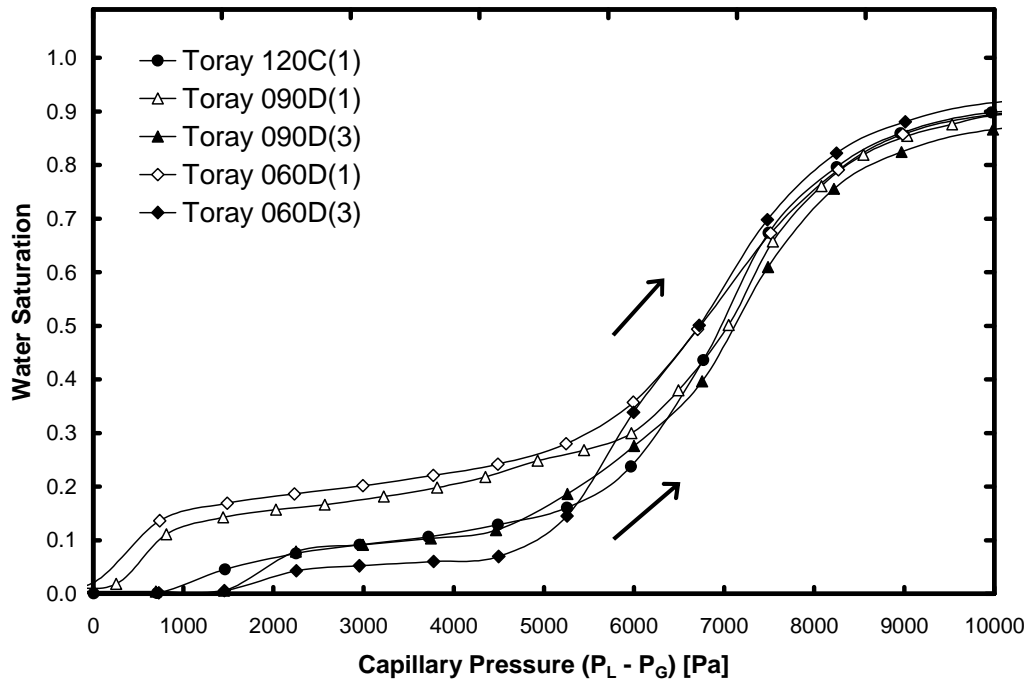
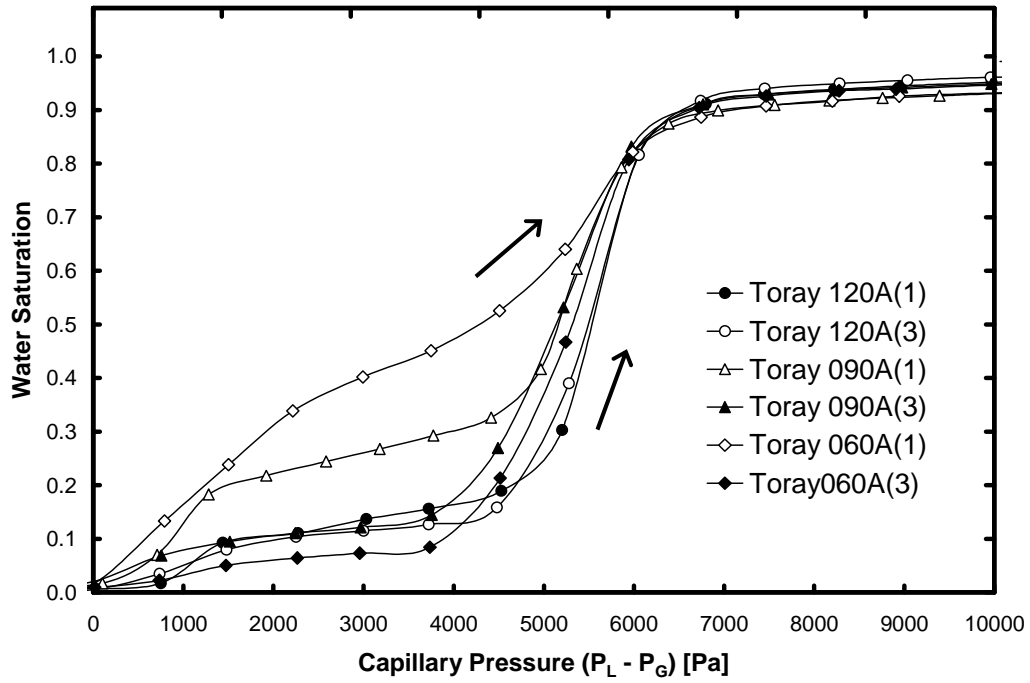


Figure 5.13: Effect of number of layers on water injection into Toray samples of various thicknesses. Top: Untreated. Bottom: Treated. (C = 10 %, D = 20% PTFE)

Increasing the GDL thickness or the number of GDL layers tested effectively increases the ratio of sample pore volume to injection face area. This ratio can also be increased by reducing the injection face area while maintaining the sample pore volume constant. The GCP method can be modified to perform single point injection as described in Section 3.4. Figure 5.14 shows the single point injection curve for Toray 090A in comparison with the full face injection curves for the other untreated Toray samples of differing thicknesses. The progression clearly shows that increasing the ratio of pore volume to surface area reduces the surface effects as expected. The single point injection shows practically no water invasion until 5000 Pa when a massive saturation jump occurs indicating that percolation has occurred. It was previously noted that the Toray 120A sample shows minimum surface effects since the addition of more layers does not reduce the shoulder in the curve. The little filling that is observed can be attributed to filling of rough contours and pores on the GDL surface. This is confirmed by the single point injection curve where the face is inaccessible to water and the saturation remains essentially zero until the percolation threshold is reached.

Figure 5.15 shows the single point injection curve for Toray 090D with PTFE coating. As expected, this curve shows no surface effects, either filling of surface pores or filling of internal pores from the surface. It does, however, show significantly delayed invasion of water. This can be explained by the same reasoning invoked to understand the decreased surface effect in treated samples. If PTFE does hinder in-plane spreading of water, then the point source injection will behave as observed in Figure 5.15 since liquid water must extend from the injection site throughout the GDL by lateral spreading in-plane. Hindered lateral spreading would account for the observed slow rise to full saturation. Conversely, the very sharp rise of saturation seen in untreated Toray during single point injection (Figure 5.14) attests to the ease of lateral water flow in the absence of PTFE since 65% of the pore volume was accessed from a single point with only an incremental pressure increase.

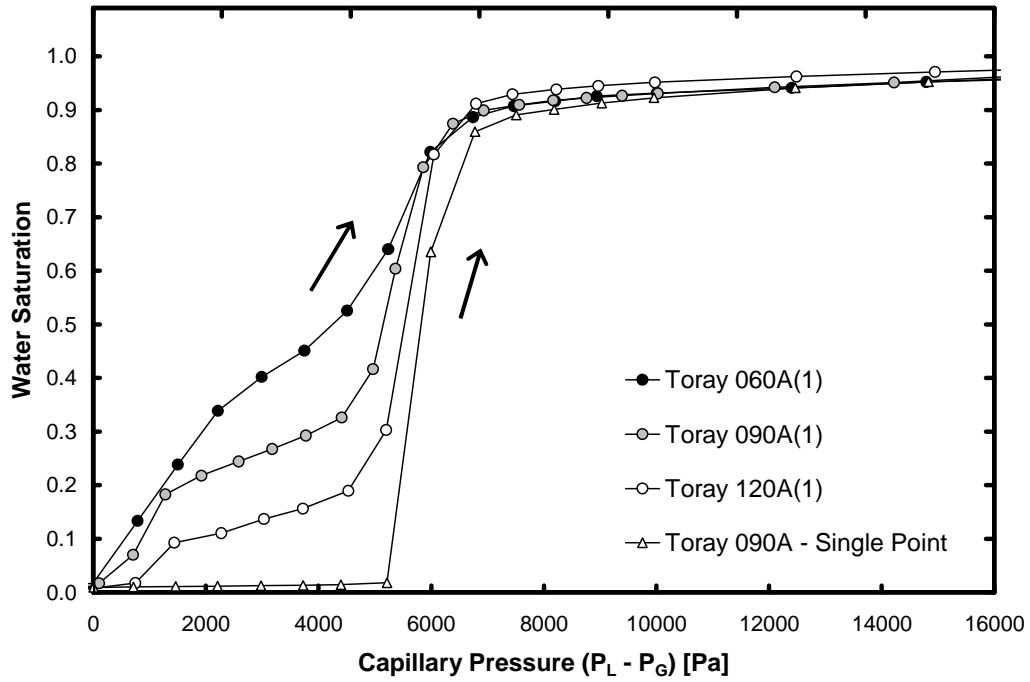


Figure 5.14: Water injection curves for untreated Toray materials. Single point injection is compared with full face injection into Toray materials with different thicknesses.

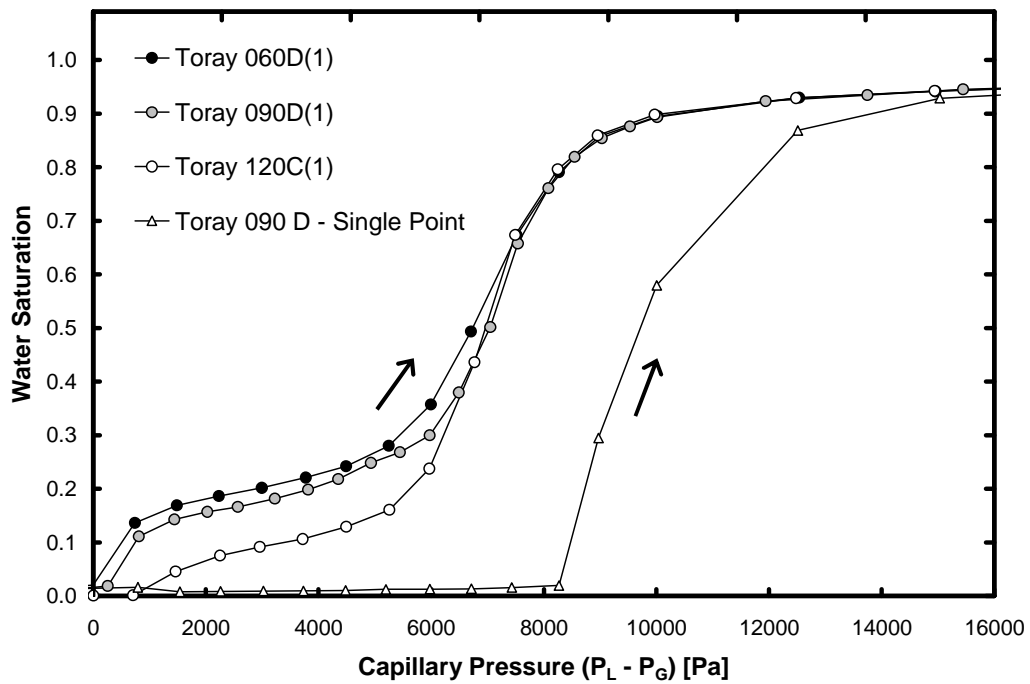


Figure 5.15: Water injection curves for treated Toray materials. Single point injection is compared with full face injection in materials with different thicknesses.

#### 5.1.3.5. Analysis of Capillary Pressure Hysteresis

The GCP method has revealed two surprising features of the air-water capillary pressure behavior of GDLs. Firstly, it shows a large hysteresis between the water injection and water withdrawal curves. The hysteresis is so large, in fact, that injection occurs at positive capillary pressure, while withdrawal occurs at negative capillary pressure. The second surprising feature revealed by GCP is the lack of water imbibition into supposedly hydrophilic materials with no PTFE and the lack of water ejection from supposedly hydrophobic materials containing PTFE. This apparent reversal of wettability and failure to display distinct hydrophilic or hydrophobic behavior warrants further investigation and demands an explanation.

In order to obtain a more detailed picture of GDL wettability, the GCP method has been used to collect internal scanning loops (i.e. reversing the pressure prior to full saturation of the GDL). Such curves reveal whether GDLs behave differently when water is withdrawn from or injected into a partially saturated material. The results in Figure 5.16 show that water does not spontaneously eject from either GDL, with or without hydrophobic polymer coating, regardless of the saturation when withdrawal commences. There is a slight tendency for water to withdraw earlier from partially saturated Toray 120C, but negative pressures are still required. Figure 5.17 shows internal scanning loops for water injection into partially saturated materials. As with the water withdrawal curves, these results do not exhibit any behavior not observed during the full scanning loops.

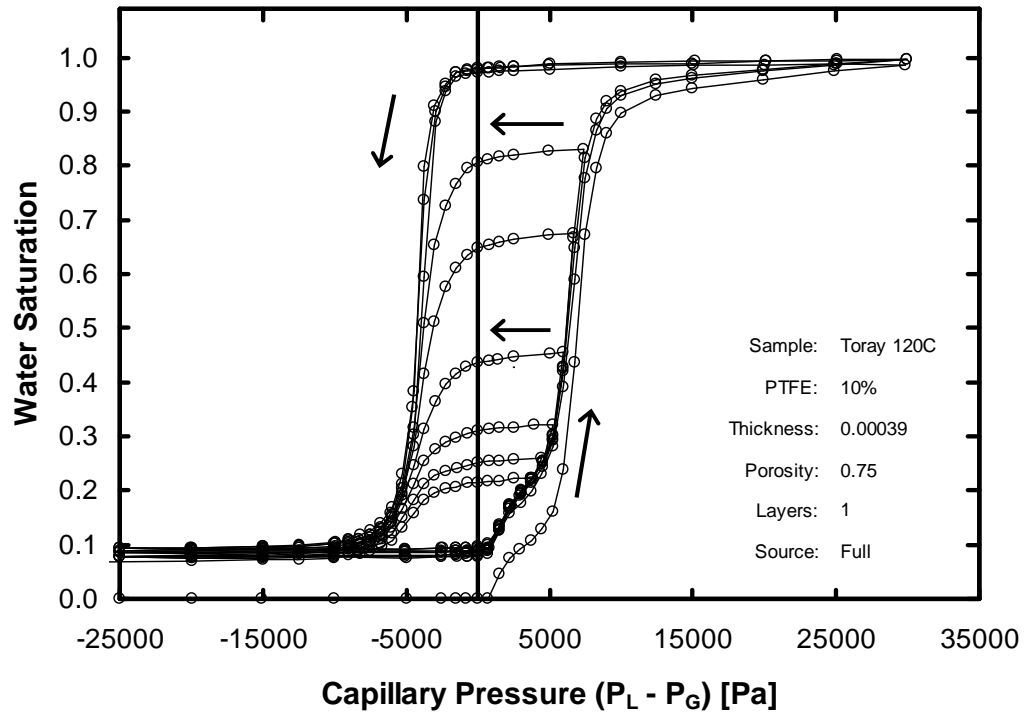
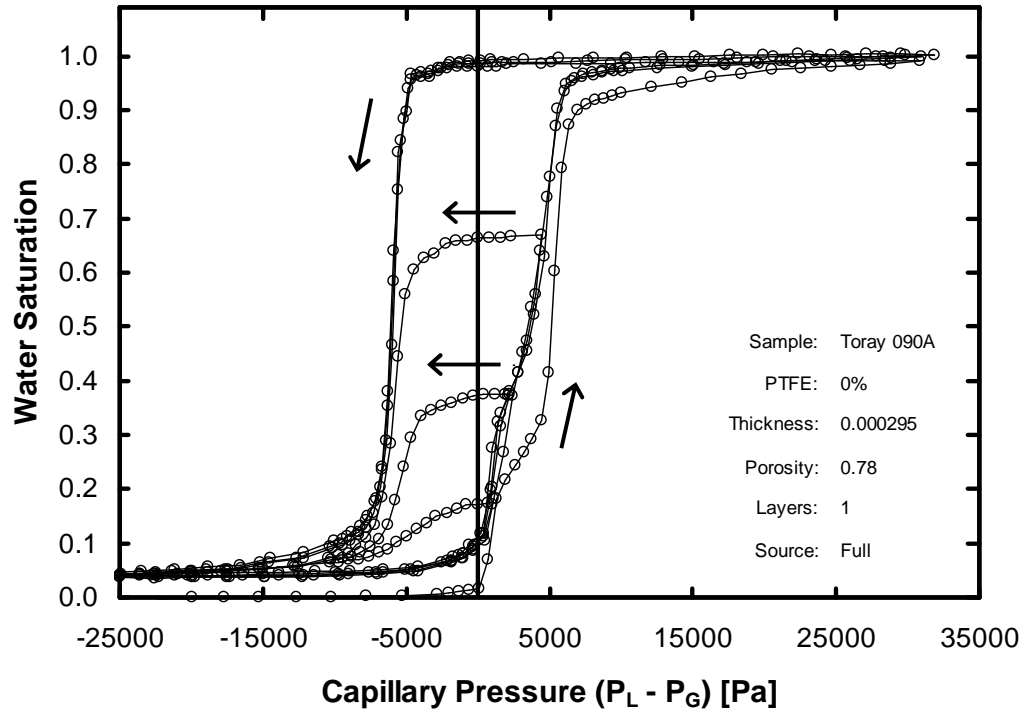
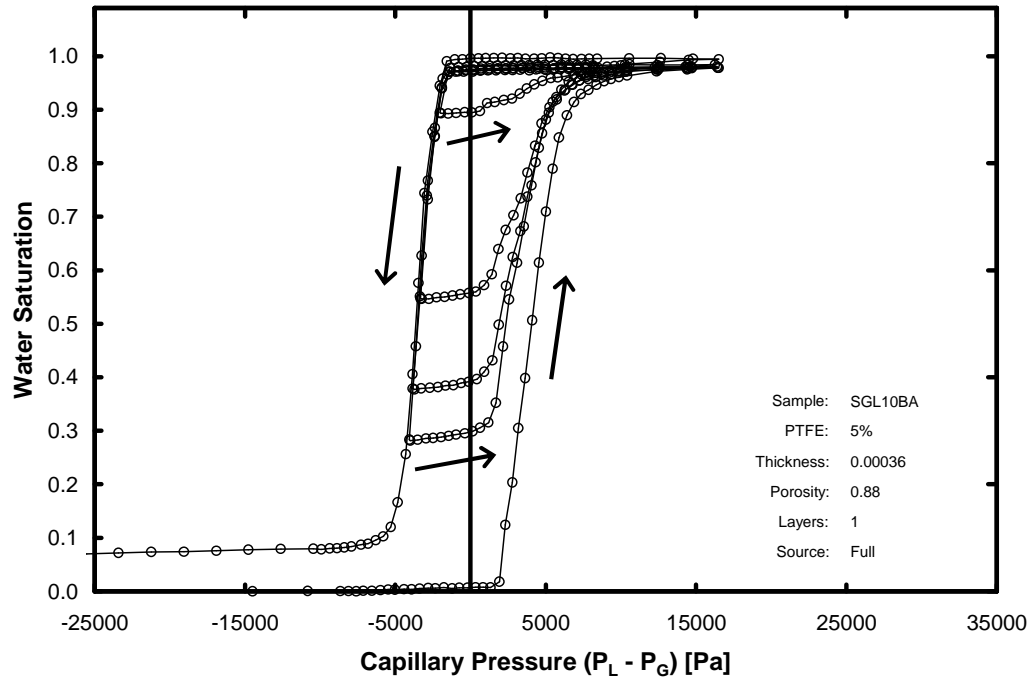


Figure 5.16: Internal scanning loops for removal of water from partially saturated GDLs. Top: Toray 090A with no PTFE. Bottom: Toray 120C with 10wt% PTFE.



**Figure 5.17: Internal scanning loops for injection of water into partially saturated SGL 10BA**

One of main factors influencing GDL capillary properties is the intermediate contact angles exhibited by both graphite and PTFE. Graphite is mildly hydrophilic ( $\theta = 86^\circ$ ) and PTFE is mildly hydrophobic ( $\theta = 108^\circ$ ). According to Anderson [194], the distinction between hydrophobicity and hydrophilicity becomes meaningless when contact angles are within  $\pm 30^\circ$  of  $90^\circ$  ( $60^\circ < \theta < 120^\circ$ ). Based on this consideration, water should not be expected to imbibe into graphite pores and air should not be expected to imbibe into PTFE pores (if such well defined pores were believed to even exist). A further repercussion of this passive wettability behavior is that water must be forced *into* all pores (since water does not imbibe) and water must be forced *out* of all pores as well (since air does not imbibe), regardless of PTFE treatment. Based on this rationale alone, the switching between states of wettability observed in GDLs is not surprising.

Although recognition that GDLs are intermediately wettable helps to validate the observed behavior, it does not explain the phenomena that control the wettability. There are a number of pore scale mechanisms that lead to hysteresis in capillary curves and wettability behavior. These were discussed in general terms in Chapter 2 and will now be

applied to GDLs specifically to explain the observed results. The principle cause of hysteresis in typical capillary pressure curves (i.e. obtained from MIP) is the fact that drainage of a wetting phase from a pore is controlled by the size of the throats leading to the pore whereas imbibition of a wetting phase into a pore is controlled by the size of the pore body. This difference leads to the hysteresis observed in the MIP results in Section 5.1.1. This mechanism can cause a shift to lower capillary pressures during water withdrawal, but it does not account for the negative values of capillary pressure required.

A second common cause of capillary hysteresis is contact angle hysteresis. This is caused by microscopic surface roughness on the solid material. Since both the GDL fibers and the PTFE coating contribute some roughness, some contact angle hysteresis is expected. Estimates can be made to determine the amount of contact angle hysteresis required to explain the observed amount of capillary pressure hysteresis. Consider the Toray 090A sample shown in Figure 5.9. The main leg of water injection occurs at 4400 Pa and the main leg of water withdrawal at -4200 Pa. If the mean pore diameter is taken to be 22  $\mu\text{m}$  [129,212], then the Young-Laplace equation can be used to estimate the contact angles for injection and withdrawal to be  $110^\circ$  and  $70^\circ$ , respectively. These values are reasonable in light of those for the constituent materials, although a contact angle hysteresis of  $40^\circ$  is somewhat large. Performing a similar calculation on the Toray 090D material, which exhibits an injection pressure of 6000 Pa and withdrawal pressure of -3000 yields contact angles of  $117^\circ$  and  $77^\circ$ , respectively. These are also reasonable values and reflect an increase in contact angles due to the addition of PTFE, but again a somewhat large hysteresis of  $40^\circ$  is obtained.

Solid structure can also affect the observed wettability by altering the curvature of the interface. The effect of diverging and converging pore throats was described in Section 2.1. This concept is very relevant to GDLs since pore throats are defined by constrictions between circular fibers. As shown schematically in Figure 5.18, the surface curvature of fluid moving through a gap between two fibers can change from negative to positive while the contact angle  $\theta_A$  remains constant. The ease of creating a switch in surface curvature direction is higher for  $\theta$  closer to  $90^\circ$ .

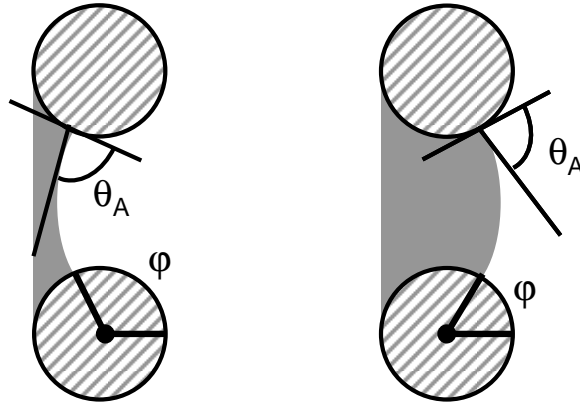


**Figure 5.18: Movement of a meniscus between two cylindrical solids. The interface curvature changes as a function of position with a constant contact angle.**

A final factor that can alter the apparent wettability is the formation of anticlastic or saddle-shaped interfaces, as shown in Figure 5.19(right). The capillary pressure defined by Eq.(2.6) depends on the mean curvature  $H$  of the surface which is calculated as:

$$H = \frac{1}{2} \left( \frac{1}{r_1} + \frac{1}{r_2} \right) \quad (5.4)$$

where  $r_1$  and  $r_2$  are the radii of curvature in two perpendicular directions. For a spherical interface,  $r_1 = r_2$  and  $H$  becomes  $1/r$ . Since these radii have opposite signs at an anticlastic interface, it becomes possible for  $H$  to take on negative net values. Anticlastic interfaces can potentially be formed, for example, when an interface simultaneously contacts two materials with distinct contact angles, such as graphite and PTFE.

Anticlastic interfaces can also arise as a result of certain fluid configurations that occur during withdrawal of a non-wetting phase. Consider the situation shown in Figure 5.20. The non-wetting phase is being removed from the bottom and vacates the smallest pores first. In this scenario, the next meniscus that will move is marked with a dashed arrow. Due to the fluid topology, however, this movement will not be a straightforward retraction. Instead, the interface is deformed into an anticlastic shape until the net curvature  $H$  is small enough to overcome the topological constraints of the fluid configuration.

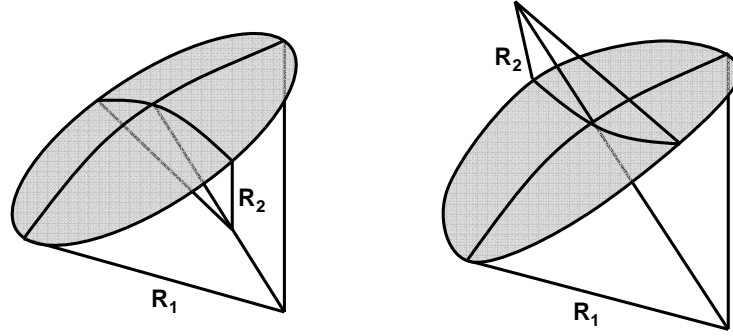


**Figure 5.19: Spherical and anticlastic interfaces. Left: Spherical interface with principle radii of curvature  $R_1$  and  $R_2$ . Right: Anticlastic interface with the same two radii of curvature but with opposite signs.**

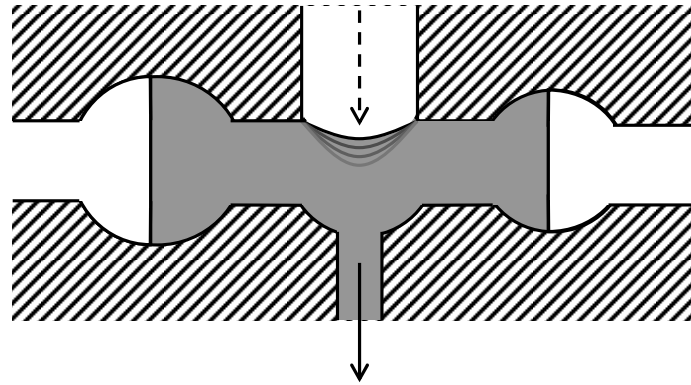


**Figure 5.20: Fluid configuration leading to an anticlastic interface during retraction of a non-wetting phase. The grey contour lines show the positively curved interface.**

This phenomenon is observed during mercury retraction from glass micromodels [213]. When an interface exhibits intermediate contact angles, this effect is sufficient to create a net negative curvature. Ioannidis *et al.* [213] use the following formula for predicting the capillary pressure required to destabilize such an interface:

$$P_C = \sigma \left( -\frac{\cos \theta_R}{r_p} - \frac{\sin \theta_R}{\sqrt{r_p^2 + 3r_t^2}} \right) \quad (5.5)$$

where  $r_p$  is the pore body radius,  $r_t$  is the throat radius and  $\theta_R$  is the receding contact angle. Neglecting contact angle hysteresis and inserting  $\theta_R = \theta = 98^\circ$  into Eq.(5.5) with  $r_p = 10 \mu\text{m}$  and  $r_t = 8 \mu\text{m}$  for Toray 090 [129] gives  $P_C = -3190 \text{ Pa}$  for water withdrawal, compared to an experimentally measured value of  $-5200 \text{ Pa}$ . This shows qualitatively that fluid configuration effects during water retraction are significant and sufficient to

generate negative capillary pressures, even when water is a non-wetting fluid ( $\theta = 98^\circ$ ). Incorporation of contact angle hysteresis would make Eq.(5.5) even more negative, bringing the calculated  $P_C$  closer to experiment.

Each phenomenon described above is capable of altering the observed wettability of a porous material. These effects are most prominent on fluids that have intermediate contact angles within  $\pm 30^\circ$  of  $90^\circ$ , which is certainly the case in GDLs. Furthermore, each of the phenomena described is very relevant to GDLs and probably contributes to the observed wettability in some way.

#### 5.1.3.6. Wettability Index

Although the intention of adding hydrophobic polymer coatings to GDLs is to alter the wettability, a quantitative description of the effect of this treatment is not available. As is evident from the air-water capillary pressure curves presented previously, the addition of a hydrophobic polymer does not alter the wetting properties in any dramatic qualitative way, although quantitative differences are seen. A means of quantifying wettability exists in the form of a wettability index, which is an empirical value obtained from capillary curves. Wettability indices are often employed to determine whether an oil-bearing formation is water-wet or oil-wet, which has a significant impact on oil recoverability. Several wettability index definitions have been proposed [194], but the US Bureau of Mines (USBM) index is the most useful for the present data. The USBM index ( $I_{USBM}$ ) is based on the observation that the area under a capillary pressure curve corresponds to the amount of work required to inject or withdraw a fluid from a porous medium [214]. Injection of a non-wetting fluid will require more work than its removal, which is aided by capillary forces. Calculation of the  $I_{USBM}$  requires determining the areas  $A_1$  and  $A_2$  as shown in Figure 5.21 and inserting them into Eq.(5.6) as follows:

$$I_{USBM} = \log\left(\frac{A_1}{A_2}\right) \quad (5.6)$$

Defined in this way, negative  $I_{USBM}$  values signify that the material tends to be non-

wetting and positive values indicate a wetting material. The magnitude of  $I_{USBM}$  also indicates the extent of wettability. A value near zero corresponds to intermediate wettability, while more positive or negative values signify hydrophilic or hydrophobic tendencies, respectively.

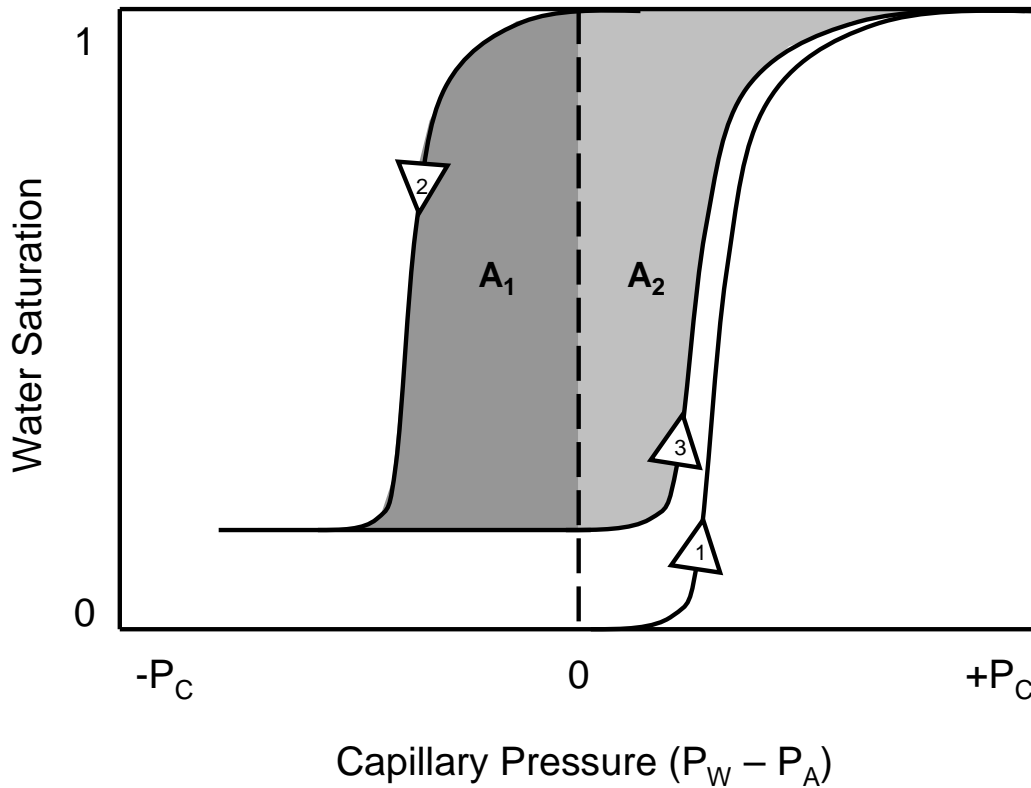


**Figure 5.21: Area definitions used in US Bureau of Mines wettability index**

Values of  $I_{USBM}$  have been determined for a number of GDL materials. Figure 5.22 shows the  $I_{USBM}$  calculated for SGL 10 series materials with varying amounts of PTFE loading. This analysis reveals that a dramatic difference in wettability is actually obtained when PTFE is added despite exhibiting only slight changes in capillary pressure curves. Interestingly, the addition of 5% PTFE is sufficient to create a large change in  $I_{USBM}$  while any further increase in PTFE loading has only a negligible effect. This suggests that increasing PTFE addition may lead to thicker deposits, but not more surface coverage as desired.  $I_{USBM}$  values for Toray materials with two thicknesses and different PTFE contents are shown in Figure 5.23. These also show a large shift toward non-wettability

when PTFE is added. As well, the comparison of the indices for samples containing 10% and 20% PTFE shows negligible increase in hydrophobicity despite a doubling of the polymer loading.

Comparison of  $I_{USBM}$  values between the SGL and Toray materials reveals that the coating on the Toray materials is considerably more effective. Both types of GDL have similar  $I_{USBM}$  values near 0.20 when no PTFE is added, yet the treated Toray samples are about twice as hydrophobic according to this index. This can be attributed to better application of the PTFE coating since structural differences are accounted for by taking the ratio of areas in Eq. (5.6). Two materials with identical wettability but different pore sizes will have the same  $I_{USBM}$  value since  $A_1$  and  $A_2$  will both change proportionally as pore sizes change. This is an important point since the addition of PTFE presumably decreases the average pore size in the GDL and effectively changes the structure.

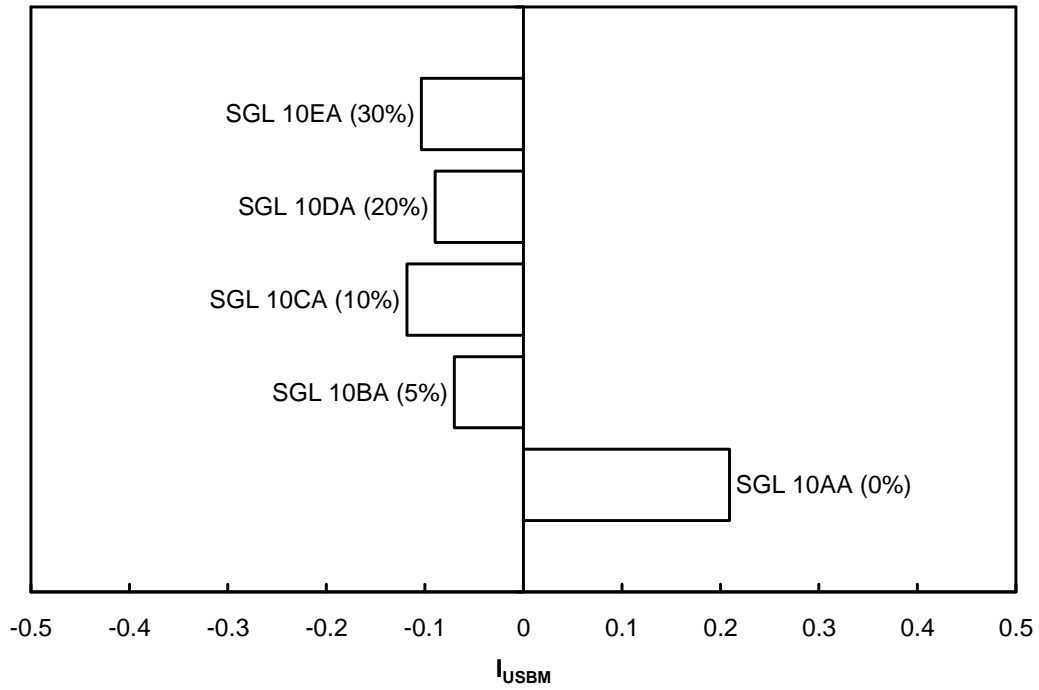


Figure 5.22: Wettability of SGL 10 series GDLs as determined by the US Bureau of Mines index

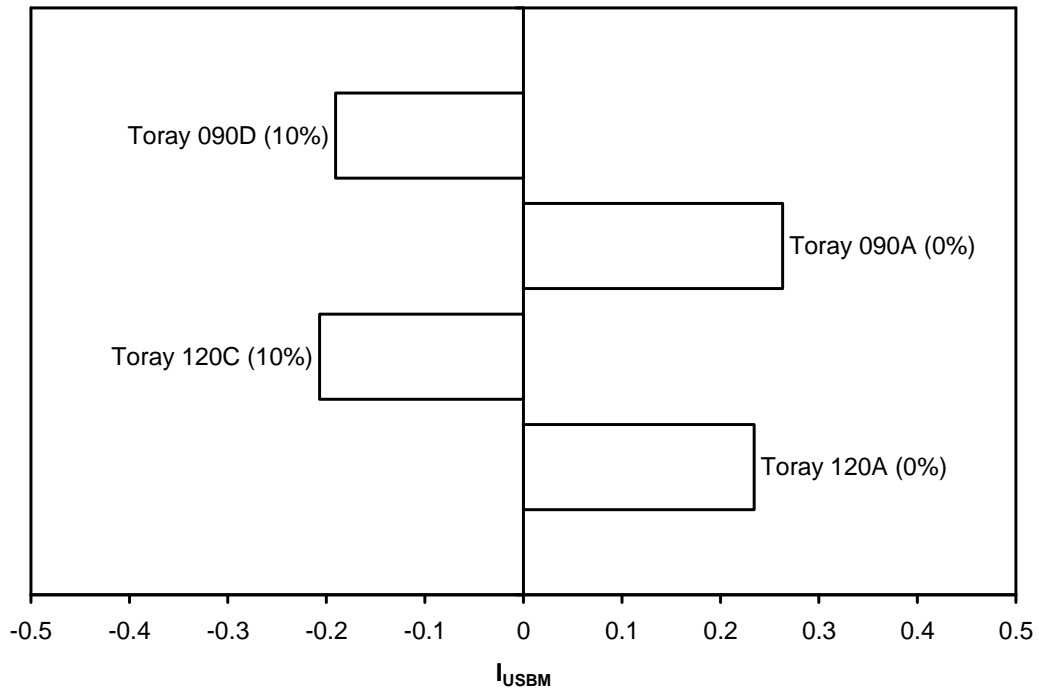
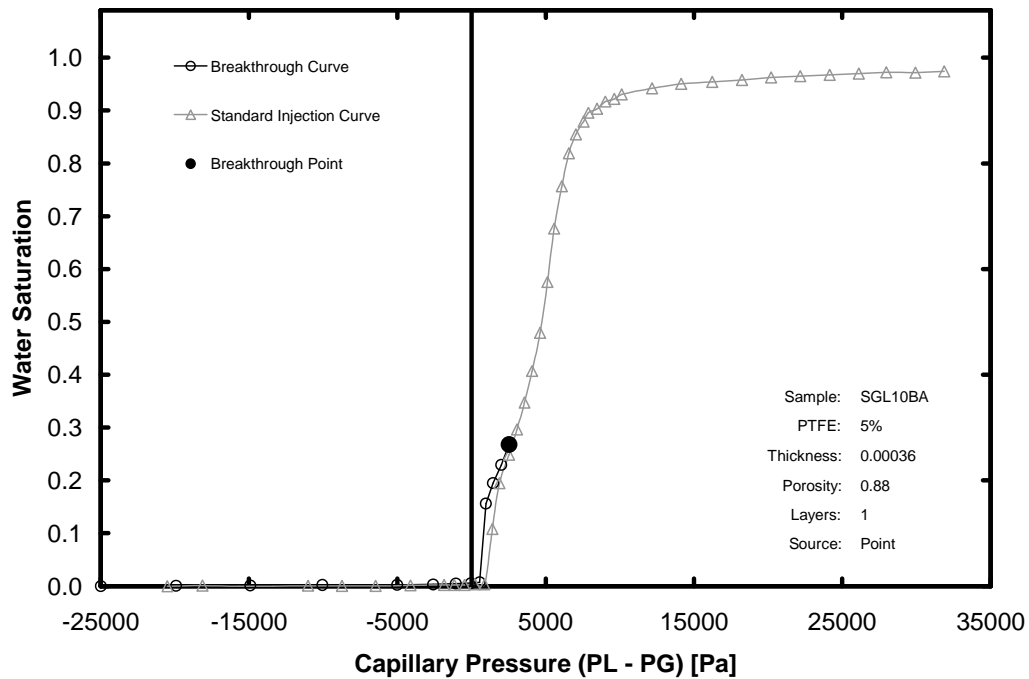


Figure 5.23: Wettability of Toray GDLs of various thicknesses as determined by the US Bureau of Mines index

### 5.1.3.7. Water Breakthrough Point

The GCP method has been adapted to simultaneously measure the pressure and saturation of GDLs at the breakthrough point. A detailed description of the adaptation is given in Section 3.3. Figure 5.24 shows the breakthrough point of SGL 10BA as well as the capillary pressure curve obtained prior to the breakthrough point. Once breakthrough occurs, the capillary pressure experiment is terminated since water contacts the dry hydrophilic membrane located above the sample. Also included in Figure 5.24 is the full standard capillary pressure curve obtained on SGL 10BA showing the two curves are in close agreement prior to the breakthrough point.



**Figure 5.24: Breakthrough point and capillary pressure curve prior to breakthrough for SGL 10BA . The full capillary pressure curve obtained on a separate sample of SGL 10BA is also shown.**

In Figure 5.25, the full capillary pressure curves and the breakthrough points for SGL 10BA are shown during full face injection and during single point injection. During standard full face injection, the SGL10BA sample reaches a saturation of 25% before breakthrough occurs. This high saturation is caused by the fact that numerous dead-end liquid clusters have entered the GDL from the surface. They do not breach the GDL, but

they do occupy pore space; in a fuel cell, this would lead to blocked gas phase transport. The breakthrough point for single point injection has also been measured and found to occur at a much lower saturation and slightly higher pressure. The saturation is lower since no dead-end clusters are able to enter the GDL. The breakthrough pressure is higher since the water enters the GDL through a single isolated location that is most likely not connected to a path that leads to the outlet face at low pressures. Instead, the water must spread throughout the GDL until it finds a path to the outlet face, something which requires higher pressures.

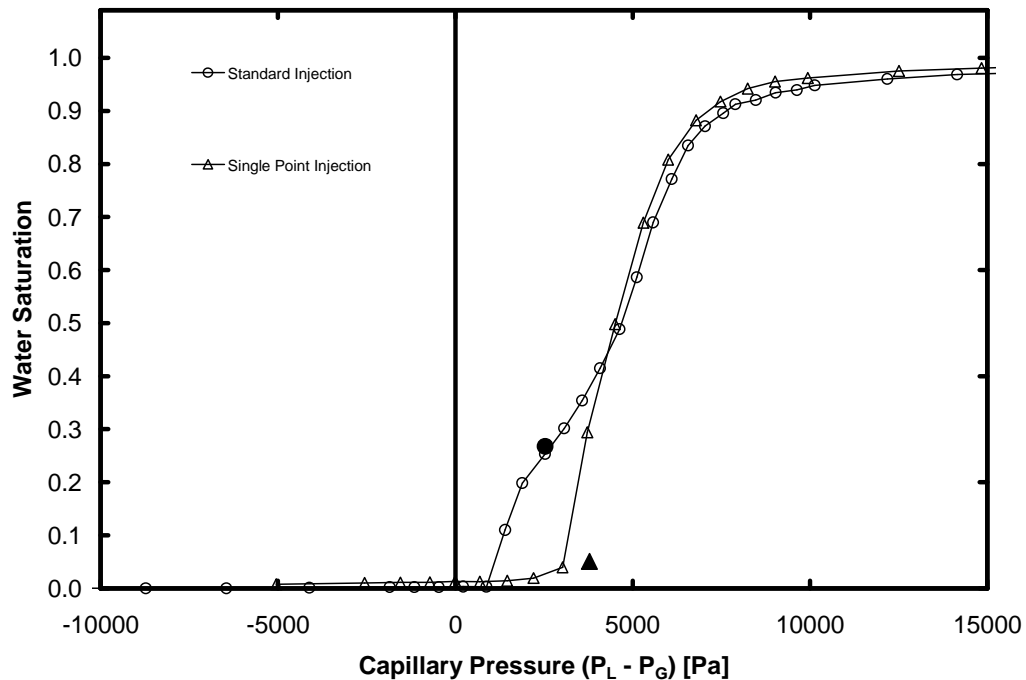


**Figure 5.25: Breakthrough points for SGL 10BA**

The breakthrough data for Toray samples without and with PTFE treatment are shown in Figure 5.26 and Figure 5.27, respectively. The same trends are visible in both materials. Full face injection leads to lower breakthrough pressures but higher saturations. Single point breakthrough occurs as soon as water enters the GDL. The rise in saturation occurs as liquid water spreads out in-plane away from the injection site.

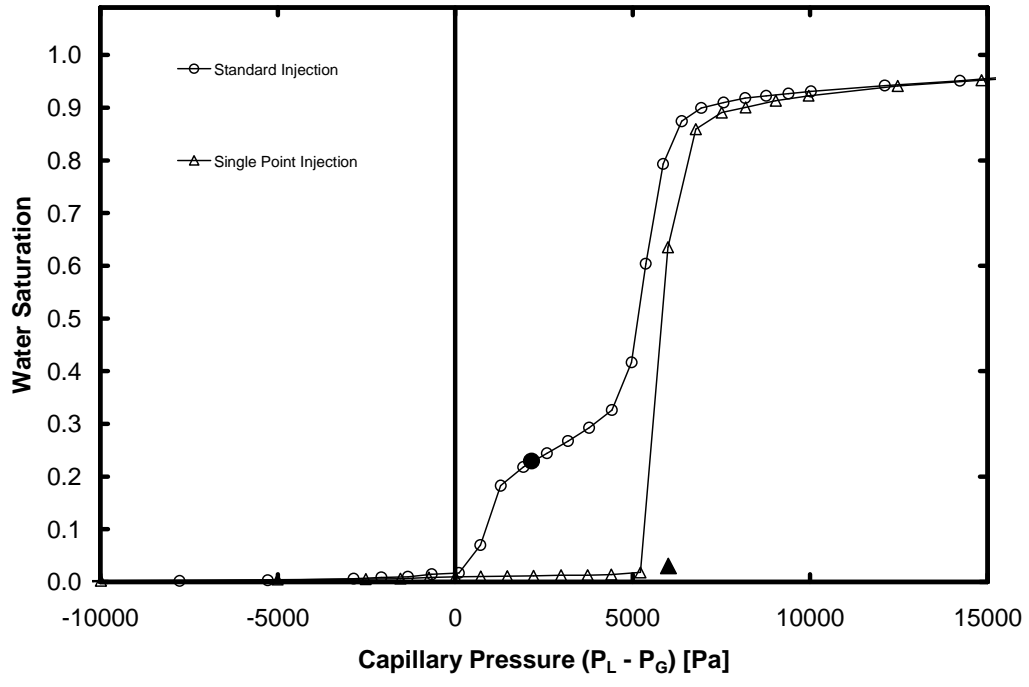


Figure 5.26: Breakthrough points for Toray 090A

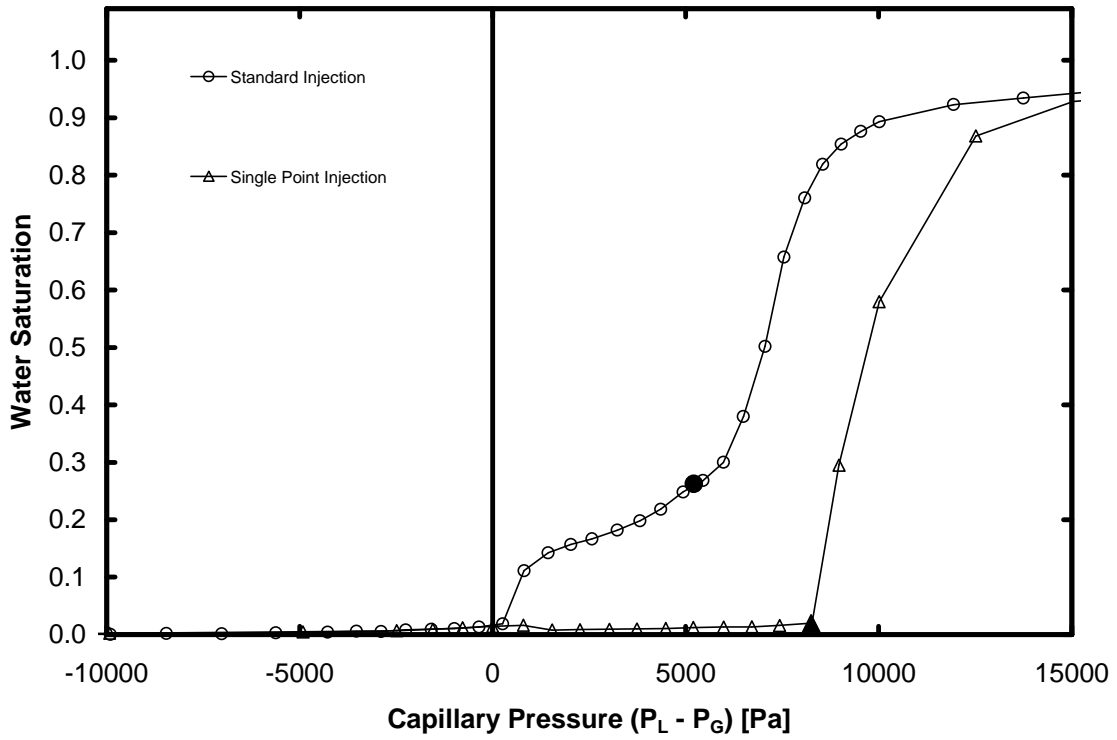


Figure 5.27: Breakthrough points for Toray 090D

## 5.2. The Role of the Microporous Layer

The low saturations observed during single point injection tests described in the previous section suggest that the MPL may somehow promote water injection into the GDL in a manner similar to single point injection. This section explores this possibility using a combination of GCP experiments and percolation concepts.

A systematic experimental study of the effect of the MPL on fuel cell performance has recently been undertaken by Ramasamy *et al.* [13]. Improved mass transfer was clearly demonstrated when an MPL was applied, both in terms of increased limiting current as well as reduced mass transfer resistance measured via AC impedance. However, the actual function of this MPL layer is still unexplained. The MPL presumably creates better electrical and thermal contact between the catalyst layer and the GDL by providing a smoother, more continuous interface. The benefits of the MPL however, are most noticeable at higher current conditions indicating that it somehow improves mass transfer. This is counter-intuitive since the MPL actually adds a diffusive resistance to mass transfer. Thus, it is generally believed that the MPL somehow alters the liquid water distribution in the cell to a more favorable arrangement for gas phase transport.

A number of theories for the function of the GDL have been offered. The first modeling studies included the MPL in the modeling domain [29,32] and showed that the MPL created a saturation discontinuity at the GDL-MPL interface due to the different capillary properties of each layer, thereby reducing the maximum GDL saturation. This effect, however, was simply due to the fact that the modeled GDL was thinner when an MPL was added and the saturation profile from the gas channel boundary to the catalyst layer was truncated. These early studies were also only half-cell models and did not consider the interaction of the membrane and anode. More recent studies have revisited the MPL problem with full cell models [47,50]. These calculations predict that the MPL acts as a capillary barrier to water entering the cathode GDL and forces water to permeate from the cathode to the anode (Figure 5.28). According to this scenario, the MPL is so hydrophobic that liquid water cannot penetrate it and instead flows through the membrane to the anode. Attempts to confirm this mechanism experimentally have been

inconclusive and contradictory. Spernjak *et al.* [158] used a transparent flow field to monitor water in the anode and found that water appears in the anode channels only when an MPL is used on the cathode side, which they offer as proof for the MPL-as-capillary-barrier mechanism. Ge and Wang [215], however, performed comparable experiments but concluded that the appearance of water in the anode was due to condensation since water droplets only appeared on channel walls and were never observed emerging from the GDL as droplets. Quantitative water balance experiments have been conducted by Atiyeh *et al.* [216] who saw improved performance when an MPL was present on the cathode side despite no discernable increase in water collected from the anode. This showed that the improved fuel cell performance could be attained without altering the water balance.

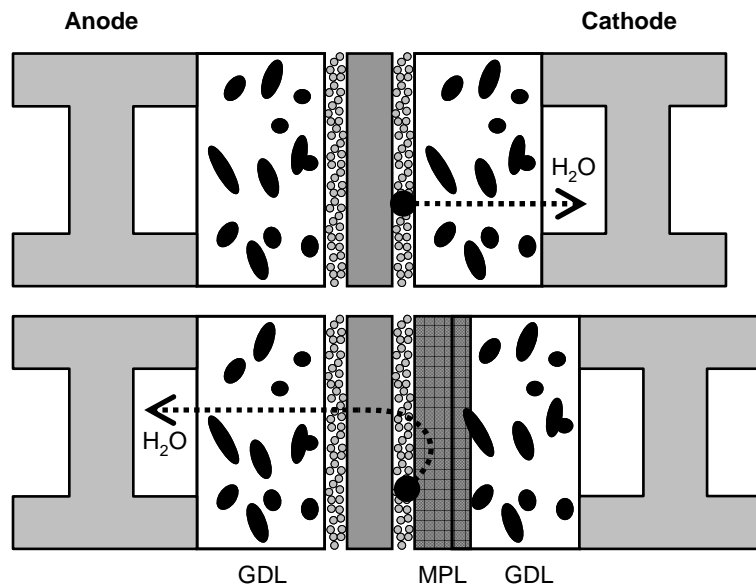


**Figure 5.28:** The prevailing conceptual picture of the function of the MPL. (Top) Without MPL, liquid water flows through the cathode GDL to the cathode flow channels. (Bottom) With MPL liquid water is forced to flow through the membrane to the anode side.

### 5.2.1. Percolation Concepts

If the MPL does not act as a capillary barrier, liquid water generated at the catalyst layer must first percolate through the MPL before it reaches the GDL. A consequence of this percolation process is that liquid will break through the MPL at a few isolated locations

on the MPL-GDL interface. This isolated breakthrough is analogous to the single point injection experiments described previously. The subsequent percolation through the GDL then proceeds from these point sources, instead of the full face of the GDL and this alters the invasion percolation process by rendering many pores inaccessible and dramatically alters GDL saturation at breakthrough. Figure 5.29 (left) shows a schematic representation of the water configuration in the GDL when no MPL is present and water is injected into the GDL from the entire inlet face. In this scenario, there exist many dead-end clusters that do not contribute to flow through the GDL and only one path that spans the sample. Figure 5.29(middle) shows the same GDL when water is injected from a point source. In this case, dead-end clusters are not invaded since they are not connected to the point source and as a result the saturation of the GDL is greatly reduced.

The percolating path shown in Figure 5.29(middle) is deliberately different than that shown in Figure 5.29(left) to highlight an aspect of percolation pertaining to finite size media. In infinite media, there is only one sample spanning or percolating cluster. This cluster forms when the pressure reaches the percolation threshold. Below this pressure, no sample spanning cluster exists; above this pressure, other formerly dead-end clusters become connected to the percolating cluster [152,153]. Since GDLs are so thin, however, with only 10 – 15 pores across the domain, it is possible for an invading cluster to span the sample without converging on the percolating cluster. The ability of any invading cluster to span the GDL before the percolation threshold is reached is the key finite size effect. Thus, a point source injection at any location can lead to a local GDL breakthrough and breakthrough can occur at much lower saturations than in infinite media.

Figure 5.29(right) shows the situation as applied to an MPL-GDL interface. Water is injected into the MPL from its full face and a single percolation cluster spans the MPL and emerges at the MPL-GDL interface at a single location. From this location, a single invading cluster enters the GDL and breakthrough occurs. Of course, this mechanism only applies for scenarios where liquid water is produced at the catalyst layer. If water vapor is produced, it could transport through the MPL and condense in GDL.

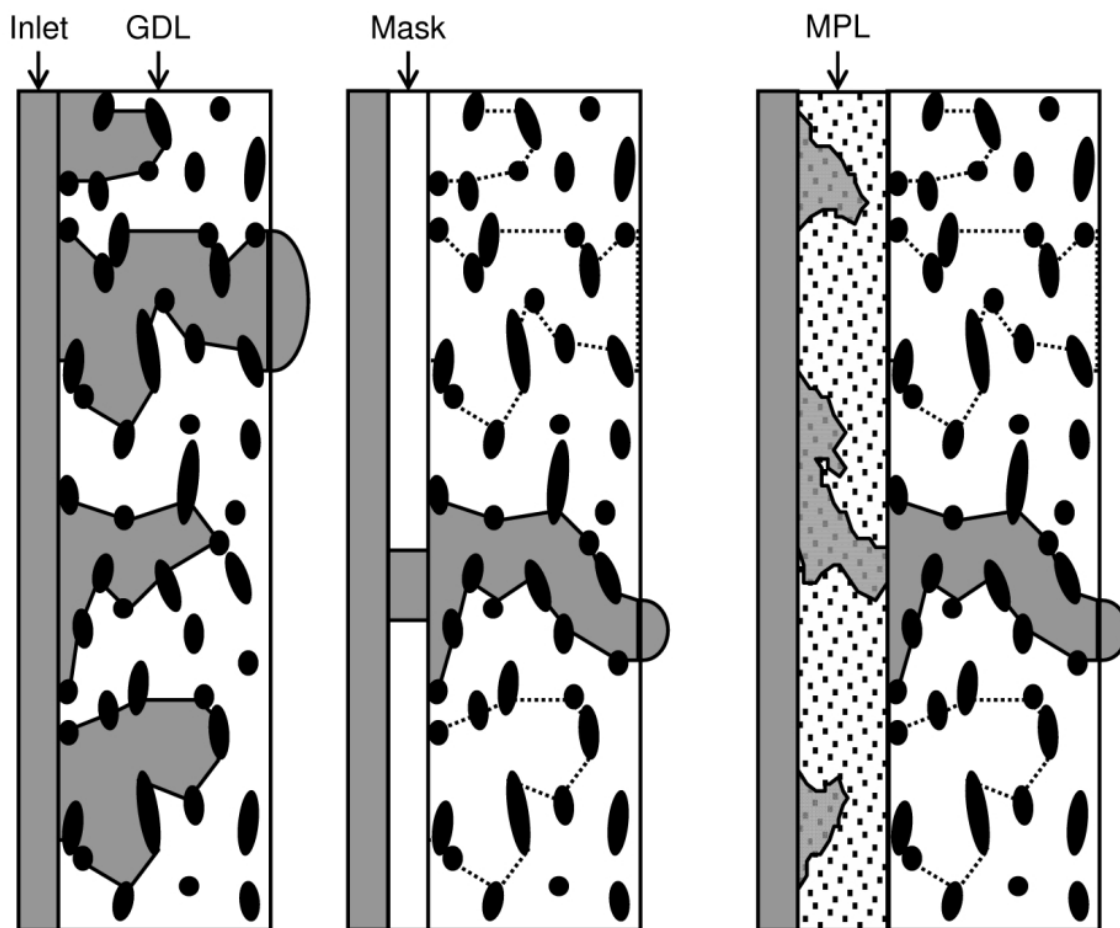


**Figure 5.29: Conceptual picture of water flow through GDL with full face injection and point source injection. Left: GDL with full face exposed to water. Middle: GDL with single point water injection. Right: GDL with MPL percolating through the MPL. Black is solid, grey represents liquid water and dotted lines show the location of the dead-end water clusters that are no longer filled.**

### 5.2.2. Experimental Evidence

To test whether liquid water injection through the MPL leads to reduced GDL saturation, the GCP method adapted to detect liquid breakthrough has been employed. Samples are mounted with the MPL facing downwards so that liquid penetrates the MPL before reaching the GDL. Tests have been conducted on SGL 10BB which is the same as the SGL 10BA materials, but with a microporous layer applied to one side. The 10BB sample is tested with the MPL facing down (toward the water injection) as well as facing up.

The breakthrough points for both SGL10BA and SGL10BB are shown in Figure 5.30 along with full capillary pressure curves obtained with the unmodified GCP method. The saturation of the plain GDL substrate material is 25% at a breakthrough pressure of 2500 Pa, while the sample with the MPL has a saturation of 4% at a breakthrough pressure of 5900 Pa. This is the first direct evidence that the MPL reduces the saturation of the GDL. This experiment also supports the theoretical considerations based on percolation theory outlined above.

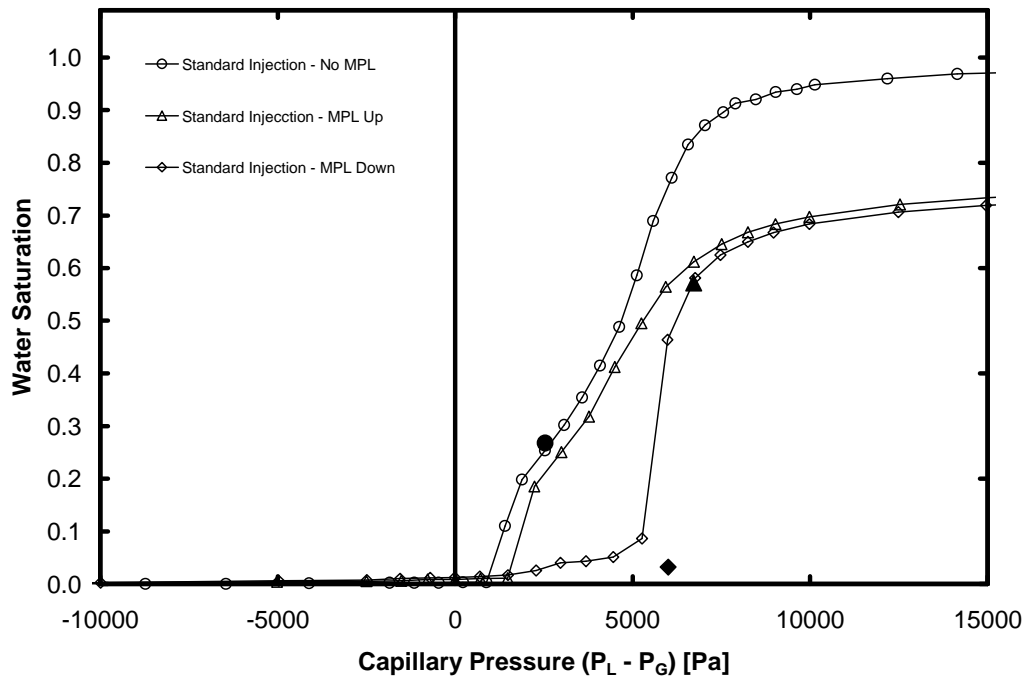


**Figure 5.30: Experimental results obtained using the GCP experiment modified to detect breakthrough. Breakthrough points are marked by solid circles.**

Also shown in Figure 5.30 are the full capillary pressure curves for 10BA and 10BB with the MPL facing both up and down. When the MPL faces up, water injects into the GDL first. In this case, the capillary pressure curve closely resembles that of the regular GDL since the MPL is not invaded at the pressures reached in this test. The water saturation only reaches 70% because the MPL intrudes into the GDL substrate and reduces the GDL pore volume as depicted in Figure 5.31. The breakthrough point is also obtained for the

MPL-up configuration. It can be seen that the GDL substrate is almost completely filled before the MPL is breached. The pressure of the breakthrough point corresponds very closely with that of the MPL-down configuration, as it should. The full capillary pressure curve obtained on the MPL-down configuration shows negligible water uptake until the MPL is breached. The sharp rise in saturation occurs as the GDL is rapidly filled once water breaks through the MPL. The MPL-up and MPL-down curves quickly converge onto the same line. Both curves reach a plateau at a reduced saturation signifying reduced pore volume in GDL due to the penetration of the MPL.

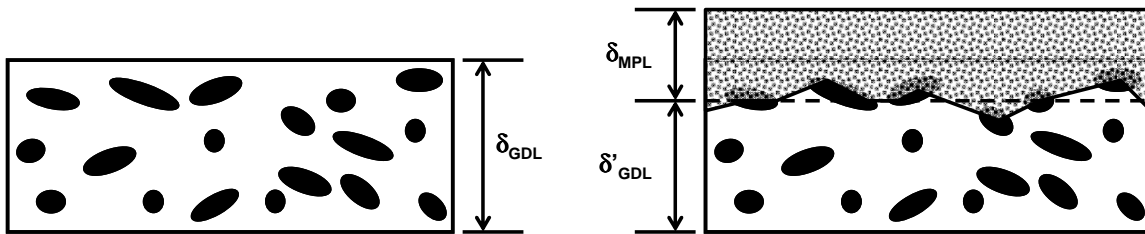


**Figure 5.31: Standard gas diffusion layer (left) vs. gas diffusion layer with microporous layer added (right), showing the loss of GDL substrate pore volume due to MPL penetration.**

The 10BB material shows a higher breakthrough pressure as expected, but a value of 3900 Pa is lower than expected given the pore size of the MPL. A close-up view of the MPL pores in Figure 5.32(left) shows that they are clearly well below 1  $\mu\text{m}$ , which implies capillary pressures in the range of  $> 50,000$  Pa. Clearly, water transport is occurring through cracks and defects in the MPL which are visible in Figure 5.32(right). These cracks are on the order to 10 – 20  $\mu\text{m}$  across and extend quite long. Entry pressures for such features would be an order of magnitude lower and therefore very close to the observed pressures. It is uncertain whether these cracks are continuous through the layer, but relatively low breakthrough pressure of the MPL suggests that they probably are continuous. Since cracks and defects appear to be the main conduits for water flow through the MPL, the conceptual picture needs to be reevaluated. It was previously proposed that water emerges at the GDL-MPL interface at discrete, isolated locations as a consequence of percolation through the MPL. If, instead, water flows through the MPL via cracks and defects, water will emerge at the MPL-GDL interface at cracks. However, since this also leads to point source water injection into the GDL, the

conceptual picture is unchanged. Interestingly, flow through the MPL via cracks would be beneficial since it eliminates the formation of dead-end clusters in the MPL that are characteristic of percolation processes (Figure 5.29). In fact, it might be advantageous to design the MPL with strategically placed holes and conduits for flow to optimize the benefits of point source injection into the GDL while reducing unnecessary infiltration of water into the MPL.

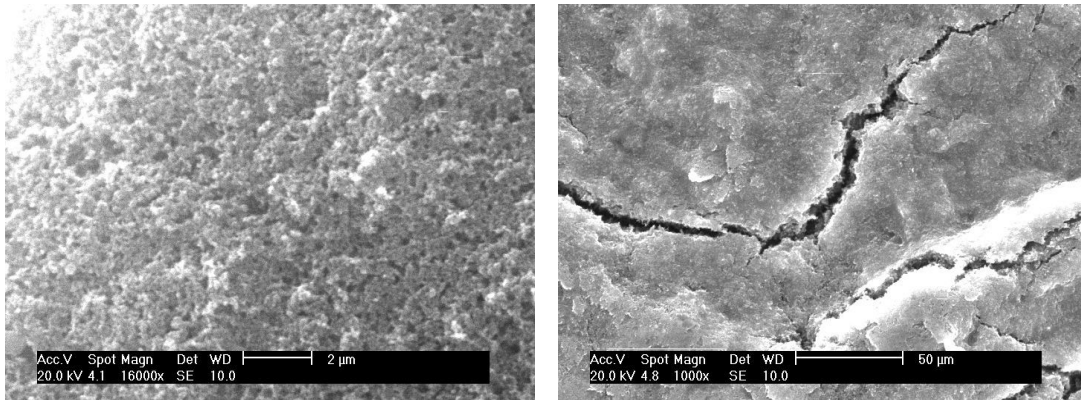


**Figure 5.32: SEM images of MPL from top. (Left) The MPL consists of very small pores, although its porosity is fairly high ( $\approx 70\%$ ) [123]. (Right) Large cracks exist over the surface. Further images of the MPL are available in Appendix B.**

### 5.3. Absolute Permeability

#### 5.3.1. In-plane Permeability

The dependence of in-plane permeability on porosity obtained for a number different GDL samples is shown in Figure 5.33. The in-plane permeability of two samples (10BA and P75) differ distinctly when measured in two perpendicular directions. Other samples show some tendency toward anisotropic behavior, but not to a significant extent (24BA and 34BA). The cloth material has only been tested in the  $0^\circ$  orientation due to the symmetry of the material when rotated  $90^\circ$ . Tests have also been performed on this material at  $45^\circ$  and yield results indistinguishable from those obtained at  $0^\circ$ . Only one experiment on the Toray 090 sample has been done due to limited material availability. Based on the random nature of this material, minimal anisotropy is expected. The permeability values for SGL 10BA are in the same range as those obtained by Ihonen *et*

*al.*[134], although direct comparison is not possible since the thickness was not reported in this earlier study. Mathias *et al.* [12] reported the permeability of Toray 060 to be in the range of  $5 - 10 \times 10^{-12} \text{ m}^2$  when compressed to 75% of its original thickness which is in agreement with the value obtained for the structurally similar Toray 090 tested here. The solid and dashed lines in Figure 5.33 correspond to the predictions of the Carman-Kozeny model with the constants given in the legend. A detailed analysis of this and other permeability models is given below.

The micrographs of the various materials in Figure 3.1 show the variability of their pore structures. The SGL samples (10BA, 24BA and 34BA) all contained 5 wt% PTFE sintered into the pore structure, while the others contained no PTFE. The two samples that show the most anisotropy in permeability (10BA and P75) also appear to have the most aligned fibers. The 10BA sample shows the most marked anisotropy in permeability with the higher value coinciding with the distinct “machine direction” [12]. The 24BA and 34BA samples consist of fibers randomly oriented in 2 dimensions and accordingly do not exhibit significant anisotropy in the plane. The Cloth ‘A’ material consists of woven bundles of fibers called ‘tows’. The tightly bundled tows would presumably have a lower permeability than the overall assembled woven structure.

As can be seen from the data in Figure 5.33, the GDL permeability is well described by the Carman-Kozeny model. The difference in the values of the constants is expected given the considerable differences in the fiber alignment and arrangement among the samples. Despite their structural differences, however, these materials still exhibit permeability with a common dependence on porosity that is well described by the Carman-Kozeny model.

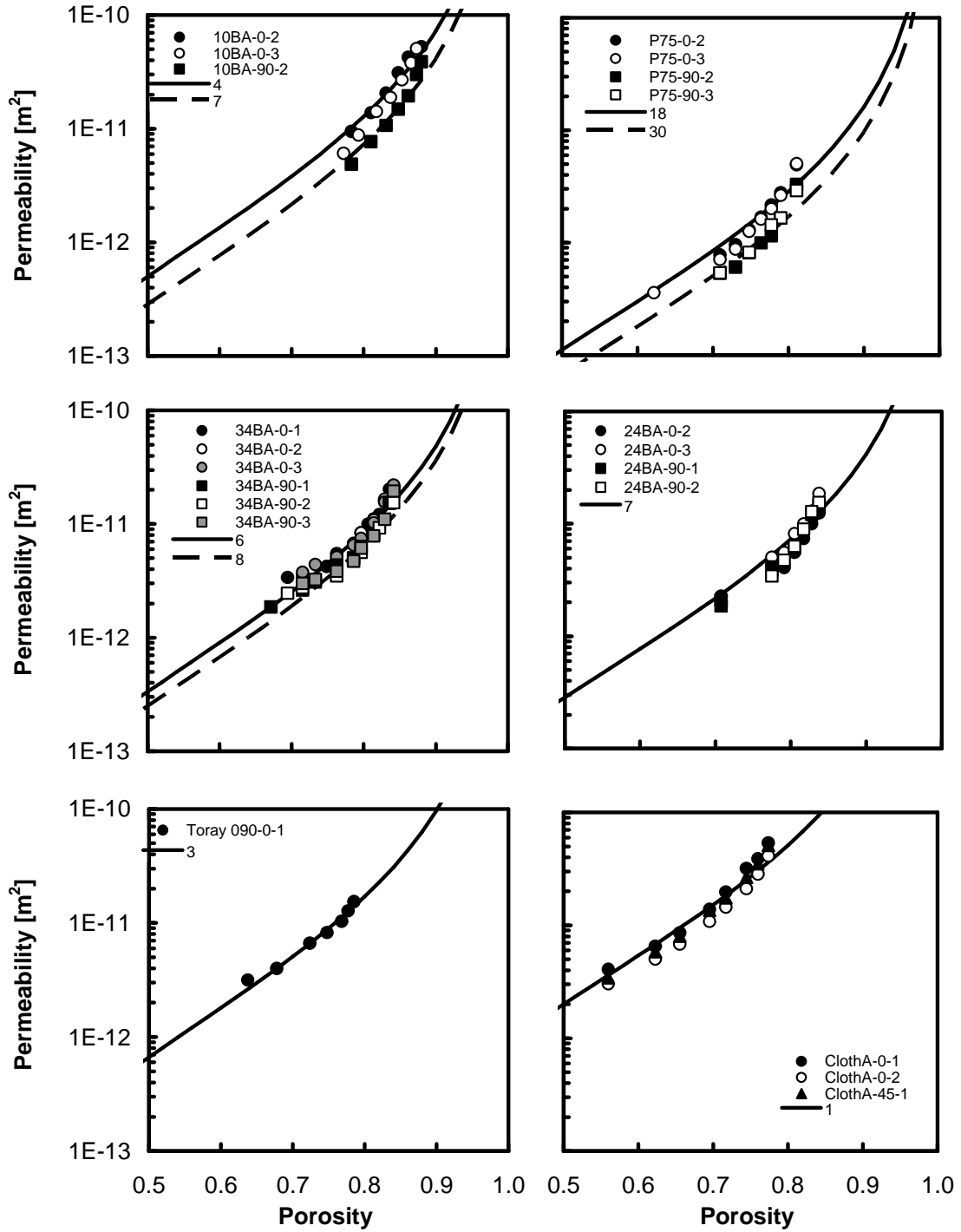


Figure 5.33: In-plane permeability vs. porosity results for several samples.

A more comprehensive model for the permeability of porous fibrous materials has been developed by Tomadakis and Sotirchos [186-188]. A summary of this model and a comparison to a large volume of literature data has been compiled by Tomadakis and Robertson[160]. The Tomadakis - Sotirchos (TS) model enables the prediction of anisotropic permeability through 1D, 2D and 3D random fiber beds without employing any fitting parameters. The model requires only fiber diameter and porosity specific to the material as input parameters. The TS model for absolute permeability is as follows:

$$K = \frac{\varepsilon}{8(\ln \varepsilon)^2} \frac{(\varepsilon - \varepsilon_p)^{(\alpha+2)} r_f^2}{(1 - \varepsilon_p)^\alpha [(\alpha + 1)\varepsilon - \varepsilon_p]^2} \quad (5.7)$$

where  $\alpha$  and  $\varepsilon_p$  are constants that depend on the fiber arrangement (aligned, random in 2D or 3D) and on the direction of flow relative to the planes of the fibers. The values of  $\alpha$  and  $\varepsilon_p$  for the various possible scenarios are given in Table 5.1. This model is compared with the experimental results in Figure 5.34. The data for Cloth 'A' have been omitted from the comparison due to its woven structure. The data for the P75 sample are also excluded since it contains a considerable amount of non-fibrous solids (i.e. filler or binder) and so has a substantially lower permeability than the other materials. All samples are considered to have a 2D random fiber structure for the purposes of selecting parameters from Table 5.1. The apparent fiber alignment in the 10BA sample suggests that the parameters for a 1D structure be appropriate. This approach predicts the permeability normal to the flow direction very well; however, the permeability parallel to flow is substantially over-predicted. On the other hand, the model could predict both directions reasonably well if a 2D structure is assumed and the parameters for parallel flow are applied to permeability in the direction of the fiber alignment (the 0° direction) and parameters for normal flow to the permeability in the 90° and through-plane directions. For the remaining samples, the parameters for normal flow are used to determine the through-plane permeability only and parallel flow parameters used for both in-plane directions. The results in Figure 5.34 show excellent agreement between the experimental in-plane permeability and those predicted by the TS model. The TS slightly over-predicts the permeability for the 10BA, 24BA and 34BA samples, presumably because of the presence of 5wt% PTFE in these samples. The Toray 090 sample which is well approximated by the TS model contains no PTFE.

**Table 5.1: Constants used in the TS model**

Structure	Flow Direction	$\epsilon_p$	$\alpha$
1D	Parallel	0	0
	Normal	0.33	0.707
2D	Parallel	0.11	0.521
	Normal	0.11	0.785
3D	All Directions	0.037	0.661

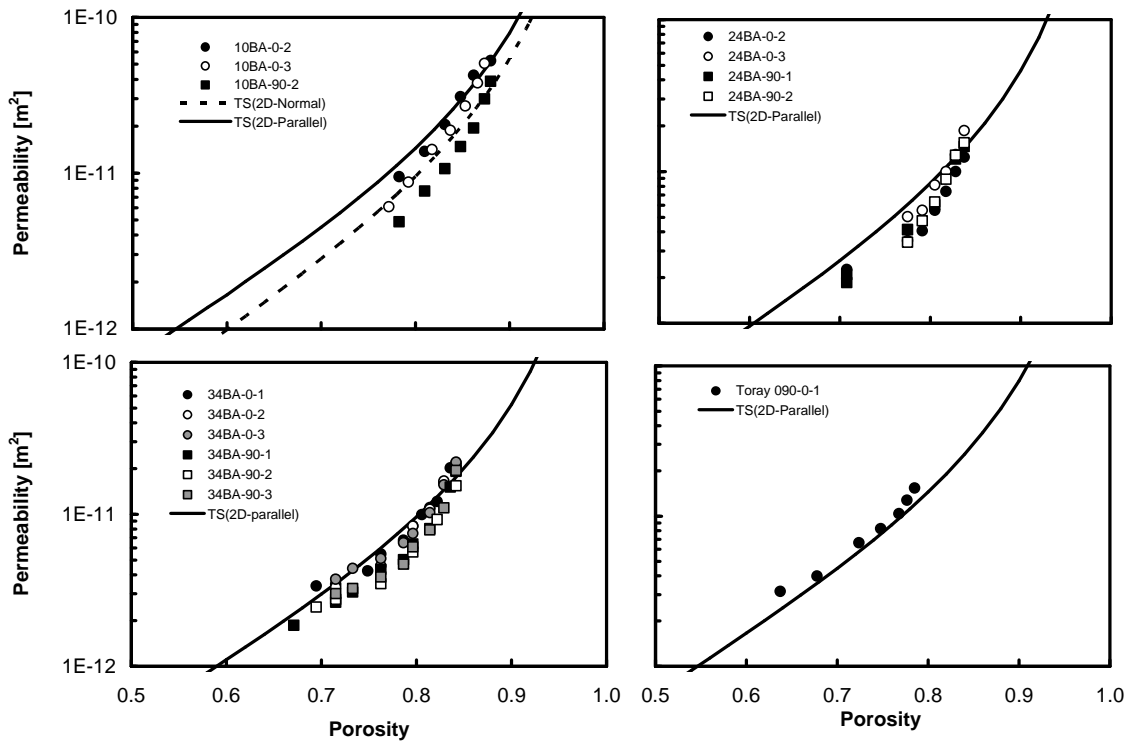


**Figure 5.34: Comparison of experimental results to the predictions of the TS model, Eq.(5.7). The solid lines were calculated using parameters for 2D parallel flow. The dashed line was calculated using parameters for 2D normal flow.**

### 5.3.2. Through-Plane Permeability

Through-plane permeability values for all samples are presented in Table 5.2. The values reported are the average of three replicates. The average deviation of each replicate from the mean is also reported in Table 5.2. Comparison of these results with available literature values shows good agreement. Williams *et al.* [133] found the through-plane

permeability for SGL 10BA and Toray 120 to be  $31.0 \times 10^{-12} \text{ m}^2$  and  $8.69 \times 10^{-12} \text{ m}^2$ , respectively. Toray 120 is slightly thicker than the Toray 090 material used in the present study, but the permeability of this material should be similar given that its structure is similar. Ihonen *et al.* [134] reported a value of  $18 \times 10^{-12} \text{ m}^2$  for SGL 10BA in the through-plane direction. Ihonen *et al.* [134] found the in-plane permeability to be twice as high as the through-plane value which is in agreement with the present findings. Mathias *et al.* [12] tested the through-plane permeability of Toray 060 and obtained a range between 5 and  $10 \times 10^{-12} \text{ m}^2$ . This is similar to their reported value for in-plane permeability of a compressed sample, indicating that the through-plane permeability is lower. Use of the TS model to predict the through-plane permeability also shows good agreement with experimental results. For instance, the through-plane permeability of Toray 090 is estimated by Eq.(5.7) using parameters corresponding to flow normal to the fibers to be  $7.78 \times 10^{-12} \text{ m}^2$ , which compares well with the experimental value of  $8.99 \times 10^{-12} \text{ m}^2$ .

**Table 5.2: Through-plane permeability values**

Material	$K_z$ [ $\text{m}^2$ ]	Average Deviation [%]	TS Model [ $\text{m}^2$ ]
SGL 10BA	$37.4 \times 10^{-12}$	3.76	$35.3 \times 10^{-12}$
SGL 24BA	$14.5 \times 10^{-12}$	7.02	$7.35 \times 10^{-12}$
SGL 34BA	$16.3 \times 10^{-12}$	5.05	$6.34 \times 10^{-12}$
Ballard P75	$5.70 \times 10^{-12}$	5.96	---
Toray 090	$8.99 \times 10^{-12}$	1.01	$7.78 \times 10^{-12}$
E-Tek Cloth 'A'	$69.4 \times 10^{-12}$	5.26	---

### 5.3.3. Inertial Coefficient

Eq.(2.17) can be fit to the data for the variation of in-plane air flux with pressure drop to yield the inertial coefficient  $\beta$ . This coefficient is known to vary with permeability [198]. Liu et al. [217] developed the following correlation between  $\beta$  and permeability from data collected from the literature:

$$\beta = 2.88 \times 10^{-6} \frac{\tau}{\varepsilon K} \quad (5.8)$$

Figure 5.35 shows the variation of inertial coefficient with permeability obtained for all materials and directions tested in the current study along with the correlation given in Eq.(5.8). For this analysis, the tortuosity of each sample is estimated using the Bruggeman relation (Eq.(2.23)).

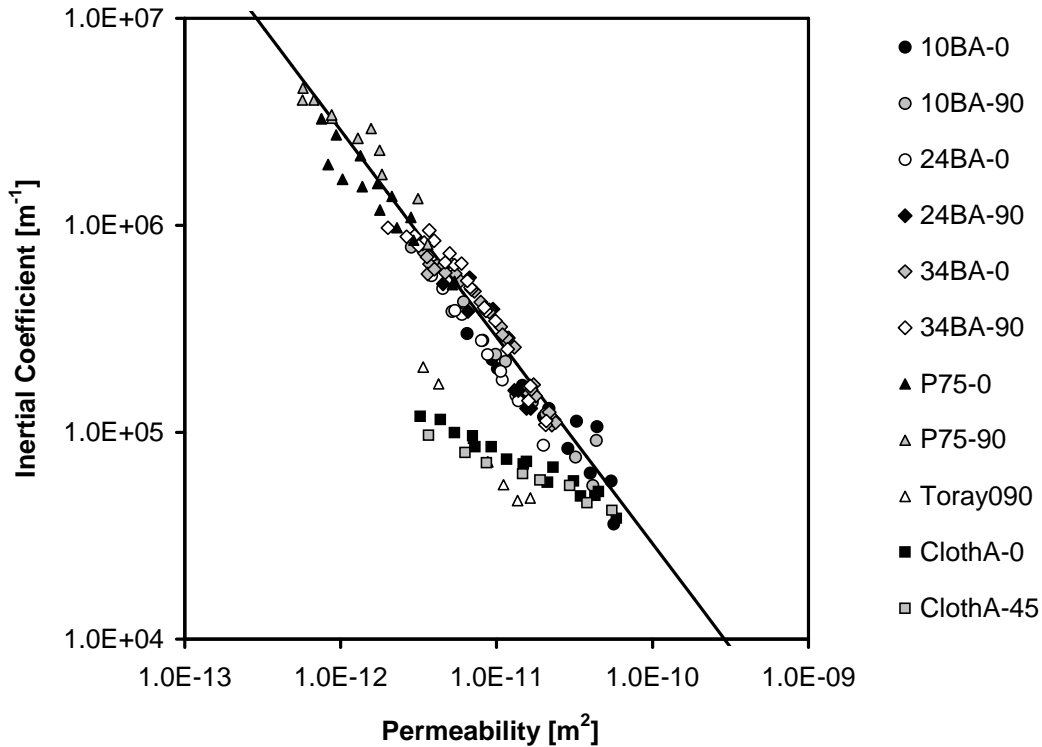


Figure 5.35: Inertial coefficient vs. permeability for all materials tested. Solid line represents the correlation of Liu et al. [217].

With the exception of Toray 090 and E-Tek Cloth ‘A’, these results follow a similar trend as expected and described by the correlation of Liu *et al.* [217]. The deviation of Cloth ‘A’ from this trend is not too surprising due to its woven structure. The variation in the behaviour of Toray 090 is somewhat surprising given that its structure is similar to that of the other paper samples; however, this may be due to the fact that Toray 090 has a much more distinctly fiber-like web structure with no PTFE, binder or filler contained between the fibers. An analysis of the importance of inertial pressure losses occurring in the GDL during PEMFC operation is given in below.

The Darcy equation (Eq.(2.16)) is a special case of the more general Forchheimer equation (Eq.(2.17)) and is only applicable for creeping flow rates through porous media. When the flow rate is higher, inertial losses become significant and Darcy's law does not accurately describe pressure drops. Zeng and Grigg [218] have recently discussed the problem of determining the point at which inertial effects become significant. To assess this quantitatively, they defined a dimensionless Forchheimer number ( $Fo$ ) as the ratio of the inertial pressure loss contribution to the viscous pressure drop contributions:

$$Fo = \frac{K\beta\rho v}{\mu} \quad (5.9)$$

This definition of  $Fo$  is equivalent to the Reynolds number where  $K\beta$  is the characteristic length [198]. A higher value of  $Fo$  signifies that inertial effects are more important and that the use of Darcy's law to calculate pressure drops becomes increasingly inaccurate. The amount of error incurred by neglecting inertial effects can be calculated as follows:

$$E = \frac{Fo}{1 + Fo} \quad (5.10)$$

In their work, Zeng and Grigg suggested that an error of 10% is tolerable for most engineering calculations, which sets the critical  $Fo$  number at 0.11. An error tolerance of 10% is arbitrary since some applications may require higher accuracy. It is worthwhile to determine  $Fo$  values for conditions typically prevailing during PEMFC operation to determine whether inertial effects need to be considered. The data of Williams *et al.* [169] provide an excellent test case for this calculation since these showed that convection through the GDL was significant. In their experiments, Williams *et al.* varied the inlet flow rate of air to the cathode between 0.050 and 0.500 SLPM. Based on the description of the experimental conditions, the mass flow rate of heated and humidified air into the cell is estimated to vary between 1.5 and  $15 \times 10^{-6}$  kg/s, which corresponds to a mass flux along the single serpentine flow channel of 2.2 to 22 kg/m<sup>2</sup>·s and a channel Reynolds number ranging from 110 to 1100. It is impossible to know precisely how much of this flow bypassed the channel and flowed through the GDL. Nonetheless, the modeling of Pharaoh [170] suggests that about 10% of the flow bypasses through the GDL when the

channel  $Re$  is 100 for a similar geometry and GDL permeability. Using this estimate with the Williams et al. [169] data for an inlet flow of 0.05 SLPM (i.e.  $Re_{\text{Channel}} = 110$ ), the mass flux through the GDL is about  $0.025 \text{ kg/m}^2 \cdot \text{s}$ , where the flow area is based on a channel length of 0.025 m and a GDL thickness of 250  $\mu\text{m}$ . In order to calculate  $Fo$ , an estimate of the transport properties appropriate for the experiments of Williams et al. [169] is required. To do this, parameters of Toray 090 are used (i.e.  $d_t$ ,  $t_o$ ,  $\varepsilon_o$ ). Compressed porosity is estimated by inserting a compressed thickness of 250  $\mu\text{m}$  into Eq.(3.10). Compressed porosity is used to calculate both permeability and tortuosity using the TS model. The inertial coefficient is not calculated using Eq.(5.8) since Toray 090 deviates significantly from the correlation. Instead, the experimentally measured  $\beta$  of  $8.22 \times 10^4 \text{ m}^2$  for  $t_c = 250 \mu\text{m}$  is used. The resulting  $Fo$  value corresponding to this mass flux is only 0.0013. However, if instead it is assumed that 50% of the gas bypasses through the GDL with the highest flow rate used by Williams et al. [169] (0.5 SLPM,  $Re_{\text{Channel}} = 1100$ ) the  $Fo$  number becomes 0.055, indicating an error of 5.2% is incurred by use of Darcy's law. This error is not negligible and the  $Fo$  number could increase to even higher values under different circumstances, such as the use of a larger cell or higher inlet humidity.

#### 5.4. Tortuosity

In addition to predicting the permeability as a function of porosity, the TS model provides a means of estimating tortuosity which is used to calculate the effective diffusivity as described by Eq.(2.22). The ability to predict the change in effective diffusivity in a compressed GDL would be useful since many recent fuel cell models include the under-land area in the modeling domain. Even a fuel cell model that does not consider convection in the GDL requires this information. Tortuosity is more commonly predicted using the Bruggeman equation given in Eq.(2.23). The main benefit of using the TS model rather than the Bruggeman equation is that the effect of anisotropy can be included in estimating the effective diffusivity. Using the 2D parameters from Table 5.1, the values of effective diffusivity determined from TS model are about 20% lower those obtained using the Bruggeman relationship. Also, the TS model predicts that the tortuosity will vary by as much as 15% between the in-plane and through-plane directions.

## 5.5. Relative Permeability

Relative permeability calculations using the pore network model are based on the assumption that the pore-scale fluid occupancy is dictated exclusively by capillary forces – an assumption appropriate for low capillary number displacements. To examine the effect of GDL anisotropy, the effective permeability has been calculated in the  $x$ ,  $y$  and  $z$  directions through the network to yield the results plotted in Figure 5.36. Non-wetting fluid invasion is always in the through-plane direction, which corresponds to liquid water flow from the catalyst layer, where it is generated, through the GDL to the flow channels. Also shown in Figure 5.36 for comparison are the curves obtained using Eq.(2.19) with  $a = 3$  for the two GDL materials. Since these results have been normalized for the intrinsic anisotropy of each material, the directional differences observed reflect the anisotropic effects caused by the presence of liquid water. This saturation dependent anisotropy is due to the preferential spreading of the invading phase in the direction of highest permeability, which is the direction of largest and most easily invaded pores. One of the major consequences of water spreading preferentially in the plane of the material is the significant reduction of gas transport in the through-plane direction. This suggests that the ideal GDL is one where the typical anisotropy ratio is not only minimized, but reversed. Higher through-plane permeability would simultaneously limit detrimental liquid water spreading and increase the intrinsic transport rates to the catalyst layer. A broad analysis of the effects of anisotropy in the GDL is given by Pharaoh *et al.*[219].

An important feature of these results is the non-zero liquid water saturation required for liquid water to break through the GDL. For Toray 090, the simulations show that liquid water saturations of 20% are necessary before a continuous liquid path spans the full thickness of the GDL. For SGL 10BA, the necessary liquid saturation is 10%. Below this critical liquid saturation, the liquid water permeability through the GDL is zero. This behavior is not described by the general form of the relative permeability function in Eq.(2.19) which predicts finite water permeability at vanishing water saturations. Despite this failure, the results obtained using Eq.(2.19) (i.e. the dashed line) agree reasonably

well for liquid flow in the through-plane direction.

Predictions of the relative gas phase permeability are also shown in Figure 5.36. The gas phase permeability has been calculated for both cases discussed in Section 4.1.5.3. In Case 1, the residual gas in an invaded pore offers no conductivity and gas flows entirely through the network of connected gas-filled pores. In Case 2, gas is allowed to flow through the non-filled portion of invaded pores. Both of these cases are somewhat unrealistic, for Case 1 prevents any flow through the space occupied by gas within water-invaded pores whereas Case 2 allocates to this space the hydraulic conductance of a straight conduit of reduced size. These cases, therefore, provide lower and upper bounds of gas permeability, respectively. The Case 1 results show that no gas conductivity exists above a critical water saturation of 65% for Toray 090 and 70% for SGL 10BA. A significant amount of gas still exists in the network at this critical saturation, but it is completely surrounded or trapped by the invading phase and is hydraulically disconnected from either the gas inlet or outlet face. Case 2 does not show a critical water saturation, since all trapped gas pores maintain some hydraulic conductivity. This case matches the behavior of Eq.(2.19) very closely. Since Case 2 unrealistically allows gas transport to occur unimpeded through the corners of pores that are mostly filled with water, then Eq.(2.19) must also represent a limiting case. Eq.(2.19) requires  $a$  to be about 5 to match the model results for Case 1.

Cases 1 and 2 exhibit other differences due to anisotropy as liquid water saturation is increased. Case 1 shows significantly reduced permeability in the through-plane direction due to spreading of liquid water in the  $x$ - $y$  direction, whereas Case 2 shows little to no anisotropy caused by additional liquid water. The latter effect arises because gas can leak through a pore even if it is mostly filled with water and allow pockets of trapped gas phase to contribute to mass transfer, thus minimizing the impact of in-plane liquid spreading.

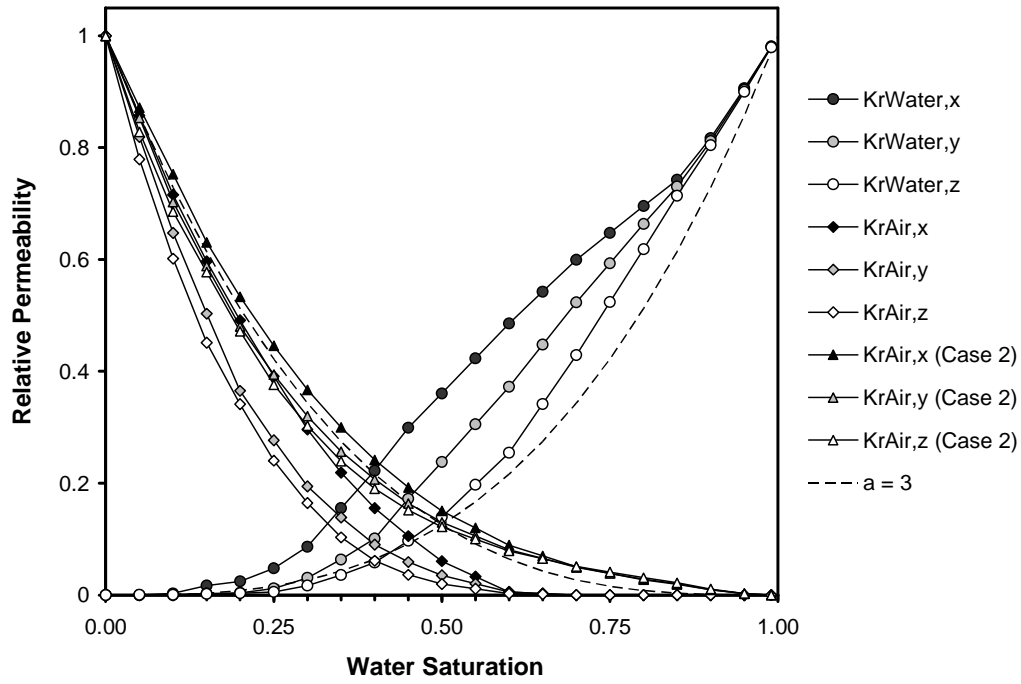


Figure 5.36: Relative permeability predictions of the pore network modeling for SGL10BA

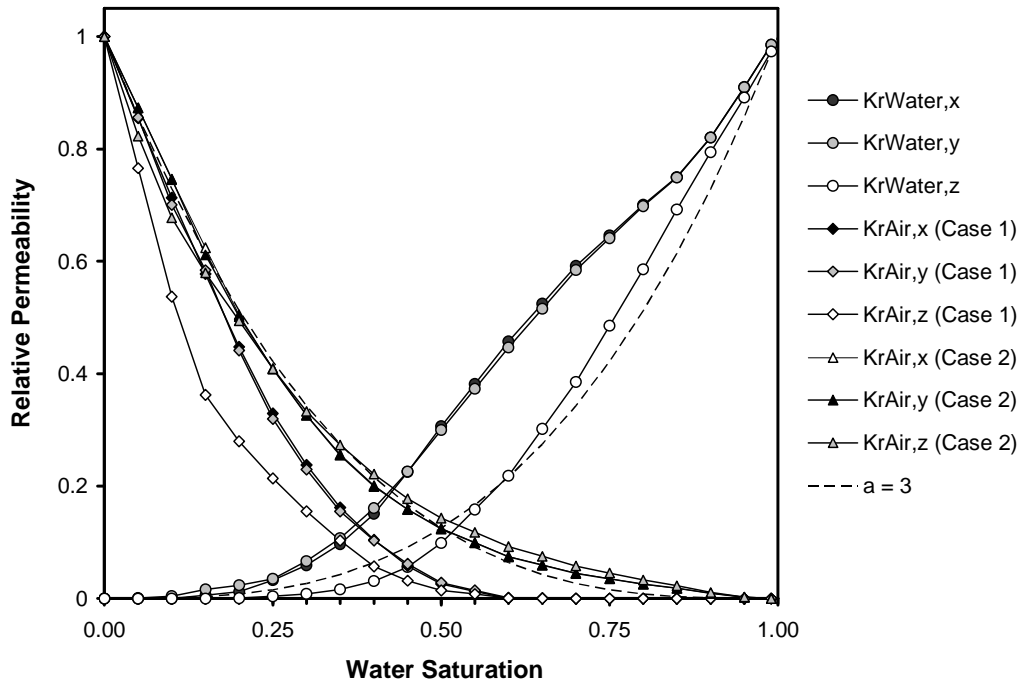


Figure 5.37: Relative permeability predictions of the pore network model for Toray 090A

As outlined in Chapter 2, a number of experimental and numerical results for relative gas and liquid permeability have recently appeared in the literature. These are plotted in Figure 5.38 and Figure 5.39. Also plotted in both figures are the results of the pore network model for Case 1 and the typically used relationship  $k_{rP} = (s_P)^a$  where  $a = 3$ . Only the experimental results of Koido *et al.* [95] agree with the pore network model predictions for relative gas permeability. Unfortunately, very little experimental detail was provided so confidence in their results is limited. The results of Becker *et al.* [149] are computed from 3D tomography data. The data of Nguyen *et al.* [220] was obtained for a different material but is shown here to provide a complete summary of scarce literature data. Owejan *et al.* [180] obtained their results from in-situ fuel cell data and required a highly convoluted analysis of flow conditions.

Fewer results are available for relative liquid permeability. Koido *et al.* [95] present values computed using the lattice-Boltzmann method on simulated microstructures. They found permeability values somewhat higher than that obtained by the pore network model. Sole [22] attempted to measure relative liquid permeability for GDL with and without PTFE coating, but the results are substantially lower than expected.

The available literature data for both relative gas and liquid permeability are rather scattered and a definitive experiment has yet to be performed. Nonetheless, the pore network model predictions are not unreasonable and still represent the best available estimate for these important multiphase flow properties.

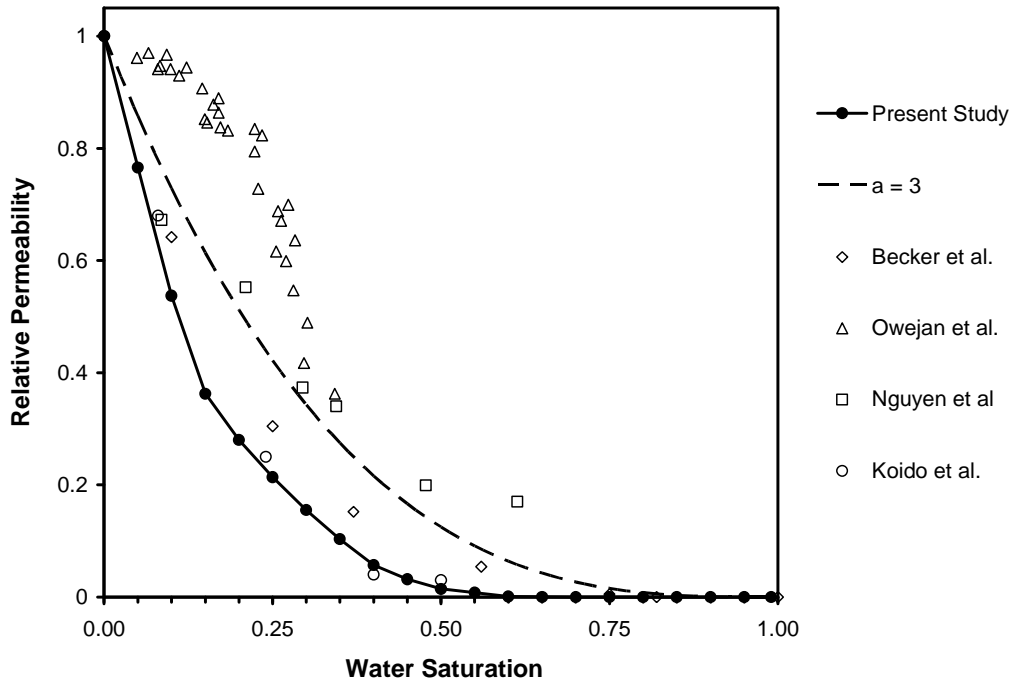


Figure 5.38: Through-plane relative gas permeability data collected from literature sources

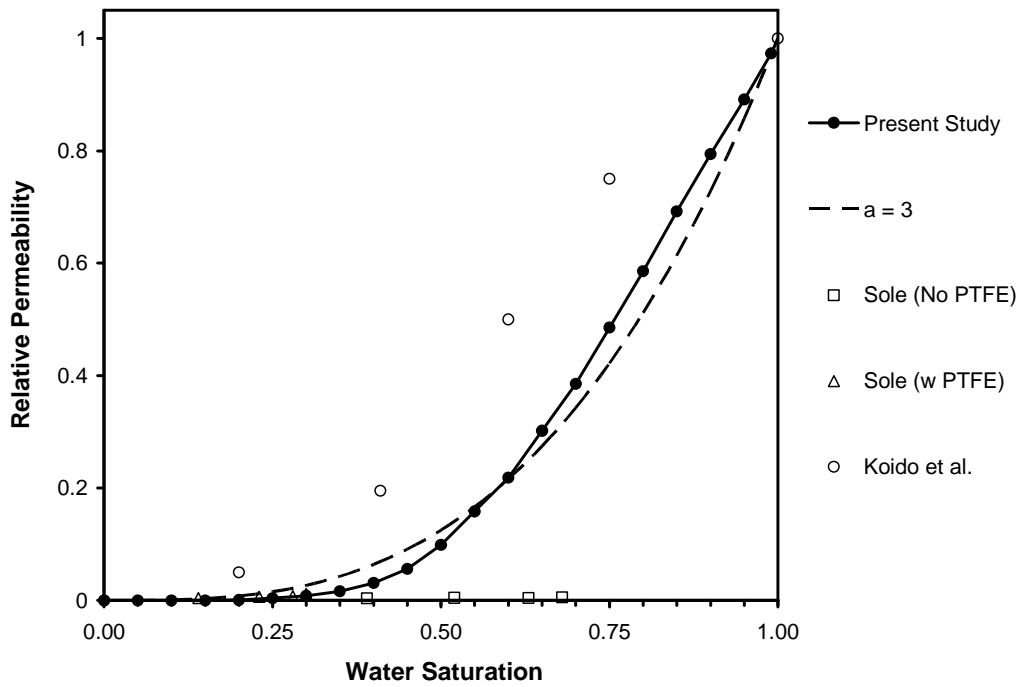


Figure 5.39: Through-plane relative liquid permeability data collected from literature sources

## 5.6. Relative Effective Diffusivity

The pore network model has also been used to calculate relative effective diffusivity in a GDL using invasion percolation concepts that more realistically describe the configuration of water expected in an operating fuel cell. Specifically, liquid water is injected into the network in the through-plane direction to simulate liquid water flowing from the catalyst layer to the gas channels. The present model also includes pore and throat size distributions that adequately reproduce both the absolute permeability and effective diffusivity through a dry network. The results are shown in Figure 5.40 along with those using Eq.(2.22) with  $a = 2$  [32].

The difference between Case 1 and Case 2 is much more dramatic for gas diffusivity than for gas permeability. This is due to the fact that diffusive conductivity is proportional to the area available for transport, while hydraulic conductivity is proportional to the square of the area. Since the area for transport through a pore is assumed to be proportional to the volume fraction of a pore that is filled with gas, the diffusive conductivity is much less hindered by the partial filling of pores. The large discrepancy between these two limiting cases underscores the need for experimental data concerning these transport processes. An argument against Case 2 is that not only does it fail to display a critical water saturation (above which effective gas diffusivity is zero), but it predicts significant diffusivity at near full-water saturation ( $D_{rG}(s_w = 0.9) = 0.1$ ), which appears unrealistic. Case 1 shows a significant decrease in diffusivity as water invades the network. Diffusivities predicted in Case 1 can be several times lower than those obtained using Eq.(2.20). An exponent of  $a = 5$  would be necessary in Eq. (2.22) to approximate the behavior of the network model in this case. Clearly, current models could be significantly overestimating the transport rates through partially saturated GDLs.

Also shown in Figure 5.40 are the liquid phase diffusivities. These values are not of direct interest to PEMFC performance calculations since liquid phase diffusion of reactants through the GDL is not significant. However, an area of research that is becoming increasingly active is the transport of ionic contaminants (e.g. Fe(II)) in the liquid phase, and the present results provide an estimate for such transport.

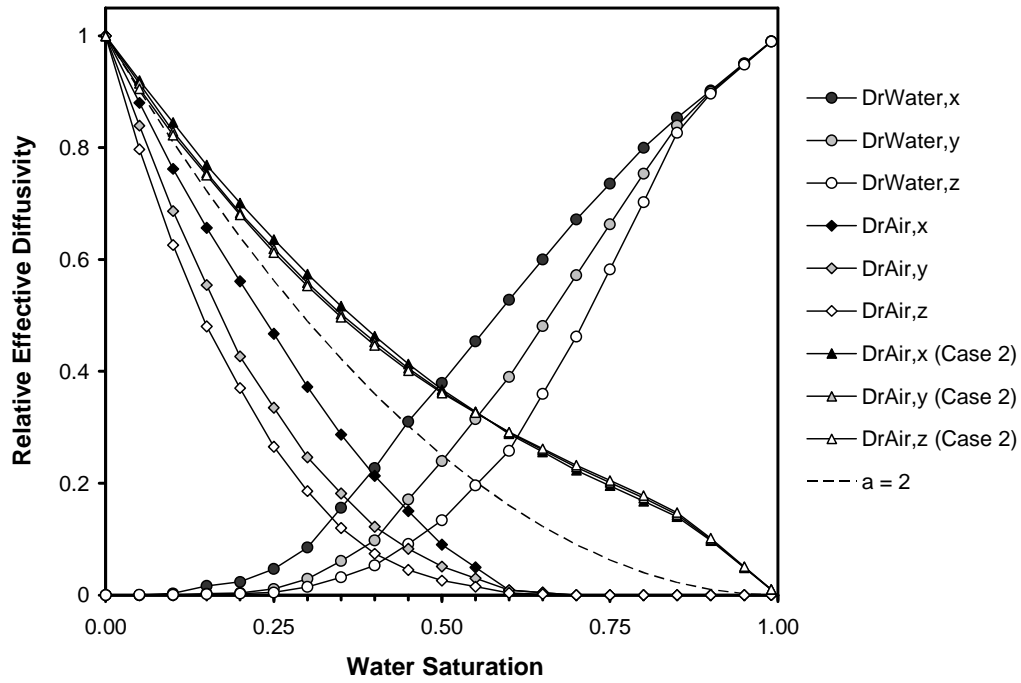


Figure 5.40: Relative effective diffusivity results predicted by the pore network model for SGL10BA

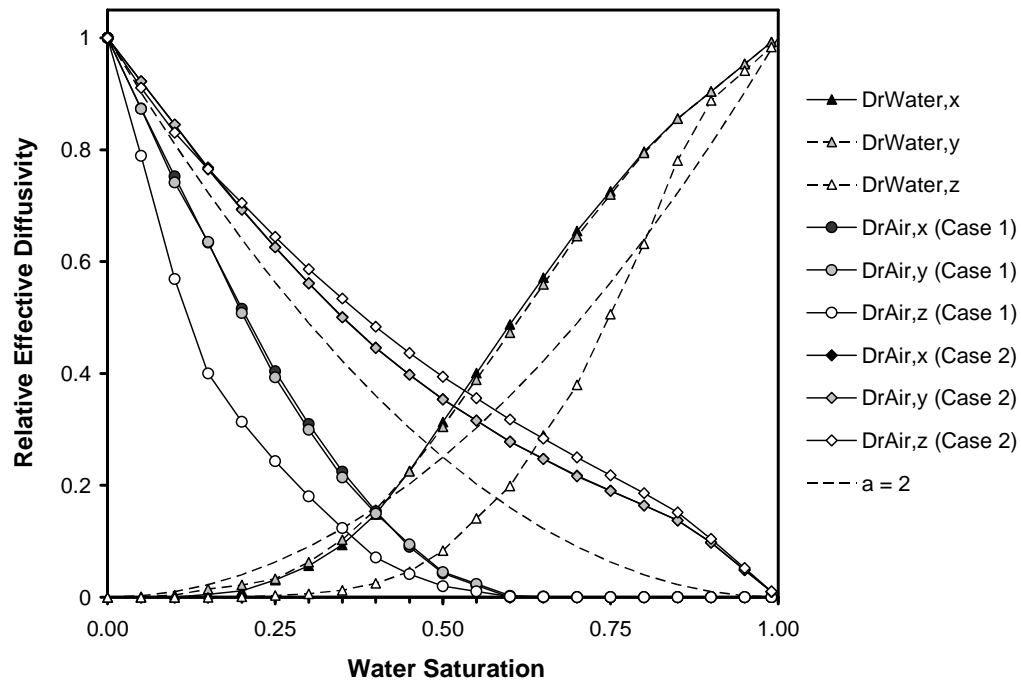
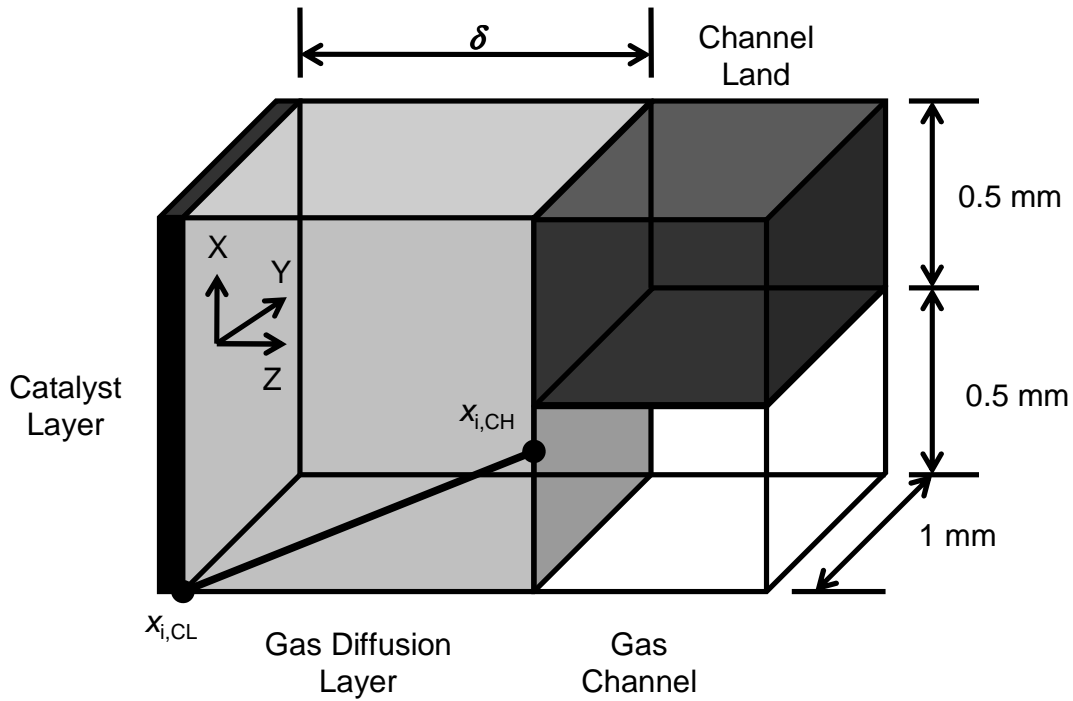


Figure 5.41: Relative effective diffusivity results predicted by the pore network model for Toray 090A

## 5.7. Limiting Current Calculations

An effort has also been made to use the pore network model developed during this thesis to predict the limiting current in an operating PEMFC assuming that the GDL is the sole source of mass transfer resistance. This is undertaken in order to determine if and when mass transfer resistance in the cathode GDL becomes a significant portion of the overall mass transfer resistance [221]. From an estimation of the maximum rate of oxygen mass transfer that can be expected through a partially saturated GDL, the limiting current is calculated and compared with values typically observed in operating cells.

The modeled domain is shown in Figure 5.42. The size of the domain is equivalent to  $1 \text{ mm} \times 1 \text{ mm} \times \delta$ , where  $\delta$  is the GDL thickness. This corresponds to a domain size of  $40 \times 40 \times 12$  pores for Toray 090 and  $26 \times 26 \times 10$  pores for SGL 10BA. On the channel side of the domain, half of the inlet face is blocked to simulate the effect of 1 mm lands and channels. The conditions in the flow channel are taken as fully humidified air at  $80^\circ\text{C}$  and 10 kPa gauge. The catalyst layer is treated as a reactive interface where the oxygen concentration is zero (i.e. limiting current conditions). Since the cell is fully humidified, no diffusion of water vapor occurs and all water generated by the electrochemical reaction is in the liquid state. As a result, the mass flux through the GDL is considered to occur by molecular diffusion of  $\text{O}_2$  through a stagnant film of  $\text{N}_2$  and  $\text{H}_2\text{O}$ . This allows the multicomponent diffusion problem to be reduced to a binary diffusion problem, provided that the diffusion coefficient is calculated with appropriate consideration for the composition of the stagnant gas mixture [222]. Once the mass flux through the GDL is known, the current density is found from Faraday's Law.



**Figure 5.42: Modeled domain for limiting current calculations**

The predicted limiting currents for both GDLs and both wetting phase conductivity cases are given in Figure 5.43. The limiting currents through dry Toray 090 and dry SGL 10BA are very similar to each other. Although Toray 090 is 25% thinner than SGL 10B, it is less porous and has a lower intrinsic effective diffusivity. These two factors offset each other and neither GDL is clearly better in terms of mass transfer performance under dry conditions. As water is added to the GDLs, however, the performance of the two materials diverges; the limiting current for SGL 10BA drops more quickly. This can be attributed to the increased spreading of liquid water in the  $x$ - $y$  plane of this material.

The overall behavior for both materials shows a dramatic decrease in limiting current as the GDL fills with water. At low water saturations (<10%), the predicted limiting current through the GDL is higher than that in a typical fuel cell, which can be between 1 and 2  $A/cm^2$ . This indicates that the GDL is not the main source of concentration polarization under relatively dry conditions and performance is limited by other factors (i.e. the catalyst layer or electrolyte phase). When the GDL becomes wet, however, a significant reduction in the limiting current occurs due to mass transfer resistance in the GDL. Case

1 predicts that at water saturations above 25% the maximum current density is less than 1 A/cm<sup>2</sup>, indicating that mass transfer resistance through the GDL could be a dominant factor limiting PEMFC performance. The limiting currents for Case 2 do not drop as sharply in the presence of water and 75% saturation must be reached before it reaches 1 A/cm<sup>2</sup>.

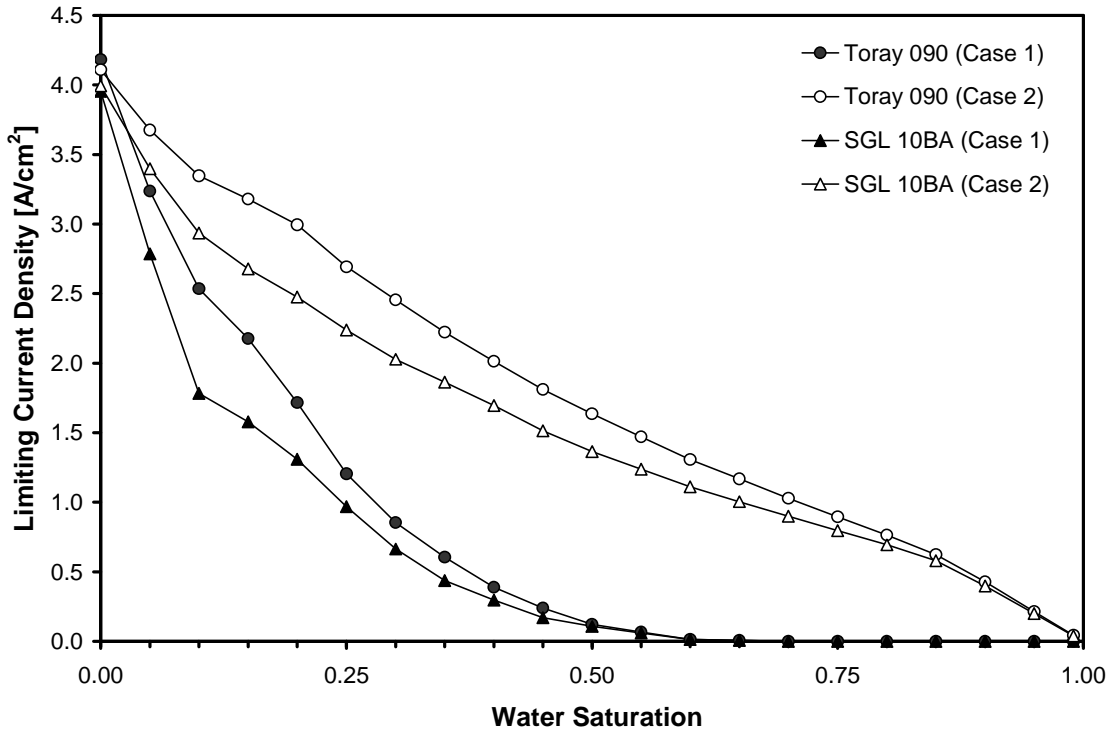


Figure 5.43: Limiting current predicted by pore network modeling as a function of GDL saturation

At present, insufficient experimental evidence is available to fully understand the configuration and connectivity of the residual gas phase in GDL pores invaded by water. Some experimental evidence concerning the amount of liquid water in the GDL of an operating fuel cell does exist, however. Kramer *et al.* [223] used neutron imaging to measure the water content in the cathode GDL during fuel cell operation and found saturations between 25% and 35% at limiting currents between 0.6 and 1.0 A/cm<sup>2</sup>, which corresponds very closely with the results of Case 1. Other neutron imaging studies suggest a limiting current above 1 A/cm<sup>2</sup> at somewhat higher water saturation (30% - 60%) [224,225], which lies between Case 1 and Case 2. Obviously, more conclusive evidence is needed to verify the present model, but the reasonable agreement with these

experimental results does lend support to the applicability of the network modeling approach.

## 6. Conclusions

This work has focused on the characterization of the capillary and transport properties of gas diffusion layers used in polymer electrolyte membrane fuel cells. At the outset of this project, the state of knowledge about GDL properties was such that researchers developing fuel cell models were forced to use the properties of porous materials such as rocks, sand and packed beds as a substitute for unknown GDL properties. Throughout the course of this work, efforts have been made to address this knowledge gap. Particular emphasis was placed on studying the capillary properties of GDLs since liquid water behavior in fuel cells is critical to overall performance.

### *Air-Water Capillary Properties*

The investigation of air-water capillary properties of GDLs is perhaps the most significant undertaking in this thesis. This effort was divided into two phases. Initial efforts were made to measure the air-water capillary pressure curve using the Method of Standard Porosimetry (MSP). The results of this work were published and represented the first such data available in the literature with respect to such properties [123]. The timely nature and the importance of the data have garnered this paper more than 40 citations to date. Furthermore, the data contained in this paper have been used in a variety of fuel cell modeling studies and performance evaluation efforts. However, we have found this method to be less than satisfactory since it only measures a limited portion of the capillary pressure curve. Furthermore, the results obtained by this method suggest that GDLs possess a mixture of strongly hydrophilic and hydrophobic pore space, but subsequent reports in the literature have contradicted this finding [20,124]. A second effort was made to obtain more definitive measurements of the air-water capillary pressure curves. We developed a method called Gas Controlled Porosimetry (GCP) to address the shortcomings of the MSP technique and improve upon other methods reported subsequent to the first MSP publication. The GCP technique shows that GDLs are hydrophobic upon water injection, even without hydrophobic treatments. This has also been confirmed by Benziger *et al.* [124]. The addition of hydrophobic polymer coating to the GDL does render the material more hydrophobic, but no dramatic changes

in the capillary pressure curves are observed. The GCP method is also able to perform water withdrawal experiments from GDLs. In this case, it was observed that GDLs behave as hydrophilic materials, even those treated with a hydrophobic polymer. This switching of wettability states depending on whether water is injected or withdrawn may not be that surprising considering the contact angles and geometry of the material involved. Since water is neither highly wetting nor non-wetting on the constituent materials, the wettability behavior is controlled by structural effects such as contact angle hysteresis and converging-diverging pore geometry. This may provide an explanation for the hydrophilic-hydrophobic duality of GDLs suggested by the early MSP results.

The GCP technique was modified to detect the breakthrough point of GDLs, providing for the first time a measurement of the saturation and pressure at the point of water breakthrough the GDL. This was used to study the role of the microporous layer (MPL), which is known to improve fuel cell performance although its mechanism is uncertain. It was found that water injection through a GDL with an MPL resulted in much lower breakthrough saturations than water injection through a GDL alone. An explanation for this behavior was offered based on percolation concepts.

#### *Permeability Tensor*

The gas permeability of several common GDL materials was measured in three perpendicular directions. In-plane measurements were made as a function of compressed GDL thickness. Not only does the demonstrated method enable a better description of in-situ cell conditions where considerable GDL compression exists, but it also provides a means of varying the porosity of the sample. The data were well described by the Carman-Kozeny model which predicts permeability as a function of porosity. Carman-Kozeny constants were determined for each material for both in-plane directions. The data were also compared to the permeability model of Tomadakis [160] and found to agree well. This predictive model requires no fitting parameters and can be applied to anisotropic materials. Through-plane and in-plane permeability were both well predicted. An added benefit of this model is that it also allows estimates of the tortuosity and effective diffusivity to be made that account for the anisotropy of the material.

This work should prove useful to future modeling studies that aim to describe 3D effects in PEMFCs since the determination of permeability in the three directions described here will allow the formulation of a permeability tensor. Also, an estimate for the effective diffusivity tensor can be made based on these findings. The detailed investigation of the effect of GDL compression on permeability in this study will also be valuable for further improving the assembly method of PEMFC stacks.

### *Multiphase Transport Properties*

A pore network model was developed to help understand the multiphase flow properties of GDL materials and estimate their multiphase flow and transport properties. A detailed description of the model was provided, with particular emphasis on integrating into the model both qualitative and quantitative aspects of the microstructure of high-porosity fibrous GDLs. The model was calibrated to two commonly used GDL materials by adjusting the model parameters to match available experimental results, specifically the absolute permeability tensor and drainage capillary pressure curves. Material-specific relative gas and liquid permeability and diffusivity were computed as functions of water saturation under conditions of quasi-static drainage of air by water. Transport rates through the pore network were also determined. The results of these simulations were compared with commonly used models of relative permeability and diffusivity. It was found that commonly used literature models tended to overestimate mass transfer in the gas phase. Typically used literature models fail to consider threshold saturations and phase continuity.

### *Fuel Cell Simulation*

Limiting current calculations based on GDL saturation limits were performed by implementing PEMFC boundary conditions and physical parameters on the network model. The limiting current was estimated at various water saturation levels for a GDL section in which one-half was open to the gas channel and the other half was covered by a land. It was shown that a dry GDL can support limiting currents of nearly  $4 \text{ A/cm}^2$ , much more than is typically observed in operating fuel cells. When liquid water is present in

the GDL, however, the predicted limiting current decreases rapidly to values typically observed in operating PEMFCs, indicating that mass transfer through the GDL may indeed be rate limiting at high current densities when the GDL is saturated with water. This is the first, and so far only, attempt to model fuel cell operation using a pore network model technique.

## **6.1. Recommendations and Future Work**

### **6.1.1. Random pore network model**

The pore network model developed in this work was based on a regular cubic lattice. This simplification of the actual pore structure is usually reasonable for low porosity materials such as rock and sand that are most commonly modeled. The highly porous nature of the GDL, however, created numerous difficulties because pores are located very close together. The necessity to prevent overlapping pores constrained the pore size distribution. A better approach would be to use a random pore network model, such as the Voronoi network approached presented by Thompson [226]. In this model, very high porosities can be achieved without overlap and with arbitrarily wide pore size distributions. This approach may allow the model to be calibrated more closely with experimental data.

### **6.1.2. Full fuel cell pore network modeling**

The pore network model was used to predict limiting current in operating fuel cells. This calculation required specifying boundary conditions for concentrations in the gas channel and catalyst interfaces of the network. To model the full range of fuel cell operation, it is more appropriate to specify a boundary condition of constant voltage at the catalyst interface. Such a condition would require utilizing the Butler-Volmer equation to relate reaction rates (i.e., current densities) to voltage. In this way, the catalyst layer becomes a source/sink or reactive interface. This modification would not only allow the prediction of overall polarization behavior but would also permit the calculation of the spatial distribution of current densities along the catalyst-GDL interface, which is of particular

interest since the pore network model provides an explicit distribution of liquid water in the GDL.

### **6.1.3. Heat transfer and condensation**

The pore network model developed here focused solely on the injection of liquid water into the GDL. This assumed that liquid water is generated at the catalyst layer and leaves the cell via capillary flow. Since heat is also generated at the catalyst layer, however, it is possible that water is produced at the catalyst layer as a vapor. In this case, water would enter the GDL as a vapor and liquid water would be formed in the GDL through condensation in the cooler areas of the GDL. Treating this situation using the pore network approach is possible, but requires an alternative to the invasion percolation concepts used here. More importantly, it would require consideration of heat transfer effects since temperature gradients, heat generation and latent heats are all critical aspects of phase change processes in the fuel cell.

### **6.1.4. Repeatability of GCP method**

The gas controlled porosimetry method (GCP) developed during this work provides high resolution measurement of the air-water capillary properties of GDLs. Determination of the repeatability of this method is difficult, however, since the GDLs themselves are not perfectly consistent. Consequently, any variability in the results cannot be clearly associated with the GDL or the method. In the present work, multiple samples from the same sheet were tested and nearly identical results were obtained for each. Samples from different sheets were not tested. Also, replicate experiments on a given sample were not done since GDL behavior was altered after the initial water injection. The repeatability of the GCP method could be determined by identifying a procedure that restores a tested GDL to its initial state, such as high temperature sintering or vacuum drying. Retesting such a sample will reveal the consistency of the GCP method.

### **6.1.5. GDL hydrophobic coating**

The ability to directly observe the effects of hydrophobic coating on GDLs using the GCP method opens up the possibility of customizing the PTFE application. The GDLs tested in the present study were all received with the PTFE applied by the manufacturer.

Custom designed GDL material with various PTFE loadings, application methods and fiber arrangements should be explored.

### **6.1.6. GDL Degradation**

Over extended periods of fuel cell operation, it is likely that the GDL wetting properties will degrade. The erosion of PTFE or the alteration of the graphite wettability could be caused by the thermal, mechanical and humidity cycles that occur inside the cell during operation. Exploration of failure modes and aging of GDL materials can be investigated using the GCP technique. Testing aged and fresh GDL samples with this technique may reveal useful information regarding GDL durability. This also opens up the possibility of developing realistic accelerated aging techniques.

### **6.1.7. Capillary properties of GDLs under compression**

The properties of GDL under compression are of interest because they are compressed during cell assembly. The permeability measurement obtained in this thesis showed strong dependence on compression. Since compression essentially decreases pore size, it is expected that the capillary properties of GDLs will also change significantly when compressed. The GCP method described in this work can be altered to allow controlled compression without much difficulty.

### **6.1.8. In-situ GDL testing**

With the ability to characterize GDL air-water capillary properties, it is now possible to relate fuel cell performance to GDL wetting properties. At present, it is unclear which features of the  $P_C$ - $S_W$  curve are advantageous to fuel cell performance. Combined with novel hydrophobic coating techniques that generate unique  $P_C$ - $S_W$  curve behavior, it

should be possible to optimize the GDL to achieve better fuel cell performance in highly humidified conditions. This would of course require a significant effort in assembling cells so that repeatable and meaningful performance results are obtained.

## References

- [1] Bockris JOM. Hydrogen Economy. *Science*, 176 (1323-&) 1972.
- [2] Jacobson MZ, Colella WG, Golden DM. Cleaning the air and improving health with hydrogen fuel-cell vehicles. *Science*, 308 (1901-1905) 2005.
- [3] Crabtree GW, Dresselhaus MS, Buchanan MV. The hydrogen economy. *Physics Today*, 57 (39-44) 2004.
- [4] Conte M, Iacobazzi A, Ronchetti M, Vellone R. Hydrogen economy for a sustainable development: state-of-the-art and technological perspectives. *Journal of Power Sources*, 100 (171-187) 2001.
- [5] Mathias MF, Makharia R, Gasteiger HA, Conley JJ, Fuller TJ, Gittleman CJ, et al. Two fuel cell cars in every garage? *Electrochemical Society Interface*, 14 (24-35) 2005.
- [6] Dhar HP. On Solid Polymer Fuel-Cells. *Journal of Electroanalytical Chemistry*, 357 (237-250) 1993.
- [7] Wilson MS, Gottesfeld S. Thin-film catalyst layers for polymer electrolyte fuel cell electrodes. *Journal of Applied Electrochemistry*, 22 (1-7) 1992.
- [8] Wilson MS, Goffesfeld S. High performance catalyzed membranes of ultra-low Pt loadings for polymer electrolyte fuel cells. *Journal of the Electrochemical Society*, 139 (28-30) 1992.
- [9] Wilson MS, Valerio JA, Gottesfeld S. Low platinum loading electrodes for polymer electrolyte fuel cells fabricated using thermoplastic ionomers. *Electrochimica Acta*, 40 (355-363) 1995.
- [10] Amphlett JC, Baumert RM, Mann RF, Peppley BA, Roberge PR, Harris TJ. Performance modeling of the Ballard Mark IV solid polymer electrolyte fuel cell I. Mechanistic model development. *Journal of the Electrochemical Society*, 142 (1-8) 1995.
- [11] Amphlett JC, Baumert RM, Mann RF, Peppley BA, Roberge PR, Harris TJ. Performance modeling of the Ballard Mark IV solid polymer electrolyte fuel cell II. Empirical model development. *Journal of the Electrochemical Society*, 142 (9-15) 1995.

- [12] Mathias MF, Roth J, Fleming J, Lehnert W. Diffusion media materials and characterization. In: Vielstich W, Gasteiger HA, Lamm A, editors. Handbook of Fuel Cells - Fundamentals, Technology and Applications. Volume 3, Part 1. New York: John Wiley & Sons; 2003. p. 517-37.
- [13] Ramasamy RP, Kumbur EC, Mench MM, Liu W, Moore D, Murthy M. Investigation of macro- and micro-porous layer interaction in polymer electrolyte fuel cells. *International Journal of Hydrogen Energy*, 33 (3351-3367) 2008.
- [14] Sone Y, Ekdunge P, Simonsson D. Proton conductivity of Nafion 117 as measured by a four-electrode AC impedance method. *Journal of the Electrochemical Society*, 143 (1254-1259) 1996.
- [15] Zawodzinski TAJ, Springer TE, Uribe F, Gottesfeld S. Characterization of polymer electrolytes for fuel cell applications. *Solid State Ionics*, 60 (199-211) 1993.
- [16] Owejan JP, Trabold TA, Jacobson DL, Arif M, Kandlikar SG. Effects of flow field and diffusion layer properties on water accumulation in a PEM fuel cell. *International Journal of Hydrogen Energy*, 32 (4489-4502) 2007.
- [17] Reiser C, inventor; International Fuel Cells Corp, assignee. Ion Exchange Membrane Fuel Cell Power Plant with Water Management Pressure Differentials. 5700595. 1997.
- [18] Gerteisen D, Heilmann T, Ziegler C. Enhancing liquid water transport by laser perforation of a GDL in a PEM fuel cell. *Journal of Power Sources*, 177 (348-354) 2008.
- [19] Knights SD, Colbow KM, St Pierre J, Wilkinson DP. Aging mechanisms and lifetime of PEFC and DMFC. *Journal of Power Sources*, 127 (127-134) 2004.
- [20] Fairweather JD, Cheung P, St Pierre J, Schwartz DT. A microfluidic approach for measuring capillary pressure in PEMFC gas diffusion layers. *Electrochemistry Communications*, 9 (2340-2345) 2007.
- [21] Nguyen TV, Lin G, Ohn H, Wang X. Measurement of capillary pressure property of gas diffusion media used in proton exchange membrane fuel cells. *Electrochemical and Solid State Letters*, 11 (B127-B131) 2008.
- [22] Sole J. Investigation of water transport parameters and processes in the gas diffusion layer of PEM fuel cells Ph.D. Virginia Polytechnical Institute; 2008.

- [23] Gallagher KG, Darling RM, Patterson TW, Perry ML. Capillary Pressure Saturation Relations for PEM Fuel Cell Gas Diffusion Layers. *Journal of the Electrochemical Society*, 155 (B1225-B1231) 2008.
- [24] Rensink D, Fell S, Roth J. Liquid water transport and distribution in fibrous porous media and gas channel. *Proceedings of the Sixth International Conference on Nanochannels, Microchannels and Minichannels*; 2008 Jun 23-2008 Jun 25; Darmstadt, Germany 2008 p. 1-7.
- [25] Berning T, Djilali N. A 3D, multiphase multicomponent model of the cathode and anode of a PEM fuel cell. *Journal of the Electrochemical Society*, 150 (A1589-A1598) 2003.
- [26] Pasaogullari U, Wang CY. Liquid water transport in gas diffusion layer of polymer electrolyte fuel cells. *Journal of the Electrochemical Society*, 151 (A399-406) 2004.
- [27] Natarajan D, Nguyen TV. Three-dimensional effects of liquid water flooding in the cathode of a PEM fuel cell. *Journal of Power Sources*, 115 (66-80) 2003.
- [28] You L, Liu H. A two-phase flow and transport model for the cathode of PEM fuel cells. *International Journal of Heat and Mass Transfer*, 45 (2277-2287) 2002.
- [29] Pasaogullari U, Wang CY. Two-phase transport and the role of micro-porous layer in polymer electrolyte fuel cells. *Electrochimica Acta*, 49 (4359-4369) 2004.
- [30] Weber AZ, Darling RM, Newman J. Modeling two-phase behaviour in PEFCs. *Journal of the Electrochemical Society*, 151 (A1715-A1727) 2004.
- [31] Lin G, He W, Nguyen TV. Modeling liquid water effects in the gas diffusion and catalyst layers of the cathode of a PEM fuel cell. *Journal of the Electrochemical Society*, 151 (A1999-A2006) 2004.
- [32] Nam JH, Kaviany M. Effective diffusivity and water-saturation distribution in single- and two-layer PEMFC diffusion medium. *International Journal of Heat and Mass Transfer*, 46 (4595-4611) 2003.
- [33] Siegel NP, Ellis MW, Nelson DJ, Von Spakovsky MR. A two-dimensional computational model of a PEMFC with liquid water transport. *Journal of Power Sources*, 128 (173-184) 2004.
- [34] He W, Yi JS, Nguyen TV. Two-phase flow model of the cathode of PEM fuel cells using interdigitated flow fields. *AIChE Journal*, 46 (2053-2064) 2000.

- [35] Natarajan D, Nguyen TV. A two-dimensional, two-phase, multicomponent, transient model for the cathode of a proton exchange membrane fuel cell using conventional gas distributors. *Journal of the Electrochemical Society*, 148 (A1324-A1335) 2001.
- [36] Divisek J, Fuhrmann J, Gartner K, Jung R. Performance modeling of a direct methanol fuel cell. *Journal of the Electrochemical Society*, 150 (811-825) 2003.
- [37] Hu M, Gu A, Wang M, Zhu X, Yu L. Three dimensional, two phase flow mathematical model for PEM fuel cell: Part I. Model development. *Energy Conversion and Management*, 45 (1861-1882) 2004.
- [38] Hu M, Zhu X, Wang M, Gu A, Yu L. Three dimensional, two phase flow mathematical model for PEM fuel cell: Part II. Analysis and discussion of the internal transport mechanisms. *Energy Conversion and Management*, 45 (1833-1916) 2004.
- [39] Wang ZH, Wang CY, Chen KS. Two-phase flow and transport in the air cathode of proton exchange membrane fuel cells. *Journal of Power Sources*, 94 (40-50) 2001.
- [40] Pisani L, Murgia G, Valentini M, D'Aguanno B. A working model of polymer electrolyte fuel cells comparisons between theory and experiments. *Journal of the Electrochemical Society*, 149 (898-904) 2002.
- [41] Mazumder S, Cole JV. Rigorous 3-D mathematical modeling of PEM fuel cells II. Model predictions with liquid water transport. *Journal of the Electrochemical Society*, 150 (1510-1517) 2003.
- [42] Noponen M, Birgersson E, Ihonen J, Vynnycky M, Lundblad A, Lindbergh G. A two-phase non-isothermal PEFC model: Theory and validation. *Fuel Cells*, 4 (365-377) 2004.
- [43] Hsuen HK. Performance equations for cathodes in polymer electrolyte fuel cells with non-uniform water flooding in gas diffusers. *Journal of Power Sources*, 137 (183-195) 2004.
- [44] Grujicic M, Chittajallu KM. Optimization of the cathode geometry in polymer electrolyte membrane (PEM) fuel cells. *Chemical Engineering Science*, 59 (5883-5895) 2004.
- [45] Sun H, Liu H, Guo LJ. PEM fuel cell performance and its two-phase mass transport. *Journal of Power Sources*, 143 (125-135) 2005.

- [46] Pasaogullari U, Wang CY. Two-phase modeling and flooding prediction of polymer electrolyte fuel cells. *Journal of the Electrochemical Society*, 152 (A380-A390) 2005.
- [47] Weber AZ, Newman J. Effects of microporous layers in polymer electrolyte fuel cells. *Journal of the Electrochemical Society*, 152 (A677-688) 2005.
- [48] Birgersson E, Noponen M, Vynnycky M. Analysis of a two-phase non-isothermal model for a PEFC. *Journal of the Electrochemical Society*, 152 (A1021-A1034) 2005.
- [49] You L, Liu H. A two-phase flow and transport model for PEM fuel cells. *Journal of Power Sources*, 155 (219-230) 2006.
- [50] Pasaogullari U, Wang CY, Chen KS. Two-phase transport in polymer electrolyte fuel cells with bilayer cathode gas diffusion media. *Journal of the Electrochemical Society*, 152 (A1574-1582) 2005.
- [51] Ziegler C, Yu HM, Schumacher JO. Two-phase dynamic modeling of PEMFCs and simulation of cyclo-voltammograms. *Journal of the Electrochemical Society*, 152 (A1555-A1567) 2005.
- [52] Meng H, Wang CY. Model of two-phase flow and flooding dynamics in polymer electrolyte fuel cells. *Journal of the Electrochemical Society*, 152 (A1733-A1741) 2005.
- [53] Wang ZH, Wang CY. Two-phase flow and transport in the interdigitated air cathode of proton exchange membrane fuel cells. *American Society of Mechanical Engineers, Heat Transfer Division, (Publication) HTD*, 366 (27-33) 2000.
- [54] Wang CY, Wang ZH, Pan Y. Two-phase transport in proton exchange membrane fuel cells. *American Society of Mechanical Engineers, Heat Transfer Division, (Publication) HTD*, 364 (351-357) 1999.
- [55] Bradean R, Promislow K, Wetton B. Phase change and two phase flow in cathode porous electrodes of fuel cells. *American Society of Mechanical Engineers, Heat Transfer Division, (Publication) HTD*, 375 (441-448) 2004.
- [56] Pasaogullari U, Wang CY, Chen KS. Liquid water transport in polymer electrolyte fuel cells with multi-layer diffusion media. *ASME, HTD; Anaheim, CA* 2004 p. 307-15.

- [57] Kulikovskiy AA, Wuster T, Egmen A, Stolten D. Analytical and numerical analysis of PEM fuel cell performance curves. *Journal of the Electrochemical Society*, 152 (1290-1300) 2005.
- [58] Coppo M, Siegel NP, Spakovskiy MR. On the influence of temperature on PEM fuel cell operation. *Journal of Power Sources*, 159 (560-569) 2006.
- [59] Senn SM, Poulidakos D. Multiphase transport phenomena in the diffusion zone of a PEM fuel cell. *Journal of Heat Transfer*, 127 (1245-1259) 2005.
- [60] Ito K, Masuda H, Miyazaki T, Kakimoto Y, Masuoka T. Investigation of flooding phenomena in PEMFC by two-phase flow numerical simulation. *Proceedings of the 3rd International Conference on Fuel Cell Science, Engineering, and Technology*, 2005; Ypsilanti, MI, United States 2005 p. 19-24.
- [61] Lin G, Nguyen TV. A two-dimensional two-phase model of a PEM fuel cell. *Journal of the Electrochemical Society*, 153 (A372-A382) 2006.
- [62] Ge J, Higier A, Liu H. Effect of gas diffusion layer compression on PEM fuel cell performance. *Journal of Power Sources*, 159 (240-246) 2006.
- [63] Song D, Wang Q, Liu ZS, Huang C. Transient analysis for the cathode gas diffusion layer of PEM fuel cells. *Journal of Power Sources*, 159 (928-942) 2006.
- [64] Acosta M, Merten C, Eigenberger G, Class H, Helmig R, Thoben B, et al. Modeling non-isothermal two-phase multicomponent flow in the cathode of PEM fuel cells. *Journal of Power Sources*, 159 (1123-1141) 2006.
- [65] Chang MH, Chen F, Teng HS. Effects of two-phase transport in the cathode gas diffusion layer on the performance of a PEMFC. *Journal of Power Sources*, 160 (268-276) 2006.
- [66] Chiang MS, Chu HS. Numerical investigation of transport component design effect on a proton exchange membrane fuel cell. *Journal of Power Sources*, 160 (340-352) 2006.
- [67] Chan SH, Tong TW, Abou-Ellail M, Beshay KR. A two-fluid mathematical model for two-phase flow in PEM fuel cells. *Proceedings of the 3rd International Conference on Fuel Cell Science, Engineering, and Technology*, 2005; Ypsilanti, MI, United States 2005 p. 129-35.
- [68] Zhan Z, Xiao J, Li D, Pan M, Yuan R. Effects of porosity distribution variation on the liquid water flux through gas diffusion layers of PEM fuel cells. *Journal of*

- Power Sources, 160 (1041-1048) 2006.
- [69] Shah AA, Kim GS, Gervais W, Young A, Promislow K, Li J, et al. The effects of water and microstructure on the performance of polymer electrolyte fuel cells. *Journal of Power Sources*, 160 (1251-1268) 2006.
- [70] Wang Y, Wang CY. A nonisothermal, two-phase model for polymer electrolyte fuel cells. *Journal of the Electrochemical Society*, 153 (A1193-A1200) 2006.
- [71] Matamoros L, Bruggemann D. Simulation of the water and heat management in proton exchange membrane fuel cells. *Journal of Power Sources*, 161 (203-213) 2006.
- [72] Sun H, Guo L, Liu H. The effect of operating parameters on water transport in PEM fuel cells. *Heat Transfer - Asian Research*, 35 (89-100) 2006.
- [73] Chang SM, Chu HS. Transient behavior of a PEMFC. *Journal of Power Sources*, 161 (1161-1168) 2006.
- [74] Tao WQ, Min CH, Liu XL, He YL, Yin BH, Jiang W. Parameter sensitivity examination and discussion of PEM fuel cell simulation model validation: Part I. Current status of modeling research and model development. *Journal of Power Sources*, 160 (359-373) 2006.
- [75] Min CH, He YL, Liu XL, Yin BH, Jiang W, Tao WQ. Parameter sensitivity examination and discussion of PEM fuel cell simulation model validation: Part II: Results of sensitivity analysis and validation of the model. *Journal of Power Sources*, 160 (374-385) 2006.
- [76] Yamada H, Hatanaka T, Murata H, Morimoto Y. Measurement of flooding in gas diffusion layers of polymer electrolyte fuel cells with conventional flow field. *Journal of the Electrochemical Society*, 153 (A1748-A1754) 2006.
- [77] Shah AA, Kim GS, Sui PC, Harvey D. Transient non-isothermal model of a polymer electrolyte fuel cell. *Journal of Power Sources*, 163 (769793-806) 2007.
- [78] He G, Ming P, Zhao Z, Abudula A, Xiao Y. A two-fluid model for two-phase flow in PEMFCs. *Journal of Power Sources*, 163 (864-873) 2007.
- [79] Hwang JJ. A complete two-phase model of a porous cathode of a PEM fuel cell. *Journal of Power Sources*, 164 (174-181) 2007.
- [80] Ju H, Luo G, Wang CY. Probing liquid water saturation in diffusion media of

- polymer electrolyte fuel cells. *Journal of the Electrochemical Society*, 154 (B218-B228) 2007.
- [81] Luo G, Ju H, Wang CY. Prediction of dry-wet-dry transition in polymer electrolyte fuel cells. *Journal of the Electrochemical Society*, 154 (B316-B321) 2007.
- [82] Weber AZ, Darling RM. Understanding porous water-transport plates in polymer-electrolyte fuel cells. *Journal of Power Sources*, 168 (191-199) 2007.
- [83] Meng H. A two-phase non-isothermal mixed-domain PEM fuel cell model and its application to two-dimensional simulations. *Journal of Power Sources*, 168 (218-228) 2007.
- [84] Vynnycky M. On the modelling of two-phase flow in the cathode gas diffusion layer of a polymer electrolyte fuel cell. *Applied Mathematics and Computation*, 189 (1560-1575) 2007.
- [85] Pasaogullari U, Mukherjee PP, Wang CY, Chen KS. Anisotropic heat and water transport in a PEFC cathode gas diffusion layer. *Journal of the Electrochemical Society*, 154 (B823-B834) 2007.
- [86] Ye Q, Van Nguyen T. Three-Dimensional Simulation of Liquid Water Distribution in a PEMFC with Experimentally Measured Capillary Functions. *Journal of the Electrochemical Society*, 154 (B1242-B1251) 2007.
- [87] Chang SM, Chu HS. A transient model of PEM fuel cells based on a spherical thin film-agglomerate approach. *Journal of Power Sources*, 172 (790-798) 2007.
- [88] Lee CI, Chu HS. Effects of temperature on the location of the gas-liquid interface in a PEM fuel cell. *Journal of Power Sources*, 171 (718-727) 2007.
- [89] Rao RM, Bhattacharyya D, Rengaswamy R, Choudhury SR. A two-dimensional steady state model including the effect of liquid water for a PEM fuel cell cathode. *Journal of Power Sources*, 173 (375-393) 2007.
- [90] Matamoros L, Bruggemann D. Numerical study on PEMFC's geometrical parameters under different humidifying conditions. *Journal of Power Sources*, 172 (253-264) 2007.
- [91] Meng H. Numerical investigation of transient responses of a PEM fuel cell using a two-phase non-isothermal mixed-domain model. *Journal of Power Sources*, 171 (738-746) 2007.

- [92] Zhan Z, Xiao J, Zhang Y, Pan M, Yuan R. Gas diffusion through differently structured gas diffusion layers of PEM fuel cells. *International Journal of Hydrogen Energy*, 32 (4443-4451) 2007.
- [93] Promislow K, Stockie J, Wetton B. A sharp interface reduction for multiphase transport in a porous fuel cell electrode. *Proceedings of the Royal Society A-Mathematical Physical and Engineering Sciences*, 462 (789-816) 2006.
- [94] Al Baghdadi MAR, Al Janabi HAK. Modeling optimizes PEM fuel cell performance using three-dimensional multi-phase computational fluid dynamics model. *Energy Conversion and Management*, 48 (3102-3119) 2007.
- [95] Koido T, Furusawa T, Moriyama K. An approach to modeling two-phase transport in the gas diffusion layer of a proton exchange membrane fuel cell. *Journal of Power Sources*, 175 (127-136) 2008.
- [96] Masuda H, Ito K, Oshima T, Sasaki K. Comparison between numerical simulation and visualization experiment on water behavior in single straight flow channel polymer electrolyte fuel cells. *Journal of Power Sources*, 177 (303-313) 2008.
- [97] Steinkamp K, Schumacher JO, Goldsmith F, Ohlberger M, Ziegler C. A Nonisothermal PEM Fuel Cell Model Including Two Water Transport Mechanisms in the Membrane. *Journal of Fuel Cell Science and Technology*, 5 (011007-011016) 2008.
- [98] Bapat CJ, Thynell ST. Effect of anisotropic thermal conductivity of the GDL and current collector rib width on two-phase transport in a PEM fuel cell. *Journal of Power Sources*, 179 (240-251) 2008.
- [99] Gurau V, Zawodzinski TA, Mann JA. Two-phase transport in PEM fuel cell cathodes. *Journal of Fuel Cell Science and Technology*, 5 2008.
- [100] Wang X, Van Nguyen T. Modeling the Effects of Capillary Property of Porous Media on the Performance of the Cathode of a PEMFC. *Journal of the Electrochemical Society*, 155 (B1085-B1092) 2008.
- [101] Shi W, Kurihara E, Oshima N. Effect of capillary pressure on liquid water removal in the cathode gas diffusion layer of a polymer electrolyte fuel cell. *Journal of Power Sources*, 182 (112-118) 2008.
- [102] Khakbaz Baboli M, Kermani MJ. A two-dimensional, transient, compressible isothermal and two-phase model for the air-side electrode of PEM fuel cells. *Electrochimica Acta*, 53 (7644-7654) 2008.

- [103] Hermann J, Ziegler C. Modeling the Dynamic Water Transport in the Porous Layers of PEM Fuel Cells Based on Numerical Upscaling. *Journal of the Electrochemical Society*, 155 (B1066-B1076) 2008.
- [104] Chen FL, Chang MH, Hsieh PT. Two-phase transport in the cathode gas diffusion layer of PEM fuel cell with a gradient in porosity. *International Journal of Hydrogen Energy*, 33 (2525-2529) 2008.
- [105] Groetsch M, Hanke-Rauschenbach R, Mangold M. Bifurcation analysis of a two-phase PEMFC model. *Journal of Fuel Cell Science and Technology*, 5 2008.
- [106] McKay DA, Siegel JB, Ott W, Stefanopoulou AG. Parameterization and prediction of temporal fuel cell voltage behavior during flooding and drying conditions. *Journal of Power Sources*, 178 (207-222) 2008.
- [107] Ju H. Analyzing the effects of immobile liquid saturation and spatial wettability variation on liquid water transport in diffusion media of polymer electrolyte fuel cells (PEFCs). *Journal of Power Sources*, 185 (55-62) 2008.
- [108] Shah AA, Walsh FC. A model for hydrogen sulfide poisoning in proton exchange membrane fuel cells. *Journal of Power Sources*, 185 (287-301) 2008.
- [109] Bapat CJ, Thynell ST. Effect of anisotropic electrical resistivity of gas diffusion layers (GDLs) on current density and temperature distribution in a Polymer Electrolyte Membrane (PEM) fuel cell. *Journal of Power Sources*, 185 (428-432) 2008.
- [110] Sinha PK, Wang CY. Two-phase modeling of gas purge in a polymer electrolyte fuel cell. *Journal of Power Sources*, 183 (609-618) 2008.
- [111] Yang WW, Zhao TS, He YL. Modelling of coupled electron and mass transport in anisotropic proton-exchange membrane fuel cell electrodes. *Journal of Power Sources*, In Press, Corrected Proof
- [112] Chang SM, Chu HS. A transient model of PEM fuel cells based on a spherical thin film-agglomerate approach. *Journal of Power Sources*, 172 (790-798) 2007.
- [113] Springer TE, Wilson MS, Gottesfeld S. Modeling and experimental diagnostics in polymer electrolyte fuel cells. *Journal of the Electrochemical Society*, 140 (3513-3526) 1993.
- [114] Bernardi DM, Verbrugge MW. Mathematical model of the solid-polymer-electrolyte fuel cell. *Journal of the Electrochemical Society*, 139 (2477-2491)

1992.

- [115] Bear J. Dynamics of Fluids in Porous Media. New York: Dover Publications; 1972.
- [116] Bird RB, Stewart WE, Lightfoot EN. Transport Phenomena. 1 ed. New York: John Wiley & Sons; 1960.
- [117] Dullien FAL. Porous Media: Fluid Transport and Pore Structure. Second ed. New York: Academic Press; 1992.
- [118] Ioannidis MA, Chatzis I, Lemaire C, Perunarkilli R. Unsaturated hydraulic conductivity from nuclear magnetic resonance measurements. Water Resources Research, 42 (W07201) 2006.
- [119] Adamson AW. Physical Chemistry of Surfaces. 4 ed. New York: John Wiley & Sons; 1982.
- [120] Yasuda T, Okuno T, Yasuda H. Contact-angle of water on polymer surfaces. Langmuir, 10 (2435-2439) 1994.
- [121] Morrow NR. Capillary-pressure correlations for uniformly wetted porous-media. Journal of Canadian Petroleum Technology, 15 (49-69) 1976.
- [122] Sinha PK, Wang CY. Liquid water transport in a mixed-wet gas diffusion layer of a polymer electrolyte fuel cell. Chemical Engineering Science, 63 (1081-1091) 2008.
- [123] Gostick JT, Fowler MW, Ioannidis MA, Pritzker MD, Volfkovich YM, Sakars A. Capillary pressure and hydrophilic porosity in gas diffusion layers for polymer electrolyte fuel cells. Journal of Power Sources, 156 (375-387) 2006.
- [124] Benziger J, Nehlsen J, Blackwell D, Brennan T, Itescu J. Water flow in the gas diffusion layer of PEM fuel cells. Journal of Membrane Science, 261 (98-106) 2005.
- [125] Wenzel RN. Resistance of solid surfaces to wetting by water. Industrial & Engineering Chemistry, 28 (988-994) 1936.
- [126] Cassie ABD, Baxter S. Wettability of porous surfaces. Faraday Society Transactions, 40 (546-551) 1944.
- [127] Barthlott W, Neinhuis C. Purity of the sacred lotus, or escape from contamination

- in biological surfaces. *Planta*, 202 (1-8) 1997.
- [128] Lafuma A, Quere D. Superhydrophobic states. *Nature Materials*, 2 (457-460) 2003.
- [129] Gostick JT, Ioannidis MA, Fowler MW, Pritzker MD. Pore network modeling of fibrous gas diffusion layers for polymer electrolyte membrane fuel cells. *Journal of Power Sources*, 173 (277-290) 2007.
- [130] Zisman WA. Relation of the equilibrium contact angle to liquid and solid constitution. In: Gould RF, editor. *Contact Angle, Wettability and Adhesion*. Washington, D.C.: American Chemical Society; 1964. p. 1-51.
- [131] Leverett MC. Capillary behavior in porous solids. *American Institute of Mining and Metallurgical Engineers -- Petroleum Development and Technology*, 142 (152-168) 1941.
- [132] Udell KS. Heat transfer in porous media considering phase change and capillarity - The heat pipe effect. *International Journal of Heat and Mass Transfer*, 28 (485-495) 1985.
- [133] Williams MV, Begg E, Bonville L, Kunz HR, Fenton JM. Characterization of gas diffusion layers for PEMFC. *Journal of the Electrochemical Society*, 151 (1173-1180) 2004.
- [134] Ihonen J, Mikkola M, Lindbergh G. Flooding of gas diffusion backing in PEFCs: Physical and electrochemical characterization. *Journal of the Electrochemical Society*, 151 (1152-1161) 2004.
- [135] Thoben B, Siebke A. Influence of Different Gas Diffusion Layers on the Water Management of the PEFC Cathode. *Journal of New Materials for Electrochemical Systems*, 7 (13-20) 2004.
- [136] Ihonen J, Jaouen F, Lindbergh G, Lundblad A, Sundholm G. Investigation of mass-transport limitations in the solid polymer fuel cell cathode. II. Experimental. *Journal of the Electrochemical Society*, 149 (448-454) 2002.
- [137] Antolini E, Pozio A, Giorgi L, Passalacqua E. Morphological characteristics of carbon/polytetrafluoroethylene films deposited on porous carbon support. *Journal of Materials Science*, 33 (1837-1843) 1998.
- [138] Han M, Xu JH, Chan SH, Jiang SP. Characterization of gas diffusion layers for PEMFC. *Electrochimica Acta*, 53 (5361-5367) 2008.

- [139] Jena A, Gupta K. An innovative technique for pore structure analysis of fuel cell and battery components using flow porometry. *Journal of Power Sources*, 96 (214-219) 2001.
- [140] Jena AK, Gupta KM. In-plane compression porometry of battery separators. *Journal of Power Sources*, 80 (46-52) 1999.
- [141] Volkovich YM, Bagotzky VS. The method of standard porosimetry. 1. Principles and possibilities. *Journal of Power Sources*, 48 (327-338) 1994.
- [142] Volkovich YM, Bagotzky VS. The method of standard porosimetry. 2. Investigation of the formation of porous structures. *Journal of Power Sources*, 48 (339-348) 1994.
- [143] Volkovich YM, Bagotzky VS, Sosenkin VE, Blinov IA. The standard contact porosimetry. *Colloids and Surfaces A: Physicochemical and Engineering Aspects*, 187-188 (349-365) 2001.
- [144] Kumbur EC, Sharp KV, Mench MM. Validated Leverett Approach for Multiphase Flow in PEFC Diffusion Media. *Journal of the Electrochemical Society*, 154 (B1295-B1304) 2007.
- [145] Kumbur EC, Sharp KV, Mench MM. Validated Leverett Approach for Multiphase Flow in PEFC Diffusion Media. *Journal of the Electrochemical Society*, 154 (B1305-B1314) 2007.
- [146] Kumbur EC, Sharp KV, Mench MM. Validated Leverett Approach for Multiphase Flow in PEFC Diffusion Media. *Journal of the Electrochemical Society*, 154 (B1315-B1324) 2007.
- [147] Kumbur EC, Sharp KV, Mench MM. A design tool for predicting the capillary transport characteristics of fuel cell diffusion media using an artificial neural network. *Journal of Power Sources*, 176 (191-199) 2008.
- [148] Toledo PG, Scriven LE, Davis HT. Pore-Space Statistics and Capillary-Pressure Curves from Volume-Controlled Porosimetry. *Spe Formation Evaluation*, 9 (46-54) 1994.
- [149] Becker J, Schulz V, Wiegmann A. Numerical determination of two-phase material parameters of a gas diffusion layer using tomography images. *Journal of Fuel Cell Science and Technology*, 5 2008.
- [150] Schulz VP, Becker J, Wiegmann A, Mukherjee PP, Wang CY. Modeling of two-

- phase behavior in the gas diffusion media of PEFCs via full morphology approach. *Journal of the Electrochemical Society*, 154 (B419-B426) 2007.
- [151] Gostick JT, Ioannidis MA, Fowler MW, Pritzker MD. Direct measurement of the capillary pressure characteristics of water-air-gas diffusion layer systems for PEM fuel cells. *Electrochemistry Communications*, 10 (1520-1523) 2008.
- [152] Stauffer D, Aharony A. *Introduction to percolation theory*. 2nd ed. London: Routledge; 2003.
- [153] Grimmett G. *Percolation*. Berlin: Springer-Verlag; 1989.
- [154] Wilkinson D, Willemsen JF. Invasion Percolation - A New Form of Percolation Theory. *Journal of Physics A-Mathematical and General*, 16 (3365-3376) 1983.
- [155] Chatzis I, Dullien FAL. Application of the Percolation Theory for the Simulation of Penetration Into Porous-Media of A Non-Wetting Fluid and the Prediction of the Relative Permeability Curve. *Revue de l Institut Francais du Petrole*, 37 (183-205) 1982.
- [156] Feindel KW, Bergens SH, Wasylshen RE. Use of hydrogen-deuterium exchange for contrast in <sup>1</sup>H NMR microscopy investigations of an operating PEM fuel cell. *Journal of Power Sources*, 173 (86-95) 2007.
- [157] Kimball E, Whitaker T, Kevrekidis YG, Benziger JB. Drops, slugs, and flooding in polymer electrolyte membrane fuel cells. *AIChE Journal*, 54 (1313-1332) 2008.
- [158] Spornjak D, Prasad AK, Advani SG. Experimental investigation of liquid water formation and transport in a transparent single-serpentine PEM fuel cell. *Journal of Power Sources*, 170 (334-344) 2007.
- [159] Jackson GW, James DF. Permeability of fibrous porous media. *Canadian Journal of Chemical Engineering*, 64 (364-374) 1986.
- [160] Tomadakis MM, Robertson TJ. Viscous permeability of random fiber structures: Comparison of electrical and diffusional estimates with experimental and analytical results. *Journal of Composite Materials*, 39 (163-188) 2005.
- [161] Gostick JT, Fowler MW, Pritzker MD, Ioannidis MA, Behra LM. In-Plane and through-plane gas permeability of carbon fiber electrode backing layers. *Journal of Power Sources*, 162 (228-238) 2006.
- [162] Wilde PM, Mandle M, Murata M, Berg N. Structural and physical properties of

- GDL and GDL/BPP combinations and their influence on PEMFC performance. *Fuel Cells*, 4 (180-184) 2004.
- [163] Lee SJ, Hsu CD, Huang CH. Analyses of the fuel cell stack assembly pressure. *Journal of Power Sources*, 145 (353-361) 2005.
- [164] Ge J, Higier A, Liu H. Effect of gas diffusion layer compression on PEM fuel cell performance. *Journal of Power Sources*, 159 (240-246) 2006.
- [165] Nitta I, Hottinen T, Himanen O, Mikkola M. Inhomogeneous compression of PEMFC gas diffusion layer: Part I. Experimental. *Journal of Power Sources*, 171 (26-36) 2007.
- [166] Lin JH, Chen WH, Su YJ, Ko TH. Effect of gas diffusion layer compression on the performance in a proton exchange membrane fuel cell. *Fuel*, 87 (2420-2424) 2008.
- [167] Wang XT, Song Y, Zhang B. Experimental study on clamping pressure distribution in PEM fuel cells. *Journal of Power Sources*, 179 (305-309) 2008.
- [168] Chang WR, Hwang JJ, Weng FB, Chan SH. Effect of clamping pressure on the performance of a PEM fuel cell. *Journal of Power Sources*, 166 (149-154) 2007.
- [169] Williams MV, Kunz HR, Fenton JM. Influence of convection through gas-diffusion layers on limiting current in PEM FCs using a serpentine flow field. *Journal of the Electrochemical Society*, 151 (A1617-A1627) 2004.
- [170] Pharoah JG. On the permeability of gas diffusion media used in PEM fuel cells. *Journal of Power Sources*, 144 (77-82) 2005.
- [171] Lee WK, Van Zee JW, Shimpalee S, Dutta S. Effect of humidity of PEM fuel cell performance. Part I. Experiments. American Society of Mechanical Engineers, Heat Transfer Division, (Publication) HTD; Nashville, TN, USA 1999 p. 359-66.
- [172] Feser JP, Prasad AK, Advani SG. On the relative influence of convection in serpentine flow fields of PEM fuel cells. *Journal of Power Sources*, 161 (404-412) 2006.
- [173] Park J, Li X. An experimental and numerical investigation on the cross flow through gas diffusion layer in a PEM fuel cell with a serpentine flow channel. *Journal of Power Sources*, 163 (853-863) 2007.
- [174] Wang Y, Wang CY. Simulation of flow and transport phenomena in a polymer

- electrolyte fuel cell under low-humidity operation. *Journal of Power Sources*, 147 (148-161) 2005.
- [175] Oosthuizen PH, Sun L, McAuley KB. The effect of channel-to-channel gas crossover on the pressure and temperature distribution in PEM fuel cell flow plates. *Applied Thermal Engineering*, 25 (1083-1096) 2005.
- [176] Prasanna M, Ha HY, Cho EA, Hong SA, Oh IH. Influence of cathode gas diffusion media on the performance of the PEMFCs. *Journal of Power Sources*, 131 (147-154) 2004.
- [177] Dohle H, Jung R, Kimiaie N, Mergel J, Muller M. Interaction between the diffusion layer and the flow field of polymer electrolyte fuel cells - Experiments and simulation studies. *Journal of Power Sources*, 124 (371-384) 2003.
- [178] Feser JP, Prasad AK, Advani SG. Experimental characterization of in-plane permeability of gas diffusion layers. *Journal of Power Sources*, 162 (1226-1231) 2006.
- [179] Gurau V, Bluemle MJ, De Castro ES, Tsou YM, Zawodzinski J, Mann J. Characterization of transport properties in gas diffusion layers for proton exchange membrane fuel cells: 2. Absolute permeability. *Journal of Power Sources*, 165 (793-802) 2007.
- [180] Owejan JP, Trabold TA, Jacobson DL, Baker DR, Hussey DS, Arif M. In situ investigation of water transport in an operating PEM fuel cell using neutron radiography: Part 2 - Transient water accumulation in an interdigitated cathode flow field. *International Journal of Heat and Mass Transfer*, 49 (4721-4731) 2006.
- [181] Nguyen TV, Lin G, Ohn H, Wang X. Measurements of two-phase flow properties of the porous media used in PEM fuel cells. *ECS Transactions*, 3 (415-423) 2007.
- [182] Kainourgiakis ME, Kikkinides ES, Charalambopoulou GC, Stubos AK. Simulated annealing as a method for the determination of the spatial distribution of a condensable adsorbate in mesoporous materials. *Langmuir*, 19 (3333-3337) 2003.
- [183] Niu XD, Munekata T, Hyodo SA, Suga K. An investigation of water-gas transport processes in the gas-diffusion-layer of a PEM fuel cell by a multiphase multiple-relaxation-time lattice Boltzmann model. *Journal of Power Sources*, 172 (542-552) 2007.
- [184] van Brakel J, Heertjes PM. Analysis of diffusion in macroporous media in terms of a porosity, a tortuosity and a constrictivity factor. *International Journal of Heat*

- and Mass Transfer, 17 (1093-1103) 1974.
- [185] Tomadakis MM, Sotirchos SV. Ordinary, transition, and Knudsen regime diffusion in random capillary structures. *Chemical Engineering Science*, 48 (3323-3333) 1993.
- [186] Tomadakis MM, Sotirchos SV. Effective diffusivities and conductivities of random dispersions of nonoverlapping and partially overlapping unidirectional fibers. *Journal of Chemical Physics*, 99 (9820) 1993.
- [187] Tomadakis MM, Sotirchos SV. Ordinary and transition regime diffusion in random fiber structures. *AIChE Journal*, 39 (397-412) 1993.
- [188] Tomadakis MM, Sotirchos SV. Transport properties of random arrays of freely overlapping cylinders with various orientation distributions. *Journal of Chemical Physics*, 98 (616-626) 1993.
- [189] Tomadakis MM, Robertson TJ. Survival and relaxation time, pore size distribution moments, and viscous permeability in random unidirectional fiber structures. *Journal of Chemical Physics*, 122 (094711) 2005.
- [190] Ye X, Wang CY. Measurement of Water Transport Properties Through Membrane Electrode Assemblies. II. Cathode Diffusion Media. *Journal of the Electrochemical Society*, 154 (B683-B686) 2007.
- [191] Baker DR, Wieser C, Neyerlin KC, Murphy MW. The use of limiting current to determine transport resistance in PEM fuel cells. *ECS Transactions*, 3 (989-999) 2006.
- [192] Kramer D, Freunberger SA, Fluckiger R, Schneider IA, Wokaun A, Buchi FN, et al. Electrochemical diffusimetry of fuel cell gas diffusion layers. *Journal of Electroanalytical Chemistry*, 612 (63-77) 2008.
- [193] Inoue G, Yoshimoto T, Matsukuma Y, Minemoto M. Development of simulated gas diffusion layer of polymer electrolyte fuel cells and evaluation of its structure. *Journal of Power Sources*, 175 (145-158) 2008.
- [194] Anderson WG. Wettability literature survey - part 2: wettability measurement. *Journal of Petroleum Technology*, 38 (1246-1262) 1986.
- [195] Yan A, Xiao X, Kulaots I, Sheldon BW, Hurt RH. Controlling water contact angle on carbon surfaces from 5° to 170°. *Carbon*, 44 (3116-3120) 2006.

- [196] Gurau V, Bluemle MJ, De Castro ES, Tsou YM, Mann J, Zawodzinski J. Characterization of transport properties in gas diffusion layers for proton exchange membrane fuel cells: 1. Wettability (internal contact angle to water and surface energy of GDL fibers). *Journal of Power Sources*, 160 (1156-1162) 2006.
- [197] Lim C, Wang CY. Effects of hydrophobic polymer content in GDL on power performance of a PEM fuel cell. *Electrochimica Acta*, 49 (4149-4156) 2004.
- [198] Geertsma J. Estimating the coefficient of inertial resistance in fluid flow through porous media. *Society of Petroleum Engineers Journal*, 10 (445-450) 1974.
- [199] Sahimi M. *Flow and Transport in Porous Media and Fractured Rock*. Weinheim: VCH; 1995.
- [200] Celia MA, Reeves PC, Ferrand LA. Recent advances in pore scale models for multiphase flow in porous media. *Reviews of Geophysics*, 33 (1049-1057) 1995.
- [201] Blunt MJ, Jackson MD, Piri M, Valvatne PH. Detailed physics, predictive capabilities and macroscopic consequences for pore-network models of multiphase flow. *Advances in Water Resources*, 25 (1069-1089) 2002.
- [202] Ioannidis MA, Chatzis I. Network modelling of pore structure and transport properties of porous media. *Chemical Engineering Science*, 48 (951-972) 1993.
- [203] Liang Z, Ioannidis MA, Chatzis I. Geometric and topological analysis of three-dimensional porous media: Pore space partitioning based on morphological skeletonization. *Journal of Colloid and Interface Science*, 221 (13-24) 2000.
- [204] Markicevic B, Bazylak A, Djilali N. Determination of transport parameters for multiphase flow in porous gas diffusion electrodes using a capillary network model. *Journal of Power Sources*, 171 (706-717) 2007.
- [205] Chatzis I, Dullien FAL. Modeling Pore Structure by 2-D and 3-D Networks with Application to Sandstones. *Journal of Canadian Petroleum Technology*, 16 (97-108) 1977.
- [206] Sinha PK, Mukherjee PP, Wang CY. Impact of GDL structure and wettability on water management in polymer electrolyte fuel cells. *Journal of Materials Chemistry*, 17 (3089-3103) 2007.
- [207] Chang D, Ioannidis MA. Magnetization evolution in network models of porous rock under conditions of drainage and imbibition. *Journal of Colloid and Interface Science*, 253 (159-170) 2002.

- [208] Berker R. Integration des equation du mouvement d'un fluide visqueux incompressible. In: Flugge S, editor. Encyclopedia of Physics, VIII. Berlin: Springer-Verlag; 1963. p. 1-384.
- [209] Tomadakis MM, Robertson TJ. Pore size distribution, survival probability, and relaxation time in random and ordered arrays of fibers. *Journal of Chemical Physics*, 119 (1741-1749) 2003.
- [210] Shirtcliffe NJ, McHale G, Newton MI, Pyatt FB, Doerr SH. Critical conditions for the wetting of soils. *Applied Physics Letters*, 89 2006.
- [211] Tsimpanogiannis IN, Yortsos YC, Poulou S, Kanellopoulos N, Stubos AK. Scaling theory of drying in porous media. *Physical Review e*, 59 (4353-4365) 1999.
- [212] Johnston PR. Revisiting the most probable pore-size distribution in filter media: the gamma distribution. *Filtration and Separations*, April (287-292) 1998.
- [213] Ioannidis MA, Chatzis I, Payatakes AC. A Mercury Porosimeter for Investigating Capillary Phenomena and Microdisplacement Mechanisms in Capillary Networks. *Journal of Colloid and Interface Science*, 143 (22-36) 1991.
- [214] Morrow NR. Physics and thermodynamics of capillary action in porous media. *Industrial and Engineering Chemistry*, 62 (32) 1970.
- [215] Ge S, Wang CY. Liquid Water Formation and Transport in the PEFC Anode. *Journal of the Electrochemical Society*, 154 (B998-1005) 2007.
- [216] Atiyeh HK, Karan K, Peppley B, Phoenix A, Halliop E, Pharoah J. Experimental investigation of the role of a microporous layer on the water transport and performance of a PEM fuel cell. *Journal of Power Sources*, 170 (111-121) 2007.
- [217] Liu X, Civan F, Evans RD. Correlation of the non-Darcy flow coefficient. *The Journal of Canadian Petroleum Technology*, 34 (50-54) 1995.
- [218] Zeng Z, Grigg R. A criterion for non-darcy flow in porous media. *Transport in Porous Media*, 63 (57-69) 2006.
- [219] Pharoah JG, Karan K, Sun W. On effective transport coefficients in PEM fuel cell electrodes: Anisotropy of the porous transport layers. *Journal of Power Sources*, 161 (214-224) 2006.
- [220] Gurau V, Edwards RV, Mann JA, Zawodzinski TA. A look at the multiphase mixture model for PEM fuel cell simulations. *Electrochemical and Solid State*

- Letters, 11 (B132-B135) 2008.
- [221] St-Pierre J, Wetton B, Kim GS, Promislow K. Limiting current operation of proton exchange membrane fuel cells. *Journal of the Electrochemical Society*, 154 (B186-B193) 2007.
- [222] Wilke CR. Diffusional properties of multicomponent gases. *Chemical Engineering Progress*, 46 (95-104) 1950.
- [223] Kramer D, Zhang J, Shimoi R, Lehmann E, Wokaun A, Shinohara K, et al. In situ diagnostic of two-phase flow phenomena in polymer electrolyte fuel cells by neutron imaging: Part A. Experimental, data treatment, and quantification. *Electrochimica Acta*, 50 (2603-2614) 2005.
- [224] Turhan A, Heller K, Brenizer JS, Mench MM. Quantification of liquid water accumulation and distribution in a polymer electrolyte fuel cell using neutron imaging. *Journal of Power Sources*, 160 (1195-1203) 2006.
- [225] Zhang J, Kramer D, Shimoi R, Ono Y, Lehmann E, Wokaun A, et al. In situ diagnostic of two-phase flow phenomena in polymer electrolyte fuel cells by neutron imaging: Part B. Material variations. *Electrochimica Acta*, 51 (2715-2727) 2006.
- [226] Thompson KE. Pore-scale modeling of fluid transport in disordered fibrous materials. *AIChE Journal*, 48 (1369-1389) 2002.

## Appendix A. Related Publications

### A.1. Refereed Journal Articles

1. Gostick J, Ioannidis M, Fowler M, Pritzker M. On the role of the microporous layer in PEM operation. *Electrochemistry Communications*, Accepted.
2. Gostick J, Ioannidis M, Fowler M, Pritzker M. Direct measurement of the capillary pressure characteristics of water-air-gas diffusion layer systems for PEM fuel cells. *Electrochemistry Communications*, v10, p1520-1523, 2008.
3. Gostick J, Ioannidis M, Fowler M, Pritzker M. Pore network modeling of fibrous gas diffusion layers for polymer electrolyte membrane fuel cells. *Journal of Power Sources*, v173, p277-290, 2007.
4. Gostick J, Fowler M, Pritzker M, Ioannidis A, Behra L A. In-plane and through-plane gas permeability of carbon fiber electrode backing layers. *Journal of Power Sources*, v162, p228-238, 2006.
5. Gostick J, Fowler M, Ioannidis A, Pritzker M, Volkovich Y, Sakars A. Capillary pressure and hydrophilic porosity in gas diffusion layers for polymer electrolyte fuel cells. *Journal of Power Sources*, v156, p375-387, 2006.

### A.2. Conference Presentations

1. Effect of Hydrophobic Polymer Treatments on the Capillary Properties of Gas Diffusion Layers for Polymer Electrolyte Membrane Fuel Cells. AICHE Annual Meeting, Philadelphia, PA, November 16 – 21, 2008.
2. Analysis and Verification of MEA Degradation Mechanism in PEMFC Through SEM Images and Direct Gas Mass Spectroscopy. 4<sup>th</sup> International Conference on Flow Dynamics, Sendai, Japan. September 26 & 27, 2007.
3. Capillary Pressure and Permeability of Gas Diffusion Layers: Measurement and Pore Network Modeling. 210<sup>th</sup> Meeting of the Electrochemical Society, Cancun, Mexico. October 29 – November 3, 2006.
4. Measurement of hydrophobic pore volume in GDLs at elevated temperatures. 9<sup>th</sup>

Grove Fuel Cell Symposium, London, UK. October 4 – 6, 2005.

5. Effectiveness of PTFE Coatings on GDLs at Elevated Temperatures. 1<sup>st</sup>  
Symposium on Manufacturing of MEAs for Hydrogen Applications, Dayton, OH.  
August 9 – 11, 2005.

## Appendix B. SEM Images of GDLs

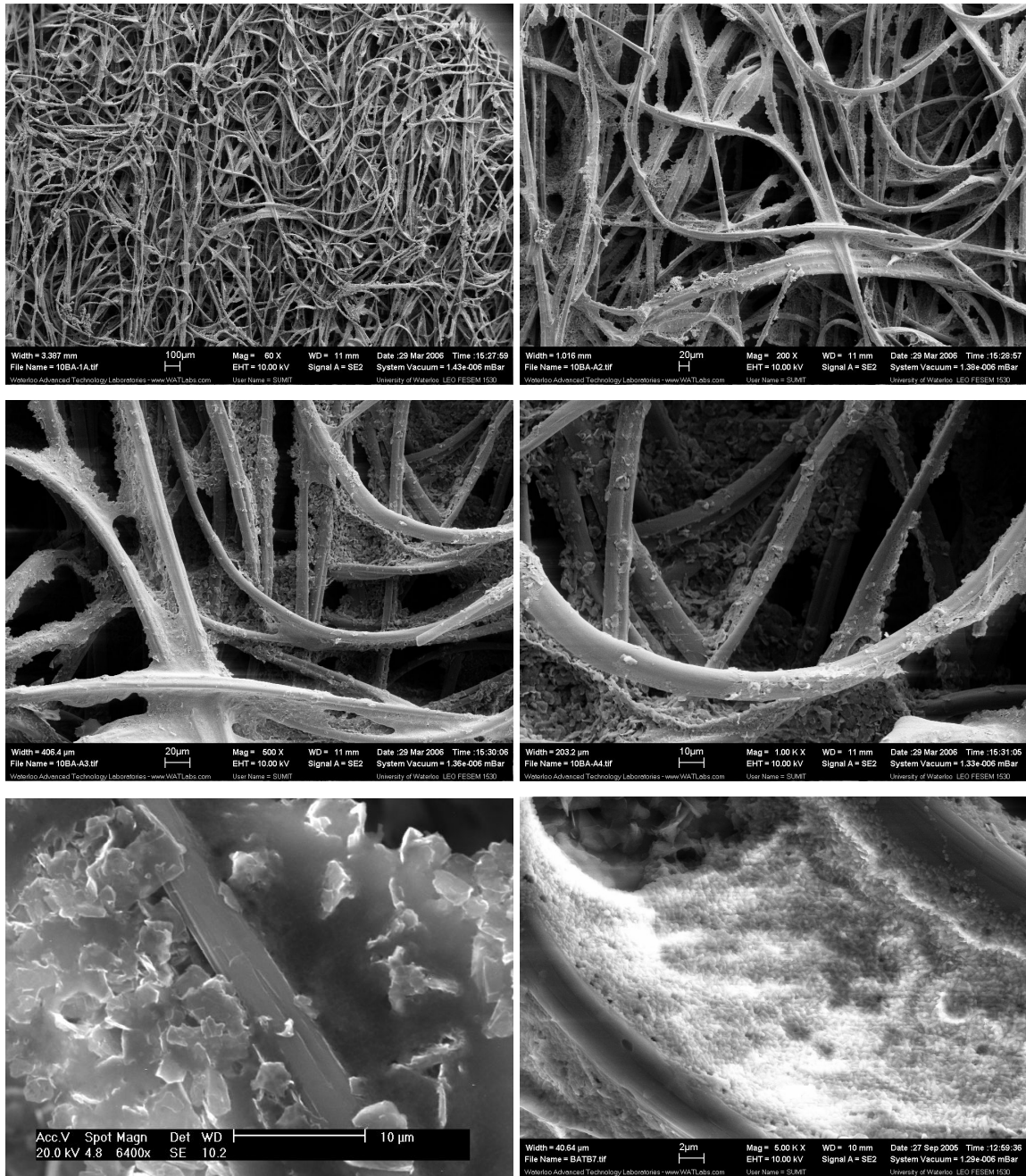
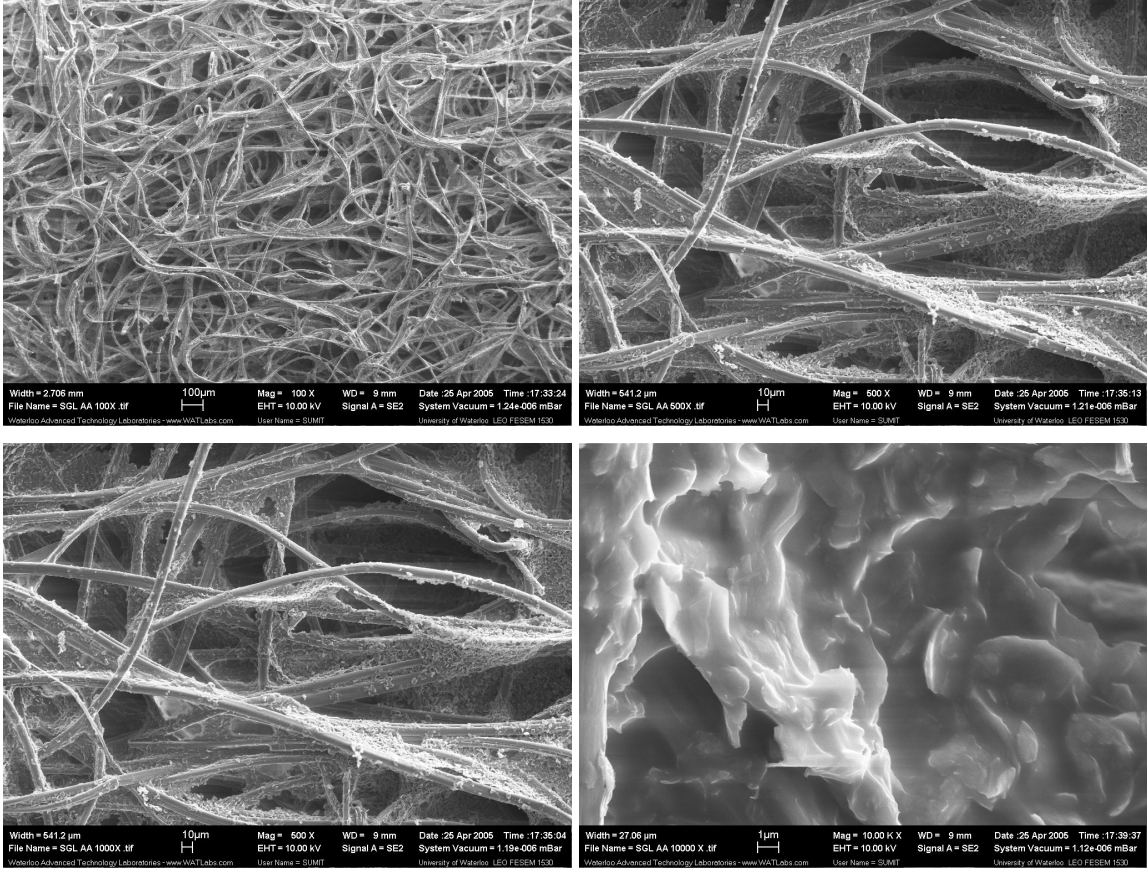
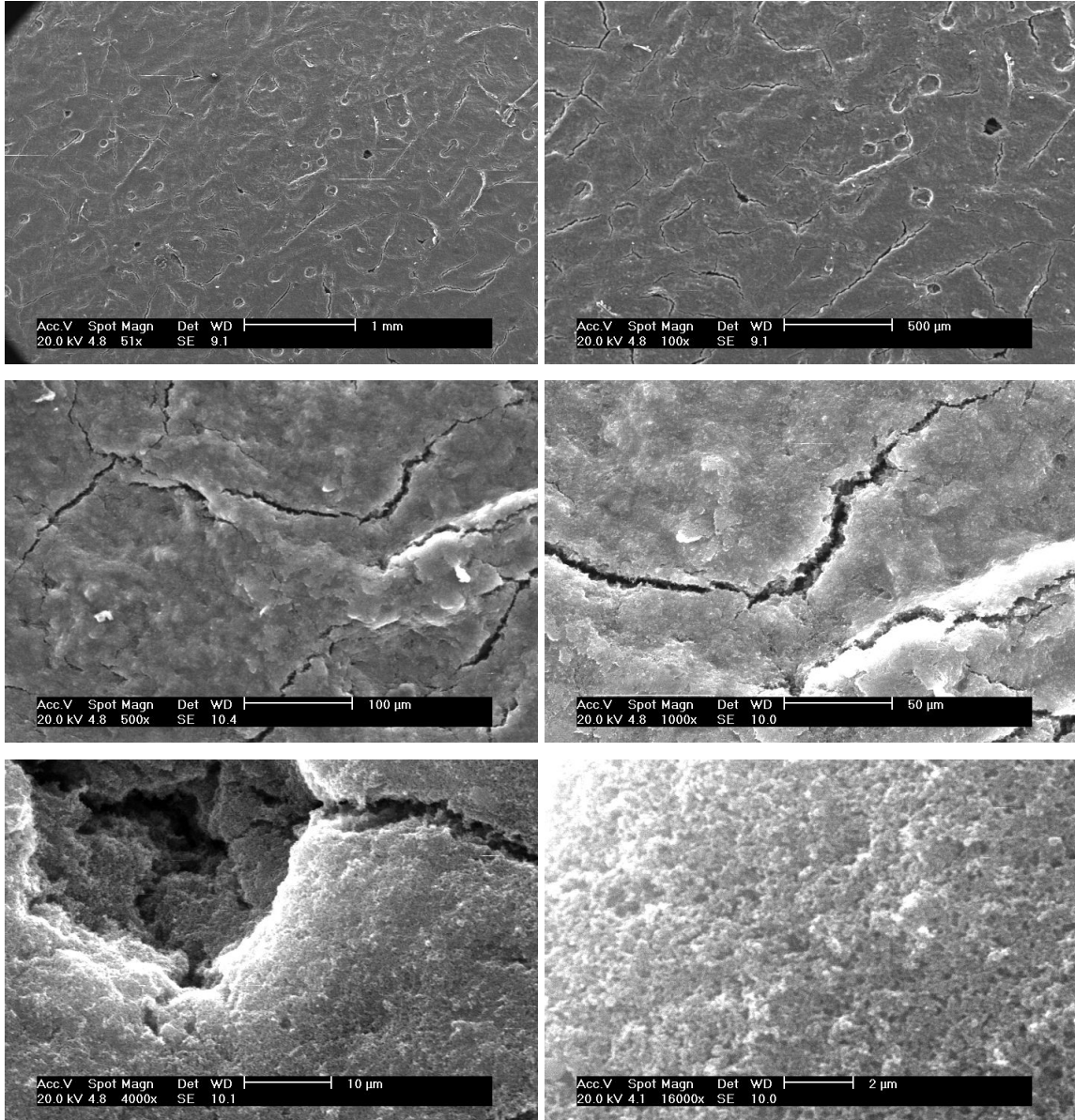


Figure B.1: SEM images of 10BA at increasing magnification



**Figure B.2: SEM images of 10AA at increasing magnification**



**Figure B.3: SEM images of 10BB Microporous layer at increasing magnification**

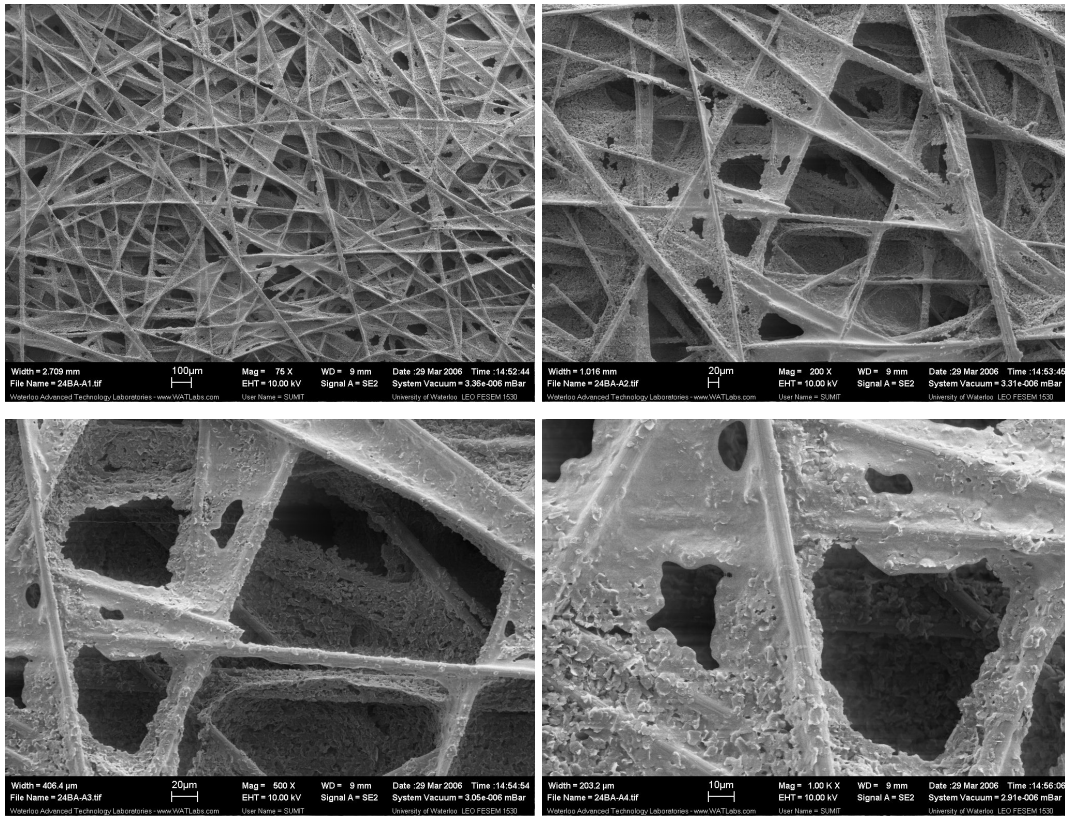


**Figure B.4: SEM images of 24BA at increasing magnification**

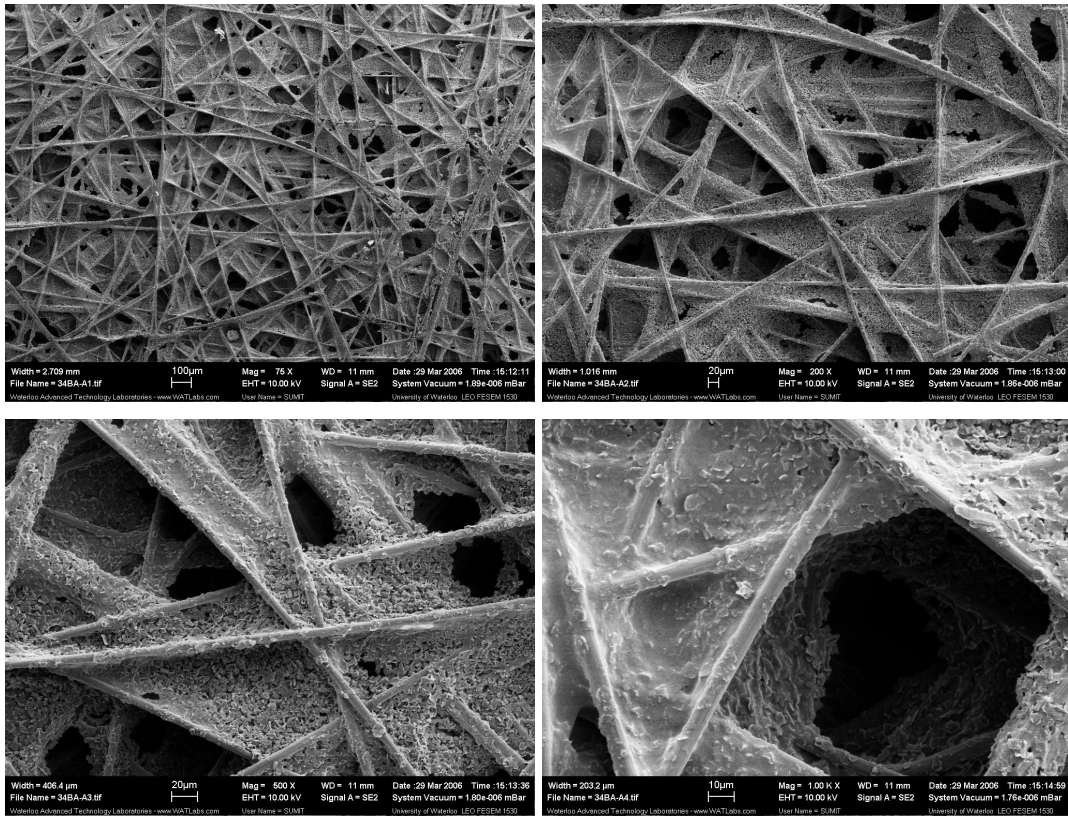


**Figure B.5: SEM images of 34BA at increasing magnification**

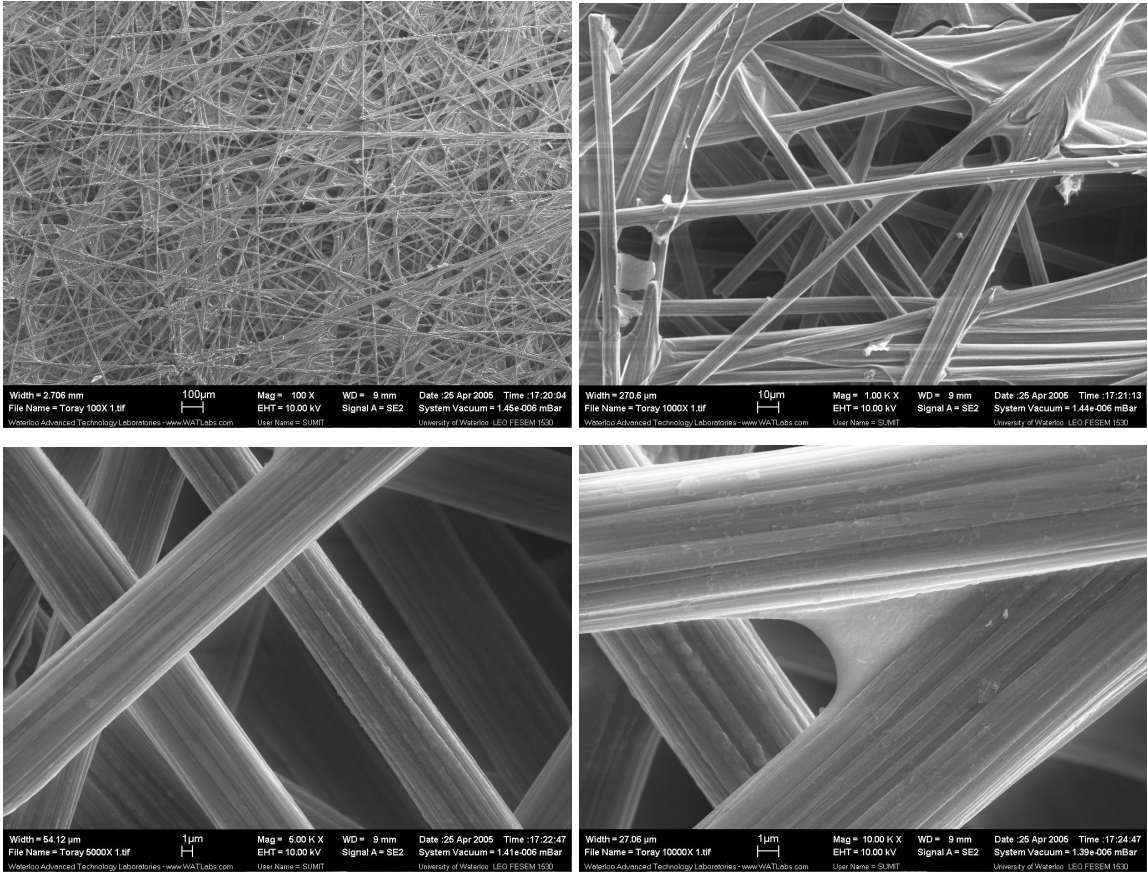


**Figure B.6: SEM images of Toray 090 at increasing magnification**

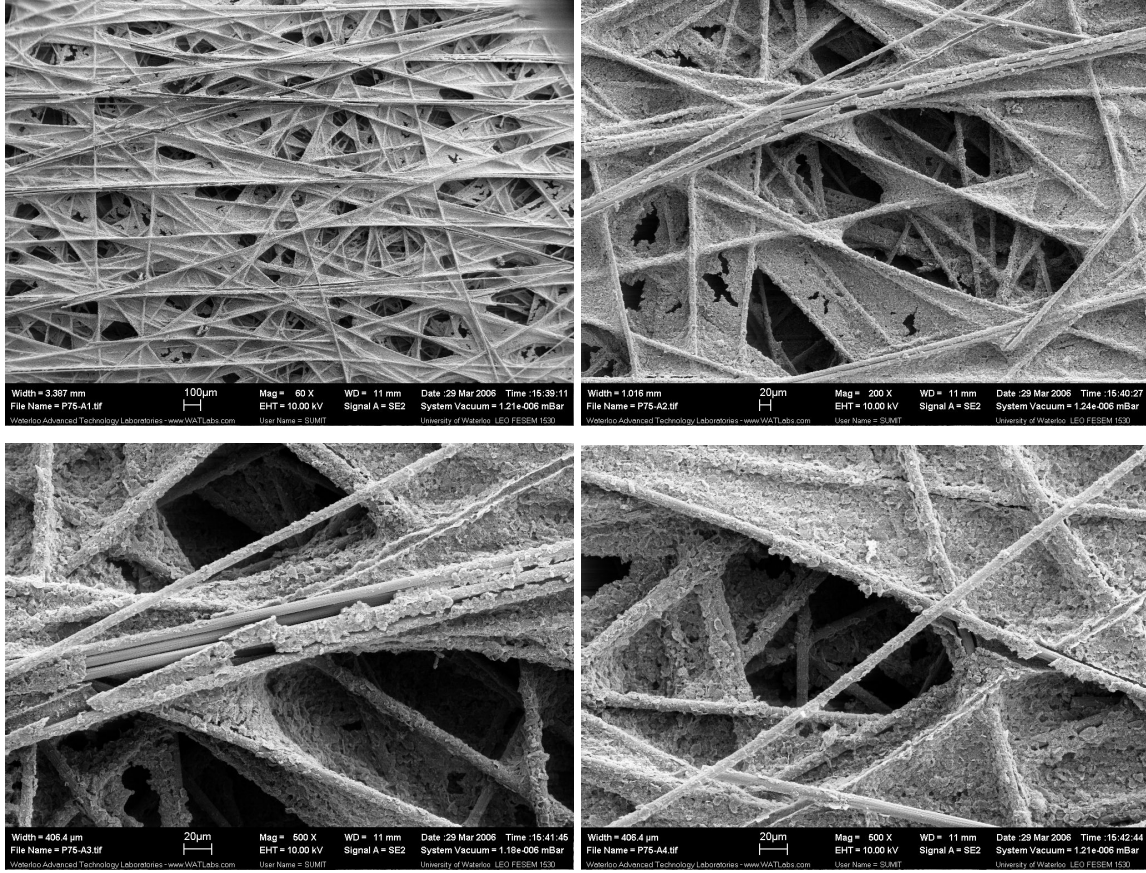


**Figure B.7: SEM images of Ballard P75 with no PTFE at increasing magnification**

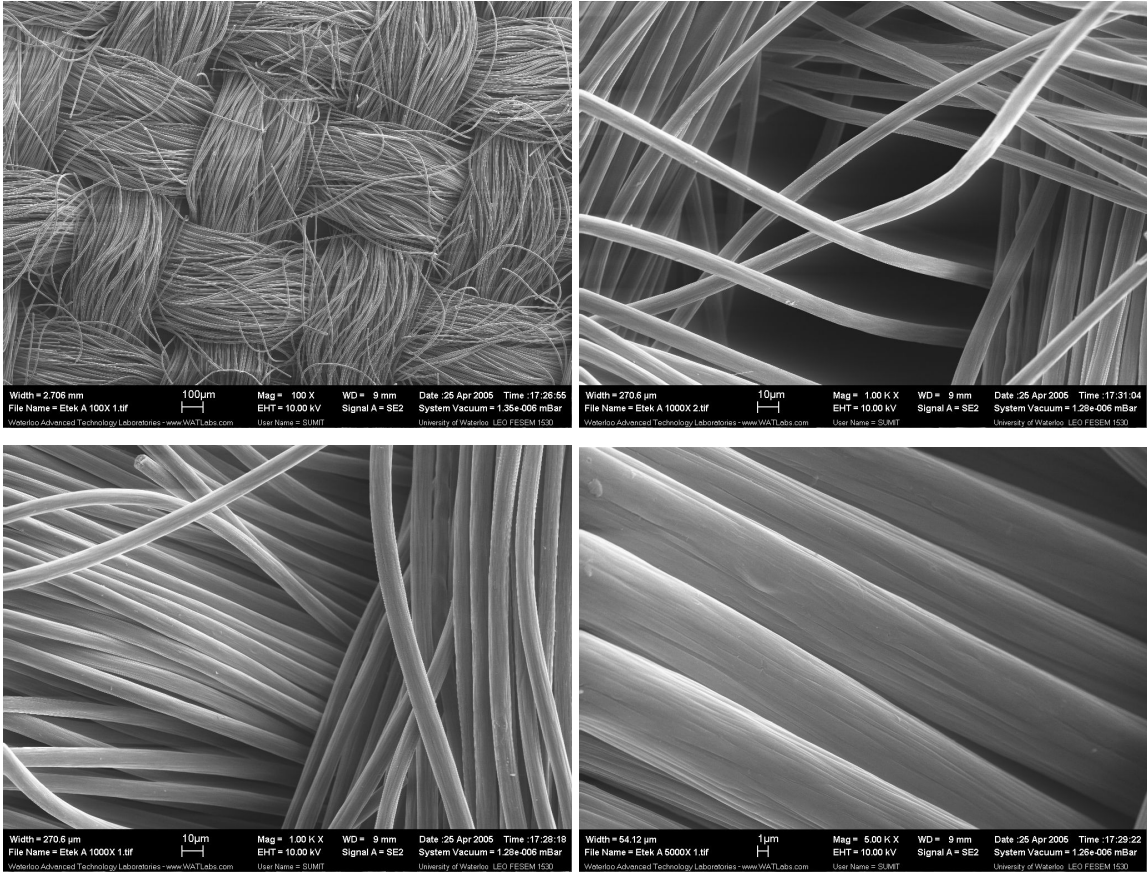


**Figure B.8: SEM images of E-Tek Cloth 'A' at increasing magnification**